Micromechanics of Finite Length Fibers in Composite Materials

by

Gregory Paul Carman

dissertation submitted to the Faculty of the

Virginia Polytechnic Institute and State University

in partial fulfillment of the requirements for the degree of

Doctor of Philosophy

in

Engineering Mechanics

APPROVED:

Kenneth L. Reifsnider, Chairman

Mark S. Cramer

D.P.H. Hasselman

Scott L. Hendricks

Edmund G. Henneke II, Dept. Head

December, 1991

Blacksburg, Virginia

Micromechanics of Finite Length Fibers in Composite Materials

by

Gregory Paul Carman

Kenneth L. Reifsnider, Chairman

Engineering Mechanics

(ABSTRACT)

A theoretical model is derived to study the point-wise stress variations which occur in the constituents of a hybrid 3-D short fiber composite subjected to arbitrary homogeneous loading conditions. The model includes the capability to analyze composites containing different types of fibers, different aspect ratios of fibers (as well as continuous fibers), and different fiber orientations. The composite's stiffness tensor is developed by volume averaging the point-wise stress field in each constituent present in the material system. Validation of the model is accomplished by comparing predicted stiffness properties to experimental data and other accepted models presently available in the literature for PMC's, MMC's, and BMC's.

A derivation of a theoretical model describing the resulting point-wise stress redistribution which occurs in the matrix and the fibrous regions caused by fiber-fiber interaction at the ends of finite length fibers or fractured fibers is also presented. This theoretical development includes the significant dependence of stress redistribution on fiber volume fraction, constituent properties, and crack size. Therefore, its use is not limited to polymeric composites but is also applicable to metal matrix and ceramic matrix systems. The model is extended to include one of the first quantitative analyses of variable fiber spacing which occurs in virtually every composite manufactured. A novel fiber discount method is proposed to study multiple fiber fractures which are of extreme importance when attempting to predict tensile strength of fiber dominated composite laminates.

A test methodology employing a macro-model composite with embedded strain gauges is presented which can be used to validate (or invalidate) micro-mechanical models currently being developed and used by the scientific community. Results obtained with the embedded resistance gauges and the embedded fiber optic strain sensors (FP-FOSS) are validated with classical test and analytical techniques. These techniques include model composites subjected to thermal effects and mechanical loading sequences. The ability to vary specific physical parameters in the experimental model, such as fiber aspect ratio, fiber volume fraction, interphase/interface, and constituent properties (i.e. model PMC's and MMC's), in a systematic fashion enables this technique to study various physical aspects present in actual composite systems. The capability to initiate a fiber fracture at a specific location and load level is demonstrated. It is revealed that significantly different strain concentration exists in PMC composites which contain different fiber volume fractions and crack sizes. By varying fiber spacing between neighbors, a study is initiated on composites containing eccentrically located fibers. These results demonstrate that an asymmetric stress state exists in composites containing variable fiber spacing and fiber fractures. The fact that multiple fiber fracture is achieved in a methodical fashion demonstrates the versatility of the model. These studies show that this experimental technique can model various physical phenomena which occur in actual composite systems.

Acknowledgements

The author would like to thank Dr. Kenneth L. Reifsnider for his confidence in the author's ability to achieve specific goals. This single philosophical commitment to an individual provides one with a sense of personal pride and accomplishment. Thanks are also due to the committee members Drs. Edmund G. Henneke, Mark S. Cramer, Scott L. Hendricks, and D.P.H. Hasselman for the time they took out of their busy schedules to oversee this student's progress. A special thanks is extended to John J. Lesko for the invaluable aid he provided the author in the laboratory and in analytical discussions. Gratitude also goes out to Ahmad Razvan, who initiated the test setup and permitted the author to continue this work. Additionally, Scott Case is appreciated for the time he spent working on laboratory tests and proof reading this dissertation. Most of all the author would like to thank his parents for their undying support and encouragement throughout his life.

Table of Contents

List of Illustrations

List of Tables

1.0 Introduction

The micromechanics of composite materials has received considerable attention in the literature during the past decade. This sudden interest has been driven, in part, by recent findings relating the ultimate strength and stiffness properties obtained at the global or laminate level to micro-parameters present in the material system. The purpose of the present dissertation is to describe the localized stress behavior which occurs in regions containing finite length fibers. To assist in relating the present results to those already established in the literature, the reader is provided with some classical formulations of related micromechanics problems. The following paragraphs present a brief synopsis of the developments under the topics:

- Stress analyses of continuous fiber composites.
- Stress analyses of short fiber composites.
- Stress analyses of composites containing fiber fractures.
- Experimental techniques for the validation of micromechanical theories.

1.1 Literature review

Hill [1] was one of the first to derive an accurate depiction of a transversely isotropic material with cylindrically shaped continuous fibers embedded in an elastic matrix. His elasticity solution provided a continuous point-wise stress/strain tensor for a 1-Dimensional (1-D) oriented composite subjected to arbitrary homogeneous loadings. By volume averaging these tensorial quantities, the stiffness and compliance matrices were calculated for this anisotropic composite material. The predicted global material properties were shown, through the use of energy concepts, to be upper and lower bounds to the actual solution depending upon the type of formulation used (i.e. displacement or traction type). A similar solution was constructed by Hashin and Rosen [2] during the same time period. Therefore, credit for this significant solution in the literature could easily be attributed to either group of individuals.

In recent years, Pagano and Tandon [3] have extrapolated the concentric cylinder model (CCM) described above, to address a more general class of continuous composite systems. These individuals have incorporated the existence of multiple finite interphase regions between the fiber and matrix and 3-D hybrid composite effects into the analysis in an attempt to provide a more realistic depiction of an actual composite. In this specific paper, a displacement formulation was used to develop the theoretical model and study the effect coatings have on the stress redistribution in a composite material.

The relationship which exists between the analysis which describes continuous fiber composites and that which describes short fiber composites should be intuitively obvious. In fact, short fiber composites which contain very long fibers in comparison with their diameter have stiffness values that are indistinguishable from their counterparts (i.e. same fiber volume fraction) in continuous fiber systems. The Halpin-Tsai [4] equations are one example of a theoretical development which was originally derived for the prediction of stiffness values for

continuous composites and subsequently extrapolated to short fiber systems. The augmented model utilizes the analytical structure for the continuous fiber theory and incorporates an extrinsic parameter calculated either from experimental evidence or other appropriate elastic analysis to account for short fiber effects. These semi-empirical relations for stiffness values, represent the effect of not only fiber aspect ratio but also fiber packing sequence (e.g. square array or hexagonal array). When compared to experimental evidence, the analysis exhibits good correlation; however it does not provide point-wise stress values for the constituent properties. These stresses are essential for accurate strength predictions.

In an attempt to extrapolate the ideas presented by Halpin-Tsai to composites containing nonaligned fibers, Berthelot [5] presented a theoretical analysis to study the effect unaligned short fibers have on the axial stiffness. The Halpin-Tsai equations [4] are used in this analytical development for the generation of stiffness values for a unidirectional short fiber composite. The author makes the assumption that the fibers in the composite are uniformly oriented within a known angle referenced by the principal axis. By utilizing the transformation relations of the fourth order stiffness tensor and volume averaging techniques, a prediction for the stiffness values was obtained. In this paper the author validates his results with comparisons between the theoretical predictions and experimentally determined values to assess the accuracy of the model.

With regard to the development of direct short fiber based micromechanical models, one of the first treatments was constructed by Cox [6] in 1952. He assumed that a regular array of aligned isotropic fibers existed in a matrix material which constituted a composite mat. The load transfer which occurs between the matrix and the fibers near the fiber ends was derived to be an exponential decay as a function of the axial coordinate. This formulation was actually a forerunner for the more popular classical solution describing the stress redistribution which occurs near a broken fiber (i.e. shear lag) in a continuous composite system. This groundbreaking analysis provided the axial stiffness values and longitudinal contraction in the composite mat subjected to a uniaxial load. The author provides a comparison between the

predicted values and the experimentally determined values for the mechanical properties calculated.

In a analogous approach, Choon and Sun [7] presented an analysis to predict the normal and interfacial shear stress distribution along the fiber/matrix interface for a short fiber composite. They developed the stress profile for a more general class of problem, that is a randomly oriented short fiber composite subjected to pure tensile loading. The formulation presented by these individuals was based on classical shear lag concepts similar to those derived by Cox. This research was aimed at investigating the effect constitutive properties and fiber aspect ratio have on the axial stiffness of sheet molding composite (SMC) materials. From the calculated maximum fiber/matrix interface shear stress values, tensile strength values were insinuated

Fukuda and Chou [8] investigated the stress distribution in unidirectional short fiber composites subjected to uniaxial tensile loading. They employed a hybrid shear lag model similar to Cox for the derivation of the stress redistribution which occurs near the fiber ends. The present analysis expanded upon previous ones with the incorporation of load transfer between the fiber ends and the surrounding matrix to represent a perfect bond at this juncture. This research initiative analyzed metal matrix composites (MMC), where significant load transfer may occur at the fiber ends due to chemical adhesion between the constituents. The fiber and matrix materials were assumed to be isotropic systems with the typical shear lag assumption aptly describing each constituent. In a subsequent paper [9], these individuals included the effect of plasticity in the matrix material, typical in MMC's, to develop tensile strength predictions for a unidirectional short fiber composite. To validate the model, they compared the theoretical results calculated with unidirectional strength values in the literature.

Some short fiber models present in the literature have attempted to model the fiber as a convenient shape, such as the classic formulation which assumes that the embedded fiber can be represented by an ellipsoid. Eshelby [10] first solved this often-referenced elasticity prob-

lem for an ellipsoidal shaped inclusion embedded in an infinite matrix by assuming that the inclusion and matrix are isotropic. The formulation was accomplished by analytically applying a traction to the inclusion. This simulated the restraining effect on the inclusion due to the matrix. A equivalent traction was also applied to the internal bulk matrix to simulate the effect the inclusion had on this material. With this analysis, he discovered that the state of strain in the inclusion was uniform and was thus able to calculate the tensorial stress components at the interface between the inclusion and matrix. However, the stress state in the matrix region around the inclusion was suggested to be complex and and was not presented in Eshelby's paper. This derivation included the capability to calculate the stiffness tensor for a composite material containing a dilute suspension of these ellipsoidal inclusions.

Russel [11] developed a solution to the short fiber problem by making the assumptions that the fibers and matrix are isotropic and the fiber shape can be represented by an arbitrary axial geometry with a circular cross section. The composite consisted of a dilute concentration of aligned fibers subjected to an arbitrary homogeneous strain. In this derivation, Russel [11] utilized the 'slender-body' theory which has been applied to flows of aerodynamic and hydrodynamic interests to develop the complete solution. The general results derived in this work can only be solved for either very small for very large aspect ratios of the inclusion, most other geometries do not have analytic solutions. Therefore in this work, the fiber geometry was subsequently chosen as ellipsoidal to circumvent this restriction. The final results were shown to be consistent with the analysis provided by Eshelby [10].

Chou et al. [12] derived relations to predict hybrid short fiber composite stiffness properties in which different fiber types are present and where the fibers are assumed to be ellipsoidally shaped, aligned, and uniformly spaced throughout the composite. This problem was solved using a self consistent approach, where the infinite matrix surrounding the inclusion of interest was assumed to have the stiffness properties of the macro composite. The model constructed is functionally dependent on fiber aspect ratio, fiber volume fraction, and constituent properties, as it should be. Stiffness results presented by these researchers are compared with

other short fiber models present in the literature. During this same time period Laws and McLaughin [13] published a similar approach to this same problem.

Takao et al. [14] studied the effect of mis-oriented ellipsoidally shaped short fibers on the axial stiffness of a composite system by presenting a solution similar to that derived by Eshelby [10] and the methodology presented by Taya, Mura, and Chou [15,16]. The elastic stiffness results derived in this analysis directly depend on stiffness parameters such as constitutive properties, fiber aspect ratio, and fiber volume fraction, and indirectly depend on fiber/fiber interaction. Results are compared with other self consistent methods which represent bounds to the exact solution.

Mikata and Taya [17] developed a solution depicting the stress field for a coated fiber embedded in an infinite isotropic matrix subjected to biaxial loading by assuming that the single fiber could be represented by two confocal spheroids with isotropic properties. Boussinesq-Sadowsky stress functions were utilized to develop the elasticity solution for the point wise stress field in the composite system. The main thrust of this research was to study the effect of coating thickness, constitutive properties, and fiber aspect ratio on the stress field in and around the embedded fiber.

Chang et al. [18] presented an analysis for a three dimensional composite containing isotropic short fibers by utilizing the results of Kelvin and the analysis for a single fiber embedded in an infinite matrix subjected to known step loading conditions along it's perimeter. This methodical approach extended the analysis of it's forerunners by characterizing a composite containing a repeating array of short fiber systems subjected to uniaxial loadings. From this analysis the researchers were able to determine the effective axial modulus and contraction ratio when the composite is subjected to axial loadings.

Owen [19] studied the stress and displacement fields which occur in aligned short fiber composites containing isotropic constituents with a equivalent material approach. He replaced the

fiber with matrix material subjected to a strain distribution which would produce the same composite response with the fiber present. The development of the model included the analysis of a composite with a free surface, as opposed to considering the composite as an infinite body. This numerical modeling effort was not validated with other experimental data or established theoretical models.

Aboudi [20] developed a micromechanics model to predict stress strain relations of short fiber composites which is also applicable to continuous fiber composites. The theory consists of identifying a repeating unit cell within the composite material and then decomposing it into subcell regions identified by their material properties. The reader should be aware that this analysis models the subcells (i.e. short fibers) as a parallelpiped, and makes the assumption that the embedded fibers have a rectangular cross-section. A linear displacement field is assumed to exist within each subcell. Using this, along with continuity of stresses and displacements at the interfaces between subcells and cells, relations are developed relating micro-parameters to global constitutive equations. Inelastic effects are also described within this paper with arbitrary yield functions for the matrix material. Validation of this analysis consisted of a comparison of the predicted global stiffness values to those reported in current literature.

Finite element programs have also been utilized to analyze short fiber composite systems, such as Carman [21], who investigated both stress redistribution and axial stiffness values in short fiber composites. He represented the fibers as square entities embedded in a matrix material and incorporated the effect of multiple fibers in the mesh to study fiber/fiber interaction. This study investigated the effect fiber aspect ratio, fiber volume fraction, and fiber distribution have on global stiffness values. Results were compared with experimentally determined values for several metal matrix composites with good agreement.

Analogous representations exist for continuous fiber composites containing fiber fractures to the above-mentioned stress analyses of finite length fiber composites. The only difference

between the two situations is the fractured fiber depicts a problem which has zero tractions at the fiber end while the finite length fiber depicts a problem which may not necessarily be traction free. Rosen [22] was one of the first individuals to investigate the stress redistribution which occurs in the vicinity of a fractured fiber in a unidirectional continuous composite material. By making what has been regarded as classic assumptions (i.e. in polymeric composite materials the matrix supports essentially no normal stresses and the fiber supports no shearing stresses) the shear lag solution was formulated. This analysis suggested that the stress terms decay exponentially at the fiber end as a function of the axial direction. These equations also provide a theoretical prediction for the size of the region subjected to the stress redistribution affected by the fiber fracture, which has been coined 'ineffective' length. The term 'ineffective' describes the inability of the fractured fiber to support any substantial load over this region.

Whitney and Drzal [23] extended the shear lag concepts to include axial load transfer in the matrix and shearing stresses in the fiber. This analysis is applicable to a single fractured fiber in an infinite matrix, but does not address stress concentration effects due to fiber/fiber interaction. With the use of the equilibrium equations, symmetry conditions, concentric cylinders model, and an assumed functional dependence of the stress functions on the radial coordinate, they were able to obtain an approximate solution to this problem. The ineffective lengths calculated for the fractured fiber were compared with experimentally determined values for two composite systems utilizing a single fiber fracture test methodology to validate the micromechanical model.

To address the stress concentration on neighboring fibers due to fiber fracture, Hedgepath and Van Dyke [24] presented an analysis utilizing shear lag concepts along with an influence function approach. They formulated the problem for 2-D and 3-D composites containing either a square or a hexagonal packing of fibers and provided stress concentration values for adjacent fibers in composites which contained multiple fiber fractures. The model, while quite useful, did not incorporate the functional dependence of fiber volume fraction or constituent

properties on stress concentration and is thus only applicable to high modulus fiber systems, very low modulus matrix systems, and large fiber volume fraction composites.

Fariborx and Harlow [25] extended the ideas presented by Hedgepath and Van Dyke [24] and Zweben [26] to formulate an analysis which includes hybrid polymeric composite effects into the stress concentration predictions. They presented a 2-D model which was derived from a simplified shear lag approach, influence functions in a more tractable form, and the specification of the far-field field strain value in the fiber. The fact that hybrid effects were considered gives the impression that stress concentration values are at least dependent upon fiber modulus ratios and fiber area ratios, but are still not dependent upon the physical properties of the matrix. One should also note that the resulting stress redistribution in this model, as in other models, fails to satisfy global equilibrium requirements.

Goree and Gross [27] approached the fiber fracture problem in a similar fashion to that described by Hedgepath and Van Dyke [24]; that is, by utilizing influence functions and shear lag. They extended the previous author's work with the inclusion in the analysis of transverse fiber displacements to the existing axial displacements already used in the previous formulation. They compared their results with 2-D shear lag solutions and with Hedgepath and Van Dyke [24] results. A similar solution was generated by Eringen and Kim [28]; the results of the latter differ from Goree and Gross [27] in the equilibrium equations used and in the 3-D geometry considered.

Adams [29] developed a finite element simulation for the single fiber fracture problem applicable to metal matrix composites. He attempted to describe the subsequent crack propagation problem which occurs in the vicinity of a fiber fracture where the crack extends into the matrix. A boundary condition was instituted which was a function of the crack size to simulate crack arrest behavior which occurs in the neighborhood of the high stress region surrounding a fiber fracture.

To derive a relationship between stress redistribution which occurs due to fiber fracture and unidirectional strength of composite systems, Batdorf [30] presented a statistical methodology. He noted that the strength of a single fiber correlated well with the distribution of flaws along its axial direction, suggestive of a Weibull distribution. With a knowledge of the stress concentration values and the ineffective length due to multiple fiber fracture, a mathematical instability can be constructed for the problem which can be used to estimate the ultimate strength of the composite.

Fukuda [31] studied unidirectional composites containing randomly spaced fibers. This theoretical development which employed classic shear lag analysis along with statistical concepts developed by Batdorf [30] to obtain strength values for the material. The stress concentrations were calculated in a similar fashion to that described by Hedgepath and Van-Dyke [24], except that fiber spacing was considered to be non-uniform. Probabilistic concepts were utilized with these stress concentration values to predict the ultimate strength of the composite. It was shown that material systems containing randomly spaced fibers exhibit smaller strength values than do material systems with uniformly spaced fibers.

Harlow and Phoenix [32] presented a more complete study of the tensile strength of a 2-D composite system utilizing a statistical analysis similar to Batdorf [30]. These investigators included a two parameter Weibull distribution based on evidence presented in the literature concerning the strength distribution in single fibers which suggested that flaws could be categorized as either major or minor. They were able to demonstrate that strength was relatively independent of the ineffective length for certain values of the Weibull parameters. It was also claimed that a two parameter Weibull distribution is apparently unnecessary when calculating the strength of composite systems.

Micro-mechanical models have typically been verified with the comparison of the averaged predicted results with macro-mechanical properties, as in the work performed by Adams [33]. He constructed a finite element program to model a representative element consisting of a

single fiber and surrounding matrix present in the composite system. The calculation of the global composite response was determined from knowledge of the localized displacements exhibited by this element along with the assumption that the cell modeled is representative of the entire composite. By comparing the response predicted by the model at the micro level to that experimentally measured at the global level, an indication of the micromechanical model accuracy is obtained. In this particular study an investigation of the interface influence on the response of a composite to transverse loading was presented.

There have been several laboratory attempts to study micro-phenomena at the local level, however most of these techniques require an accurate micro-mechanical model to interpret the experimental results. Verpost, Desaeger, and Keunings [34] have presented a review of three classical test methods of micromechanical properties to study interphase strength. The three techniques are the pull-out test, push-in test, and single fiber fragmentation test. All of these test methods, and associated ones in the literature (e.g. micro-bead test), rely on micromechanical models to imply quantitative values of the interphase shear strength. The discrepancies in results, both qualitatively and quantitatively and the dependence on the test technique used, renders these test techniques inappropriate for accurate validation of either theoretical models or micromechanical properties.

Macro-model composites have begun to be used to provide a better understanding of some micro-tests. Pigott and Dai [35] utilized a macro-model composite to assess the micro-pullout test classically used to study interphase strength. These scientists embedded a finite length steel rod (millimeters in diameter) in an epoxy matrix in an attempt to study the effectiveness of the pull-out test. It was demonstrated that the debonding force required to pull the rod out fit an empirical relation quoted extensively in the literature. A suggestion was made that this technique should be capable of providing not only the debonding energy at the fiber matrix interphase but also the frictional constants mathematically describing the sliding of the fiber past the matrix.

Ashbee and Ashbee [36] utilized photoelastic methods to investigate the stress redistribution which occurs at short fiber ends embedded in composites. They were particularly interested in the effect different interphase regions have on the as-cured stress state near the fiber ends. A discussion was also presented in this publication describing the effect water absorption has on the stress redistribution in short fiber composites. All data discussed in this paper were of a qualitative nature, describing the differences between two distinct situations as compared to quantitative numbers regarding actual stress transfer.

James, Morris, and Cox [37] presented a methodology to measure micro-details on the surface of composite specimens. These individuals compared SEM and/or optical micrographs taken before and after the application of a thermo/mechanical load to the material system. Relative displacements were measured with cross-correlation techniques of pre- and post-surface texture conditions in the composite system. This methodology is conjectured to have an accuracy of plus or minus 10 angstroms for the SEM micrographs, and may be quite useful for surface-related micromechanical issues. However, only limited applications are possible for internal damage evaluation.

Waite et al. [38] embedded an optical fiber into a woven glass epoxy composite to asses the viability of measuring internal strains. The polarization fiber optic is 10 times larger in diameter than the structural fibers used in this study, and should not be regarded as unobtrusive. The optical fiber was coated with several different substances to effectively alter the adhesion between the optic and the host material. It was shown that application of certain interphases to the optical fiber provided a more optimal output from the embedded sensor. The ability to measure accurate strain data inside the composite was concluded by the researchers to be "coarse", with additional investigation being required to fully assess its viability as an embedded strain gauge.

1.2 Summary

As described in the previous section, there are a number of models available in the literature which quantify the effects of various physical parameters on the stiffness properties of short fiber composites. These models can be classified into several different categories depending upon their theoretical development. The first group discussed was formulated on the results obtained from continuous fiber systems and the empirical relations derived from experimental evidence (or other theoretical considerations)and were used to predict composite stiffness values. However, these models are usually case specific and do not provide point-wise stress variations in the constituents. The second class of short fiber models described in the literature review was derived from concepts typified by shear lag analyses. These models considered only axial loading cases, and such, were only able to provide axial stiffness predictions and axial Poisson ratios. Nonetheless, point-wise stress predictions were generated for these distinct loading cases in each constituent. The majority of these models also did not consider the substantial stress transfer which can occur at the fiber ends. These stated limitations are mainly due to the inherent assumptions in the shear lag analyses (e.g. the matrix is incapable of supporting a normal load). It was also shown in the preceding section that a few authors have used approximating shapes, such as ellipse, in the analysis of short fiber systems. The ellipsoidal inclusion model is an exact elasticity solution to the specific problem posed. However, these models are only applicable to dilute concentrations and they do not accurately depict the significant stress redistribution at the fiber ends, at least in cylindrically shaped fibers. The literature review also discussed models developed on the assumption that the fibers could adequately be depicted as parallelpipeds. This included finite element formulations for the short fiber problem. However, once again these models can not provide the detailed stress information near the fiber ends which are essential for the study of strength properties.

As stated previously, short fiber models and fractured fiber models have similar types of formulations. This is evident in reviewing the number of short fiber models which have been developed on shear lag arguments. In the literature review, it was shown that virtually every model proposed to study the fractured fiber problem was formulated on shear lag assumptions. These models, while providing general information concerning fiber/matrix interaction, fall short of supplying the scientific community with a complete analysis of the fiber fracture problem. The shortcomings in these models include a relationship between stress/strain concentration and constituent properties. The models also suggest that a functional dependence does not exist between stress/strain concentration and fiber volume fraction. The limitations noted above are attributed to the inherent assumptions made in the shear lag type of formulations. These shortcomings, as well as others, inevitably lead to solutions which are case specific and are not applicable to a general class of material systems. In the literature review, some authors used finite elements to study the fiber fracture problem to gain a better understanding of this physical phenomena. However, this methodology is computationally intensive and does not involve the correct physics to describe the singular effects at the crack tip.

The methodologies presented in the previous section to validate micromechanical models were shown to be accomplished by several indirect techniques. First, a number of authors used volume averaging techniques to compare macro-level stiffness predictions with experimentally obtained results. This technique smears out significant details which address stress redistribution at the micro-level and is thus not complete. Some researchers attempted to measure physical quantities such as ineffective length and infer micro-behavior from micromechanical analysis. This requires accurate micro-analysis to generate precise data, and thus leads to circular arguments of providing corroboration of theoretical developments. Studies involving the measurement of surface related phenomena were also presented which suggest subsurface behavior could be inferred with the use of micromechanical analysis. However, these methodologies inevitably lead to circular arguments (i.e. precise microme-

chanics are required to accomplish the task of understanding micromechanics). In the literature review, scientists were beginning to embed internal sensors, such as fiber optics, in composites to measure internal damage states. The problem in using this technique on actual composites was the size of the sensor. The sensing mechanism disturbs the phenomena being studied (Heisenberg uncertainty principle) and is thus obtrusive. Macro-models were also being employed in the study of micro-phenomena to circumvent the size problem, however these models were used to gain a qualitative understanding of micro-tests and were not involved in obtaining quantitative data.

In this dissertation a short fiber model will be developed which provides point-wise stresses in a 3-D composite subjected to general homogenous loads. The formulation is similar in context to shear lag solution described in the previous subsection, however this model incorporates a matrix capable of transferring a normal load and is thus not limited to polymeric composites. Furthermore, the analysis will be formulated to include transverse and longitudinal shear loading cases, unlike the shear lag solutions which only address axial loading. By utilizing a characteristic element concept, a 3-D composite will be constructed which contains different types of fibers and aspect ratio, unlike previous models. By volume averaging the point-wise stresses in each constituent, a complete stiffness and compliance matrix is generated for the composite.

To address fiber-fiber interaction, an analytical model is presented which is also applicable to continuous fiber composites containing fiber fractures. This model is developed with mechanics of materials arguments utilizing equilibrium of constitutive elements, and thus does not suffer from the shortcomings present in shear lag formulations. The analytical model developed provides strain concentration values which are dependent on fiber volume fraction and constituent properties. The model is therefore applicable to a general class of material systems containing fiber ends or fiber fractures, unlike shear lag models. The model is constructed, in such a fashion, to include matrix cracks which occurs near the ends of the fractured fibers. These matrix cracks will be shown to significantly alter the stress redistribution

profile near the fiber end. The concepts described in this paragraph have not been incorporated into models currently available in the literature. The model is subsequently expanded in this dissertation to include variable fiber spacing which provide one of the first quantitative analyses which address this topic. With the incorporation of a unique fiber discount methodology, multiple fiber fracture is studied and evaluated. The results predicted by the model are verified with a direct quantitative measurement technique, believed to be the first of its kind.

The methodology, presented to validate the analytical results, utilizes a scaled up version of an actual composite laminate. It is demonstrated that a desired damage event can be produced in the composite at a prescribed location and load level. With the use of embedded sensors in each constituent, a strain concentration measurement near the internal damage site is performed at the fiber diameter level. The experimental model has the versatility to vary specific physical parameters such as interphase, constituent properties, and fiber volume fraction in a controlled fashion to quantitatively study the effect each has on the stress redistribution in a composite. The test methodology outlined in this dissertation not only validates the models described herein but is also applicable to other micromechanical models under development and present in the literature. It is believed that models such as this one will actually aid in guiding future theoretical developments.

2.0 Short fiber modeling

Short fibers are presently being introduced into sheet molding compounds (SMC), metal matrix composites (MMC), brittle matrix composites (BMC), and a variety of other materials to enhance the mechanical properties exhibited by these composites. Improvements include increased stiffness, increased strength, increased toughness, high temperature durability, reduction in specific gravity, and improved machinability, to name but a few. The scientific community endeavors to theoretically represent the complex interaction between the short fibers and the surrounding matrix, both globally and locally, in an attempt to infer material behavior.

The micro-mechanical behavior of short fiber composites has been analyzed by a variety of authors using a number of different analytical techniques. The demand for this knowledge is presently being driven by the wide use of short fiber composites in aerospace systems and power plant technology as well as in automotive and sporting goods industries. Due to this broad range of applications, the engineer is met with a unique challenge to accurately describe the various mechanical phenomena associated with these different types of composites and their intended use. Also, present day scientists and engineers are faced with a special opportunity and a difficult task, in the sense that they are required to develop new material systems which exhibit predisposed mechanical behavior as opposed to designing systems

around existing materials. In order to meet the current demand created by industry, that is, to be capable of designing new innovative composites and systems, the scientist must have knowledge concerning internal conditions, such as stress variations at the micro-level, to be capable of predicting the desired material characteristics at the global level. This knowledge may include characterizations of property variations within different material regions, geometrical variations of the phases or fibers present, interfacial strengths between phases, and processing parameters. This information combined with a proper theoretical evaluation allows for explicit material development to satisfy specific performance requirements demanded of new innovative material systems.

The model developed in this chapter provides the fundamental basis essential in addressing developmental issues of short fiber composites at the micromechanical level. This analysis makes use of ideas described by Hashin and Rosen [2], Pagano and Tandon [3], Whitney and Drzal [23], and Rosen [21] to depict the localized stress variation in each constituent present in the material system. The short fiber model derived herein depicts a general three dimensional short fiber composite subjected to arbitrary uniform global strains. The solution is presented in closed form and does not incorporate an axisymmetric loading assumption in the theoretical development. The analytical model is also general enough to be applicable for the evaluation of stresses in a continuous three-dimensional composite which contains broken fibers. In this analytical approach, the fibers in the composite are divided into separate categories determined by their orientations, aspect ratio, and fiber type. Each fiber system is depicted by a set of concentric cylinder assemblages and are constructed from the appropriate fiber and matrix material properties, fiber lengths, and fiber volume fractions. A far-field solution is calculated utilizing an elasticity approach for an infinite fiber and matrix cylinder assemblage with the assumption that a state of generalized plane deformation exists. This provides the stress field in the constituents far from the fiber ends. A unique near-field solution is derived with equilibrium equations and boundary conditions to depict the state of stress in the fiber and adjacent matrix near the fiber ends. These two solutions are super-

imposed to obtain the full field stress for each constituent present in the composite. To obtain the global stiffness values, the stress field in each composite cylinder assemblage is volume averaged to determine the global stress tensor. These values are subsequently related to the global strains to develop an accurate lamina level constitutive relation.

This formal analysis expands upon the work performed by previous authors with the introduction of essential items into the theoretical analysis. These include the development of the stress redistribution profile in the constituents of a short fiber composite which is subjected to transverse and shear loads. Previous analyses did not incorporate these significant loading sequences into the formulation of cylindrically shaped fibers. The present analysis also provides the point-wise stresses in the constituents in both the matrix and fiber at the fiber ends for off-axis fiber systems. This provides the capability to study 3-D hybrid short fiber composite affects. The previous analytical developments only address uni-axial oriented fiber systems. With these capabilities, stiffness values as a function of aspect ratio, fiber volume fraction, and fiber orientation are generated. Therefore, the present approach provides a more complete and precise representation of the local stress fields in a short-fiber or a broken-fiber composite, and furnishes a firm foundation for the prediction of composite stiffness and strength properties, as well as the analysis of damage development and long term behavior in these materials.

Validation of the model consists of comparing the predicted elastic properties for several short fiber composites to experimentally determined elastic properties for both polymeric matrix composites and metal matrix composites presently available in the literature. Additional comparisons are also made between the current theoretical analysis and other classical analytical models describing polymeric matrix composites. The versatility of the model is demonstrated by presenting a set of parametric studies for stiffness predictions in a brittle/ceramic matrix composites. To establish the models applicability to continuous fiber reinforced composites, a stiffness reduction section displays the effect multiple fiber fractures have on de-

creasing the apparent stiffness of a polymeric composite subjected to long-term loadings such as fatigue.

2.1 Analysis

A point-wise continuous stress analysis is developed in the following section for a 3-D hybrid short fiber composite subjected to arbitrary homogeneous loadings. The general assumptions involved in this analysis are the following: The constituents present in the composite exhibit linear elastic behavior. The embedded fibers are transversely isotropic, and the surrounding matrix material is isotropic. The fiber/matrix interface is a 'perfect' bond, such that decohesion does not occur between the two materials. Fiber-fiber interactions (i.e. side by side, as treated in chapter 3) are neglected, however this does not neglect axial stress transfer between short fiber ends (i.e. end to end) which may be in close proximity to one another. In the ensuing analysis a short fiber composite is specifically addressed, however the derivation is presented in a sufficiently general fashion to include continuous fiber systems containing broken fibers.

In this analysis, the characterization of specific physical parameters such as fiber type (Ξ), fiber orientation (Γ), and fiber aspect ratio (Λ) present in the composite system is a necessity to provide an accurate depiction of the stress variation in each constituent. These variables Ξ, Γ, and Λ are inherently defined to be integer quantities which provide simple labels for the various fiber elements (see Figure 1) in the composite and which provide the basic set of elements required to completely describe the composite. Each set of variables defines a fiber system (e.g. fiber(Ξ, Γ, Λ)) which is constructed out of a single fiber and a representative region of matrix. To clarify this nomenclature a typical example follows. If a composite contains two different types of fibers and all the fibers are aligned with some general axis and have the same aspect ratio there would be a fiber(1,1,1) and a fiber (2,1,1). While there may

be virtually thousands of fiber systems in the composite, only two representative ones are required to provide a complete representation of the mechanical response exhibited by this particular composite (see Christensen [39]). When analyzing a general hybrid 3-D composite, the number of fiber systems required to describe the composite would be equal to $Num = \Xi_{max}\Gamma_{max}\Lambda_{max}$, where the subscript max represents the largest integer quantity in the set.

The integer quantities Ξ, Γ, and Λ represent the physical parameters which are used to characterize the composites mechanical response. In regards to Ξ; the different fiber types which are used in the manufacturing process of the composite are characterized by the stiffness tensor which provides a complete description of the fiber's mechanical response. The contracted stiffness matrix is represented in this dissertation by C^n_{ij}, where the superscript n, throughout refers to either a fiber region (n=1) or a matrix region (n=2) in the representative element considered. In regards to Γ; the fiber orientations in a general 3-D fibrous material are described by the solid angles ϕ and ω present in a global spherical coordinate system. These angles are measured with respect to a principal global cartesian axis $[X_1, X_2, X_3]$ determined at the lamina level as shown in Figure 1. The angles will be used in later analysis to develop transformation matrices from the global cartesian coordinate system into a local fiber oriented cartesian coordinate system. Therefore the reader is cautioned not to confuse the various coordinate systems (i.e.global cartesian $[X_1, X_2X_3]$, global spherical $[\phi, \omega]$, local cartesian $[x,y,z]$, and local cylindrical $[r, \theta, z]$) which will be introduced in this derivation (see Figures 1 and 2). In regards to Λ; the fiber aspect ratio in short fiber composites is an important quantity which severely influences the mechanical properties of the material, this value relates the fiber length to its diameter (note: certain papers define this quantity differently). In the present dissertation, the fiber aspect ratio (α) for each fiber system is defined as the fiber length divided by the fiber diameter.

The analysis begins by evaluating the stress and strain state existing in a single fiber system embedded in the composite, labeled by fiber(1, 1, 1). From this solution, other fiber systems

of different fiber type, fiber orientation, and fiber aspect ratio are easily formulated to arrive at a general solution for a 3-D hybrid short fiber composite.

The analytical model generated in this chapter is accomplished in a two stage process. First: an elasticity formulation is constructed to develop the point-wise continuous stress/strain field in a fiber and matrix region which is located at a spatial position far removed from the fiber end with respect to the fiber diameter. This solution essentially corresponds to a continuous fiber composite, that is, end effects are insignificant in these regions. The derivation presented for this analytical portion is referred to as the far-field solution (σ_{ij}). Second: an approximate point-wise stress field is constructed from the traction boundary conditions, the equilibrium equations, and an exponential function to simulate the stress redistribution occurring at the fiber end. The derivation presented for this portion of the analysis is referred to as the fiber end solution ($\tilde{\sigma}_{ij}$). These two solutions are subsequently superimposed to obtain the full 3-D stress field (σ'_{ij}) in the fiber and the surrounding matrix region. The following equation is thus representative of the methodology outlined above for fiber system (1,1,1).

$$\sigma'^{n}_{ij} = \sigma^{n}_{ij} + \tilde{\sigma}^{n}_{ij} \qquad [2.1]$$

The solution to both problems is accomplished with concentric cylinder elements constructed as follows. It is generally accepted that the typical fiber system (1,1,1) can be adequately represented geometrically by a set of concentric cylinder elements (see Figure 2), consisting of both fiber and matrix regions. The radii of the cylinders are chosen such that the ratio of the fiber radius to the matrix radius is equivalent to the fiber volume fraction of fiber(1,1,1) (i.e. $v_f = \frac{r_f^2}{r_m^2}$) in the composite material. It should be noted that the radii may be adjusted to model local variations of fiber volume fraction in the material which predominantly occurs in short fiber composite systems.

In solving the far-field solution, these cylinders are assumed to exhibit a state of generalized plane strain at large axial distances from the fiber ends compared to the fiber diameters. The

boundary conditions prescribed for the problem are formulated by hypothetically applying a displacement to the exterior of the global composite (see Figure 2), such that a uniform global strain exists at that boundary. This global strain value is a known quantity in the analysis. It has been postulated that the fiber system (1,1,1) under consideration must also exhibit this strain value on an average basis, that is, to be a representative element in the composite (see Christensen [39]). Therefore the local average strains in the element can be calculated from the global strains and a rotation matrix. The strains defined with respect to the local cartesian coordinate system are related to the global strains by the following transformation relations

$$\bar{\varepsilon}'_{ij} = a_{ir} a_{js} \bar{\varepsilon}_{rs} \qquad [2.2]$$

where ε_{ij} is the linear global strain tensor, bars denote average quantities, and the prime on the strain quantity represents the local cartesian coordinate system of fiber system (1,1,1). The transformation tensor a_{ij} is constructed with the previously introduced solid angles of fiber(1,1,1) and is represented in the following matrix form.

$$\begin{bmatrix} \cos\omega & \sin\omega\cos\phi & \sin\omega\sin\phi \\ -\sin\omega & \cos\omega\cos\phi & \cos\omega\sin\phi \\ 0 & -\sin\phi & \cos\phi \end{bmatrix} \qquad [2.3]$$

The local cartesian coordinates are defined such that z (see Figure 2) is aligned with the axis of fiber(1,1,1) and $z=0$ represents the interface between the fiber end and the matrix. Note, for the development of the far-field solution we assume that $z \gg r_f$. The displacement boundary conditions u_i on the outer edge of the cylinder assemblage can be evaluated with the use of the local cartesian strains and the local position vector. The displacements are functionally related to the local cartesian strains $\bar{\varepsilon}'_{ij}$ and the local cartesian position vector x_j (i.e. [x,y,z]) through the following equation.

$$u_i = x_j \bar{\varepsilon}'_{ij} \qquad [2.4]$$

With the use of the basic transformation relation between cylindrical and cartesian coordinates, the displacements in terms of the cylindrical coordinate system are explicitly expressed as,

$$u_r = \bar{\varepsilon}'_{xx}\frac{r}{2}(1+\cos 2\theta) + \bar{\varepsilon}'_{xy}r\sin 2\theta + \bar{\varepsilon}'_{xz}z\cos\theta + \bar{\varepsilon}'_{yz}z\sin\theta + \bar{\varepsilon}'_{yy}\frac{r}{2}(1-\cos 2\theta)$$

$$u_\theta = -\bar{\varepsilon}'_{xx}\frac{r}{2}\sin 2\theta + \bar{\varepsilon}'_{xy}r\cos 2\theta - \bar{\varepsilon}'_{xz}z\sin\theta + \bar{\varepsilon}'_{yz}z\cos\theta + \bar{\varepsilon}'_{yy}\frac{r}{2}\sin 2\theta \qquad [2.5]$$

$$u_z = \bar{\varepsilon}'_{xz}r\cos\theta + \bar{\varepsilon}'_{yz}r\sin\theta + \bar{\varepsilon}'_{zz}z$$

The relations between the local cartesian and the local cylindrical coordinates are as usually defined, $z = z$, $x = r\cos\theta$ and $y = r\sin\theta$. The boundary conditions in Equation 2.5 suggest that the displacement fields within the cylinder assemblages may be explicitly expressed in terms of θ and z, that is on an r face the functional dependence of θ and z must be continuous. The displacement functions must also satisfy the strain-displacement, constitutive relation, and equilibrium equations. The equilibrium equations are provided as follows

$$\frac{\partial\sigma^n_{rr}}{\partial r} + \frac{1}{r}\frac{\partial\sigma^n_{r\theta}}{\partial\theta} + \frac{\partial\sigma^n_{rz}}{\partial z} + \sigma^n_{rr} - \frac{\sigma^n_{\theta\theta}}{r} = 0$$

$$\frac{\partial\sigma^n_{\theta r}}{\partial r} + \frac{1}{r}\frac{\partial\sigma^n_{\theta\theta}}{\partial\theta} + \frac{\partial\sigma^n_{\theta z}}{\partial z} + \frac{2\sigma^n_{\theta r}}{r} = 0 \qquad [2.6]$$

$$\frac{\partial\sigma^n_{zr}}{\partial r} + \frac{1}{r}\frac{\partial\sigma^n_{z\theta}}{\partial\theta} + \frac{\partial\sigma^n_{zz}}{\partial z} + \frac{\sigma^n_{zr}}{r} = 0$$

the constitutive relations are written as,

$$\sigma^n_{zz} = C^n_{11}\varepsilon^n_{zz} + C^n_{12}\varepsilon^n_{rr} + C^n_{12}\varepsilon^n_{\theta\theta}$$

$$\sigma^n_{rr} = C^n_{12}\varepsilon^n_{zz} + C^n_{22}\varepsilon^n_{rr} + C^n_{23}\varepsilon^n_{\theta\theta}$$

$$\sigma^n_{\theta\theta} = C^n_{12}\varepsilon^n_{zz} + C^n_{23}\varepsilon^n_{rr} + C^n_{22}\varepsilon^n_{\theta\theta} \qquad [2.7]$$

$$\sigma^n_{r\theta} = (C^n_{22} - C^n_{23})\varepsilon^n_{r\theta}$$

$$\sigma^n_{\theta z} = 2C^n_{55}\varepsilon^n_{\theta z}$$

$$\sigma^n_{rz} = 2C^n_{55}\varepsilon^n_{rz}$$

the strain-displacement relations are written as,

$$\varepsilon^n_{zz} = \frac{\partial u^n_z}{\partial z}$$

$$\varepsilon^n_{rr} = \frac{\partial u^n_r}{\partial r}$$

$$\varepsilon^n_{\theta\theta} = \frac{1}{r}\left[\frac{\partial u^n_\theta}{\partial \theta} + u^n_r\right] \qquad [2.8]$$

$$\varepsilon^n_{r\theta} = \frac{1}{2}\left[\frac{1}{r}\frac{\partial u^n_r}{\partial \theta} + \frac{\partial u^n_\theta}{\partial r} - \frac{u^n_\theta}{r}\right]$$

$$\varepsilon^n_{\theta z} = \frac{1}{2}\left[\frac{\partial u^n_\theta}{\partial z} + \frac{1}{r}\frac{\partial u^n_z}{\partial \theta}\right]$$

$$\varepsilon^n_{rz} = \frac{1}{2}\left[\frac{\partial u^n_z}{\partial r} + \frac{\partial u^n_r}{\partial z}\right]$$

By substitution of strain displacement equations 2.8, into the constitutive relations in 2.7, and finally into the equilibrium equations 2.6, the general governing equations for a cylindrical coordinate system are written as,

$$C^n_{22}(u^n_{r,rr} + \frac{u^n_{r,r}}{r} - \frac{u^n_r}{r^2}) + \frac{C^n_{44}}{r^2}u^n_{r,\theta\theta} + C^n_{55}u^n_{r,zz} + \frac{(C^n_{22} - C^n_{44})}{r}u_{\theta,r\theta} - \frac{(C^n_{22} + C^n_{44})}{r^2}u_{\theta,\theta} + (C^n_{12} + C^n_{55})u_{z,rz} = 0$$

$$(C_{12}^n + C_{55}^n)(u_{r,rz}^n + \frac{u_{r,z}^n}{r} + \frac{u_{\theta,z\theta}^n}{r}) + C_{55}^n(u_{z,rr}^n + \frac{u_{z,r}^n}{r} + \frac{u_{z,\theta\theta}^n}{r^2}) + C_{11}^n u_{z,zz}^n = 0 \qquad [2.9]$$

$$C_{44}^n(u_{\theta,rr}^n + \frac{u_{\theta,r}^n}{r} - \frac{u_\theta^n}{r^2}) + \frac{C_{22}^n}{r^2} u_{\theta,\theta\theta}^n + C_{55}^n u_{\theta,zz}^n + \frac{(C_{22}^n - C_{44}^n)}{r} u_{r,r\theta} + \frac{(C_{22}^n + C_{44}^n)}{r^2} u_{r,\theta} + \frac{(C_{12}^n + C_{55}^n)}{r} u_{z,\theta z} = 0$$

It has been shown by Pagano and Tandon [3]. that the general displacement solutions for each constituent corresponding to Equation 2.9 subjected to boundary conditions in the form of Equation 2.5 are written as,

$$u_r^n(r,\theta,z) = U_1^n(r)\cos 2\theta + U_2^n(r)\sin 2\theta + U_3^n(r) + U_4^n(r)z\cos\theta + U_5^n(r)z\sin\theta$$

$$u_\theta^n(r,\theta,z) = V_1^n(r)\sin 2\theta + V_2^n(r)\cos 2\theta + V_4^n(r)z\sin\theta + V_5^n(r)z\cos\theta \qquad [2.10]$$

$$u_z^n(r,\theta,z) = zW_3^n(r) + W_4^n(r)\cos\theta + W_5^n(r)\sin\theta$$

where,

$$U_1^n(r) = A_1^n r^3 + \frac{A_2^n}{r^3} A_3^n r + \frac{A_4^n}{r}$$

$$U_2^n(r) = B_1^n r^3 + \frac{B_2^n}{r^3} + B_{p3} r + \frac{B_4^n}{r}$$

$$U_3^n(r) = D_1^n r + \frac{D_2^n}{r}$$

$$U_4^n(r) = F_2^n$$

$$U_5^n(r) = H_2^n \qquad [2.11]$$

$$V_1^n(r) = -\frac{(3C_{22}^n + C_{23}^n)}{2C_{23}^n} A_1^n r^3 + \frac{A_2^n}{r^3} - A_3^n r + \frac{(C_{23}^n - C_{22}^n)}{2C_{22}^n} A_4^n \frac{1}{r}$$

$$V_2^n(r) = \frac{(3C_{22}^n + C_{23}^n)}{2C_{23}^n} B_1^n r^3 - \frac{B_2^n}{r^3} + B_3^n r + \frac{(C_{23}^n - C_{22}^n)}{2C_{22}^n} B_4^n \frac{1}{r}$$

$$V_4^n(r) = F_1^n$$

$$V_5^n(r) = H_1^n$$

$$W_3^n(r) = D_3^n$$

$$W_4^n(r) = \frac{F_3^n}{r} + F_4^n r$$

$$W_5^n(r) = \frac{H_3^n}{r} + H_4^n r$$

With use of Equations 2.7, 2.8, 2.10, and 2.11 the point-wise continuous stress field for the far-field problem is written as

$$\sigma_{zz}^n = Z_1^n(r) \cos 2\theta + Z_2^n(r) \sin 2\theta + Z_3^n(r)$$

$$\sigma_{\theta\theta}^n = \Theta_1^n(r) \cos 2\theta + \Theta_2^n(r) \sin 2\theta + \Theta_3^n(r)$$

$$\sigma_{rr}^n = R_1^n(r) \cos 2\theta + R_2^n(r) \sin 2\theta + R_3^n(r) \qquad [2.12]$$

$$\sigma_{rz}^n = RZ_1^n(r) \cos \theta + RZ_2^n \sin \theta$$

$$\sigma_{\theta z}^n = \Theta Z_1^n(r) \sin \theta + \Theta Z_2^n(r) \cos \theta$$

$$\sigma_{r\theta}^n = R\Theta_1^n(r) \sin 2\theta + R\Theta_2^n(r) \cos 2\theta$$

Where Z_i^n, Θ_i^n, R_i^n, RZ_i^n, ΘZ_i^n, and $R\Theta_i^n$ are defined to be

$$Z_1^n(r) = -2C_{12}^n C_{44}^n \left[\frac{3A_1^n r^2}{C_{23}^n} + \frac{A_4^n}{C_{22}^n r^2} \right]$$

$$Z_2^n(r) = -2C_{12}^n C_{44}^n[\frac{3B_1^n r^2}{C_{23}^n} + \frac{B_4^n}{C_{22}^n r^2}]$$

$$Z_3^n(r) = C_{11}^n D_3^n + 2C_{12}^n D_1^n$$

$$\Theta_1^n(r) = 2C_{44}^n[-\frac{3(C_{22}^n + C_{23}^n)}{C_{23}^n} A_1^n r^2 + \frac{3A_2^n}{r^4} - A_3^n]$$

$$\Theta_2^n(r) = 2C_{44}^n[-\frac{3(C_{22}^n + C_{23}^n)}{C_{23}^n} B_1^n r^2 + \frac{3B_2^n}{r^4} - B_3^n]$$

$$\Theta_3^n(r) = C_{12}^n D_3^n + (C_{22}^n + C_{23}^n) D_1^n + \frac{2C_{44}^n D_2^n}{r^2}$$

$$R_1^n(r) = 2C_{44}^n[-\frac{(C_{22}^n + C_{23}^n)}{C_{22}^n}\frac{A_4^n}{r^2} - \frac{3A_2^n}{r^4} + A_3^n]$$

$$R_2^n(r) = 2C_{44}^n[-\frac{(C_{22}^n + C_{23}^n)}{C_{22}^n}\frac{B_4^n}{r^2} - \frac{3B_2^n}{r^4} + B_3^n]$$

$$R_3^n(r) = C_{12}^n D_3^n + (C_{22}^n + C_{23}^n) D_1^n - \frac{2C_{44}^n D_2^n}{r^2}$$

$$RZ_1^n(r) = C_{55}^n[F_2^n - \frac{F_3^n}{r^2} + F_4^n] \qquad [2.13]$$

$$RZ_2^n(r) = C_{55}^n[H_2^n - \frac{H_3^n}{r^2} + H_4^n]$$

$$\Theta Z_1^n(r) = C_{55}^n[F_1^n - \frac{F_3^n}{r^2} - F_4^n]$$

$$\Theta Z_2^n(r) = C_{55}^n[H_1^n + \frac{H_3^n}{r^2} + H_4^n]$$

$$R\Theta_1^n(r) = C_{44}^n[-\frac{3(C_{22}^n + C_{23}^n)}{C_{23}^n} A_1^n r^2 - \frac{6A_2^n}{r^4} - 2A_3^n - \frac{(C_{23}^n + c_{22}^n)}{C_{22}^n}\frac{A_4^n}{r^2}]$$

$$R\Theta_2^n(r) = C_{44}^n[\frac{3(C_{22}^n + C_{23}^n)}{C_{23}^n} B_1^n r^2 + \frac{6B_2^n}{r^4} + 2B_3^n + \frac{(C_{23}^n + C_{22}^n)}{C_{22}^n}\frac{B_4^n}{r^2}]$$

This represents the solution to the far-field problem in terms of calculable constants A_f^n, B_f^n, D_f^n, F_f^n, and H_f^n. These are evaluated from the boundary conditions stated in Equation 2.5 and the continuity of tractions and displacements which is assumed to exist between the fiber and matrix. Additionally the stresses and the displacements in the fiber are bounded, such that constants associated with $\frac{1}{r}$ terms are set equal to zero and infinite stresses or displacements do not occur. These conditions may be expressed in terms of the following equations

$$A_4^1 = A_2^1 = B_4^1 = B_2^1 = D_2^1 = F_3^1 = H_3^1 \equiv 0 \qquad [2.14]$$

$u_i^1(r_f, \theta, z) = u_i^2(r_f, \theta, z)$, and $\sigma_{ri}^1(r_f, \theta, z) = \sigma_{ri}^2(r_f, \theta, z)$

With the use of Equation 2.5, the constants in Equations 2.10 and 2.11 are be evaluated in terms of the applied strains where each constant is generated by a specific local strain term $\bar{\varepsilon}'_{ij}$. By comparing Equation 2.5 to Equations 2.10 and 2.11, it is quite easy to deduce which strain generates the various constants. One finds that A_f^n and B_f^n are functionally dependent on $\bar{\varepsilon}'_{xx}$, $\bar{\varepsilon}'_{yy}$, and $\bar{\varepsilon}'_{xy}$, D_f^n are functionally dependent on $\bar{\varepsilon}'_{xx}$, $\bar{\varepsilon}'_{yy}$, and $\bar{\varepsilon}'_{zz}$, and F_f^n and H_f^n are functionally dependent on $\bar{\varepsilon}'_{xz}$ and $\bar{\varepsilon}'_{yz}$. This dependence can be extrapolated to investigate the influence of strains on the stress terms. For example, the stress term $\sigma_{r\theta}^n$ is generated by in-plane strain terms (i.e. $\bar{\varepsilon}'_{xx}$, $\bar{\varepsilon}'_{yy}$, and $\bar{\varepsilon}'_{xy}$). Therefore for this problem, the stress term $\sigma_{r\theta}^n$ is uncoupled from the out of plain strains, that is the constants A_f^n and B_f^n in Equation 2.12 and 2.13 for $\sigma_{r\theta}^n$ are independent of $\bar{\varepsilon}'_{zz}$, $\bar{\varepsilon}'_{xz}$, and $\bar{\varepsilon}'_{yz}$. This functional dependence of the stress is uti-

lized in the development of the fiber end solution in subsequent paragraphs. This completes the derivation of the far-field analysis of fiber system (1,1,1).

The second part of the stress analysis, presented in Equation 2.1 and corresponding to the fiber end solution (i.e. $\tilde{\sigma}_{ij}$), is addressed in the following paragraphs to complete the development of the short fiber or broken fiber problem (see Figure 3). For a broken fiber in a continuous composite system, it is known that the fiber ends are traction free; however the tractions on a short fiber are not necessarily zero unless no chemical bonding has taken place between the fiber and matrix. To address this dilemma, there may be a variety of ways to approximate the tractions existing at the fiber end of a short fiber which could include axial stress transfer between fiber systems (e.g. Carman and Berry [40]). The form provided in this chapter, while general in context, is case specific. The tractions at the fiber end are equivalent to a composite where all fibers have been replaced by matrix material. This is representative of a homogenous composite consisting entirely of matrix material subjected to the boundary conditions stated in Equation 2.5. In accordance with these statements, it can be easily shown by reviewing the development of Equations 2.12, that the tractions at the end of fiber (1,1,1) can be represented as

$$\sigma'^{1}_{zz}(r,\theta,0) = Z_1^{mat}(r)\cos 2\theta + Z_2^{mat}(r)\sin 2\theta + Z_3^{mat}(r)$$

$$\sigma'^{1}_{rz}(r,\theta,0) = RZ_1^{mat}(r)\cos\theta + RZ_2^{mat}\sin\theta \qquad [2.15]$$

$$\sigma'^{1}_{\theta z}(r,\theta,0) = \Theta Z_1^{mat}(r)\sin\theta + \Theta Z_2^{mat}\cos\theta$$

where the superscript "mat" refers to the solution for a composite made of pure matrix material subjected to the boundary conditions stated in Equation 2.5. The dependence of the functions Z_i^{mat}, RZ_i^{mat}, and ΘZ_i^{mat} on the radial coordinate are the same as presented in Equation 2.13, but the reader should be aware that $Z_i^{mat} \neq Z_i^2$, $\Theta Z_i^{mat} \neq \Theta Z_i^2$, and $RZ_i^{mat} \neq RZ_i^2$. The evaluation of the constants (i.e. $A_{1,2}^{mat}$, $B_{1,2}^{mat}$, F_i^{mat} , and H_i^{mat}) in these functions are from the boundary conditions, Equations 2.5, applied to the monolithic matrix material. As an aside,

different boundary conditions could have been imposed to study other types of physical phenomena taking place in the composite. For example, when considering a broken fiber where the fiber end is traction free, the constants are found to be to zero. By using Equations 2.15, 2.12, and 2.1 the traction boundary conditions for the fiber end solution are written as follows.

$$\tilde{\sigma}^1_{zz}(r,\theta,0) = (Z_1^{mat}(r) - Z_1^1(r))\cos 2\theta + (Z_2^{mat}(r) - Z_2^1(r))\sin 2\theta + Z_3^{mat}(r) - Z_3^1(r)$$

$$\tilde{\sigma}^1_{rz}(r,\theta,0) = (RZ_1^{mat}(r) - RZ_1^1(r))\cos\theta + (RZ_2^{mat}(r) - RZ_2^1(r))\sin\theta \qquad [2.16]$$

$$\tilde{\sigma}^1_{\theta z}(r,\theta,0) = (\Theta Z_1^{mat}(r) - \Theta Z_1^1(r))\sin\theta + (\Theta Z_2^{mat}(r) - \Theta Z_2^1(r))\cos\theta$$

The above equations provide explicit functions in terms of r and θ for the stress terms $\tilde{\sigma}^1_{zz}$, $\tilde{\sigma}^1_{rz}$, and $\tilde{\sigma}^1_{\theta z}$ in the fiber end solution. The stress tensors functional dependence on the axial coordinate z will be similar in form to that postulated by Whitney and Drzal [23]. which has been shown to give credible forms of the solution. As noted in the introduction of this chapter, this solution is extended to analyze unsymmetrical loading cases and allows the possibility of load transfer at the fiber ends. With these equations and the the equilibrium Equations 2.6, the entire stress tensor on a point-wise basis is developed as explicit functions of r,θ, and z. This is accomplished systematically by addressing the traction in Equations 2.16 resulting from the application of a given strain term (e.g.$\bar{\varepsilon}'_{xx}$) independently. From the traction condition at the fiber, the functional dependence of specific fiber stresses (i.e.$\tilde{\sigma}_{zi}$) can be inferred, as was accomplished for the far-field solution. With the use of equilibrium Equations 2.6, the full stress tensor in the fiber region is generated. Thus, the following equations are representative of the fiber stress field for the fiber end solution of fiber(1,1,1).

$$\tilde{\sigma}^1_{zz} = [S_1 + 2P_1 r^2\cos 2\theta + 2Q_1 r^2 \sin 2\theta](1+\lambda z)e^{-\lambda z}$$

$$\tilde{\sigma}^1_{\theta\theta} = [\frac{S_1 r^2}{4} + S_2 + \frac{P_1 r^4}{2}\cos 2\theta + \frac{Q_1 r^4}{2}\sin 2\theta](-\lambda^2 + \lambda^3 z)e^{-\lambda z} + [E_1 r\cos\theta + G_1 r\sin\theta]\lambda^2 z e^{-\lambda z}$$

$$\tilde{\sigma}^1_{rr} = [\frac{S_1 r^2}{4} + S_2 + \frac{3P_1 R^4}{10}\cos 2\theta + \frac{3Q_1 r^4}{10}\sin 2\theta](-\lambda^2 + \lambda^3 z)e^{-\lambda z} + [E_1 r\cos\theta + G_1 r\sin\theta]\lambda^2 z e^{-\lambda z}$$

$$\tilde{\sigma}^1_{rz} = [\frac{S_1 r}{2} + P_1 r^3\cos 2\theta + Q_1 r^3\sin 2\theta]\lambda^2 z e^{-\lambda z} + [E_1\cos\theta + G_1\sin\theta](1+\lambda z)e^{-\lambda z} \qquad [2.17]$$

$$\tilde{\sigma}^1_{\theta z} = [-P_1 r^3\sin 2\theta + Q_1 r^3\cos 2\theta]\lambda^2 z e^{-\lambda z} + [-E_1\sin\theta + G_1\cos\theta](1+\lambda z)e^{-\lambda z}$$

$$\tilde{\sigma}^1_{r\theta} = 0$$

To develop the stresses in the matrix region for fiber (1,1,1), we will rely on the same methodology presented above. The tractions across the interface (i.e.$r = r_f$) are continuous, and thus explicit forms of the matrix stresses $\tilde{\sigma}^2_{rr}$, $\tilde{\sigma}^2_{r\theta}$, and $\tilde{\sigma}^2_{rz}$ in terms of z and θ are obtained. Furthermore, use is made of the fact that matrix stresses must decay for increasing values of r, such that as r approaches infinity the stresses go to zero. This and the previous equilibrium Equations 2.6 results in the following explicit forms for the matrix stresses as a function of r for fiber system (1,1,1).

$$\tilde{\sigma}^2_{zz} = [\frac{S_3}{r^4} - \frac{4P_2}{r^4}\cos 2\theta - \frac{4Q_2}{r^4}\sin 2\theta](1+\lambda z)e^{-\lambda x}$$

$$\tilde{\sigma}^2_{\theta\theta} = [\frac{S_3}{4r^2} + \frac{P_2}{2r^2}\cos 2\theta + \frac{Q_2}{2r^2}\sin 2\theta](-\lambda^2 + \lambda^3)e^{-\lambda z} + [\frac{-E_2}{r}\cos\theta - \frac{G_2}{r}\sin\theta]\lambda^2 z e^{-\lambda z}$$

$$\tilde{\sigma}^2_{rr} = [\frac{S_3}{4r^2} + (\frac{-3P_2}{2r^2} + \frac{P_3}{r})\cos 2\theta + (\frac{-3Q_2}{2r^2} + \frac{Q_3}{r})\sin 2\theta](-\lambda^2 + \lambda^3)e^{-\lambda z} + [\frac{E_3}{r}\cos\theta + \frac{G_3}{r}\sin\theta]\lambda^2 z e^{-\lambda z}$$

$$\sigma^2_{rz} = [\frac{-S_3}{2r^3} + \frac{P_2}{r^3}\cos 2\theta + \frac{Q_2}{r^3}\sin 2\theta]\lambda^2 z e^{-\lambda z} + [\frac{E_2}{r^2}\cos\theta + \frac{G_2}{r^2}\sin\theta](1+\lambda z)e^{-\lambda z} \qquad [2.18]$$

$$\sigma^2_{\theta z} = [-\frac{P_2}{r^3}\sin 2\theta + \frac{Q_2}{r^3}\cos 2\theta]\lambda^2 z e^{-\lambda z} + [\frac{E_2}{r^2}\sin\theta - \frac{G_2}{r^2}\cos\theta](1+\lambda z)e^{-\lambda z}$$

$$\tilde{\sigma}^2_{r\theta} = 0$$

Note that the stress terms $\tilde{\sigma}^n_{r\theta}$ in Equations 2.18 and 2.17 are defined to be zero, which should not be surprising when recalling Equations 2.12 and 2.13 and the discussion which followed them. It is stated in these paragraphs that the stress term $\sigma^n_{r\theta}$ was independent of out-of-plane tractions (i.e. σ_{rz}, $\sigma_{\theta z}$, and σ_{zz}), such that the fiber end solution appears to be correctly modeled as an out-of-plane problem (i.e. Equation 2.16), and thus the stress term $\sigma_{r\theta}$ should be negligible. It should also be noted that all of the stresses presented in Equation 2.18 approach zero as either $r \gg r_f$ or $z \gg r_f$ as they should.

The constants in Equations 2.18 and 2.17 are evaluated by applying the boundary conditions in Equation 2.16 and the traction continuity conditions at the fiber matrix interface. These values can be represented in terms of previously defined constants introduced in Equations 2.11, 2.13 and the constitutive material parameters. The coefficient λ in the present model is formulated by the techniques presented by Rosen [22] which takes into account a finite fiber volume fraction. The following equations reflect the influence of these constants.

$$\lambda = \frac{1}{r_f}\left[\frac{1}{2}\left(\frac{1 - v_f^{1/2}}{v_f^{1/2}}\right)\frac{1}{S_{11}^1 C_{44}^2}\right]^{-\frac{1}{2}}$$

$$S_1 = -C_{11}^1 D_3^1 - 2C_{12}^1 D_1^1 + C_{11}^{mat} D_3^{mat} + 2C_{12}^{mat} D_1^{mat}$$

$$S_2 = -\frac{S_1}{2} r_f^2$$

$$S_3 = -S_1 r_f^4$$

$$P_1 = \frac{3C_{12}^1 C_{44}^1}{C_{23}^1} A_1^1 - \frac{3C_{12}^2 C_{44}^2}{C_{23}^2} A_1^{mat}$$

$$P_2 = P_1 r_f^6$$

$$P_3 = \frac{9}{5} P_1 r_f^5$$

$$Q_1 = \frac{3C_{12}^1 C_{44}^1}{C_{23}^1} B_1^1 - \frac{3C_{12}^2 C_{44}^2}{C_{23}^2} B_1^{mat} \qquad [2.19]$$

$$Q_2 = Q_1 r_f^6$$

$$Q_3 = \frac{9}{5} Q_1 r_f^5$$

$$E_1 = - C_{55}^1 (F_2^1 + F_4^1) + C_{55}^2 (F_2^{mat} + F_4^{mat})$$

$$E_2 = E_1 r_f^2$$

$$E_3 = E_2$$

$$G_1 = - C_{55}^1 (H_2^1 + H_4^1) + C_{55}^2 (H_2^{mat} + H_4^{mat})$$

$$G_2 = G_1 r_f^2$$

$$G_3 = G_2$$

Once again the constants in Equation 2.19 are generated by specific local strain values $\bar{\varepsilon}'_{ij}$. By using Equations 2.18, 2.17 and 2.12 in Equation 2.1, the full 3-D stress field is developed for the short fiber system (1,1,1) and it may easily be evaluated for other fiber systems (Ξ,Γ,Λ) in the composite material.

The problem of evaluating the contracted stiffness matrix of the short fiber composite is addressed as follows. The stress-strain relations for an anisotropic composite are written in contracted notation as

$$\bar{\sigma}_i = C_{ij}^c \bar{\varepsilon}_j \qquad [2.20]$$

where, once again, the over-bars denote the average stress and strain in the continuum. It is a relatively safe assumption that the transient stresses in the matrix have little effect on the average stress state in the composite. First, the dominant stress terms occur in the fibrous region and not in the matrix, at least in composites where $C^2_{f1} < C^1_{f1}$. Secondly, almost all short fiber composites have relatively small (i.e.$v_f < .5$) volume fractions of fibers and thus the transient stresses developed in the matrix, while very important with regard to failure stress and strength of the composite, should have little effect on the average stress in the composite. Based on this analysis, the average stress in the composite can now be obtained by volume averaging the stresses in the composite over each material region (i.e. fiber and matrix). This may be accomplished as follows

$$\bar{\sigma}_{ij} = (V_c)^{-1}\{\sum_{1}^{\Xi_{max}}\sum_{1}^{\Gamma_{max}}\sum_{1}^{\Lambda_{max}}[\int\int\int \sigma^2_{ij} dV_m + \int\int\int \sigma'^1_{ij} dV_f]\} \qquad [2.21]$$

where V defines a volume and subscripts f, m, and c refer to the fiber, matrix, and composite respectively. The summations refer to the stress contributions from each fiber(Ξ, Γ, Λ) which has a given fiber type, fiber orientation, and fiber aspect ratio. Note that the volume averaged stress in the matrix region only includes the far-field solution, which is consistent with previous discussions. The rows of the contracted stiffness matrix are constructed by applying a unit global strain for each component in the composite strain tensor to simulate the displacement boundary condition described in Equation 2.5. From this, the stresses in Equations 2.12, 2.17, and 2.18 are evaluated and found to be functionally dependent on the applied displacement (or strains). By using Equation 2.21 the average stresses can be calculated as a linear function of the applied global strain values. Using these results in Equation 2.20, the complete stiffness matrix can be computed for a 3-D hybrid composite material system.

2.2 Results and discussion

In order to validate the theoretical model, a comparison is made between experimentally measured elastic properties and the current theoretical predictions for short fiber polymeric and metal matrix composites. Further theoretical validation of the model consists of comparing the present theoretical predictions for a PMC with other theoretical models which are well established in the literature, such as Aboudi's [20] square fiber model, Halpin-Tsai's [4] equations, and Russel's [11] ellipsoidal inclusion. It should be noted that none of the aforementioned models predict point-wise stress variations in the fiber and matrix, as does the current model. Point-wise stress values are essential to understanding the damage and failure mechanisms present in composite systems at the micromechanics level which are known to severely alter the laminate properties. To demonstrate the large range of application the current model has in short transversely-isotropic short fiber systems, a study is presented on the effect of fiber aspect ratio and fiber volume fraction on the properties of brittle ceramic matrix composite systems. To further demonstrate the applicability of this analytical model to continuous fiber systems containing fiber fractures, a study is performed on the stiffness reduction which occurs in PMC as a function of life (i.e. fiber fractures).

This section is thus divided into the following subsections;

- *Polymeric matrix composites* presenting a comparison between the current analytical predictions of stiffness, experimental data on stiffness, and classical accepted models of stiffness.

- *Metal matrix composites* encompassing a comparison between the predictions of the tensor stiffness values generated by the present model and experimental data.

- *Brittle/ceramic matrix* composites describing the dependence of stiffness properties on fiber volume fraction and fiber aspect ratio.

- *Stiffness reduction in continuous fiber composites* which occurs in PMC's subjected to fatigue loading which causes multiple fiber fracture.

2.21 Polymeric matrix composites

A comparison between the current theory, classic theories, and experimental results is presented for a variety of polymeric composite systems discussed in this section. An analysis of epoxy based matrices containing E-glass, copper, and steel fibers of different aspect ratios and different fiber volume fractions are presented. The classical theories which are used in this study for comparison purposes are Aboudi's [20] model, Halpin-Tsai [4] equations, and Russel's [11] ellipse model. The constitutive properties used for all the theoretical calculations discussed in this section are presented in Table 1.

2.211 Axial modulus

The first experimental validation is accomplished by comparing experimentally measured elastic properties of a 2-D E-glass/epon-828 mat with the current theory. This represents a composite whose fiber-to-matrix stiffness ratio (i.e.C_{11}^f/C_{11}^m) is approximately 20. The well-documented experimental data developed by Kacir [41] describes a material system containing 50 percent fiber volume fraction E-glass bundles having aspect ratios of 53 or 136. Kacir et al [41] studied the effect misoriented fibers have on the axial stiffness properties of this composite material by accurately determining the fiber orientations in the short fiber composite. This was accomplished with the use of dyed fibers along with x-ray technology to determine the precise alignment of the fibers in the actual composite system. Table 2 presents

the results of their tests describing the fiber orientation in terms of the percent fibers aligned at the solid angle ω. Note ω is discussed in section 2.1 and for a 2-d composite the solid angle $\phi \equiv 0$. In Table 3, a presentation of the results for both the experimental data and the current theoretical predictions for axial stiffness values is published. With respect to the computation process used for the theoretical predictions, the fiber assemblages are constructed such that the local fiber volume fraction was the same as the global fiber volume fraction. In regard to composites "a-c" in Table 3 which have an aspect ratio of 136, the largest discrepancy between the experimental and theoretical predictions is exhibited by composite "a" which represents a 2 percent error. For composites "d-h" which have an aspect ratio of 53, half of the aspect ratio in the previous composites, the largest error between the experimental data and theoretical results is 4 percent. Therefore, it appears that the correlation between the test data and the analytical predictions are remarkably accurate for each fiber orientation and fiber aspect ratio studied; that is, the dependence on aspect ratio and orientation appears to be correctly modeled.

As a last note, the experimental data published by Kacir et. al. [41] is viewed as a concise representation of a 2-D short fiber composite and should thus provide accurate values of the longitudinal stiffness for this particular short fiber composite system. The ability to accurately predict the elastic properties with the current theory strongly suggests that the derivation described in section 2.2 should provide an adequate representation of the point-wise stress state existing in each constituent. That is the global stiffness values were calculated from the volume averaged stress quantities for each region (fiber and matrix).

For further validation of the present theory, experimental data on the stiffness properties of a PMC as determined by Berthelot [5] are compared to the models predictions. That investigator studied the effect fiber volume fraction has on the axial stiffness (i.e. E_{11}) of short fiber composites consisting of an epoxy matrix with steel or copper fibers. The steel fibers had an aspect ratio of either 50 or 100 with a fiber to matrix stiffness ratio of 75, and the copper fibers had an aspect ratio of either 60 or 100 with a fiber to matrix stiffness ratio of 40. It is important

to note that the short fibers embedded in the composite were misaligned at plus or minus 10 degrees with the loading axis due to inherent manufacturing defects.

The results for axial stiffness of the steel/epoxy composites as a function of fiber volume fraction and fiber aspect ratio are addressed first. Experimental results along with current theoretical predictions are presented in Figures 4 and 5 for an steel/epoxy material with aspect ratios of 50 and 100, respectively. In each plot, two theoretical curves are drawn. These are representative of theoretical predictions for:

1. all fibers aligned with the principal axes ($\omega = 0$)
2. all fibers aligned at 10 degrees with the loading axis. ($\omega = 10$)

For both aspect ratios, Figure 4 and Figure 5, the theoretical curves bracket the experimental results, as expected. In other words, the experimental data are representative of a composite containing fibers variably aligned between plus and minus 10 degrees and, thus, should lie between the two theoretical curves which represent bounds on this composite's measured stiffness values. In Figure 6 and Figure 7, a comparison is presented between the current theoretical predictions and other classical theories (i.e.Aboudi [20], Halpin-Tsai [4], and Russel's [11] ellipse) for the same material system, that is, steel/epoxy aspect with an ratio of 50 and 100, respectively. As one can see, for both aspect ratios studied, the trends predicted by all models as a function of fiber volume fraction appear to be quite similar. However, the comparison of these models demonstrates that the Aboudi [20] model predicts values below that of the present theory, the Halpin-Tsai [4] equations predicts similar values to that of the present theory, and the ellipsoidal [11] model predicts larger values. Insights are gained by comparing Aboudi [20] results, Figure 6 and 7, with Berthelot [5] short fiber data, Figures 4 and 5. We find that the square fiber model consistently predicts a slightly less stiff composite than the experimental results suggest. However, the experimental data are for misaligned fibers while theoretical predictions are based on fibers aligned with the loading axis, which should result in stiffer predicted values rather than the less values obtained. With regard to the results of the ellipsoidal [11] model, Figures 6 and 7, it predicts significantly

larger stiffness value than that exhibited by the experimental data, Figures 4 and 5, a discrepancy which cannot be argued away by misorientation effects. The Halpin-Tsai [4] equations, on the other hand, provide reasonable results when compared with the experimental data and are in relatively good agreement with the present theory. Note that this model is based on empirical relations derived from experiments.

A comparison is also made between axial stiffness values determined by experimental methods described by of Berthelot [5] and the present model for a copper/epoxy composite system. In Figures 8 and 9, the plots of the theoretical curves and the experimental data are presented for a composite with embedded copper fibers with aspect ratios of 60 and 100. As noted above, the two theoretical curves shown in each graph correspond to predictions of composites containing either fibers aligned with the loading axis or oriented 10 degrees away from the loading axis. For these plots, the curves also bracket the experimental data points, with the exception of a few outlying data points for the smaller fiber volume fractions. In Figures 10 and 11, a comparison with other theoretical predictions are shown for the copper/epoxy material system. In this plot, the Aboudi [20] model deviation from the present theory is much smaller than that shown for the steel/epoxy systems in Figures 6 and 7. When comparing the Aboudi [20] model, Figures 10 and 11, to the experimental data, Figures 8 and 9, one finds much better agreement for this material system as compared to the steel/epoxy which may be attributed to the relative decrease in the fiber/matrix stiffness ratio from the steel to copper system, that is, from a value of 75 to 40. With regard to the plots for the Halpin-Tsai [4] equations presented in Figure 10 and 11, they tend to provide overestimates for this particular composite.

This section thus demonstrates the models accuracy at predicting the axial stiffness values of actual composite materials. This included three different fiber to matrix stiffness ratios (i.e. 20, 40, and 75) and five different fiber aspect ratios (i.e.50, 53, 60, 100, and 136). Therefore the theory developed in this chapter appears to accurately predict the axial stiffness for all ma-

terial systems, and incorporates the correct functional dependence on fiber volume fraction and aspect ratio.

To demonstrate the ability of the theoretical model to predict the complete stiffness matrix for a general composite material, the following paragraphs will compare a variety of commonly used mechanical constants calculated for a transversely isotropic material systems with the predictions of different modeling methodologies. The material system will be a steel/epoxy material consistent with the constituents described above.

2.212 Transverse modulus

The variation of transverse stiffness for a unidirectional short fiber composite as a function of fiber volume fraction is presented in Figure 12. The dependence of transverse stiffness on aspect ratio is known to be minimal; therefore, only one aspect ratio (i.e.100) is shown. The agreement between Aboudi [20] model and the present theory for this composite system are extremely close; in fact, the largest difference between the two is only about 3 percent. One should also note the sharply nonlinear dependence of this mechanical property, predicted by both models, as a function of fiber volume fraction. On the other hand the ellipsoidal [11] model predicts significantly different values from either of the two previously discussed models, and appears to suggest a linear dependence on fiber volume fraction.

2.213 Axial shear modulus

A comparison of the predicted axial shear modulus (i.e. G_{12}) calculated by the three models is presented in Figure 13. The Aboudi [20] model suggests only small variations in the shear modulus as a function of the fiber aspect ratio for this particular composite, and so only one curve is plotted (for an aspect ratio of 100). In fact, that model exhibits little to no changes (i.e.,

less than 2 %) in G_{12} for fiber aspect ratios larger than 10, however for aspect ratios below this value the the changes in G_{12} are significant. The ellipsoidal [11] model also exhibits no dependence of G_{12} on fiber aspect ratio, and the results suggest a linear dependence of this property on fiber volume fraction. On the other hand the current theory, while exhibiting similar trends in the shear modulus as a function of fiber volume fraction to that of Aboudi [20], suggests that there is a dependence of G_{12} on fiber aspect ratios larger than 10. One can easily make arguments which would suggest that fiber aspect ratio should effect axial shear modulus. The fact that the problem involves the shear transfer from the matrix to the fiber which is similar to the shear lag problem, would demand that a dependence on length exists.

2.214 Transverse Poisson ratio

A comparison of Poissons ratio (ν_{23}) in the transverse plane for the different modeling methodologies is plotted in Figure 14. The Aboudi [20] model and the current model exhibit similar trends for increasing fiber volume fraction and increasing fiber aspect ratio, however the present theory suggest slightly larger values in ν_{23}. The two models once again predict similar trends in this mechanical property as a function of fiber volume fraction and fiber aspect ratio (i.e. as fiber aspect ratio increases, ν_{23} increases). Note that both of these dependences are of a highly nonlinear nature and are not a simple linear function as has been suggested by rule of mixtures arguments. Only one curve is presented for the ellipsoidal [11] model due to the small variations caused by aspect ratio changes in the material modeled. The Poisson ratios calculated using the ellispoidal [11] model appear to provide erroneous data for increasing fiber volume fraction. One expects that the Poisson ratio of the composite should approach the fiber's value for large fiber volume fraction, which does not occur. Therefore, it appears that the Aboudi [20] model and the current theory predict reasonable trends in the variation of ν_{23} and are in close agreement with each other, while the ellipsoidal [11] model provides outlying predictions.

2.215 Axial Poisson ratio

The last comparison to be made between theoretical models for polymeric composites in this section involves the axial Poissons ratio, ν_{21}, as a function of fiber volume fraction. When comparing the three models (Figure 15), it is noted, that all the models exhibit similar trends in the functional dependence of ν_{21} on fiber volume fraction. Only one curve is shown for the ellipse, due to the fact that virtually no dependence exists in this model on fiber aspect ratio. The Aboudi [20] model suggests the largest predicted value and the the ellipse provides the smallest predicted value, with the present theory lying between the two. The ordering of the curves with respect to increasing fiber aspect ratio for both the Aboudi [20] and the current model appear to behave in a similar fashion. This suggests that a reasonable correlation exists between these models, and they should provide reasonable estimates for the prediction of ν_{21}.

In conclusion for this section, one should immediately note the excellent agreement between the axial stiffness predictions of the present model and the experimental data. It also appears that the agreement between the present theory and the Aboudi [20] model for the five independent elastic constants describing a transversely isotropic composite is good. One should note, however, that the axial stiffness predictions of the present model were demonstrated to be more accurate, and should thus be regarded as a more precise model for the study of these material systems. The ellipse model appears to be an inadequate tool to study material property dependence on fiber volume fraction, at least for large fiber volume fractions. It should also be remembered that none of these other modeling techniques are capable of providing the point-wise stresses in each constituent as is the present model.

2.22 Metal matrix composite

A comparison between the current theory and experimental results of Johnson and Birt [42] is presented for a MMC consisting of a silicon carbide whisker ($r_f = 0.25\mu m$) embedded in an aluminum matrix. The experimental data generated by these researchers represents an exceptional characterization of an actual metal matrix composite, which is briefly described in the ensuing paragraph. These investigators manufactured 2-D laminas of varying thickness, fiber volume fraction, fiber orientation, and fiber aspect ratio to evaluate the effect these micromechanical parameters have on the lamina mechanical properties, that is, the transverse and axial stiffness values, of metal matrix composites. A total of 3 different plate thickness (i.e. 6.35, 3.18, and 1.8 mm) and two different fiber volume fractions (i.e. 15 and 30 percent), each having an experimentally measured fiber distribution and fiber aspect ratio, were presented. The manufacturing of the 2-D plates involved hot rolling the material into billet shapes. This process causes fiber damage in the composite and introduces an inherent amount of debris into the matrix, as well as decreasing the effective fiber volume fraction. With the use of image analysis, the researchers were able to characterize the amount of debris present in the matrix and published augmented stiffness values for the matrix material and fiber volume fraction to account for the apparent changes in the constituents due to fiber damage (see Table 4). With the same process (i.e. image analysis) they determined the fiber distribution, that is the average percent of fibers aligned at ω as well as the average fiber aspect ratio in the composite (see Figures 16 and 17). Therefore, these individuals provided a highly detailed experimental description of this 2-D metal matrix composite.

In Figures 18 and 19, plots of the experimental data and theoretical predictions for the axial and transverse stiffness of a 15 percent fiber volume fraction metal matrix composite described above are presented. The results shown in these figures corresponds to a composite with fiber alignment and fiber aspect ratio data provided in Figure 16. The reader should note that two theoretical curves are plotted in each figure of this section, one corresponding to a

composite without debris as well as an unadjusted fiber volume fraction, and the second corresponding to a composite with debris and an adjusted fiber volume fraction. Considering Figure 18, which depicts the variation of axial stiffness as a function of plate thickness, the largest discrepancy between the present theory and the data exists for the theory without debris. The maximum error in the axial stiffness predictions occurs in the 3.18 mm plate and is approximately 7 percent in disagreement with the experimental data. On the other hand, the theory without debris, is much closer to the experimental data and has a maximum error of only 3 percent. One would intuitively believe that the theory without debris should provide an upper bound approximation (i.e. if the fiber alignment parameters and fiber aspect ratio were correctly measured by Johnson and Birt [42], the composite with intact fibers should exhibit larger stiffness properties than a composite containing damaged fibers). Nonetheless, the error in either of the theoretical predictions, that is with or without debris, is relatively small, and both results are regarded as providing excellent correlation with the experimental data. In fact, when reviewing Figure 19 depicting the variation in transverse stiffness, one finds a remarkable correlation (almost exact) between the theoretical results for the theory without debris and the experimental data. The theory containing debris differs only slightly from the experimental results, that is on the order of about 1 to 2 percent which is well within acceptable error bounds. From the results presented in these two figures, the modeling of metal matrix composites with the present theory appears to be quite good and provides stiffness results which differ from experimental data by no more than 7 percent, which are well within experimental errors.

To demonstrate the ability of the current theoretical model to predict stiffness values for other fiber volume fraction metal matrix composites, a 30 percent material is presented for comparison purposes. In Figures 20 and 21, a plot of the experimental data and the two theoretical predictions (as done in the previous example) for the axial and transverse stiffness of the metal matrix composite are presented. These results correspond to the fiber alignment and fiber aspect ratio data of a composite described by the data presented in Figure 17. Figure 20

depicts the variation of the axial stiffness as a function of plate thickness for this composite material. When viewing this plot, one can see that the theory without debris provides larger predictions than suggested by experimental data, as it should. The largest error between this theoretical curve and the data is approximately 9 percent and occurs for the 6.35 mm thick plate. On the other hand, the theory with debris, which should provide more accurate predictions, does an excellent job of predicting the axial stiffness values for these composites. These latter predictions only deviate from the experimental data by at most 4 percent. When reviewing the variations in predictions of transverse stiffness values presented in Figure 21, the comparison between the theories and the data is quite good. The largest error for either prediction occurs in the 6 mm plate modeled and is at most 4 percent for the theory with debris and 3 percent for the theory without debris. These error values can be considered to be small and well within the experimental error bounds.

From the plots described above, one can readily deduce that the present theory does an excellent job of modeling metal matrix composites. The fact that the largest error is less than 9 percent is a good indication of the models accuracy in describing short fiber metal matrix composites. In fact, remembering that the average aspect ratio, fiber volume fraction, and fiber alignment parameter is included in the results presented in this section, one concludes that the model correctly depicts the influence of these micro-parameters and provides highly concise predictions for the stiffness properties with stress volume averaging techniques. These results also suggest that the point wise stress state calculated with the model should give reasonable results, especially since the stiffness values are determined by averaging the point-wise stress tensor in each constituent.

2.23 Brittle/Ceramic matrix composite

To demonstrate the ability of the current model to provide stiffness results as well as the point-wise stress variations for a general composite system, a parametric study is performed on a brittle/ceramic matrix composite. The composite used in this analysis consists of a high modulus (HMU) graphite fiber (which is a transversely isotropic) material embedded in an borosilicate glass matrix (which is an isotropic material). The mechanical properties of these constituents are are presented in Table 5. This particular composite has been utilized by previous investigators (see Dunyak [43]) to study ceramic matrix composites manufactured with injection molding techniques into tubular specimens. This shape is commonly used in filter and heat exchanger systems of power generation units, and is also an ideal specimen to study multi-axial loadings of material systems. The present analysis is directed at determining the effect of fiber volume fraction and fiber aspect ratio on the five independent elastic constants of this unidirectional, short fiber composite material. These results, along with the point-wise stress predictions, can subsequently be used to analyze the strength variation existing in these tubular specimens due to misoriented fibers. This is believed to be a cause of low strength in these specimens.

2.231 Axial modulus

Figure 22 depicts the variation in the axial stiffness property as a function of fiber volume fraction for 5 different (i.e.10, 20, 40, 60, and 80) fiber aspect ratios. For each aspect ratio considered in Figure 22, as the fiber volume fraction increases the axial stiffness increases and approaches the axial stiffness value of the fiber. This is easily explained by classic rule of mixture arguments presented in detail by Christensen [39]. Furthermore, as the fiber aspect ratio increases from 10 to 80, the stiffness values of the composite increases as it should due to the additional reinforcement in the axial direction provided by the longer fiber. However,

the degree to which this value increases for increasing aspect ratios is not constant, that is, for larger aspect ratio composites (i.e. 60 and 80) the relative difference in stiffness values is smaller as compared to the smaller aspect ratios (i.e.20 and 40). In fact, for very large aspect ratios (not shown on this graph) the difference in stiffness values becomes indistinguishable and virtually nonexistent. This should be expected; that is, as the fiber becomes very large, the stress redistribution near the fiber ends becomes negligible when compared to the uniform stress (generalized plane strain) state which exists far from the fiber ends. Thus, composites with fibers of comparatively large aspect ratios respond in the linear region identical to continuous fiber composites. However, the strength of short fiber composite is expected, and found to be significantly smaller, due to stress concentration effects at the fiber ends. Therefore, the model correctly depicts the influence of the fiber aspect ratio and fiber volume fraction on the axial stiffness values of BMC and CMC.

2.232 Transverse modulus

Figure 23 depicts the variation in transverse stiffness as a function of fiber volume fraction and aspect ratio. In this figure, only two aspect ratios are presented due to the relative independence of the transverse stiffness on this quantity, i.e., the transverse displacement response of a unidirectional composite subjected to transverse loading should not be significantly influenced by the length of the fibers in the axial direction. One immediately notes that as the fiber volume fraction increases the composites transverse stiffness values increase and approach that of the fiber. The reader should be aware of the nonlinear functional dependence existing between transverse stiffness and fiber volume fraction predicted by this theory, as pointed out in section 2.212.

2.233 Axial shear modulus

Figure 24 depicts the variation in the longitudinal shear modulus as a function of fiber volume fraction and fiber aspect ratio. In this figure, the axial shear modulus displays a decrease for increasing fiber volume fraction as contrasted to increasing values noted in the previous paragraphs. This is simply due to the fact that the axial shear modulus of the fiber is smaller than that of the matrix. The other interesting point to be made concerning this graph is that as the aspect ratio increases the shear modulus decreases, which can be explained as follows. For composites which have fiber modulus less than that of the matrix, the largest axial shearing stresses occur in the fiber end and not at the fibers center, thus as the fiber becomes longer the average shearing stress in the fiber actually decreases which results in a decrease in the shearing modulus (see Equation 2.21). The reader should be aware that for composite such as ceramic and brittle matrix material one may find a decrease in various stiffness values as a function of fiber aspect ratio, depending on the relative ratio of fiber to matrix properties.

2.234 Axial Poisson ratio

Figure 25 depicts the variation of Poissons ratio (i.e.ν_{21}) as a function of fiber volume fraction and fiber aspect ratio. The Poissons ratio ν_{21} is defined as the ratio of the contraction in the axial direction (i.e. 1) to the contraction in the transverse direction when the composite is subjected to a transverse force. As the fiber volume fraction increases, the value ν_{21} approaches the Poissons ratio of the fiber; however, as fiber aspect ratio increases, ν_{21} decreases. When the aspect ratio of the fiber increases, it provides additional reinforcement in the 1-direction, thus increasing the stiffness (or decreasing the strain for an applied load) in this direction (see Figure 22). Therefore, as this stiffness value increases, one would also expect to see a relative decrease in the axial strain when a transverse load is applied to the

composite, resulting in a smaller ratio of the axial strain to transverse strain for this loading sequence. This causes a decrease in ν_{21} for increasing fiber aspect ratio in this particular composite.

2.235 Transverse Poisson ratio

Figure 26 depicts the dependence of Poissons ratio (i.e. ν_{23}) on fiber volume fraction and fiber aspect ratio. The Poissons ratio ν_{23} is defined as the ratio of the contraction in the transverse direction (i.e.3 direction) to the contraction in the direction of the applied load, that is the transverse direction, 2 in this case. As with previous plots, when the fiber volume fraction increases, the composites mechanical property tends toward the fiber's mechanical property. Also, as the fiber aspect ratio increases, the mechanical property increases, which can be explained with arguments similar to those presented in previous paragraphs. That is, when the aspect ratio increases, the contraction in the axial direction (i.e., 1 direction) due to an applied transverse load (i.e., 2 direction) decreases. To minimize the volume change, a larger contraction in the transverse direction (i.e., 3 direction) is necessary and causes an increase in ν_{23} for increasing aspect ratios for this fiber dominated material.

These plots demonstrate the versatility of this theoretical analysis to model, not only polymeric and metal matrix composite, but is also applicable to brittle and ceramic matrix system which cannot be characterized by shear lag type solutions. The fact that some of the mechanical properties of the fiber are less than that of the matrix attests to this fact. It was also shown that the correct dependence of fiber volume fraction and fiber aspect ratio was exhibited by each of the five independent elastic constants. This suggests that an accurate depiction is provided for the theoretical point-wise stress variation in each constituent as a function of fiber volume fraction and fiber aspect ratio, since stiffness properties were derived from stress averaging techniques.

2.24 Stiffness reduction in continuous fiber composites

The analysis portion of this section alluded to the fact that the model is applicable to continuous fiber reinforced composites containing fiber fractures. In the final section of this chapter, the effect of multiple fiber fractures on the stiffness reduction in continuous composites is examined. To model fiber fractures in a composite, as described in section 2.1, the constants presented in Equation 2.15 and calculated from the fiber end traction condition (i.e. for a fiber fracture the fiber is traction free) are found to be zero. This provides the point-wise stress variation in the fractured fiber and surrounding matrix depicted by Equation 2.1.

The composite chosen for this study is a typical E-glass/epoxy material system having the constituent properties presented in Table 1. It is hypothesized that a unidirectional continuous fiber composite is subjected to fatigue loading and that these loading sequences cause multiple fiber fractures throughout the composite. These fracture events are evenly distributed and occur in a uniform fashion; that is, each fiber is thought to have fractured into the same number and length of segments. As the strength or life of the composite decreases, the length of the embedded fiber segments continues to decrease due to fiber fracture and alters the apparent stiffness of the composite. The reduction in stiffness is calculated with the model by employing the traction free condition and Equations 2.20 and 2.21. This analysis does not consider the significant stiffness reductions which occur due to nonlinear effects and matrix cracking. In accordance with the above statements, the following paragraphs describe the stiffness reduction as a function of the continuous composites remaining life, or fiber aspect ratio.

2.241 Axial modulus

Figure 27 represents the functional dependance of the normalized axial stiffness property on life or fiber aspect ratio for a continuous PMC (note: all stiffness properties are normalized to a composite containing no anomalies, that is no fiber fractures). The number of fracture events which occur in the composite are described in the context of the effective fiber aspect ratio following the fiber breaks, that is, as fibers are fractured, they successively break into smaller segments and thus decrease the net aspect ratio of the embedded fibers. Therefore, a decrease in aspect ratio is representative of a reduction in composite life. The three curves presented in Figure 27 are for an E-glass/epoxy composite containing different fiber volume fractions of 75, 50, and 25 percent. As loading sequences progress, a larger number of fibers develop multiple fractures, the fiber aspect ratio becomes smaller, and the stiffness properties of the composite decrease. It is interesting to note that the composites containing the smaller fiber volume fraction (i.e. 25 percent) exhibits larger stiffness changes in early life (i.e.larger l/d ratios) and the stiffness changes gradually increase in later stages of life. However, the larger fiber volume fraction composite (i.e. 70 percent) exhibits relatively no change in stiffness properties early in life but drastic changes occur during late life.

2.242 Axial shear modulus

Figure 28 depicts the variation of normalized axial shear modulus as a function of life for the three different fiber volume fractions studied. As life proceeds or as fiber length decreases, the shear stiffness of the composite decreases. The rate at which this happens appears to be somewhat independent of fiber volume fraction, as compared to axial stiffness reductions.

2.243 Axial Poisson ratio

Figure 29 depicts the variation in normalized Poissons ratio (i.e.ν_{21}) as a function of life for the three fiber volume fractions studied. For this figure, one immediately notes that ν_{21} increases as the aspect ratio decreases. This is in sharp contrast to the decrease exhibited by both the axial stiffness and shear modulus values (i.e. Figures 27 and 28). This can be explained as follows; when fiber fractures occur in the composite, the axial stiffness decreases as shown in Figure 28, causing larger contractions in the axial direction when a transverse load is applied. This results in larger values of ν_{21} for decreasing aspect ratios or decreasing life. One can also see from this plot that significant changes occur in ν_{21} earlier in life for the smaller fiber volume fraction composite than for composites with larger fiber volume fraction, as is described for the axial stiffness values.

The above results demonstrate that the analysis presented in this dissertation is also applicable to fiber fracture phenomenon in continuous fiber composites. The parametric studies presented, address the stiffness reduction which occurs in material systems subjected to fatigue loading where fiber fracture dominates the subsequent changes in composite stiffness properties. This analysis did not address the significant stiffness reduction which occurs due to matrix cracking and subsequent nonlinear material behavior. This arise largely due to fractured fibers and fiber end effects and the interaction which occurs in the composite. The interaction between fibers is the topic of the next chapter.

3.0 Fiber-fiber interaction

The influence of micro-parameters (e.g.interphase between fiber and matrix) on the behavior of composite materials is only now beginning to be realized by the scientific and engineering communities. The fact that there is a direct relationship between these parameters and macro-mechanical properties (Madhukar & Drzal [44]) has initiated a research thrust in this country for the development of accurate micromechanical representations of such phenomena. The literature currently abounds with micro-solutions to a number of various problems which are formulated on certain inherent assumptions which, if inaccurate, could drastically effect the analytical results. Until now, the validation of these micromechanical models has been accomplished with the use of volume averaging concepts and comparisons with macro-mechanical predictions, not with the more appropriate comparisons which utilize direct local measurements. The latter has not occurred due to experimental constraints including the dimensions involved (i.e. micro scale) and the internal nature of the problem. Verification of the models with volume averaging methods, on the other hand, leads to a "smearing" out of important details in the analysis which results in questionable validation of the models.

In this chapter, an analytical model is developed which provides an approximate stress state in fibers and matrix adjacent to a fractured fiber or finite length fiber. This extends the theoretical development presented in Chapter 2 for short fiber composites to include fiber/fiber

interaction near the fiber ends. This is essential to accurate macro-level strength predictions. The model developed in this chapter is validated with a unique methodology which provides a means to directly verify the model with experimental evidence. This novel technique, described in detail in Chapter 4, is the first methodology presented to directly validate various micro-mechanical analyses.

It has been well established in the literature that the tensile strength of most unidirectional continuous fiber composites (and fiber-dominated multi-axial laminates) is controlled by the interaction of fiber failures, while in short fiber composites it is controlled by the interaction of fiber ends. A fiber fracture/end generally causes large strain concentrations to exist in the surrounding fiber, matrix, and interphase regions. In the previous chapter the strain concentrations on adjacent fibers were smeared into a homogeneous effect in the composite, where in the present formulation a more detailed description is given. Various models, proposed in the literature (see Chapter 1), predict the stress/strain concentration which occurs in the vicinity of fiber ends and fiber fractures. These models are subsequently used in a strength formulation, such as that described by Batdorf [30] to "bridge" the gap between micromechanical models of the problem and the desired laminate level strength predictions. However, all these fiber interaction models are limited in one context or another by the inherent assumptions (e.g. virtually every model in the literature is based on shear lag and is thus limited to polymeric matrix composites). These include a lack of point-wise stress concentration dependence on material properties, fiber volume fraction, crack size, multiple fiber fracture, interphase effects, and variable fiber spacing. While each model, in it's own right, provides highly useful information, they do not however incorporate all the required parameters to adequately address a wide class of problems. Furthermore, a lack of direct experimental evidence supporting their formulation leads to questionable results.

In this dissertation, a model is presented which is capable of incorporating these parameters in a concise and clear formulation. The analytical model developed provides point-wise stress variations (radially and axialy) for a general class of composites containing single/multiple fi-

ber fractures with eccentrically oriented fibers. The stresses are valid for each constituent region (i.e. fiber, matrix, and interphase) in the composite. This approximate solution is developed based on a mechanics of materials approach and classical elasticity concepts. An assumption is made in the analysis that the adjacent fibers can be modeled as annular rings to eliminate the local stress variation with angle. Through fracture mechanic arguments and experimental evidence, a functional dependence of axial strain on radial position is formulated. By using force balance, constitutive relations, equilibrium equations, and boundary conditions, an approximate solution describing the point-wise continuous stress field in each material region is obtained. Multiple fiber fractures/ends are addressed with a unique fiber discount and linear superposition principal to arrive at a full stress field in the adjacent fiber and matrix systems. Variable fiber spacing is incorporated into the model with the inclusion of multiple fibrous rings which represent the eccentrically placed fibers. With these concepts, a formulation which is straightforward yet rigorous is presented.

The formal analysis described in this chapter provides a more detailed description of the fiber interaction problem than presently available in the literature. This analysis incorporates a dependence of the stress redistribution profile on the constituents constitutive properties. This permits analysis of a general class of composite systems (i.e. PMC, MMC, and CMC) while the current models in the literature only address polymeric composite systems. The analysis presented herein also includes a functional dependence of stress redistribution on fiber volume fraction which is not available in the shear lag type of models (these assume the matrix supports no axial load, and thus fiber volume fraction does not effect the strain concentration values). The model also provides analysis of a matrix crack which occurs due to fiber fracture and propagates a finite distance into the matrix. Other models make the assumption that only the fiber fails and the matrix is unaffected. The model developed in this study also utilizes a unique methodology to analyze multiple fiber fractures which occur in composite materials. Also included in this analysis is a more appropriate model of variable fiber spacing which occurs in virtually every composite manufactured.

The analytical results of strain concentration calculated with the model are compared with direct experimental measurements to validate the theory. This provides a firm foundation, not only for results provided by the model, but also for the assumptions inherent in the analysis. To demonstrate the versatility of the model, parametric studies are performed with variables such as fiber volume fraction, constituent material properties, and crack size to investigate their significance on single fiber fracture/end. Specific results are presented for both polymeric and metal matrix composites, however the model is also applicable to the analysis of ceramic matrix composites containing cracks. A section is presented on multiple fiber fracture to demonstrate the models accuracy in predicting these strain concentration values. The final section of this chapter addresses variable fiber spacing with both experimental verification and parametric studies.

3.1 Theoretical development

In the following section, a derivation is presented which predicts the point-wise stress state in the local vicinity of a fractured fiber or finite length fiber embedded in a composite subjected to uniaxial loading. This analysis extends the concepts presented in chapter 2, which describe short fiber effects, to include fiber-fiber interaction, variable fiber spacing, and multiple fiber fracture/ends, which are significant issues when attempting to predict the strength of composite materials.

In obtaining the stress field for each constituent which is present in the composite, a classic superposition of two solutions is employed, as was accomplished in chapter 2 and is presented in Figure 30. This involves separating the problem into a far-field analysis and a near field analysis represented by the following equation.

$$\sigma'^{n}_{ij} = \sigma^{n}_{ij} + \tilde{\sigma}^{n}_{ij} \qquad [3.1]$$

In Equation 3.1 the stresses with primes (i.e.σ') represent the full field stress solution, the stresses with tildes represent the near-field solution, and the stresses without any markings represent the far-field solution. The superscript "n" refers to either the matrix, fiber, or interphase regions. The far-field solution was derived in chapter 2 and will not be addressed in this section. The near-field solution presented in Equation 3.1, should not be confused with that presented in Equation 2.1. The latter solution did not incorporate fiber-fiber interaction or multiple fiber fracture/end effects into the analysis.

In posing the near-field problem, a fiber fracture/end is assumed to exist in a unidirectional composite containing a hexagonal array of fibers (see Figure 31). The following analysis specifically addresses a hexagonal array, however the analysis is general enough to model a variety of fiber packing arrangements which could be present in the composite. In Figure 31, r_f is the radius of the fiber, r_c is the crack size, and r_a is the closest adjacent fiber dimension. The size of the fracture r_c may (or may not) extend a finite distance into the matrix up to the adjacent fibers (i.e.$r_c = r_a$). Prior to the formation of the crack, load was transferred across this material region, however, following crack propagation the surface of the crack is traction free. To simulate this mathematically in the context of the near field solution, a traction is applied to the crack face, such that when added to the far-field solution (Equation 3.1 and Figure 30), the net traction on the crack face is zero for the fiber fracture problem. To calculate the net force applied to the crack face in the near field solution, the following equation is used.

$$P_0 = \int_0^{2\pi}\int_0^{r_f} \sigma^{f}_{zz} r \, dr \, d\theta + \int_0^{2\pi}\int_{r_f}^{r_c} \sigma^{m}_{zz} r \, dr \, d\theta \qquad [3.2]$$

Note that the stress terms used for the calculations in Equation 3.2 are the far-field stress terms presented in Equation 2.12. The first integral term in Equation 3.2 represents the load

originally transferred by the fractured fiber while the second integral term is the load originally transferred by the cracked matrix. If the crack does not extend into the matrix, the second integral term is exactly zero. Equation 3.2 is thus representative of the net force P_0 resulting from the applied traction in the near-field solution.

With regard to embedded finite length fibers in composites, there is load transfer between the matrix and fiber end which is due solely to the chemical bond existing between the two. Therefore the fiber end is not traction free in a finite length fiber embedded in a composite. The traction supported by the fiber end was discussed in detail in Section 2.1 of this dissertation and can thus be determined. To calculate the net force which must be applied to the fiber end in the near field solution of the short fiber problem, Equations 2.12 and 2.15 are used to develop the following relationship

$$P_0 = \int_0^{2\pi}\int_0^{r_f} (\sigma_{zz}^f - Z_1^{mat}(r)\cos 2\theta - Z_2^{mat}(r)\sin 2\theta - Z_3^{mat}(r))rdrd\theta \qquad [3.3]$$

Where the stress term with superscript "mat" is defined by Equation 2.5. For the case of no chemical bond $\sigma_{zz}^{mat} = 0$ and Equation 3.3 reduces to 3.2 for $r_c = r_f$. It is convenient in this analysis to utilize an equivalency argument by representing the adjacent fibers as a convenient shape. To this end, the adjacent fibers surrounding the fractured fiber/fiber end are assumed to be depicted by an annular ring of fibrous material (see Figure 31). This basic assumption results in an axisymmetric problem in which stresses and strains are not a function of θ. The inner radius of the annular ring is represented by the inner dimension of the closest fiber r_s and the outer radius of the ring r_o is chosen such that the area of the ring is equivalent to the surrounding fibers (e.g. for hexagonal array the ring area is equal to $6\pi r_f^2$). By taking a representative slice of the composite, at the plane of the crack, a typical force element can be constructed as shown in Figure 32. By summing the forces on this element the following equation can be constructed.

$$P_0 - F_1 - F_2 - F_3 = 0 \qquad [3.4]$$

where

$$F_n = \int_0^{2\pi} \int_{r_{inner}}^{r_{outer}} \tilde{\sigma}_{zz}^{n} r \, dr \, d\theta$$

The superscripts "inner" and "outer" in Equation 3.4 define the inner an outer radial dimensions of the n'th ring in the model. The F's are representative of the average force present in each of the finite regions depicted in Figure 32 due to the near-field traction represented by either Equation 3.2 or 3.3. These F's are calculated by area averaging the stresses $\tilde{\sigma}_{zz}$ on each face as presented in Equation 3.4, however, these stress terms are unknown at this time. To solve this problem, knowledge of the functional dependence of each axial stress term on the radial coordinate must be known. In addressing this dilemma, it is first noted that the axial strain (i.e. $\tilde{\varepsilon}_{zz}^{n}$) is a continuous function in r (if slip does not occur) across all boundaries without point discontinuities except at the crack tip. This can easily be verified with the displacement continuity requirements at the interface between constituents and constitutive relations presented in Equation 2.7. Based on fracture mechanics and experimental evidence (Lesko et. al. [45]), it is proposed that the radial variation of the axial strain for the region $r > r_c$ can be obtained. This problem has historically been treated as a shear transfer problem between constituents. Fracture mechanics arguments (this analysis does not include singular effects) state that the shear stress should decay as $1/r^5$, which strongly suggests the dependence of the axial stress on the radial coordinate should be written as follows (as discussed in a later paragraph).

$$\tilde{\varepsilon}_{zz}^{n} = \frac{B}{r^{1.5}} f(z) \qquad [3.5]$$

B in the above equation is an unknown constant and the function f(z) represents the dependence of the axial strain on the z variable (note: it is convenient to define f(0) = 1) which is yet

to be determined. Noting that the axial stress for each constituent is dominated by the axial strain for this problem, (i.e. $\tilde{\varepsilon}_{zz} >> \tilde{\varepsilon}_{rr}$ or $\tilde{\varepsilon}_{\theta\theta}$) the following reduced constitutive relationship is written.

$$\tilde{\sigma}^n_{zz} \simeq C^n_{11}\tilde{\varepsilon}_{zz} \qquad [3.6]$$

C^n_{ij} is defined to be the contracted stiffness tensor for the n'th constituent in the composite. By using equations 3.2-3.6 an explicit relation for B can be obtained in terms of the applied load, the fiber volume fraction, crack radius, and the constituent material properties. This is represented in the following equation

$$B = \frac{1}{4\pi} P_0[C^m_{11}(r_a^{1/2} - r_c^{1/2} + r_4^{1/2} - r_0^{1/2}) + C^f_{11}(r_0^{1/2} - r_a^{1/2})]^{-1} \qquad [3.7]$$

Where r_4 defines the outer most radius of the matrix region presented in Figure 31. All of the quantities presented in Equation 3.7 are known, therefore a solution is presented for the axial strain/stress redistribution on the neighboring fibers, and matrix regions at the crack plane ($z=0$). Note that these values are dependent upon the distance from the crack and thus predict a variation in strain concentration across the width of the fiber and matrix. From these results a maximum (i.e.$r = r_a$), minimum (i.e.$r = r_o$), and an average strain concentration (i.e. area average) can be calculated for the fibers in the composite. These quantities will be used in parametric studies presented in Section 3.2-3.27.

The preceding analysis only provides the axial stress variation in the plane of the crack; however, it is desirable to obtain the full field stress state in each constituent. In solving this problem, the equilibrium equations are utilized in a similar fashion to that accomplished when determining the out-of-plane stress terms in laminate analysis. The equilibrium equation for an axisymmetric problem are written as follows.

$$\frac{\partial \sigma_{rr}}{\partial r} + \frac{\partial \sigma_{rz}}{\partial z} + \frac{\sigma_{rr} - \sigma_{\theta\theta}}{r} = 0 \qquad [3.8]$$

$$\frac{\partial \sigma_{zz}}{\partial z} + \frac{\partial \sigma_{rz}}{\partial r} + \frac{\sigma_{rz}}{r} = 0$$

By using equations 3.5 and 3.6 and assuming that $\sigma_{rr} = \sigma_{\theta\theta}$, the solution to the partial differential in Equations 3.8 is obtained for the shear and radial stresses as a function of r and z.

$$\tilde{\sigma}^n_{rz} = \frac{\partial f(z)}{\partial z}\left[\frac{D^n_1}{r} - \frac{2BC^n_{11}}{r^{1/2}}\right] \qquad [3.9]$$

$$\tilde{\sigma}^n_{rr} = \frac{\partial^2 f(z)}{\partial z^2}\left[-D^n_1 \ln(r) + 4BC^n_{11} r^{1/2} + D^n_2\right]$$

The D's in Equation 3.9 are constants determined by the boundary conditions of the near field problem which has not been posed at this time. The reader should note the $1/r^{1/2}$ dependence in the $\tilde{\sigma}_{xr}$ term which is consistent with the fracture mechanics arguments given in previous paragraphs. To evaluate the constants presented in Equation 3.9, an internal traction is applied at $r = r_c$ (i.e.$\tilde{\sigma}_{rz}(r_c,z)$ and $\tilde{\sigma}_{rr}(r_c, z)$). This approach utilizes a form of the boundary conditions present in the analysis presented by Whitney and Drizal [23]. By enforcing continuous tractions at each interface between constituents, the entire stress field for each region is found which are represented by the following sets of equations.

$$\tilde{\sigma}_{rz}(r_c, z) = \frac{-P_0}{2\pi r_c}\lambda^2 z e^{-\lambda z} \qquad [3.10]$$

$$\tilde{\sigma}_{rr}(r_c, z) = \frac{P_0}{4\pi}(-\lambda^2 + \lambda^3 z)e^{-\lambda z}$$

$$\tilde{\sigma}^n_{ir} = \tilde{\sigma}^{(n+1)}_{ir}$$

In the above equations, lambda is a parameter which controls the distance normally referred to as the ineffective length. This quantity dictates the length over which this stress decays as a function of the z variable. The relationship between the crack size, constituent parameters and volume fraction to this parameter are currently being studied to provide an accurate

functional dependence to the scientific community. To provide results regarding the shear stress variation, an experimentally determined value for λ is used in this chapter based on the evidence presented in Chapter 4.

Therefore, the entire stress field in the vicinity of the crack/fiber end has now been determined for a single fiber in a composite containing regular fiber spacing. The point-wise stresses are dependent on crack size, constituent properties, and fiber volume fraction unlike any analysis present in the literature. This analysis augments the results presented in chapter 2 by providing the stress state, not only in the cylinder assemblage being addressed, but also in neighboring cylinder assemblages. The model still requires the incorporation of multiple fiber fracture/end effects and variable fiber spacing; these are discussed in the following sections.

3.11 Multiple fiber effects

A methodology is proposed in this section for the analytical development of multiple fiber fracture/fiber end effects in composites with the use of results derived in the previous section along with a unique fiber discount method and a superposition technique. This analysis provides the stress/strain concentrations for each constituent in regions containing more than one fiber fracture/end. It is believed that this novel technique provides reasonable results for the predictions of the point-wise stress redistribution values in regions containing multiple fiber fracture.

In this dissertation a description of the formulation for a composite which contains two adjacent fiber fracture/end (see Figure 33) is presented. The subsequent methodology for multiple fiber fracture/end is easily inferred from the basic approach presented here. The fracture/ends in each of the two fibers are assumed to exist in the same axial (i.e. $z=0$) plane of the composite. Therefore, it is postulated that the second fractured fiber (or fiber end) does not sup-

port any of the load redistributed from the first fractured fiber. This seems reasonable when considering the plane defined by $z=0$ (i.e.crack plane) and the cracked fiber problem. Here both fibers are fractured, and neither is capable of supporting any load in this region. Therefore, the second fractured fiber is discounted from the initial part of our analysis. This mathematically consists of reducing the area of the fibrous annular ring surrounding the first fiber fracture (see Figure 31) by an amount equal to second fiber fractured πr_f^2 (i.e. $r_o^2 - r_s^2 = 5r_f^2$). This effectively increases the load which must be supported by the unbroken fibers adjacent to the first fractured fiber when the second fiber fails. By using Equations 3.2-3.10 as described in the preceding section, the stress redistribution in neighboring regions is calculated.

To address the stress redistribution caused from the second fractured fiber, the process described above is repeated, however, the first fractured/end fiber is discounted and the stress redistribution around the second is analyzed. Once the solution to the second fractured fiber is obtained, it is superposed on the solution to the first fractured fiber problem, thus providing a complete point-wise solution to the problem. The first and second fibers have different sets of neighbors (see Figure 33), which results in an unsymmetrical stress distribution in the composite.

To analyze a composite containing multiple fiber fractures the same sequence of steps is employed. Each fractured fiber is analyzed as a separate problem which requires that all other fractured fibers be discounted from the analysis. After analyzing the stress redistribution which results from each fiber fracture separately, the solutions are superposed to develop the full stress field in a composite containing multiple fiber fractures/ends. It should be noted that the resulting stress redistribution due to multiple fiber fractures is no longer symmetric (see Figure 33), and in fact, predisposes itself to strain concentrations which are larger on specific fiber assemblages. This suggest a distinct failure pattern should propagate throughout the composite based on maximum strain concentration arguments.

3.12 Variable fiber spacing

A similar methodology to that outlined in the initial section, is employed to study the effect variable fiber spacing has on the stress redistribution near a fiber fracture/end. For simplicity, this issue is addressed, as was done in previous sections, in the context of a hexagonal array of fibers. The analysis begins by assuming that only one of the fibers is eccentrically oriented in the array during the manufacturing process (see Figure 34). The present methodology can easily be applied to numerous misaligned fibers including a randomly oriented system. It is proposed that the problem can be represented by an annular ring of fibers as described in the initial formulation. However, multiple fibrous rings are required to adequately address this problem.

For a composite containing one fiber eccentrically oriented, two fibrous rings are constructed around the fractured fiber (see Figure 34) to represent this situation. The outer fibrous ring depicted in this figure is representative of the 5 regularly spaced fibers and is located at the inner radius corresponding to r_a and the outer ring is adjusted such that the area is equal to $5\pi r_f^2$. The inner fiber ring, which represents the single eccentric fiber, is located at r'_a and the outer radius of this ring corresponds to an equivalent area represented by πr_f^2. By utilizing equations 3.2-3.6, the axial stress variation in each of the constituent regions can be obtained.

In describing the results of this analysis, it is convenient to define an eccentricity parameter η as follows (see Figure 34)

$$\eta = \frac{r'_a - r_f}{r_a - r_f} \qquad [3.11]$$

When η equals unity the composite contains regularly spaced fibers and when it is zero the eccentrically oriented fiber touches the fractured fiber. As noted above, the solution is not

limited to only one eccentrically oriented fiber. By the addition of multiple rings, any number of variably spaced fibers can be represented.

In the following sections, results are presented to substantiate the present analysis with experimental evidence. The reader is also provided with insight into the complex stress state which occurs in actual composite systems containing fiber fracture which have resulted from either manufacturing or in service use.

3.2 Results and discussions

In this section, direct experimental verification (the first known verification for a micromechanics model) as well as a number of parametric studies are presented which depict the influence that specific physical parameters have on the stress redistribution in composites containing fractured fibers. A comparison is first provided between experimental data and theoretical results to confirm the current analysis. Having shown the validity of the approach, a study of the effect constituent properties, fiber volume fractions, and crack size have on the strain concentrations in adjacent fibers is furnished. The point-wise stress states for a polymeric and metal matrix composite containing fractured fibers is discussed. A section is dedicated to the effect multiple fiber fracture has on a typical polymeric matrix composite. The final section introduces the results of various parametric studies concerning variable fiber spacing and its effect on strain concentration. Included in this section is a validation of the present model furnished by the comparison of the theoretical predictions with experimental data.

3.21 Experimental verification (uniform spacing)

The reader is first provided with a direct experimental validation of the theoretical micromechanics model developed in this chapter, believed to be the first of its kind. The experimental data are generated with a unique test methodology utilizing embedded sensors in a macromodel composite which is described in detail in Chapter 4. The experimental setup represents a typical polymeric composite having the elastic properties published in Table 6.

The initial set of experimental results described in this section depicts a polymeric model composite (see Table 6) whose fiber spacing is representative of a fiber volume fraction of $v_f = 0.15$. In this particular set of composites, the fiber fractured and the crack arrested at the fractured fiber matrix interface, that is the size of the crack in the material is equal to the diameter of the fiber (i.e.$r_c = r_f$). In Figure 35, a plot of the experimentally determined and theoretically calculated strain concentrations are shown. In this figure, the y abscissa represents strain concentration which is defined as the full field axial strain (Equation 3.5 in Equation 3.1) normalized to the far-field axial strain (i.e.$\varepsilon'_{zz}/\varepsilon_{zz}$ = strain concentration). The x abscissa represent the normalized distance from the crack tip (e.g. fractured fiber is located at $r/r_f = 1$) at the plane of the crack, that is $z = 0$ in both the theoretical calculations and test data. The experimental data is presented for both the fiber (determined by resistance strain gauges) and the matrix regions (determined by Fabry-Perot fiber optic strain sensors FP-FOSS). These techniques allow for a detailed mapping of strain concentration in a highly localized region of the composite. The data point at $r/r_f = 1.6$ presented in Figure 35 is representative of the strain concentration in the matrix region adjacent to the fractured fiber and differs the most with the theoretical predictions. This test data is about 18 percent lower than the theoretical prediction. This is explained as follows, the strain sensor provides an average strain reading over it's gauge length. The peak strain occurs at $z = 0$ and decays continuously as a function of the axial coordinate, therefore the strain measured should be smaller than the strain prediction at the plane of the crack (i.e. the largest strain). Furthermore, this particular sensor

has a comparatively longer gauge length (i.e. 2.66 r_f) than the other sensors used and should thus provide the largest deviation when compared with the theoretical predictions. Nonetheless, the overall agreement between the theoretical and experimental results presented in Figure 35 are excellent when considering the complexities which arise from internal measurements.

In subsequent experiments, composites having the same fiber volume fraction as described above were tested, however in these tests the fiber fractured and the crack propagated in the matrix up to the adjacent fiber. The crack size is thus equal to the adjacent inner fiber dimension, that is $r_c = r_a$. In Figure 36 a plot of the experimentally determined data and the theoretical predictions is presented for these experiments. The sensors in the composite were placed at different axial distances from the crack plane (i.e. $z \neq 0$). Therefore, multiple theoretical curves (i.e. $z = 0$, $z = 1.66r_f$, and $z = 2.0r_f$) are presented with each curve corresponding to the actual location of a strain gauge. One immediately notes the better agreement between the theory and the test data shown in Figure 36 than provided in Figure 35. This is mainly due to a more accurate measurement of the axial location of the strain gauges in the experiments represented in Figure 36. In fact the largest discrepancy between the theory and the experimental data is only 6 percent, which leads one to the conclusion that the present model is providing highly accurate predictions. The results from the larger crack depicted in Figure 36 is also contrasted with the smaller crack presented in Figure 35 (i.e. $r_c = r_f$ versus $r_c = r_a$). The reader should immediately note that a much larger strain concentration is predicted and measured for this larger crack size (compare Figures 35 and 36); in fact the value increased by almost 50 percent. Present models in the literature do not incorporate a crack parameter into their theoretical calculations and thus suggest no dependence of strain concentration on crack size. However, as one can plainly see from the experimental results this dependence is significant. By corroborating the present model with the results presented in the previous two figures, a validation of the models dependence on crack size is accomplished.

To substantiate the models depiction of the dependence on fiber volume fraction, a comparison is made with a relatively larger fiber volume fraction composite than presented in the previous paragraphs. In Figure 37, a plot of experimental data and theoretical predictions for a 20 percent fiber volume faction polymeric model composite is provided. For this particular set of composites the fiber fractured and the crack did not propagate into the matrix material (i.e. $r_c = r_f$). This size of crack is analogous to the results presented in Figure 35 for a smaller fiber volume fraction. When comparing Figure 35 to Figure 37 one finds that the smaller fiber volume fraction exhibits, both theoretically and experimentally, larger strain concentrations. Once again, the reader should be aware that the current models in the literature do not incorporate a dependence of strain concentration on fiber volume fraction. When reviewing the results presented in Figure 37, one finds the discrepancy between theory and experiments is less than 5 percent for all the data points, which is remarkable. These results provide a firm foundation which suggest that the correct dependence of strain concentration on fiber volume fraction is represented in the model.

In subsequent experiments with a composite having the same fiber volume fraction composite (i.e. $v_f = 0.20$), the crack propagated up to the adjacent fibers (i.e. $r_c = r_s$). The results of the experimental tests along with the theoretical predictions are provided in Figure 38. This crack is similar to the one depicted by the results presented in Figure 36 for a smaller fiber volume fraction. When comparing the two figures (Figures 36 and 38), the larger fiber volume fraction does not appreciably alter the strain concentration, for this particular PMC composite and crack size. This is exhibited by both the theoretical predictions and the experimental data, which suggest that in PMC containing large cracks $r_c = r_s$, the strain concentration is relatively independent of fiber volume fraction for this very specific crack and material system. In Figure 38, the largest error between analytical predictions and the test data is about 7 percent which is once again an extremely accurate correlation. This further corroborates the statement made at the end of the previous paragraph (i.e. the model contains the correct functional dependence on fiber volume fraction).

In conclusion, two fiber volume fraction polymeric composites, each having different crack geometries which comprise a total of four different data sets, have been compared with the current analysis. The largest error between the theoretical results and the experimental data was shown to be less than 18 percent, which was primarily due to the the large gauge length of the particular FOSS used and inaccurate measurement of its exact axial location. Nonetheless the agreement between the theory and experiments was well within the experimental error which is inherent when performing internal measurements and should thus be regarded as excellent correlation. Furthermore, the model exhibited the appropriate functional variations in strain concentration with fiber volume fraction and crack size, where other models suggest independent behavior. Therefore, these studies validate the models depiction of the dependence on fiber volume fraction and on crack size and gives a direct experimental verification of the micromechanics model. In the following sections of this chapter, a set of parametric studies is presented to demonstrate the significant alterations which occur in the strain concentration profiles predicted by the current theory.

3.22 Constituent properties

In Figure 39, a plot is presented of the average strain concentration in the plane of the crack in adjacent fibers versus constituent properties. Average strain concentration is calculated by area averaging the strain values over the fiber's face at $z=0$. It is important to recognize that this plot is constructed with a crack which does not propagate into the matrix (i.e. $r_c = r_f$). The three curves plotted in the figure represent different fiber volume fractions. One immediately recognizes that strain concentration increases with increasing C_{11}^f/C_{11}^m as it should. That is, as the matrix stiffness decreases relative to the fiber stiffness, the fiber supports a larger portion of the load. Note for larger values of C_{11}^f/C_{11}^m, the strain concentration values appear to become independent of material properties (i.e.constant). However, the value which this occurs at varies as a function of v_f. For a $v_f = 0.65$ this occurs at approxi-

mately $C_{f_1}/C_{\eta} = 15$, for $v_f = 0.40$; $C_{f_1}/C_{\eta} = 20$, and for $v_f = 0.20$; $C_{f_1}/C_{\eta} = 30$. This suggests, for composites which fall to the right of these values (typically polymeric) in Figure 39, matrix properties have little influence on strain concentration, while for composites which fall to the left of these values (typically ceramics and metal matrix) the load carrying capabilities of the matrix significantly effects strain concentration. Therefore, Figure 39 provides a definitive bound for the applicability of the models which have been formulated on shear lag assumptions (e.g. Hedgepeth & Van Dyke [24] and Fukuda [30]). For these latter types of analyses, which assume the matrix does not support a normal load, the strain concentrations are not expected to be a function of constituent properties.

3.23 Fiber volume fraction

Figure 40 depicts the variation of the average strain concentration in adjacent fibers at the plane of the crack ($r_c = r_f$) as a function of v_f for a typical polymeric composite (see Table 6). The maximum, minimum, and average strain concentrations, described in the previous section, are presented in this plot. As v_f increases the maximum and average strain concentrations increase, as intuition would suggest. However the minimum strain concentration exhibits a maximum value at approximately $v_f = 0.20$. It is believed, as the fibers are moved closer together (i.e.larger v_f), the fiber region nearest the fractured fiber (i.e.r_o) is actually supporting a larger portion of the load, which results in a decrease in the load supported by the outer fiber region (i.e.r_0) This hypothesis is substantiated by the steady increase exhibited in the maximum strain concentration for increasing v_f. The reader should also notice, for larger fiber volume fraction, the average strain concentration becomes relatively constant. Models present in the literature (Hedgepath & Van Dyke [24]) actually suggest this independence of stress/strain concentration on fiber volume fraction for polymeric materials, as modeled here. However, these latter models do not depict the extreme stress/strain variation which actually exists across the fiber dimension predicted by the current theory and presented

in Figure 40. In the context of macro-strength predictions, these stress variations are essential to an accurate representation.

3.24 Stress variations

As presented in Section 3.1 of this dissertation, the model provides more than just axial fiber strain concentrations at the crack plane for discrete values of r. To demonstrate this, the methodology described in Equations 3.8-3.10 is used to provide stress results for continuous values of r at given z locations. The results presented are for a typical glass/epoxy composite ($r_c = r_f$) containing 65 percent fiber volume fraction. The normalized stresses (note: near field stress versus far-field fiber stress $\tilde{\sigma}_{ij}^n/\sigma_{zz}^f$) plotted in Figure 41 correspond to σ_{zz} at $z=0$ and σ_{rz} (note: absolute value was plotted to provide results on same graph) at $z = 1/\lambda$. λ was assumed to be $0.58/r_f$ for these calculations. The reader should immediately notice in Figure 41, a variation in axial stress exists in both the fiber and matrix materials. This plot suggests that for this polymeric system the fiber supports the majority of the axial load, as expected. However, unlike shear lag analysis, the matrix supports a normal stress equivalent to approximately 10% of the fiber axial stress. Figure 41 depicts another point of interest concerning the variation of shear stress in the radial direction. First, it appears that the transfer of normal load to the fiber is through a matrix shearing mechanism, as expected. However, the shear is predominately dissipated in the fiber region and not the matrix. Thus, unlike the shear lag models, a substantial shear stress is also present in the fiber. The shearing stress is seen to be virtually nonexistent outside the first fiber ring. These relationships provide the necessary information to understand the interaction which occurs between constituents present in polymeric composites containing fiber fracture.

To demonstrate the current analytical models applicability to other model systems, the stress variation in a SiC (nicalon)-Al MMC ($v_f = 0.40$ and $r_c = r_f$) is presented in Figure 42. The mate-

rial properties for the constituents are presented in Table 4. As in the previous figure, the normalized axial and shear stress terms are shown for axial locations similar to those mentioned above, that is maximum shear and normal stress. It can be seen in Figure 42 that the normal stress supported by the matrix region is as significant as the normal stress supported by the adjacent fiber region, which contradicts shear lag-type of arguments (i.e. the matrix supports no normal load). The fact that the matrix does support a significant normal load should be of no surprise when comparing the stiffness of the fiber to the stiffness of the matrix, that is the ratio C_{f_1}/C_{m_1} is approximately 4. This is in sharp contrast to the normal stress supported in the PMC depicted in Figure 41 whose stiffness ratio is about 20. With regards to the shearing stress presented in Figure 42, one notes that the majority of the stress is dissipated in the matrix region and not by the fiber for this material system. This is in sharp contrast to the results presented in Figure 41 for the PMC where the majority of the shear stress is dissipated in the adjacent fiber.

In conclusion, the present model provides point-wise stress states in material systems which are a function of the constituent parameters, unlike models currently in the literature. These added features will provide more accurate predictions of strength in PMC, materials and will provide one of the first accurate models to predict strength in MMC's. The fact that shear lag models are not applicable to MMC's renders them inappropriate for strength predictions in these material systems.

3.25 Crack size

In Figure 43, the variation of average strain concentration on adjacent fibers in the plane of the crack as a function of normalized crack size (i.e.$(r_c - r_f)/(r_c - r_f)$) is presented for a typical glass/epoxy system. At a normalized value equal to 0, the crack does not extend into the matrix $r_c = r_f$, and when it is unity, $r_c = r_a$ the crack extends up to the adjacent fiber. Results

for three different fiber volume fractions (i.e. 0.20, 0.30 and 0.65) are provided in this figure. When the crack does not extend into the matrix, the smaller v_f composites exhibit a smaller strain concentration, as expected. However, when the crack propagates to the neighboring fibers (i.e.normalized value of 1) there is a reversal in the ordering of the strain concentration, which is explained as follows. For large fiber spacing (i.e. smaller v_f), a crack which propagates up to the adjacent fibers is actually a larger crack as compared to the small fiber spacing (i.e.larger v_f). Furthermore, the larger fiber spacing causes a larger P_0 due to the bigger region of matrix cracked (see Equation 3.2). That is, for smaller v_f composites, the load transferred due to the matrix crack is actually greater. Therefore, the interaction between fiber volume fraction and crack size significantly alters the strain concentrations in the composite material. As noted previously, current models in the literature do not incorporate these important parameters.

A parametric study is presented in Figure 44 depicting the effect larger cracks (i.e. $r_c = r_a$) have on the average strain concentration in adjacent fibers at the plane of the crack as a function of the constituent properties. The reader will remember that a similar comparison was presented in Figure 39 for a smaller crack $r_c = r_f$. It can be seen by viewing Figure 44 that the strain concentrations decay for increasing values of the stiffness ratio. However, this is the exact opposite effect from that which was presented in Figure 39 for the smaller crack. When considering a composite with a larger crack, P_0 represents a combination of the forces originally supported by the fractured fiber and the fractured matrix (see Equation 3.2), while in the composite with the smaller crack, P_0 represents only the force originally supported by the fractured fiber. The composite with the larger crack thus has a larger P_0 which results in a larger strain concentration in the adjacent fibers as compared to the smaller crack sizes, as one would intuitively expect. However, as the stiffness of the matrix decreases (i.e. C_{f_1}/C_{m_1} increases) the load originally supported by the cracked matrix decreases, which results in a decrease in P_0, thus resulting in a decrease in strain concentration as a function of increasing stiffness ratio. One can also see in Figure 44 that the ordering of the strain concentration as

a function of fiber volume fraction is exactly the opposite as that presented in Figure 39. Composites with smaller fiber volume fractions contain fibers which are spaced further apart. Thus when a fiber fracture propagates to the adjacent fibers systems the crack in the smaller fiber volume fraction composites is actually larger. Furthermore, since the crack is larger, the term P_0 is larger due to the additional matrix region cracked in the composite (see Equation 3.2), and this causes smaller fiber volume fraction composites to exhibit larger strain concentration for large crack size. One can begin to understand the importance of parameters such as crack size, constituent properties, and fiber volume fraction which have been shown in the previous figures to significantly alter not only the strain concentrations but the actual trends in strain concentration as a function of each parameter.

Therefore, from this analysis, one may conclude that smaller v_f composites with larger matrix cracks should exhibit larger average strain concentrations. This important fact does not show up in any other model present in the literature due to their relative simplicity. By extending these results to actual composite systems, the analysis can assist design and processing methods to improve tensile strength of MMC's, PMC's and CMC's. For instance, it may be desirable to minimize the strain concentration in a composite intended for a specific design application. With the present model, one can tailor the constituent properties, fiber volume fraction, and crack size for the intended use. The crack size can be altered with the application of an interphase coating (see chapter 4) and/or by adding toughening agents to the matrix material. A model, such as this one, which is capable of providing an accurate depiction of the physical phenomena present at the micro level, is of extreme importance to the design of new material systems. Furthermore, this is the first model of its type to predict a functional dependence of strain concentration on the parameters provided in this section.

3.26 Multiple fiber fracture

Figure 45 depicts the effect of multiple fiber fractures on average strain concentration in adjacent fibers in a glass/epoxy composite. It is assumed in these calculations that fiber fractures occur in fibers which are adjacent to one another (see Figure 33). The strain concentration values presented in the plot are representative of the fiber which exhibits the largest average strain concentration in the composite for the given number of fibers fractured. The curves in the figure are representative of predictions made for four combinations of v_f and r_c in Figure 45 for a typical polymeric composite. As expected, with increasing fiber failures, the strain concentration increases, however the increase is highly nonlinear. Note, that after 5 fibers have fractured, there is a drastic increase in strain concentration, which suggests that the composite should be incapable of sustaining a large number of fractured fibers in a given region prior to composite failure. This is validated by the experimental results presented by Jamison [46] and the theoretical predictions of Batdorf [30]. Furthermore, one should realize that the $v_f = 0.20$ curves actually bracket the larger $v_f = 0.65$. This phenomena was noted and explained in a previous paragraph of this section. Experimental results on multiple fiber fracture in a 2-D model glass/epoxy composite have shown that for two adjacent fiber fractures the strain concentration is 1.7 while current theory predicts a strain concentration value of 1.68. The excellent agreement between theoretical and experimental results provide a firm validation for this model. The ability to make macroscopic predictions utilizing the proposed theory is a natural extension of this work.

3.27 Variable fiber spacing

A validation of the analytical results predicted by the model for variable spacing is initially made in this section for a glass/epoxy composite. A comparison between the experimental

data for a model composite $v_f = 0.15$ described in Chapter 4 with the current theory is presented in Figure 46 for different crack geometries (i.e.$r_c = r_f$ and $r_c = r'_a$). The two theoretical curves presented for each crack geometry correspond to the maximum strain concentration on either the eccentric fiber $r = r'_a$ or an aligned fiber $r = r_a$ (see Figure 46). Experimental results are shown for three different η values of 0.16, 0.31, and 1.0 (see Equation 3.11) with $\eta = 1.0$ representative of uniformly spaced fibers. The experimental data are represented in the figure with the unfilled symbols corresponding to the curves with the solid symbols. The reader should be aware that the predicted results are calculated at the precise location the experimental data were obtained, as accomplished in Section 3.21. The comparison between the present theory and experimental results appears to be fairly reasonable. With regards to the strain readings accomplished at $r = r'_a$ for the composite with the crack $r_c = r'_a$, the theoretical predictions are well within 10 percent error of the experimental data points for both values of η (i.e.0.16 and 1.0). In regards to the strain readings at $r = r'_a$ for the crack size of $r_c = r_f$, the error is less than 20 percent. This relatively larger value may be explained by inaccurate measurements of the crack size during the test. Nonetheless, the trend in the test data as a function of eccentricity parameter and crack size is the same as that predicted by the theoretical model. Therefore, the comparison between the experimental data and the analytical results are regarded as good.

Having demonstrated the validity of the analytical results concerning variable fiber spacing, a parametric study is undertaken for a typical glass/epoxy PMC. In Figures 47 and 48, plots are presented for the maximum strain concentration versus the eccentricity parameter η, for the the eccentrically located fiber $r = r'_a$ and the adjacent fiber $r = r_a$. The plots depicted in the figures are representative of two crack sizes, a fiber fracture (i.e.$r_c = r_f$) and a full matrix crack (i.e. $r_c = r'_a$). In Figure 47, the results for a typical polymeric composite $v_f = 0.20$ are presented. Note the extreme differences in strain concentration for a fiber fracture as compared to a full matrix crack as was described in the preceding section. For increasing alignment (i.e.η increases) the eccentrically located fiber (i.e. $r = r'_a$) exhibits a decrease in strain concentration

for either crack size, as expected. However, the aligned fibers (i.e.$r = r_a$) display an increase in strain for increasing alignment. The aligned fibers are required to support a larger portion of the load as the eccentrically located fiber becomes more aligned. In Figure 48 a similar plot for $v_f = .65$ is presented. One immediately notices a difference when comparing this plot to Figure 47. The strain concentration in a higher fiber volume fraction composite (Figure 48) does not have as large a dependence on crack size or η, as does the strain concentration in a smaller fiber volume fraction. Therefore, one can conclude that eccentricity parameters effect smaller v_f composites more severely than they do the larger v_f composites. This appears reasonable, noting that for small v_f composites, the measured distance between the eccentrically located fiber and the aligned fibers is greater than in large v_f. The larger distance correspondes to larger strain concentration effects. This does not imply that the larger fiber volume fraction composites are not effected. One can plainly see from Figure 48 this is not the case (in fact for metal matrix and ceramic matrix composites the effect is severe).

In Figure 49 a plot of maximum strain concentration versus v_f is presented for an eccentrically located fiber for three different η. This figure depicts the significant effect eccentricity has on strain concentration. First, for fibers uniformly spaced (i.e.$\eta = 1$), the strain concentration increases for increasing fiber volume fraction. However, for $\eta = 0$ the exact opposite trend is noted. That is, as v_f increases, strain concentration decreases. A value of $\eta = 0.5$ is also presented to show the apparent trend from an increasing strain concentration to a decreasing strain concentration as a function of v_f. This drastic change in the variation of strain concentration for different values of η can be explained as follows. As described in the previous section, in polymeric composites with uniformly spaced fibers and small crack size, the maximum strain concentration increases as the fiber volume fraction increases. For a composite containing an eccentrically located fiber the maximum strain concentration may decrease depending on the degree of eccentricity. Assuming that the eccentrically located fiber touches the fractured fiber (i.e.$r'_a = r_f$). For small v_f the aligned fibers are a large distance from the fractured fiber (i.e.$r_a \gg r_f$) Therefore, the eccentrically located fiber supports the majority of the

load in this scenario. When v_f increases, the aligned fibers become closer to the fractured fiber and begin to support a larger portion of the load. This decreases the strain concentration on the eccentrically located fiber. Thus, a drastic difference in the dependence of strain concentration on v_f is noted for varying degrees in the uniformity of fiber spacing. From these plots it is relatively easy to understand why micromechanical concepts such as these are of extreme importance when predicting the strength of composite materials.

In conclusion, the agreement between the experimental data and the theoretical predictions was relatively good. The dependence of strain concentration on the eccentricity parameter was shown to be more significant in smaller fiber volume fraction composites, at least PMC's. The eccentricity parameter was also demonstrated to alter the dependence of strain concentration on fiber volume fraction (i.e. increasing or decreasing) which is extremely important to design engineers.

In the following chapter the description of the experimental setup will be presented. This unique methodology has applications far beyond those provided for validation of the current model presented in this chapter.

4.0 Model composite

As stated in previous chapters, micro-level damage events in composite materials are extremely important issues when addressing the remaining strength and life of the system. These events include fiber fractures, matrix cracks, and fiber end effects. Development of accurate representations of these phenomena at the local level is difficult, and until this time has been unverifiable. The thrust of the current research is aimed at presenting a direct approach to understanding and validating analytical micromechanical models under development or already present in the literature. The ability to critique these models with experimental results is of extreme importance to the engineering community. The data generated from these tests forms a basis for validating models, and will provide guidance for future research. Traditionally, the largest problems in obtaining this type of data are the inability to closely examine internal damage events as they occur and the relatively small dimensions being examined.

The fact that parameters at the micro level significantly influence the strength of composite materials signifies that the micromechanics models should be accurate in every detail. This can only be accomplished with a novel technique utilizing direct experimental verification. A test methodology such as this one will also assist in identifying new directions for subsequent modelling efforts, particularly for optimizing the selection of fiber, matrix, and interphase for specific applications. The knowledge gained from investigations such as these in continuous

fiber composite systems will also have direct application to smart materials analysis and design [45].

Previous attempts to validate theoretical micromechanical models fall into two categories: volume averaging techniques [6-8, 12-14, 20, 21, and 30] and qualitative studies [23, 34, 36, and 37] on modelled situations. While both approaches yield useful information, they fall short of providing the quantitative data correlation needed to assess the validity of the micromechanical predictions. The volume averaging techniques smear out micro-details which are addressed in the analysis and are essential to global-level strength predictions. Likewise, the techniques which employ a modelled situation rely on theoretical micromechanics that have not yet been validated to verify their own predictions. However, the model composite, described in this dissertation does not suffer from these inconsistencies, and thus offers the unique opportunity to quantitatively assess the micro-details of internal strain concentrations which effect strength predictions. This unique investigation employs a scaled-up representation of a composite lamina (one ply of a multi-layered composite or laminate). Scaling up the fiber-matrix interaction allows for the quantitative and qualitative studies of typical damage states without loss of generality. At this level, continuum mechanics (see Fredrick [47) accurately describes the fiber/matrix interaction at the model composite level and the actual composite laminate level, for which the theory is developed. Within this macro-model composite, internal quantitative measurements of strain are obtainable in all constituents (i.e. fiber, matrix, and interphase) in the presence of particular damage events which are simulated in a controlled and known manner. Quantitative measurements are made with embedded fiber optic strain sensors and resistance strain gauges while qualitative measurements are made with photelastic resin and visual inspection. The use of embedded sensors in a composite to interrogate the state of the material is also directly applicable to the study of smart material structures.

The model composite developed for the current study is unique in the sense that a macro-scale is being utilized to study a local phenomenon in the composite lamina. This provides a

method to visually and remotely measure and control internal damage events. The tests conducted with the model composite provide experimental evidence concerning the interaction between fiber, interphase, and matrix in the presence of various internal disturbances, otherwise unobtainable. These studies investigate the stress redistribution around stress risers which are present in actual composite systems, which is of paramount concern to the scientific community. Experimentally determined values for the magnitude of stress concentration and for the size of affected regions are of primary interest in the present analysis, because of their importance to strength predictions. The principal focus of developing the current methodology is to examine the effects of fiber volume fraction, irregular fiber spacing, constituent properties, bond strength, and interphases on stress redistribution.

Results presented in this chapter include stress redistribution in short fiber composites. This demonstrates the applicability of the experimental model to various composite systems. Continuous fiber reinforced composites containing a fiber fracture are the main focus of the present study and thus represent the bulk of the data discussed. A fiber fracture in the model composite is shown to be achieved in a controlled manner at a pre-determined location in the composite. The stress concentration and ineffective length due to the fiber fracture are quantitatively and qualitatively measured for different fiber volume fractions and interphases. Results suggest that crack propagation plays a significant role in subsequent stress redistribution. A methodology is thus presented to directly study the effect of various physical parameters and their relation to internal damage events on micro level stress redistribution.

4.1 Materials

The matrix material used in the manufacturing process of the macro-model composite is an epoxy resin system (PLM-9 micromeasurement group). This material is a brittle thermoset

and is representative of typical matrices currently being used in actual polymeric composites. The PLM-9 resin also possesses photoelastic properties and is easily cast into relatively large rectangular shapes with minimum fabrication tools being required. Therefore, this material is an ideal choice to study the stress redistributions that occur around a fiber fracture in a macro-model.

The mechanical properties of the monolithic matrix material (PLM-9) are determined with standard experimental tests. These tests demonstrate that the mechanical properties of the manufactured matrix are the same as those published by the supplier. They also reveal that the stiffness properties do not sufficiently change with cure cycle (i.e. the cure temperature does not appreciably alter the elastic modulus). In fact, the discrepancies in the elastic modulus determined for specimens cured at 37° *C* and 110° *C* are found to be less than 3 percent (the lower cure temperature actually exhibits a larger elastic modulus which is believed to be due to consolidation effects). On the other hand, the creep rates exhibited by the specimens are extremely sensitive to the cure temperature. The specimens cured at room temperature display significantly larger creep rates than specimens cured at elevated temperatures. To provide a more complete depiction of this monolithic material, the matrix glass transition temperature, T_g, was determined by differential scanning calorimetry (DSC) to be between 102 and 113 degree C. A summary of the PLM-9 mechanical properties are presented in Table 6.

The fibers used in the manufacturing process of macro-model composite are borosilicate glass rods. These rods represent the structural fibers present in a typical polymeric composite material. The "fibers" used are glass stirring rods 3 mm in diameter, which can be found in most chemistry laboratories and are easily obtainable. This glass/epoxy model composite represents an E-glass/epoxy system scaled up 150:1 times. In fact, the fiber to matrix stiffness ratio (C_{f_1}/C_{f_1}) calculated with the introduction of this fiber into the PLM-9 matrix is approximately 20. This value is indistinguishable from an E-glass/epoxy material system used in a large number of composites currently manufactured for various uses. The glass fibers also

bond extremely well with the PLM-9 matrix with virtually no voids existing along the surface of the fibers, and thus offer an appropriate system to study. The bond strength at the interface is easily determined with a fiber push-thru test utilizing a continuous ball indenter. The glass fibers are a brittle material and exhibit purely linear elastic behavior prior to ultimate failure. This mechanical response offers an ideal opportunity to study proposed linear elastic models. A comprehensive summary of the glass fibers mechanical properties used in these tests are presented in Table 6.

Wooden dowels were also introduced into the model composite to represent structural fibers. These dowels are easily obtainable at hobby and speciality shops. With the introduction of these fibers into the PLM-9 matrix, a composite is generated which has a fiber to matrix stiffness ratio of approximately 4. This value is representative of a typical SiC-Al metal matrix composite used in aerospace application that has been scaled up 100:1 times. The work performed with this material system is not at the stage where definitive results are being generated. However, the feasibility study performed demonstrates that the adhesion between the wood and the matrix is sufficient to provide an excellent representative MMC system.

To study the stress redistribution in the vicinity of a fiber fracture in composite materials, a controlled fiber failure needs to occur at a predetermined location. This controlled failure is accomplished by notching the fiber with a diamond saw prior to manufacturing. The flaw introduced on the fiber surface provides a sufficient stress concentration to fracture the embedded fiber during tensile loading of the composite. This allows a fiber fracture to be initiated at a predetermined location in the composite. With this a priori knowledge, sensors can be embedded in the composite near the internal position of interest during the manufacturing process. Data on the stress redistribution behavior in the vicinity of the strain concentration can subsequently be obtained from the sensors. It has been demonstrated, through tests of 10 individual glass fiber samples, that these notched fibers fail at a load level of 200 Newtons plus or minus 30 Newtons. The notch, in some of the more recent model composite tests, is replaced with a mechanical score. This introduces a comparatively larger stress concen-

tration on the fiber and causes it to fail at a lower applied load level. This enables the researcher to control the load at which internal fiber failure occurs, and thus offers the opportunity to obtain vital stress redistribution data before and after fiber fracture.

A variety of materials are currently under examination which may be applied to the fibers to alter the fiber/matrix interface in the model composite system. The coatings are applied to the fibers prior to manufacturing. Some of the materials being investigated are silane coupling agents which promote adhesion, and vacuum grease which prevents adhesion. The silane coupling agent should promote the existence of a comparatively stronger chemical bond [48] between the glass rods and the matrix material. The vacuum grease applied to the glass rods should prevent adhesion and minimize the mechanical interlocking at the fiber/matrix interface. The vacuum grease applied to the wooden rods should also prevent adhesion, however it should not decrease the mechanical interlocking to the degree exhibited by the glass rods. This is mainly due to the porous nature of the wooden dowels.

A variety of materials are also being investigated to represent a finite interphase region between the fiber and matrix in the model composite. These include bismalimide (BMI) which provides a finite region of a thermoset material, polyethersolfone (PES) which provides a finite region of a thermoplastic material, and epoxide which provides a finite region of a thermoset material.

The bismalimide represents a relatively a brittle interphase which should bond well with the matrix material (i.e. both are thermosets). The epoxide is also a thermoset which should provide excellent adhesion between the interphase and matrix region, however, this material is relatively more ductile than the bismalimide and offers a distinctly different type of interphase to study. The PES material is a thermoplastic and should not chemically bond with the matrix material, however, there should be mechanical interlocking due to surface texture and thermal contraction affects (i.e. residual stress due to manufacturing caused by the thermal mismatch

between fiber and matrix). These interphases should provide a fundamental basis on which future tests can be guided in an attempt to study specific interphase types and gain a better understanding of the micromechanical phenomena associated with this region.

4.2 Measurement techniques

In this study both quantitative and qualitative methods are utilized to study the stress redistribution around internal disturbances in composite materials. The qualitative method used in this study employs photoelastic data obtained from the matrix material. By viewing the composite in the desired states (i.e. with an applied load following fiber fracture), qualitative information about the localized stress redistribution is obtained. The stress gradients produce different hues of color which correspond to isostress regions produced by the internal strain concentration. When investigating the response of the matrix in the presence a of fiber fracture, approximate measurements of ineffective length can be obtained using this technique. Photographs, taken at applied load levels, are subsequently analyzed and compared to provide qualitative information about the effect local fiber volume fraction and interphases have on local stress gradients in the vicinity of a disturbance (e.g. fiber fracture or fiber end). Although this technique provides a good indication of the general aspects associated with redistribution of stress, precise quantitative information is difficult to obtain from this technique. This is mainly due to the interaction between fibers, causing a 3-D stress field. This results in superposition and interference of the stress fields when the hues of colors are viewed through the thickness of the composite.

Resistance strain gauges (350 ohms) are applied on the surface of the external composite to obtain quantitative information about the axial global response. Such gauges are normally applied to a defect-free composite to ensure no interaction occurs between the internal dis-

turbance and the external strain patch. The external strain patches have a gauge length of 6.35 mm. The purpose of this strain patch is two fold. First, it provides definitive data on the elastic modulus of the composite. Second, in a defect-free composite the external strain patch should measure the same strain as an embedded sensor (i.e. generalized plane strain assumption). These results can be used to validate (or invalidate) internal measurements being employed to study localized fiber fracture.

Resistance strain gauges are one method employed to generate quantitative data on stress redistribution at predetermined locations in the composite. The resistance strain gauges are attached to the fiber surface of the embedded fiber with epoxy adhesive (AE-10 micromeasurments group) These high resistance (4500 ohm) strain gauges provide highly sensitive measurements of strains experienced by the embedded structural fibers with minimal heat dissipation. Strain gauges are placed on both the fibers and interphase regions prior to the manufacturing process. The internal resistance strain gauges have a sensing length of 2.54 mm, and are smaller than a fiber diameter. This allows measurements of fiber strains at the d_f level. With the present system strain measurements can be made at a resolution of 3 $\mu\varepsilon$.

All gauge positions are referred to the z coordinate (see Figure 50 presented in context of fiber fracture) whose origin is defined by the strain concentration (e.g. short fiber and fiber crack) present in the composite. The location of the gauges on the fibers can be divided into 4 generic categories: near-field (NF), far-field (FF), outer-field (OF), and transient (T)(see Figure 50). The near-field area is defined as the strain on an adjacent fiber next to either a fiber fracture or a fiber end (e.g. short fiber). Note that the near-field faces the crack (i.e. smallest r component) and should represent the highest strain concentration (S.C.) in the fiber. The far-field defines a region which is far removed from any disturbances present in the composite (i.e. $z \gg d_f$). The outer-field is defined as the region on the adjacent fiber face furthest removed from the strain concentration (i.e. largest r value). The transient field is defined as the strain on the actual broken or short fiber in the vicinity of the strain concentration. These generic

terms are used in the results section of this chapter to describe data trends in specific regions. This methodology allows for the measurement of internal strains experienced by the embedded structural fibers or interphase region in composite material at specific locations.

Fabry-Perot Fiber Optic Strain Sensors (FP-FOSS) are another quantitative method employed to study the internal stress redistribution in composite materials. FP-FOSS's interferometers are embedded in the composite during the manufacturing process to measure matrix strains in the vicinity of the strain concentration. The sensing length of these transducers vary from sensor to sensor due to the unique nature of the FP-FOSS (i.e. each interfermoter is individually made by hand). Nominally the length varies from 3 mm to 4 mm which permits internal matrix strain measurements at the d_f level. This is compared to the 2.54 mm gauge length of the internal resistance gauges applied to the fibers. The resolution of the FP-FOSS gauge is reported to be 0.11 $\mu\varepsilon$. For a determination of the strains from the output signal, fringe counting is performed. For a detailed description of the manufacture of the FP-FOSS and the analysis of the data, the reader is referred to Lesko et.al. [45].

These methods allow for a qualitative understanding of the perturbed stress region around a fiber fracture. They permit a direct quantitative measurement of the strains in internal structural fibers and matrix region. This includes detailed strain mappings around local disturbances such as fiber fractures and fiber end effects. The quantitative external strain measurements supply data on the global response and offer an excellent opportunity to validate the internal measurements.

4.3 Fabrication

The mold was thoroughly cleaned with acetone prior to manufacturing the model composite. TFE release agent was applied to the mold to permit easy extraction of the composite. The TFE release agent appeared to produce out-gassing during the cure cycle of the composite. Therefore, in the majority of the tests performed, the TFE release agent is subsequently wiped off the mold with a dry clean cloth immediately following its application. This appeared to minimize the presence of surface bubbles present in the composite. The reader should also be aware of the researchers attempt to bake the mold prior to manufacturing the composite in an attempt to minimize air bubbles. This apparently does not significantly alter the amount of air bubbles present.

Following mold preparation, a choice must be made on the fiber number, the fiber spacing, and the fiber type to be introduced into the composite. The present macro-model composite represents a 2-D model capable of containing six fibers aligned in a row. For a composite containing one fiber, the global fiber volume fraction is 1.87 percent while for a six fiber composite it is 11.2 percent. The fiber spacing within the mold is easily adjusted, such that a variety of local fiber volume fractions can be studied. In this dissertation, the results of two uniform fiber spacings are presented. These center to center fiber spacings are 4.6 mm and 6.2 mm, representative of 20 percent and 15 percent fiber volume fractions respectively (larger fiber spacing correlates to smaller fiber volume fraction). Variable fiber volume fraction is obtained by skewing the central fiber in the composite towards one of its neighbors. This represents a composite containing unevenly spaced fibers. By embedding fiber lengths smaller than the length of the composite, short fiber systems can be manufactured.

Having chosen the fiber spacing, the fibers are cleaned with acetone to remove any oils which may have been deposited on them. The fibers and sensors are placed in their appropriate

locations and secured in the base of the composite. This includes the fibers which have strain gauges adhered to them and the fibers which have been notched. The positioning of these fibers in the mold is extremely important, since this will determine the location of the fiber fracture and the location from which data is obtained on stress redistribution in the composite. Following the placement of the structural fibers, the fiber optic strain sensors are put in the composite. Once again, the orientation of the sensor's gauge length is extremely important since this will be the location that data will be recorded. With the fibers and sensors in the desired location (see Figure 51), the mold is sealed and put in an oven to soak for a minimum of 1 hour at 50° *C*.

While the mold is being preheated the PLM-9 matrix material can be prepared for pouring. Following the manufacture's recommended instructions, the appropriate amounts of hardener and curing agent are heated to the appropriate temperatures and thoroughly mixed. Once the mold is preheated, the matrix material is poured slowly along the inside corner of the mold. This is done to minimize introduction of bubbles into the composite during the curing process. The mold encompassing the matrix material and fibers is placed in an controlled oven at the desired cure temperature for an allotted time period.

The temperature and time period to cure the composite are extremely crucial. If the composite is cured at an elevated temperature, significant residual stresses are present in the fiber and matrix. In fact, for composites cured at 100° *C*, the residual compressive stresses in the fiber are so large that internal fiber fracture cannot be achieved without failing the entire composite. Therefore, to circumvent this problem, a cure cycle of 24 hours at 37 degrees C (which differs from the manufacturer's instructions) is utilized in the current research. This cure cycle minimizes the compressive stresses in the fibers, but serves to expedite the fabrication of the composite and appears to provide a sufficiently cured composite with only minimal residual stresses present.

In removing the fabricated composite from the mold, it is sometimes necessary to place the composite and mold in a refrigerator for 5 minutes. This facilitates the removal process by capitalizing on the differences in thermal expansion coefficients between the composite and the mold. A depiction of the fabricated composite with internal sensors and notched fibers is shown in Figure 52.

4.31 Interphase

The interphase/interface coatings are applied to the fibers prior to positioning them in the mold, but following the application of the resistance strain gauges. The two coatings applied to the fiber to alter the level of fiber/matrix adhesion are silane coupling agent (z-6040) and vacuum grease. These materials are not regarded as depositing a finite interphase region on the fiber. The silane coupling agent (45 parts by volume) is thoroughly mixed with isopropyl alcohol (5 parts) and distilled water (50 parts) and allowed to age for six hours. The fibers are subsequently dipped into the solution once and allowed to dry. This theoretically deposits one atomic layer of the silane coupling agent on the glass rod. In contrast, the vacuum grease is applied to the fibers by hand and subsequently wiped off.

The thermoset BMI comes in a liquid form which is somewhat viscous at room temperature. The BMI is initially preheated to decrease the viscosity of the polymer. The BMI is subsequently poured over the fibers in an attempt to provide a finite interphase region approximately 0.1 mm thick. The manufacturer recommends curing the BMI at 250 deg C, however the strain gauge adhesive is rated at 100 deg C. Therefore, the fibers are baked at 100 deg C for a minimum of 1 hour to cure the deposited BMI which is adhered to the fibers.

The more ductile thermoset used in these tests is an epoxide resin. The epoxide is mixed following the manufacture's recommended instructions. Once prepared, the liquid mixture is

poured over the fibers to deposit a finite interphase region approximately 0.1 mm thick, like the BMI. The epoxide is than allowed to dry at room temperature overnight.

The manufacture of the thermoplastic interphase is accomplished by dissolving a powder form of PES in methylene chloride. The fibers are dipped into this solution and allowed to dry at room temperature for 24 hours. As noted above, all of these manufacturing methodologies described for the interphase region result in coating thickness of approximately 0.1 to 0.2 mm. Some of the coatings are non-uniform; however by taking more care, uniformity has been improved in the most recent samples.

4.4 Results & discussion

A variety of results are presented in this section which describe the ability of the model composite to represent (and the embedded sensors ability to measure) specific physical situations which occur in actual composite systems. To ensure that the internal measurements are accurate, a subsection details a validation procedure for the sensors. Following the validation of internal measurements, a brief description is presented on the experimental results pertaining to a short fiber composite. This addresses load transfer which occurs at the ends of finite length fibers, however, the bulk data presented in this dissertation details stress redistribution which occurs near a fiber fracture. A number of subsections are presented which describe the results obtained on fiber fracture in composites containing single fiber, three fiber (this subsection describes two distinct types of crack propagation sequences), and six fiber systems. A subsection is also dedicated to the presentation of data obtained from tests performed on composites containing variably spaced fibers. The final subsection presents results describing interphase effects in composites and their relation to fiber fracture and

crack propagation. Specific problems which arose in the fabrication of composites containing a variety of interphases is also discussed.

The test results presented in this section are representative of a typical glass/epoxy composite system scaled up 150 times unless otherwise noted. The tests performed on the model composite system include thermal loading sequences and uniaxial tension/compression applied with a controlled oven and a servo-hydraulic test machine, respectively. All strain readings presented in this dissertation are taken at thermal equilibrium with thermal strain compensation made through the appropriate strain bridge configuration. When obtaining thermal data, the composite is held at a fixed temperature for a minimum of 1 hour prior to obtaining the data. A single fiber composite and a three fiber composite are defined to be a model composite with one and three structural embedded fibers respectively.

4.41 Validation

Before embedded sensors can be used to corroborate theoretical micromechanical predictions, the data obtained from the sensors must be validated with standard testing and analytical techniques. This is accomplished by applying uniaxial tension (load in the z-direction of Figure 50) to the composite which is void of strain concentrators (i.e. fiber fractures, matrix cracks). For this state of stress it is assumed that the composite experiences a state of generalized plane strain. This implies that the strain experienced by the composite is equal to that experienced by the fiber and matrix. This classic theoretical argument, for continuous fiber composites, is mathematically expressed as,

$$\varepsilon_{zz}^{matrix} = \varepsilon_{zz}^{fiber} = \varepsilon_{zz}^{comp} \qquad [4.1]$$

The generalized plane strain assumption stated above is generally accepted, and makes it directly possible to test the strain sensing ability of the FP-FOSS and the embedded resistance

strain gauges. This is accomplished by comparing the strain measurements made by the external strain patch ε_{zz}^{comp} to measurements made by the internal sensors (i.e. the resistance gauges ε_{zz}^{fiber}, and the FP-FOSS $\varepsilon_{zz}^{matrix}$). Upon making this comparison, the strain response from all three sensors should be indistinguishable (see Equation 4.1). When comparing the strain record for the three sensors as a function of applied stress (Figure 53) for a three fiber system (global $v_f = 5.67$ percent), a small deviation of about 5 percent is found. This small deviation is well within the expected experimental error. When comparing the strain response of these sensors to an accepted micromechanical prediction for an upper bound on composite stiffness (i.e. Concentric Cylinders Model), reasonable agreement is observed. Note that the CCM model was formulated assuming the model composite could be represented with cylindrical elements such that $d_f^2/d_m^2 = v_f$ (global value). The embedded sensor also appears to be a non-intrusive technique for the measurement of strain in this in-homogeneous system. This is substantiated by noting the excellent agreement between the external measurements and those made internally.

A summary of test data obtained on defect free model composites for both single and three fiber systems are presented in Table 7. The mechanical properties shown in this table were determined with data obtained with the internal resistant strain gauges and Equation 4.1. Theoretical results calculated from a displacement formulation with a CCM model (upper bounds) are also presented in the table.

In all the mechanically loaded tests performed on the model composite, the stress versus strain plots were essentially linear curves (see representative Figure 53). The experimentally determined E_{11} data shown in Table 7 for the three fiber system is representative of 18 tests with a range in data of plus or minus 0.50 GPa, while in the single fiber composite, 3 test specimens exhibited a range in data of plus or minus 0.41 GPa. With regard to the thermal data (α_{11}) shown in Table 7 (fiber optic senors were not employed for the thermal loading sequences analyzed), the strain versus temperature plots (see Figure 54) are linear curves below 87 degree C and nonlinear above this temperature. It appears that the matrix thermal

expansion coefficient and longitudinal modulus become functionally dependent on temperature as the glass transition temperature is approached (see Section 4.1). The experimental results presented in Table 7 are representative of the linear portion of the curves analyzed. The α_{11} data presented for these composites are an average of two tests with a variance of plus or minus 2 percent.

The comparison between the results obtained with internal measurements utilizing the FP-FOSS and the resistance strain gauges to validate the experimental techniques was shown to be excellent. The comparison of elastic modulus and thermal expansion coefficient calculated with internal resistant strain gauges and with an upper bound theoretical model are consistent. Thus, the FP-FOSS and the resistance strain gauges are reliable means of making accurate quantitative measurements of internal strains.

The reader should be aware that in the initial tests performed on the model composite with the FP-FOSS, discrepancies in the strain measurements were found. These were solely due to inaccurate measurement of the sensor gauge lengths during their manufacture. The problem was identified in the first set of experiments, and therefore all test data presented in this dissertation are with precise knowledge of the sensors gauge length, which provides accurate strain measurements.

4.42 Short fiber systems

The short fiber composite results presented in this section assist in demonstrating the ability of this technique to model various physical situations which occur in composites. A transient ($z = 4.8$ mm) and a far-field resistance strain gauge are employed to study the stress redistribution in a short single fiber system subjected to uni-axial tension and compression. A plot of applied composite stress versus the local strain at each gauge location is displayed in

Figure 55. The curves generated from the strain data obtained from the gauges are linear for either loading condition. The stress/strain slope at the far-field gauge is 3.6 GPa in tension and 3.5 GPa in compression. The slope at the transient gauge is 6.9 GPa and 6.4 GPa in tension and compression, respectively. By taking a ratio of the transient slope to the far-field slope, an effective decrease in strain at the fiber end is computed to be 0.53 (i.e.$\frac{T}{FF}$). By analyzing photographs of the stress redistribution, as depicted by the photoelastic data, an approximate ineffective length of 15 mm is measured.

A comparison between the experimental results described above to various micro-mechanical models present in the literature is presented as follows. Calculations accomplished with the Whitney and Drizal [23] model of a single fiber in an infinite matrix suggest an ineffective length of 51 mm. Performing a similar calculation with Rosen's [22] classical shear lag solution an ineffective length of 62 mm is computed (efficiency parameter is taken to be 0.95 and the global fiber volume fraction is used 0.0187). Both theoretical results appear to significantly overestimate the experimental data presented above (15 mm). On the other hand, by back calculating an actual λ from the experimental results (i.e. $\lambda = 0.316\, mm^{-1}$) in the short fiber model presented in Chapter 2 and using this result in the stress analysis, one calculates an effective decrease in strain of 0.50. This is nearly identical (within 6 %) to the measured value (0.53) presented above. Therefore, it appears that the functional dependence (i.e. exponential) of stress and thus strain on z is being adequately addressed in this model. However, the experimental findings suggest that the derivation of the parameter λ in the theoretical models needs to be reevaluated.

The results provided in this section serve to demonstrate the current experimental methodology's potential to study individual parameters in micro-mechanical models. These results suggest that specific areas need to be readdressed in the study of short fiber composites and related micromechanical phenomenons.

4.43 Continuous fiber systems

Experimental studies on stress redistribution in a continuous fiber reinforced model composites containing a fiber fracture, serves to further validate the proposed methodology. Strain concentration is defined for a continuous fiber composite system as the strain at a particular gauge location following fiber fracture divided by the strain at the same location prior to fiber fracture. Thus, a far-field gauge, as defined in Section 4.1, exhibits no strain concentration or S.C. = 1.0. In this study, single fiber, three fiber, and six fiber composites are employed. All tests results presented in this paper involving fiber fracture are accomplished by loading the composite in uni-axial tension. Initial tests on fiber fracture were accomplished by applying a thermal load to the composite and utilizing the constituents thermal mismatch to start a fiber fracture. However, this led to additional curing of the composite and increased the residual compressive stresses on the fiber which negated the phenomena being studied (fiber fracture).

When a model composite, which contains a notched fiber, is loaded in uni-axial tension, the notched fiber fractures with an audible acoustic emission. For a single fiber system the traction on the composite at which the fiber fractures is 1.2 MPa (2 samples), while for a three fiber system, with no interphase, it occurs at 3.55 MPa (18 samples). By comparing these results, one finds the applied stress at which the fiber fractures in a three fiber system is approximately three times greater than the single fiber system (this is for the notched fibers). This should not be surprising, considering that the fibers are significantly stiffer than the matrix in this particular composite system and will, therefore, support the majority of the axial load. This suggests that fiber fracture in the three fiber composite should occur at an applied load three times greater than the single fiber composite. Also, using the assumption that generalized plane strain exists prior to fiber fracture, the load supported by the fibers at fiber fracture can be calculated with the use of Tables 6, 7, and the results presented above. Performing the calculations, one finds that the fiber fractures at an applied load between 160 and

270 Newtons. These results are consistent with individual fiber tests presented in Section 4.1. However, the latter experimental results are slightly higher and more scattered than the individual fiber tests. This may be attributed to residual compressive loads which are present in the embedded fibers following the manufacturing process (i.e. shrinkage and thermal contraction).

In recent tests on the model composite, the applied load at which the notched/scored fiber fails appears to be more random than in the initial tests performed. This may be due to alterations in the notch size which could occur during the grinding process. The reader should also be aware that by scoring the fiber, a 25 percent decrease in the tensile load at which fiber fracture occurs in the model composite is found.

4.431 Single fiber test

The following results are representative of notched single fiber test performed with the model composite. These tests are performed to assess the success of the methodologies employed to create a fiber fracture at a prescribed location in the composite at a specified load. Once satisfactory results are obtained, studies can be undertaken on composite systems containing multiple fibers. When the fiber fractures in the composite, energy is released in a manner similar to a spring which has instantaneously broken. The energy released is dissipated in the form of a shock wave, matrix cracking, and fiber slipping. In the single fiber model composites, the fiber fractured and a crack propagated a finite distance into the matrix. This distance is usually less than 1 mm for a single fiber composite. By viewing the composite with an applied load under polarized plates, a representative stress redistribution pattern in the vicinity of the fiber fracture (see Figure 56) is observed. From pictures such as this, an approximate measurement of ineffective length is determined. The ineffective length for a single fiber composite appears to be approximately 13 mm. This length measurement is comparable (as it should be) to the results presented In Section 4.42 for the single short fiber composite. As

noted in that section, the analytical models currently in the literature appear to overestimate this length. This strongly suggests that a revaluation of this quantity may be necessary in these analytical developments.

4.432 Three fiber system (small crack)

For the uncoated three fiber (one fiber notched/scored) model composite systems, two distinct fracture patterns are discovered, that is a large crack ($r_c = r_s$) and a small crack ($r_c = r_f$) (see Figure 31). The results obtained on composites containing the small crack are first presented, while the results typical of a large crack are described in a subsequent section. In the current section, two distinct fiber spacings are addressed, that is, a center to center spacing of 4.6 mm and 6.2 mm representing a local fiber volume fraction of 15 and 20, percent respectively. A small crack occurs in a model composite when a fiber fractures and the crack propagates a small distance into the matrix. This length is typically smaller than 1 mm and crack arrest occurs at or near the fractured fiber/matrix interface. A typical photograph depicting this fiber fracture pattern is presented in Figure 57.

In the 6.2 mm fiber spacing composite, the small crack occurred in 8 out 15 specimens tested. The center fiber fractures at an applied traction of approximately 3.3 MPa. From strain gauges placed on adjacent fibers in the near-field region at $z=0$, a strain concentration measurement of approximately 1.28 is determined. While for strain gauges placed on adjacent fibers in the outer field region at $z=0$, a strain concentration measurement of 1.14 is found. With the use of photographs taken of the composite with an applied load under polarized lights an ineffective length is measured to be on the order of 6-10 mm (see Figure 58). Employing Rosen's [22] shear lag model to provide a theoretical prediction for comparison purposes, a 30 mm length is calculated. In this calculation, the local fiber volume fraction is assumed to be 15 percent. As eluded to in in previous sections of this dissertation, the theoretical value determined for

the ineffective length from Rosen's [22] model is larger than the measured value determined from the test data generated from the photoelastic resin.

In model composite tests performed on a comparatively larger fiber volume fraction composites (20 percent), 5 of 15 specimens exhibited small cracks ($r_c = r_f$). The fiber fractured in these composites at an applied traction similar to that quoted above (i.e. 3.3 MPa). The measured strain concentration on an adjacent fiber in the near field region at $z=0$ for this fiber volume fraction is determined to be 1.4. This strain concentration value is larger than that measured (i.e.1.28) in the smaller fiber volume fraction composite described above. In composites with relatively larger fiber volume fraction the fiber spacing is smaller, and thus the strain concentration should be larger (that is the adjacent fiber is closer to the crack). From strain data obtained in the outer field region at $z=0$ on an adjacent fiber, a strain concentration of 1.11 is found. This value is actually lower than the previous value for a larger fiber volume fraction. The reader will remember that in Figure 40 this trend was depicted by the theory presented in Chapter 3. That is the maximum strain concentration ($r = r_f$) increases but the minimum strain concentration ($r = r_s$) may actually decrease as fiber volume fraction increases. For the 20 percent fiber volume fraction composite, the ineffective length measured from the photoelastic data (Figure 59) gave values between 4 to 8 mm. These values are less than those measured (i.e. 6-10 mm) for the smaller fiber volume fraction quoted above (also compare Figure 58 to Figure 58). As the fiber volume fraction increases the local stiffness of the composite increases, and thus decreases the length over which the stress is redistributed. Using Rosen's [22] shear lag model, an ineffective length of 26 mm is calculated for comparison purposes. This once again appears to be an overestimate of the measured value determined from the photoelastic results.

In conclusion, the results presented in this section strongly suggest that strain concentration values are dependent on fiber volume fraction. The strain concentration increases from 1.28 to 1.40 in a 15 to 20 percent fiber volume fraction model composite respectively. Furthermore, the test results clearly show that a significant stress gradient exists across the width of the

fiber, that is the strain concentration decreases from the near field region to the outer field region in adjacent fibers. As noted in Chapter 3, models currently available in the literature (not including the one derived in chapter 3) suggest no functional dependence of strain concentration on these parameters. It was also demonstrated in this section (by means of test results obtained from the photoelastic resin) that theoretical predictions for ineffective length currently in the literature may be overestimating the size of the region affected by the fiber fracture. However, due to the qualitative nature of these tests results, the latter conclusion should only be regarded as an initial observation. Nonetheless, the data obtained from the photoelastic results did substantiate the idea that composites containing larger fiber volume fractions have ineffective lengths which are smaller.

4.433 Three fiber system (large crack)

The following section describes the tests results obtained on model composite systems containing a large crack ($r_c = r_a$). As in the preceding section, two distinct fiber spacings are addressed which are representative of local fiber volume fractions of 15 and 20 percent. A larger crack occurs in a model composite when the fiber fractures and the crack propagates up to the adjacent fibers. The reader should be aware that the crack size decreases with increasing fiber volume fraction in composites which contain large matrix cracks. That is in a 15 percent v_f model composite $r_c = 6.4$ mm while in the 20 percent v_f model composite $r_c = 4.2$ mm. A typical photograph depicting this fiber fracture with subsequent crack propagation is presented in Figure 60, which is in sharp contrast to the small crack depicted in Figure 57.

For the 15 percent fiber volume fraction composite, a large crack occurred in 7 of the 15 specimens tested. Strain data obtained at the near field gauge location at $z = 0$ provided a strain concentration measurement of 1.76. This is in sharp contrast to the 1.28 value measured (presented in previous section) in a composite containing the same fiber volume fraction with a small crack. For the outer field region at $z = 2.5$ mm a strain concentration of 1.25 is

measured on the adjacent fiber. This suggest that a large strain gradient exists across the diameter of the fiber. The ineffective length measured from pictures taken of the photoelastic resin did not seem to be consistent with the test performed on the larger crack size. Values as low as 16 mm and as large as 26 mm are observed. A typical photograph depicting the photoelastic data utilized in measuring the ineffective length is presented in Figure 61. The inability to distinguish a definitive demarcation in the fringe patterns along the boundary of the ineffective length caused a high degree of skepticism in these measurements. Nonetheless, this length is considerably larger than the ineffective length experimentally determined for the same fiber volume fraction composite with a small crack (i.e.6-10 mm). Referring once again to Rosen's [22] shear lag model, the ineffective length is independent of crack size and thus predicts the same value quoted in the previous section (i.e. 30 mm) for this fiber volume fraction. This theoretical value appears to be a reasonable estimate of the ineffective length for this fiber volume fraction and crack size in view of the difficulties involved in accomplishing these measurements.

In the 20 percent fiber volume fraction composite containing a large crack, some interesting discoveries are presented. Considering the strain data obtained on an adjacent fiber in the near field region at $z=0$, the strain concentration values measured are virtually indistinguishable (i.e. within the accuracy of the measurement devices) from the measurements made on the 15 percent fiber volume fraction composite (i.e. 1.76). Once again, this is in sharp contrast to the measurement made on the same fiber volume fraction composite with a smaller crack size (i.e.1.40). The ineffective length measurements accomplished with this composite system and crack size is also comparable to that described above (14 to 24 mm compared to 4-8 mm for similar fiber volume fractions with smaller crack size). The length measured in these tests is also subject to some skepticism due to the lack of a definitive demarcation. As noted in the previous section, Rosen's [22] shear lag model predicts an ineffective length for this fiber volume fraction of 26 mm. This value appears to be a reasonable estimate of the experimentally determined length for this crack geometry.

Therefore, these results first demonstrate that significant strain gradients exists across the diameter of adjacent fibers, as suggested in the previous section. The most notable result presented in this section suggests that strain concentration and ineffective length are significantly affected by matrix crack size. For larger matrix cracks, these quantities increase. Current models in the literature do not address the functional dependence of strain concentration on these parameters. However, the model presented in Chapter 3 not only incorporates these parameters into the theoretical development, but also provides excellent correlation between the test results and theoretical predictions (see Figures 35-39). On the other hand, Rosen's [22] shear lag model appears to provide reasonable estimates of the ineffective length in polymeric composites which contain large crack sizes. For these composites (this is a very specific material system and crack size) the strain concentration values are relatively independent of fiber volume fraction as depicted by shear lag models. The fact that the model developed in this dissertation is applicable to this situation and also provides accurate results attests to its improvements, over these classical solutions.

4.434 Six fiber system

The following subsection details the results obtained on a model composite containing six fibers. The fiber spacing in this composite system is 4.2 mm fiber center-to-center, and represents a composite whose local fiber volume fraction is 20 percent. This fiber volume fraction is identical to the three fiber system with a comparable fiber spacing described in the two previous sections. The results presented in this subsection depict the model composite's ability to investigate multiple fiber fracture which occurs in composite systems. In the current study, the two centered fibers are notched, however one is notched more severely. The more severely notched fiber should theoretically fail first, followed by the less severely notched fiber. Strain gauges in this composite system are attached to fibers in the near field region closest to the more severely notched fiber at $z=0$, and in the near field region of the fiber

closest to the less severely notched fiber at z=21 mm. That is, the strain gauges bracket the notched fibers at the specified axial locations.

Upon loading the six fiber composite, the more severely notched fiber fails at an applied traction of 3.15 MPa. The fiber fracture did not propagate a crack into the matrix (see Figure 62) and could be adequately represented by a small crack ($r_c = r_f$). Following this fiber failure, data is collected from the two strain gauges to determine the strain concentration which exists in the neighboring fibers. The strain concentration determined from the results of the gauge located at z=21 mm is found to be 1; or in other words the gauge exhibits no strain concentration. The strain concentration on the near field gauge at z=0 is found to be 1.40. This value is nearly identical to the strain concentration value determined for the three fiber composite with a similar crack size and fiber spacing described in Section 4.432. These results strongly suggest that the stress field is unperturbed outside the first ring of fibers (as assumed in the derivation of the theoretical model presented in chapter 3).

After collecting these data, the composite is again loaded until the second fiber fails. This occurs at at an applied traction of 2.43 MPa. When the second fiber fails in the composite, a crack does not form in the matrix material. Thus, the two fractured fibers are adequately represented by small crack sizes (see Figure 63). The data collected from the strain gauges on the fibers reveal a strain concentration at z= 21 mm of 1.1 while at z=0 the strain concentration is 1.7. As noted in Section 3.26, this experimental value is compared to a prediction of 1.68 made with the model developed in that section.

After collecting these data, the composite is again loaded at which time two more fibers fail. These fibers fail at an applied traction of 4.54 MPa and the crack does extend into the matrix material. Only the two end fibers and the matrix material outside this region remain intact (see Figure 64). The strain concentration calculated from the strain gauges located at z= 21 mm is found to be 0.6 (net decrease due to fiber fracture) while the gauge at z=0 became inoperable due to damage.

The results presented in this subsection serve to validate the current test techniques and our ability to study various physical phenomena which occur in continuous fiber composites. This includes single fiber fracture, multiple fiber fracture, and the effect fiber volume fraction has on these quantities. It is believed that this test technique can aid in answering a number of significant micromechanical issues by providing a be better understanding of the physical phenomena present. This will assist engineers and scientists in their quest to design actual composite systems beginning from a constituent perspective.

4.44 Variably spaced fibers

This subsection addresses model composites which contain three fibers (center fiber notched) and which are variably spaced. The results of strain redistribution for two distinct fiber spacings are presented in this study the first is 7.8 mm and 4.6 mm center-to-center fiber spacing (as measured form the center fiber) representative of $\eta = 0.313$ (Equation 3.11). The local fiber volume fraction for this composite is 15 percent. The second fiber spacing is 4.6 mm and 9.2 mm center to center fiber spacing, representative of $\eta = 0.163$ and $v_f = 14$ percent.

The data were obtained on the $\eta = 0.313$ model composites; the fiber fails in the composite at an applied traction of approximately 2.12 MPa. The fiber fracture which occurs in these specimens does not propagate a crack into the matrix (i.e.$r_c = r_f$). However, by increasing the applied traction on one of the composites up to 4.36 MPa, the crack is caused to propagate into the matrix and up to the adjacent fibers. The ability to propagate a matrix crack following fiber fracture can not be achieved in the uniformly spaced fiber model composites. The strain concentration data obtained from these tests are depicted in Figure 46 by the open symbols.

With regard to the results gathered from the model composite system with $\eta = 0.163$, the central fiber fractures at an applied traction of 2.47 MPa. In these studies, only one of the

composites exhibits a small matrix crack (i.e. $r_c = r_f$) while all others contain large matrix cracks (i.e.$r_c = r_{s'}$). Upon increasing the traction (up to 5 MPa) on the composite which contains the small crack, the crack extends up to the adjacent fibers (i.e. large crack). This phenomena is analogous to the crack propagation event presented in the previous paragraphs. The test results obtained on these composite systems ($\eta = 0.16$) are presented in Figure 46. A representative photograph depicting the stress redistribution in a variably spaced composite with a fiber fracture is presented in Figure 65. It can be seen that the stress patterns are unsymmetrical about the center fiber. This suggests a significant amount of bending stress is present in this composite system.

The test methodology described in this section further validates the current test technique to study various physical parameters and their effects on stress redistribution in actual composite systems containing internal disturbances. The ability to understand the effect variable fiber spacing has on the local stress redistribution could be a major concern when addressing strength issues at the laminate level. The ability to propagate a matrix crack once a fiber fracture has been achieved attests to the fact that different stress mechanisms are present in these type of composites as compared to uniformly spaced composites.

4.45 Interface

As noted in Section 4.1, both silane coupling agent and vacuum grease were applied to the structural fibers to alter the adhesion between the fibers and the surrounding matrix. The silane coupling agent applied to the glass rods generates a composite with sporadic voids or air pockets along the interface between the fiber and matrix. These voids predominantly occur around the resistance strain gauges attached to the fibers. Nonetheless, in regions which are devoid of these air pockets the adhesion between the glass rods and the matrix is strong. However, the difference in the fiber/matrix interface strength in silane treated fibers as com-

pared to untreated fibers appears to be insignificant. This statement is based on a fiber push through test accomplished on a coated and an uncoated specimen. Therefore, the application of the silane coupling agent to the structural fibers does not appear to significantly increase the fiber/matrix bond strength between of this composite system. The fact that an uncoated fiber exhibits adequate adhesion and the silane coupling agent actually causes sporadic voids along the interface leads one to the conclusion that an uncoated fiber is an excellent choice for the study of composites in which the fibers are strongly bonded to the matrix.

The vacuum grease used in altering the fiber/matrix interface strength is applied to both the glass rods and the wooden dowels embedded in the composite. Its application to the glass fibers produce a composite in which virtually no adhesion occurs between the fiber and matrix, that is no chemical bond and only minimal mechanical interlocking exists. The fact that the glass rods can actually be removed from the composite by hand attests to this fact. With applying vacuum grease to the wooden dowels, no chemical bond is found to exist between the fiber and matrix, however, mechanical interlocking is present. This is mainly due to the porous nature of the wooden dowels and the ability of the matrix to infiltrate into these regions. In initial tests performed on model composites containing wooden fiber coated with vacuum grease, a crack was introduced into the the matrix material during the manufacturing process with the use of a circular shaped capton film placed around the center fiber. The matrix crack is a typical strain concentration found in ceramic composites (the ratio of fiber to matrix stiffness values for this composite is typical of ceramics) and is thought to control the ultimate strength of the composite. However, when the composite is loaded in an attempt to release the capton film, the crack propagates the entire width of the composite but does not fracture the fiber. At this point the fibers are bridging the gap between the cracked matrix region (the reader should be aware that the crack was not intended to propagate the entire width of the composite) and supporting a load supplied from the test machine. The exposed portion of the fibers were void of matrix material (as could be seen by eye), which substantiates the claim that no chemical bond existed between the fiber and matrix. However, since the

fibers still transferred load into the matrix, mechanical interlocking must be present. Tests, such as the ones described in this section, demonstrate the versatility of the model composite to analyze other physical phenomena (e.g. matrix cracks with fiber bridging) as well as fiber end effects. These results also corroborate that the model composite can be representative of material systems other than polymeric (such as metal matrix and ceramic systems).

4.46 Interphase

The results presented in this section describe the data obtained on model composite systems with embedded glass rods coated with PES, BMI, or epoxide. The composites tested with these interphases contained three fibers, with the center fiber notched in all tests. The major portion of the results presented in this section details the physical relationship which evolves during the manufacturing process between the fiber, interphase, and matrix region, such as the quality of adhesion.

In model composites containing embedded glass fibers coated with epoxide, a number of small air bubbles are present along the surface of the interphase (i.e. interface between the interphase and matrix). However, in several composites manufactured, the air bubbles are not present at all (for a comparison see Figure 67). The differences noted between the batches is that the amount of hardener added to one batch was different from the other. In the majority of the composites manufactured with the epoxide interphase, the air bubbles present on the interphase surface inhibited accurate strain measurements at gauge locations near fiber fractures. This is mainly due to the fiber (or really the interphase) slipping in the matrix which causes a slip stick-phenomena to be recorded. However, in these tests it is found that when the composite fails the fibers pull out of the matrix. The exposed fiber length remains coated with the epoxide, such that failure occurred between the interphase and matrix re-

gions. That is, the interface strength between the fiber and interphase is stronger than the interface between the interphase and matrix.

In composite materials containing fibers coated with BMI, there appears to be regions of relatively large voids along the interface between the interphase and matrix (see Figure 66). This may be due to the relatively low cure temperature cycle (i.e.100 degree C instead of 200 degree C) performed on the interphase material prior to manufacturing the composite. This cure cycle is used because of the thermal constraints on the gauge adhesive used to secure the strain gauges to the fibers (as stated in Section 4.3). The large voids present in this composite are in sharp contrast to the small bubbles present in the epoxide coated composite system (Figure 66) Once again due to the presence of these voids no accurate strain measurements can be accomplished regarding fiber fracture. Upon loading the composite the strain readings jump, thus signifying a fiber/interphase slip. One of the more important results obtained during this test involves the catastrophic failure of the composite. As noted for the composite described above, when the composite fails the fibers pull out of the matrix region. However in this case, the fiber is clean (as could be seen by eye). The failure occurs between the interphase and the fiber in this composite system (the adhesion between the fiber and interphase is smaller than the adhesion between the interphase and the matrix).

The only quantitative results regarding the effect of interphases on strain redistribution presented in this dissertation are with data obtained from a PES coated fiber system. The presence of voids along the interphase surface is minimal in this composite system. Also when the composite catastrophically fails, little to no fiber pullout is present. This further signifies that the interface between fiber/matrix/interphase is sufficiently strong to transfer load between the fiber and matrix. Therefore, this material system represents an adequate model to initiate studies on interphase affects and their relationship to stress redistribution in the presence of fiber fracture.

In tests performed on the PES coated three fiber model composite system, the center fiber fails at an applied traction of approximately 3.35 MPa. This value is comparable to the stress level achieved in a large portion of the uncoated three fiber systems. When the fiber fractures, the crack propagates half the distance between the fiber and matrix ($r_c = (r_a + r_f)/2$). In comparison to composites containing uncoated fibers made under the same circumstances, the crack propagated up to the adjacent fiber ($r_c = r_a$). The latter crack is a larger crack. This significant result suggests that the interphase coating is capable of effectively altering the subsequent crack propagation into the matrix during fiber fracture. The energy released when the fiber fractures is distributed between shock wave formation, matrix cracking, and fiber slip. It is believed that in an uncoated fiber system no slip occurs. However in a coated system, especially for PES coatings where only mechanical interlocking should occur (see Section 4.1), fiber slip may occur. This would tend to decrease the size of the crack formed in the matrix. In fact, a smaller crack is observed in composites coated with PES. No definitive results are presented which indicate that local fiber slip is actually occurring in this composite even though it is postulated in this dissertation. The data obtained on a near field gauge placed on an adjacent fiber at $z=0$ reveals a strain concentration of 1.46 while the strain concentration on an outer field gauge at $z=0$ reveals a strain concentration of 1.14. These strain concentration values are not believed to be significantly altered by the interphase coating. This statement is based on the assumptions that the interphase is capable of transferring load between the fiber and matrix, the interphase stiffness is not appreciably different than that of the fiber and matrix, and the interphase region is not extraordinary large. This statement is further substantiated by results obtained by adhering strain gauges to the interphase region. Comparisons performed between the data obtained from these sensors to strain measurements performed at comparable locations on the fiber revealed indistinguishable results.

The final results obtained with the PES coated fiber system involves a regular array of fiber breaks in the composite. The composite is initially loaded until the notched fiber fractures (see figure 67) at which time data is gathered on strain concentration affects. An additional

load is applied to the composite at which time more fiber fractures occur in the composite (note these fibers were not notched). One can see from viewing Figure 68 that three fiber fractures are present in the composite at this stage of life. Upon further loading of the composite an additional fiber fractured (see Figure 69), thus totaling 4 separate fiber fractures in the composite. The composite is again loaded and prior to ultimate failure another fiber fracture occurred (see Figure 70). This phenomenon of stair-casing fiber fractures is not noted in any of the uncoated experiments performed. However it is recorded in a number of the coated fiber systems studied. This results suggest that the strain concentration in coated composites may be redistributed over a larger region (i.e. larger ineffective length), such that multiple fiber fracture occurs in the composite as opposed to catastrophic failure. This significant result has a direct relationship to strength predictions.

In conclusion, it has been shown that a number of distinctly different interphases can be applied to the structural fibers embedded in the model composite to study a variety of physical phenomena present in actual composite systems. The results of this section suggest that a strong bond between the interphase and matrix is achieved with the BMI coated fiber systems, while a strong interface exists between the fiber and interphase in the epoxide coated fiber system. The author is fully aware that more work needs to be performed on these systems to minimize the presence of the voids. It was shown that with an application of PES to the fibers, the size of the crack and subsequently the magnitude of the strain concentration can be altered. It appears that the interphase does not significantly alter the strain redistribution profile in the plane of the fracture. Furthermore, with the application of an interphase to the fibers, the stress redistribution along the axial direction (i.e. ineffective length) of the adjacent fibers may be altered in such a fashion to actually decrease the strain concentration and cause the composite to exhibit stair-casing fiber fracture as opposed to catastrophic localized planar failure.

5.0 Conclusions

An approximate method has been presented for determining the point-wise stress tensor in the constituents of a hybrid 3-D short fiber composite subjected to arbitrary homogeneous loading conditions. The model includes the capability to analyze composites containing different types of fibers, different aspect ratios of fibers (as well as continuous fibers), and different fiber orientations. The composite's stiffness tensor was calculated from the volume averaged stress quantities in each constituent present in the material system. Validation of the model was achieved by comparing predicted stiffness properties to experimental data and other accepted models presently available in the literature for PMC's, MMC's, and BMC's.

In polymeric matrix composites, comparisons were made between longitudinal stiffness values determined from experimental tests and theoretical predictions for systems containing five different aspect ratios (i.e. 50, 53, 60, 100, and 136), three different stiffness ratios (i.e. $C_{f_1}/C_{m} =$ 20, 40 and 75), assorted fiber orientations, and a variety of fiber volume fractions. It was shown that excellent correlation existed between the current theory and the test data for each system modeled. These results suggested that the point-wise stress values provided by the model are an accurate depiction of the stress variation which exists in each constituent. Comparisons were also made between typical mechanical properties of a transversely isotropic composite predicted by analytical models well established in the literature and the

current theory with some discrepancies noted. However, the current model was demonstrated to provide a relatively more accurate correlation with experimental data on these particular composite systems. Furthermore, the comparison models which provided reasonable results, do not provide point-wise stress variations in the fiber/matrix region as does the current model.

In metal matrix composites, comparisons were made on longitudinal and transverse stiffness values determined by experimental tests and theoretical predictions for systems containing six different aspect ratios, six different fiber alignments, and two different fiber volume fractions. It was shown that good agreement existed between the test data and the theoretical predictions for all cases considered, including those with debris. These results validated the model's applicability to a general composite system (e.g. metal matrix) and demonstrated that the model was not limited to polymeric matrix composites. To further substantiate this point, several parametric studies (i.e.varying fiber volume fraction and fiber aspect ratio) were presented for stiffness predictions calculated with the current analysis modeling a brittle/ceramic matrix composite. A demonstration of the model's applicability to continuous fiber systems containing fiber fractures was also discussed.

The derivation of a model describing the resulting point-wise stress redistribution which occurs in the matrix and the fibrous regions caused by the fiber-fiber interaction at the ends of finite length fibers or fractured fibers was presented. This theoretical development included the significant dependence of stress redistribution on fiber volume fraction, constituent properties, and crack size, unlike shear lag analysis, which presently dominates the literature. Therefore, its use is not limited to polymeric composites but is also applicable to metal matrix and ceramic matrix systems. The fact that it provides bounds for classical polymeric models which incorporate shear lag assumptions was also demonstrated. The model was extended to include one of the first quantitative analyses of variable fiber spacing which occurs in virtually every composite manufactured. A novel fiber discount method was proposed to study

multiple fiber fractures which are of extreme importance when attempting to predict tensile strength of fiber dominated composite laminates.

A validation of the fiber-fiber interaction model was achieved with comparisons between calculated strain concentration values from the current model and test data obtained with direct experimental measurements. This was accomplished for two different fiber volume fractions and two different crack sizes (a total of four different data sets). These test data sets substantiated the model's accurate dependence of strain concentration on fiber volume fraction and crack size. Corroboration of the model's prediction of strain concentration as a function of multiple fiber fractures was also initially achieved with a comparison of data obtained experimentally. The correlation between test data and theoretical predictions of strain concentration for variable spaced fiber composites was good. These tests consisted of three eccentricity parameters and two crack sizes. A number of parametric studies were also performed with this model. The following general conclusions were drawn:

- Average strain concentration increases as the stiffness ratio C_{11}/C_{11} increases in a composite with $r_c = r_f$. However, in composites which contained a relatively larger crack ($r_c = r_s$), the average strain concentration decreases.

- In polymeric composites containing small crack sizes ($r_c = r_f$), the average and the maximum strain concentration increases as fiber volume fraction increases and the minimum strain concentration decreases. However, in composites with $r_c = r_s$ the opposite trend was noted.

- Normal stresses in the matrix and shearing stresses in the fiber (not considered in shear lag analysis) are significant terms which must be addressed when studying stress redistribution around a fiber fracture. The current analytical model demonstrates that these stress terms become even more significant in MMC's and BMC's.

- Crack size was shown to significantly alter the stress redistribution in composites.

- Multiple fiber fracture studies demonstrated that significantly large strain concentrations exist in the composite following five adjacent fiber fractures. This suggests that catastrophic failure of the composite ensues shortly thereafter.

- Variable fiber spacing was shown to significantly alter the effect fiber volume fraction has on the maximum strain concentration in the composite. Depending upon the degree of eccentricity this value may increase or decrease.

A test methodology employing a macro-model composite with embedded strain gauges was presented which may be used to validate (or invalidate) micro-mechanical models currently being developed and used by the scientific community. Results obtained with the embedded resistance gauges and the embedded fiber optic strain sensors (FP-FOSS) were validated with classical test and analytical techniques. These techniques included model composites subjected to thermal effects and mechanical loading sequences. The ability to vary specific physical parameters in the experimental model, such as fiber aspect ratio, fiber volume fraction, interphase/interface, and constituent properties (i.e. model PMC's and MMC's), in a systematic fashion enables the current technique to study various physical aspects present in actual composite systems. The capability to initiate a fiber fracture at a specified location and load level was demonstrated. It was also insinuated that other damage mechanisms such as matrix cracks could be studied with this model system (these are important to the study of CMC's). In the fiber fracture tests, it was revealed that significantly different strain concentrations exist in PMC composites which contain different fiber volume fractions and crack sizes. By varying fiber spacing between neighbors, a study was performed on composites containing eccentrically located fibers. These results demonstrated an asymmetric stress state exists in composites containing variable fiber spacing and fiber fractures. The fact that multiple fiber fracture could be achieved in a methodical fashion demonstrated the versatility

of the model. These studies show that this experimental technique can model various physical phenomena which occur in actual composite systems.

A variety of interfaces were applied to the structural fibers used in the model composite system. The silane treatment did not appear to alter the interface appreciably between the glass and the epoxy resin. The vacuum grease altered the adhesion between the glass and the epoxy significantly while its application to the wooden dowels resulted in only moderate effects (which was desired in the study of fiber pull-out). A variety of finite interphase regions were applied to the fibers in the composite. These results suggested that distinctly different failure mechanisms are present depending on the interphase. The most uniform interphase coating in a manufactured composite was achieved with the PES coated fibers. In this composite, the coating appeared to alter the subsequent crack propagation following initial fiber fracture (maybe due to slip mechanisms). This reduced the size of the crack and the subsequent strain concentration in the plane of the crack on the adjacent fibers. However, it is not believed that the presence of the interphase region following crack propagation significantly alters the strain concentration in the plane of the crack. Nonetheless, it appeared that distinctly different stress redistribution occurred along the axial direction of the coated fiber (as compared to uncoated fiber), evidenced by the stair casing fiber fracture prior to composite failure.

In summary, a theoretical model has been generated which provides a more complete and precise representation of the local stress fields in a short/broken fiber composite. Furthermore, a theoretical model was presented which describes a more accurate representation of the interaction that occurs in composite systems containing short/broken fibers than is presently available in the literature. A novel methodology has also been described which can substantiate micromechanical models which are essential for the manufacture and design of material systems for specific applications. This technique may guide future developments of theoretical micromechanical models. The package presented in this dissertation thus pro-

vides a firm foundation for the prediction of composite stiffness and strength properties, as well as the analysis of damage development and long term behavior of these materials.

References

1. Hill, R. , "Theory of Mechanical Properties of Fibre Strengthened Materials: I.Elastic Behavior, " *J. Mech. Phys. Solids*, V. 21, pp. 199-212, (1964).

2. Hashin, Z. and Rosen, R.W., "The Elastic Moduli of Fiber-Reinforced Materials," *J. of Appl. Mech.*, pp. 223-232, (1964).

3. Pagano, N.J., and Tandon, G.P., "Elastic Response of Multi-directional Coated-fiber Composites," *Comp. Sci. and Tech.*, V. 31, pp. 273-293, (1988).

4. Ashton, J.E., Halpin, J.C., and Petit, P.H., *Primer on Composite Materials: Analysis,* Technomic Publ. Inc., pp. 77-83, (1969).

5. Berthelot, J.M., "Effect of Fibre Misalignment on the Elastic Properties of Oriented Discontinuous Fibre Composites," *Fibre Sci. and Tech.*, V. 17, pp. 25-39, (1982).

6. Cox, H.L., "The Elasticity and Strength of Paper and Other Fibrous Materials," *British J. of Appl. Physics*, V. 3, pp. 72-79, (1952).

7. Choon, T.C., and Sun, C.T., "Stress Distributions Along a Short Fibre in Fibre Reinforced Plastics," *J. of Mat. Sci.*, V. 15, pp. 931-938, (1980).

8. Fukuda, H. and Chou, T., " An Advanced Shear-Lag Model Applicable to Discontinuous Fiber Composites," *J. Comp. Mat.,* V. 15, pp. 79-91, (1981).

9. Fukuda, H. and Chou, T., "Stiffness and Strength of Short Fibre Composites as Affected by Cracks and Plasticity," *Fibre Sci. and Tech.*, V. 15, pp. 243-256, (1981).

10. Eshelby, J.D., "The Determination of the Elastic Field of an Ellipsiodal Inclusion, and Related Problems," *Proceedings Royal Society*, V. a241, pp. 376-396, (1957).

11. Russel, W., "On the Effective Moduli of Composite Materials: Effect of Fiber Length and Geometry at Dilute Concentrations," *J. of Applied Math. and Physics*, V. 24, pp. 582-600.

12. Chou, T., Seiichi, N., and Minoru, T., "A Self-Consistent Approach to the Elastic Stiffness of Short-Fiber Composites," *J. of Comp. Mat.,* V. 14, pp. 178-187, (1980).

13. Laws, N., and McLaughlin, R., "The Effect of Fibre Length on the Overall Moduli of Composite Materials," *J. Mech. Phys. Solids*, V. 27, pp. 1-13, (1979).

14. Takao, Y., Chou, T.W., and Taya, M., "Effective Longitudinal Young's Modulus of Misoriented Short Fiber Composites," *Trans. of the ASME*, V. 49, pp. 536-540, (1982).

15. Taya, M. and Chou, T.W., "On Two Kinds of Ellipsoidal Inhomogeneities in an Infinite Elastic Body: An Application to a Hybrid Composite," *Int. J. of Solids and Struct.*, V. 17, pp. 553-563, (1981).

16. Taya, M., and Mura, T., "On Stiffness and Strength of an Aligned Short-Fiber Reinforced Composite Containing Fiber-End Cracks Under Uniaxial Applied Stress," *ASME J. of Appl. Mech.*, V. 48, pp. 361-377, (1981).

17. Mikata, Y. and Taya, M., "Stress Field in and Around a Coated Short Fiber in an Infinite Matrix Subjected to Uniaxial and Biaxial Loadings," *J. of Appl. Mech.*, V. 52, pp. 19-24, (1985).

18. Chang, C.I., Conway, H.D., and Weaver, T.C., "The Elastic Constants and Bond Stresses for a Three-Dimensional Composite Reinforced by Discontinuous Fibers," *Fibre Sci. and Tech.*, V. 5, pp. 143-162, (1972).

19. Owen, D.R.J., "Analysis of Fibre-Reinforced Materials by an Initial Strain Method," *Fibre Sci. and Tech.*, V. 5, pp. 37-60, (1972).

20. Aboudi, J., "Elastoplasticity Theory for Composite Materials," *Solid Mechanics Archives*, V. 11, pp. 141-183, (1986).

21. Carman, G.P., "Modeling the Elastic Behavior of Current and Proposed Metal Matrix Composites," Master Thesis, University of Alabama Tuscalosa, (1988).

22. Rosen, B. W., "Fiber Composite Materials," *Am. Soc. of Metals* , chap. 3, pp. 37-75, (1964).

23. Whitney, J. M., and Drzal, L. T., "Axisymmetric Stress Distribution Around an Isolated Fiber Fragment," *ASTM STP 937* , pp. 179-196, (1987).

24. Hedgepeth, J.M., and Van Dyke, P., "Local Stress Concentration in Imperfect Filamentary Composite Materials," *J. of Comp. Mat.* , V. 1, pp. 294-309, (1968).

25. Fariborz, S.J., and Harlow, D.G., "The Tensile Behavior of Intraply Hybrid Composites II: Micromechanical Model," *J. of Comp. Mat.* , V. 21, pp. 856-875, (1987).

26. Zweben, C., "Tensile Strength of Hybrid Composites," *J. Appl. Mech.*, V. 6, pp. 1-20, (1977).

27. Goree, J.G. and Gross, R.S., "Stresses in a Three Dimensional Unidirectional Composite Containing Broken Fibers," *Eng. Fract. Mech.*, V. 13, pp. 395-405, (1980).

28. Erigen, A.C. and Kim, B.S., "Stress Concentrations in Filamentary Composites with Broken Fibers," Tech. Rep. no. 36, ONR, Contract N-0001406701-0151-0004, (1973).

29. Adams, D.F., "Micromechanical Predictions of Crack Propagation and Fracture Energy in a Single-Fiber Boron/Aluminum Composite," *NASA-Lewis*, Technical report, UWME-DR-201-101-1, Nsg-3217, (1982).

30. Batdorf, S.B., "Tensile Strength of Unidirectionally Reinforced Composites - I" *J. Reinforced Plastics & Comp.* , V. 1, pp. 153-177, (1981).

31. Fukuda, H., "Statistical Strength of Unidirectional Composites with Random Fiber Spacing," *Composites 86: Recent Advances in Japan & U.S.* , Kawata K. ed., Proceedings Japan U.S. CCM-III, Tokyo, pp. 307-314, (1986).

32. Harlow, G., and Phoenix, S.L., "Probability Distributions for the Strength of Composite Materials I:Two-Level Bounds," *Int. J. of Fracture* , V. 17, No. 4, pp. 347-372, (1981).

33. Adams, D.F., "Micromechanical Predictions/Experimental Correlations of the Influence of the Interface and Physical Properties of a Unidirectional Composite," *International Conference on Composite Interfaces*, Cleaveland Ohio, (1986).

34. Verpoest, I., Desaeger, M., and Keunings, R., "Critical Review of Direct Micromechanical Test Methods for Interfacial Strength Measurements in Composites," *Controlled Interphases in Comp.* , pp. 653-665, (1990).

35. Piggott, M.R., and Dai, S.R., "Debonding and Friction at Fibre-Polymer Interfaces. II: Macroscopic Model Experiments," *Comp. Sci. and Tech.*, V. 31, pp. 15-24, (1988).

36. Ashbee, K.H.G. and Ashbee, E., "Photoelastic Study of Epoxy Resin/Graphite Fiber Load Transfer," *J. of Comp. Mat.*, V. 22, pp. 602-615, (1988).

37. James, M.R., Morris, W.L., and Cox, B. N., "A High Automated Strain-Field Mapper," *Exp. Mech.*, pp. 60-67, (1990).

38. Waite, S.R., Tatam, R.P., and Jackson A., "Use of Optical Fibre for Damage and Strain Detection in Composite Materials," *Composites* , V. 19, no. 6, pp. 435-442, (1988).

39. Christensen, R.M., *Mechanics of Composite Materials*, Wiley Interscience Publication, (1979).

40. Carman, G. P., and Berry, J. T., "Modeling the Mechanical Behavior of Current and Proposed Metal Matrix Composites," *Winter Annual Meeting of ASME* , Advances in Mecahnical Behavior and Properties Evaluations, V. 7 , pp. 59-69, (1988).

41. Kacir, L., Ishai, O., and Narkis, M., "Oriented Short Glass-Fiber Composites. IV. Dependence of Mechanical Properties on the Distribution of Fiber Orientations," *Poly. Eng. Sci.*, vol.18, no. 1, pp. 45-52, (1978).

42. Johnson, W.S. and Birt, M.J., "Evaluation of Several Micromechanics Models for Discontinuously Reinforced Metal Matrix Composites," *NASA Technical Mem. 102719*, pp. 1-30, (1990).

43. Dunyak, T. "Properties and Performance of Ceramic Composite Components," Dissertation, E.S.M., Va. Tech, March (1991).

44. Madhukar, M.S. and Drzal, L.T., "Effect of Fiber-Matrix Adhesion on Longitudinal Compressive Properties of Graphite/Epoxy Composites," *Proceedings of the 5th Technical Conference of Am Soc. of Comp.* , pp. 849-858, (1990).

45. Lesko, J.J., Carman, G.P., Fogg, B.R., Miller, W.V., Vengsarkar, A.M., Reifsnider, K.L., and Claus, R.O., "Embedded Fabry-Perot Fiber Optic Strain Sensors in the Macro-Model Composite," *Optical Engineering SPIE* , Accepted for publication, (1991).

46. Jamison, R.D., "Advanced Fatigue Damage Development in Graphite Epoxy Laminates," Dissertation, E.S.M., Va. Tech, pp. 146-180, (1982).

47. Fredrick, D. and Chang, T. S., *Continuum Mechanics*, Scientific Publishers Inc., pp. 34-37, (1972).

48. Walker, P., "The Use of Silane Adhesion Promoters in Polymer Industries," *Materials and Processing*, pp. 227-235, (1989).

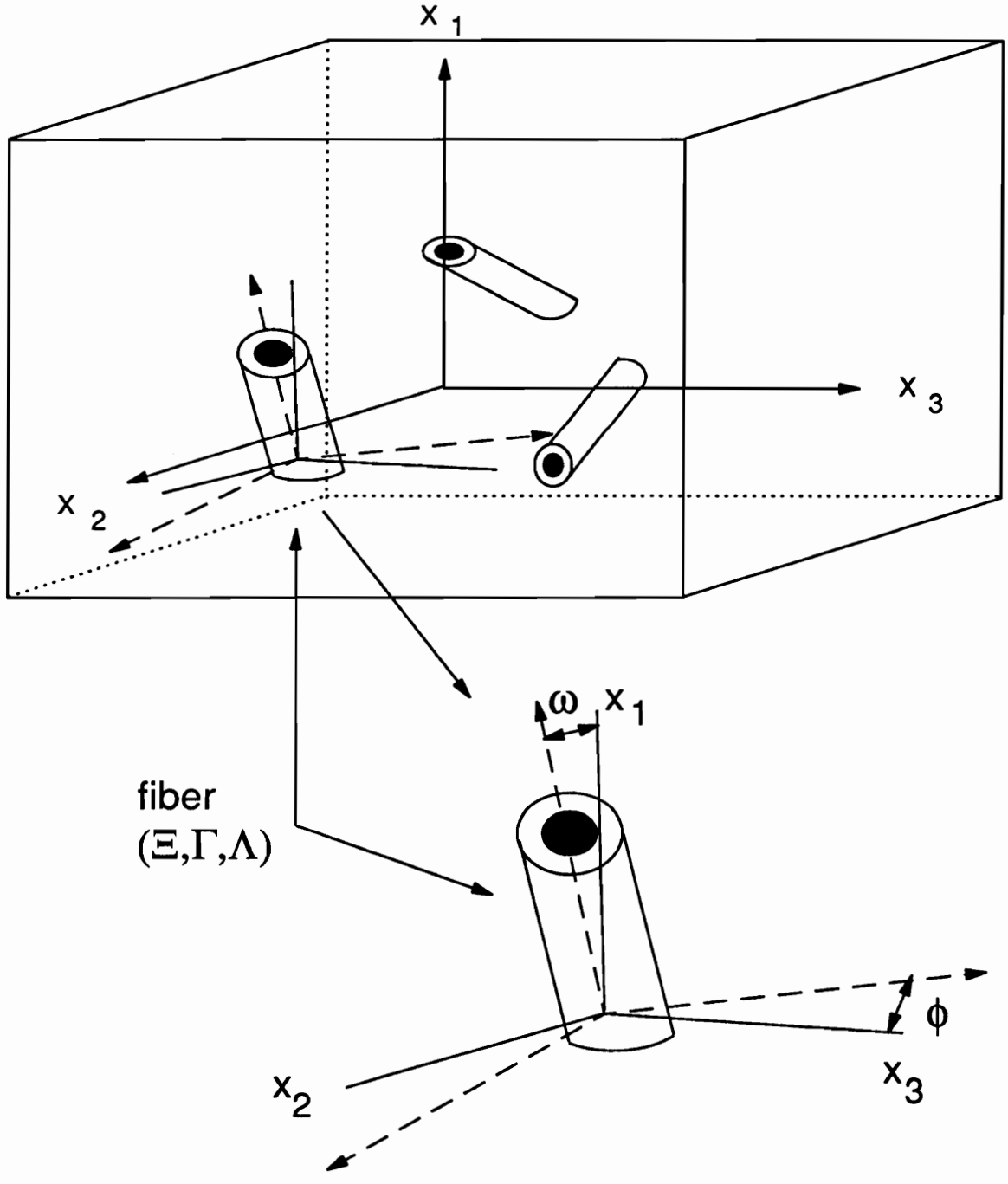

Figure 1. 3-D Hybrid Composite: Illustration of a typical 3-D hybrid short fiber composite depicting the global cartesian coordinate system, global spherical coordinate system, and the fiber labeling nomenclature.

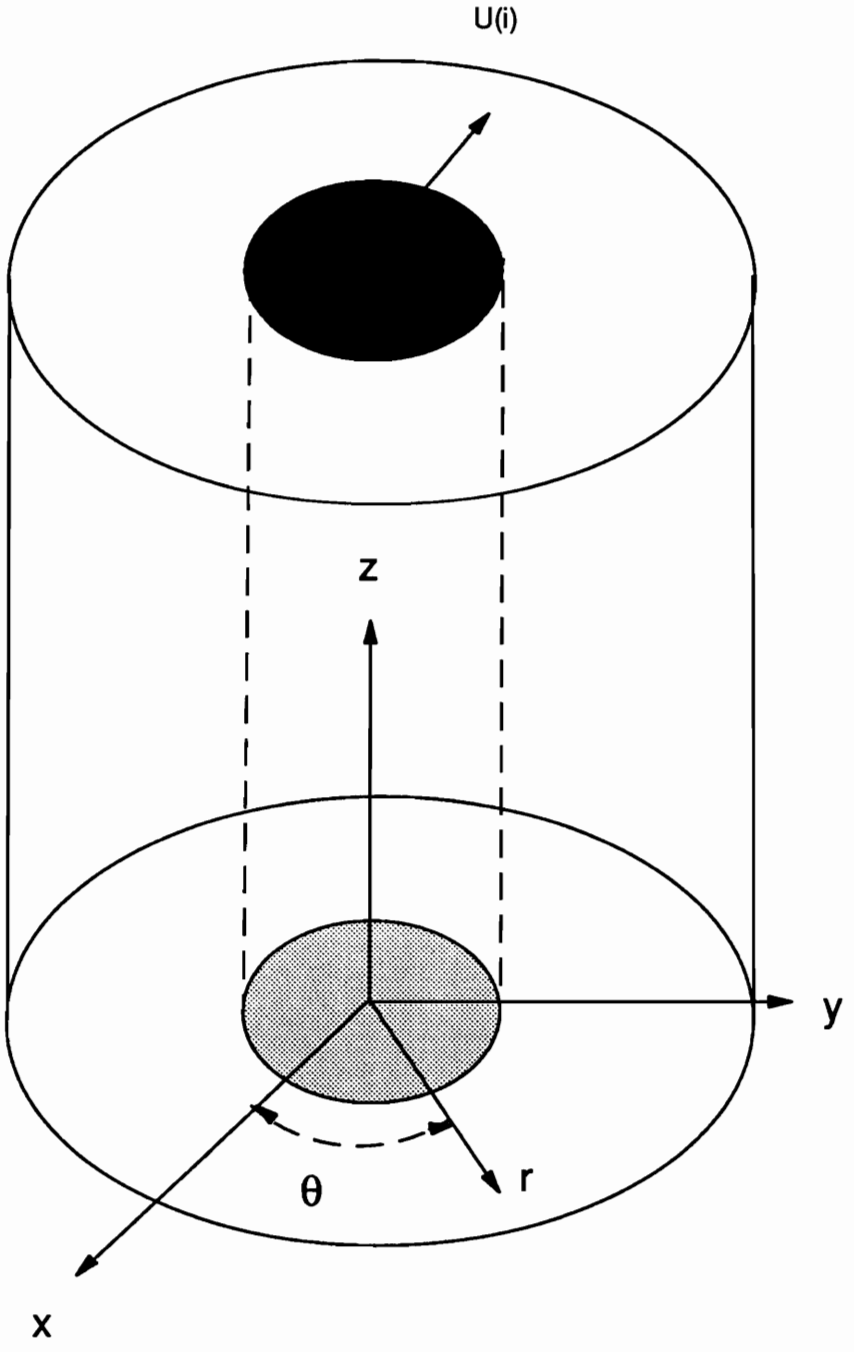

Figure 2. Concentric Cylinder Model: Illustration of a composite cylinder model depicting the local cartesian coordinate system, the local cylindrical coordinate system, and the applied displacement.

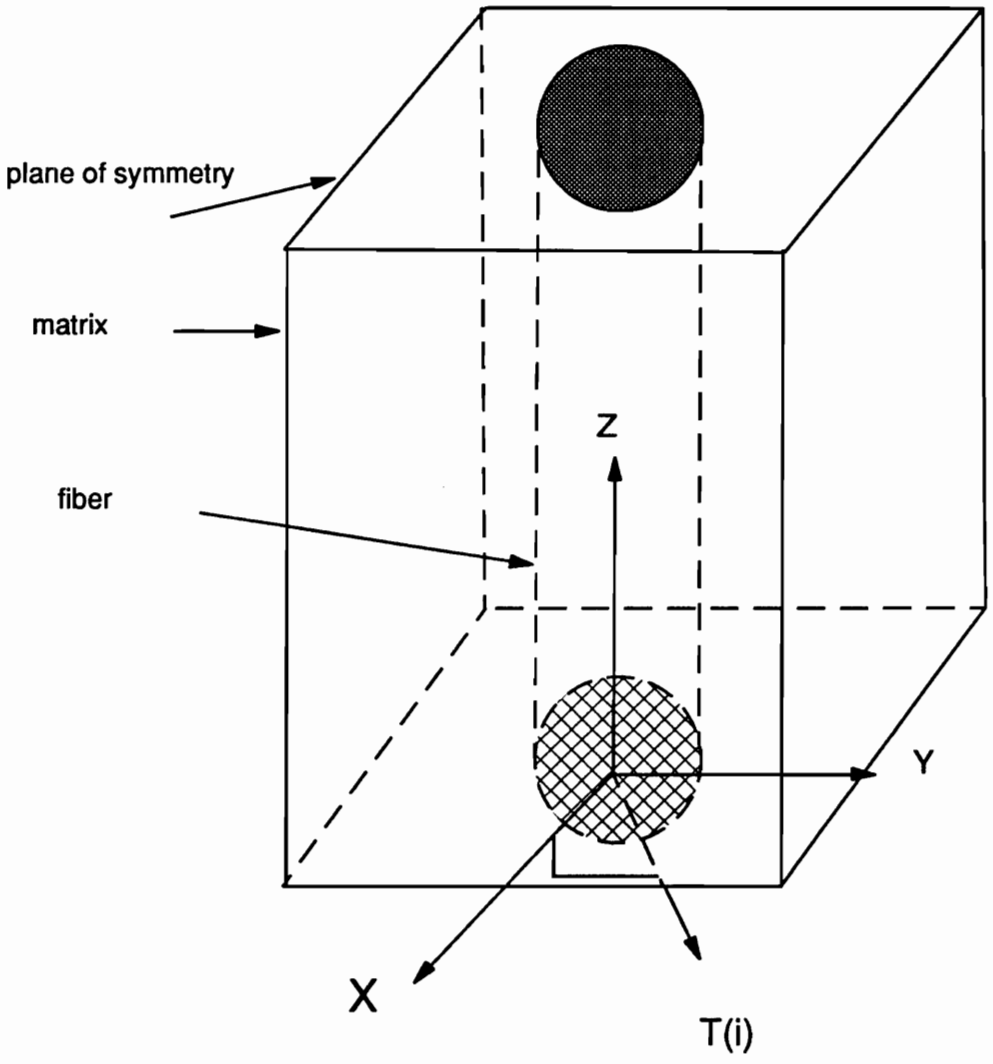

Figure 3. Fiber End Problem: Illustration of the fiber end problem depicting the applied traction at the fiber/matrix interface.

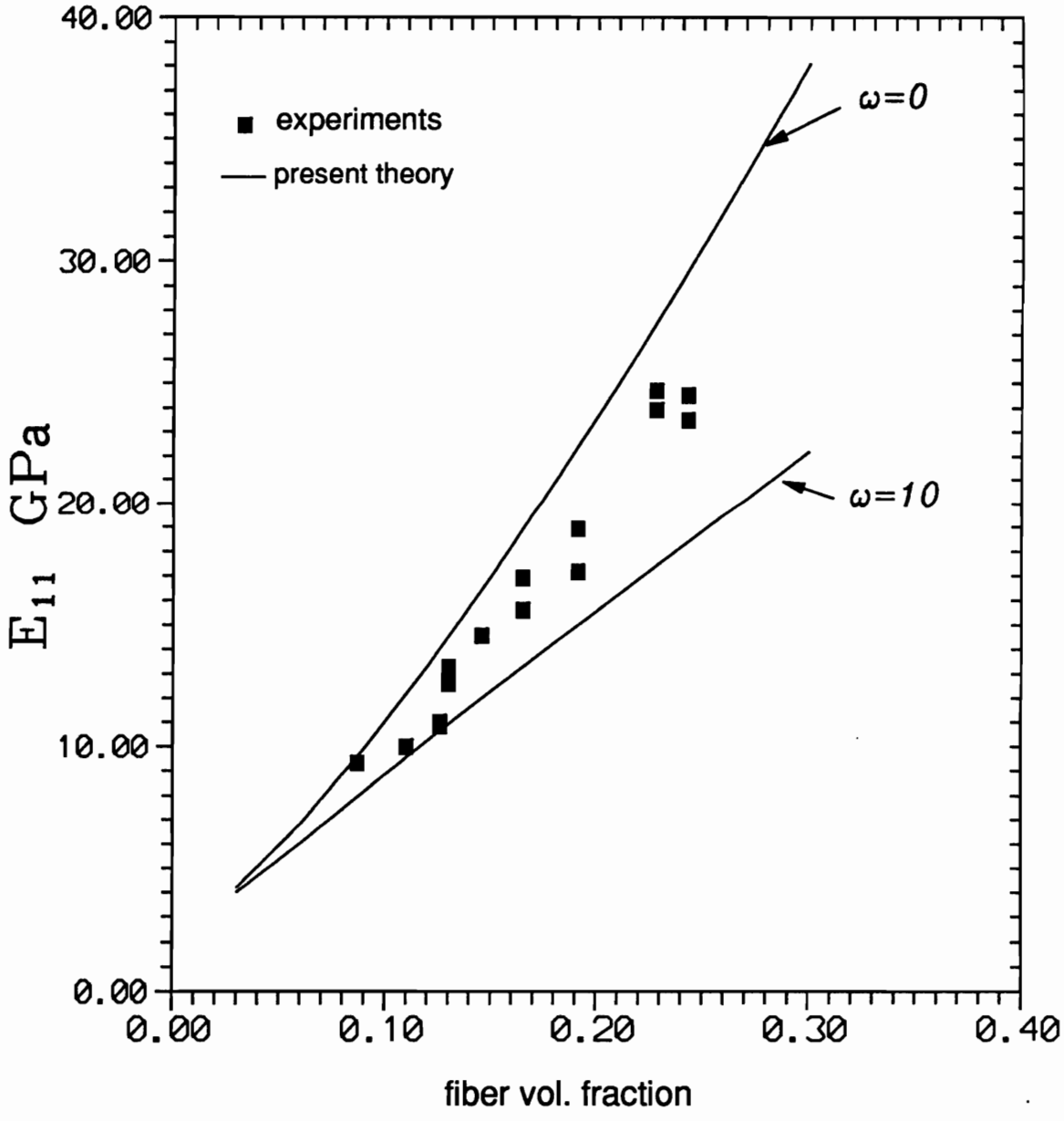

Figure 4. Axial Modulus vs Fiber Volume Fraction (steel/epoxy l/d=50): Comparison of Berthelot's [5] experimental data and the current theory for an steel/epoxy material with aspect ratio of 50 as a function of fiber volume fraction.

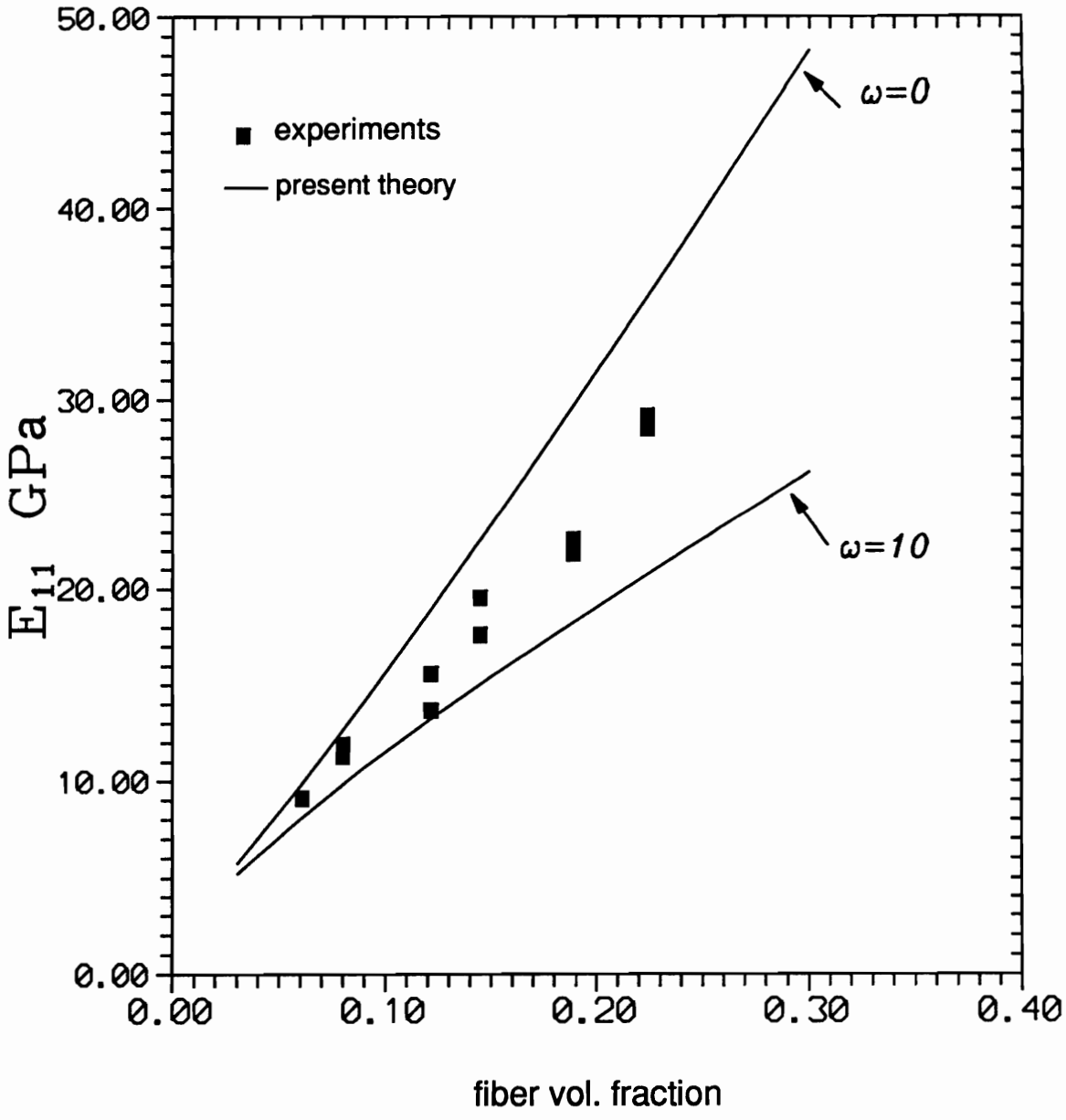

Figure 5. Axial Modulus vs Fiber Volume Fraction (steel/epoxy l/d=100): Comparison of Berthelot's [5] experimental data and the current theory for an steel/epoxy material with aspect ratio of 100 as a function of fiber volume fraction.

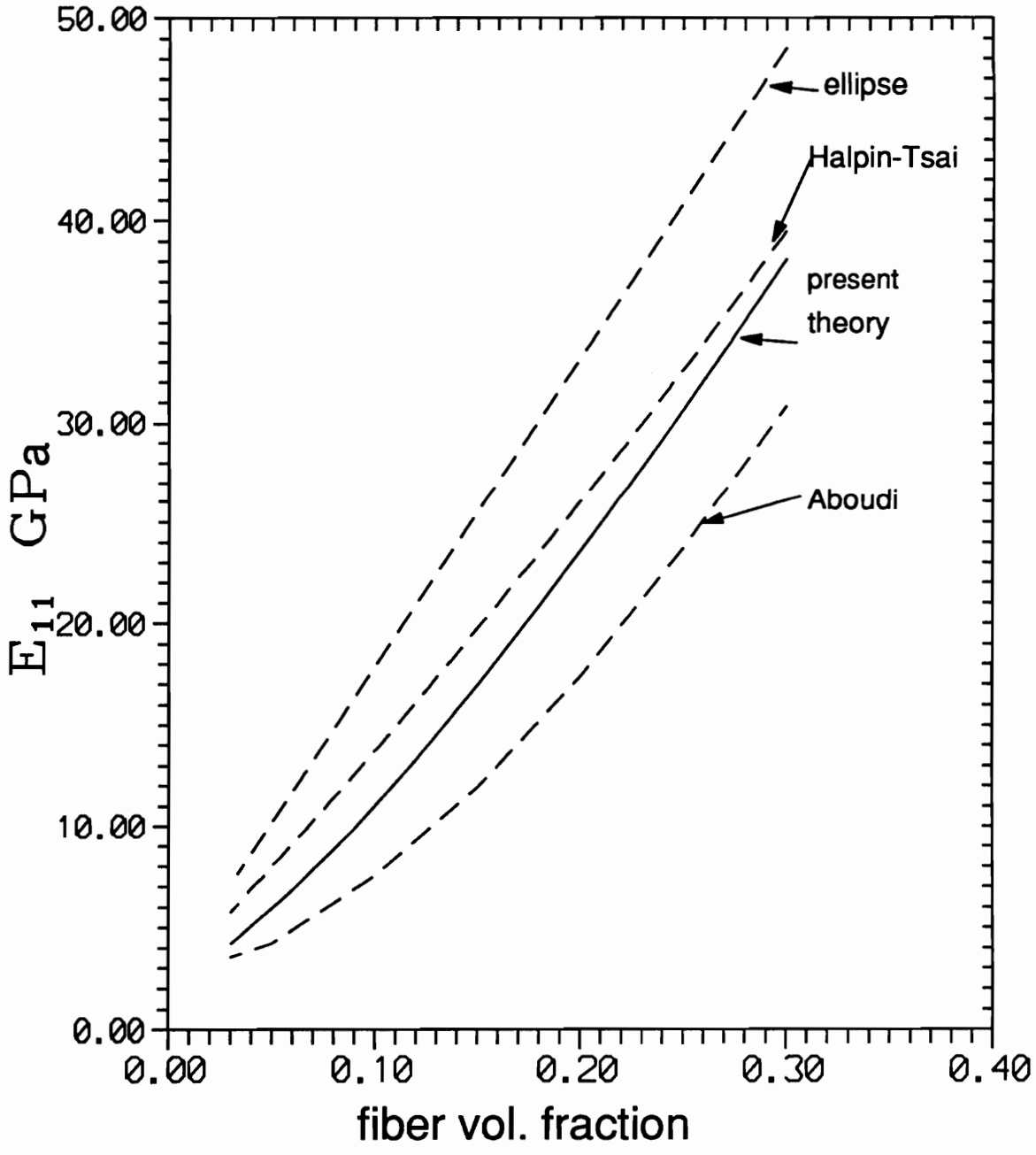

Figure 6. Axial Modulus vs Fiber Volume Fraction (theory l/d=50): Comparison of predicted E_{11} values for various theories in an steel/epoxy material with aspect ratio of 50 as a function of fiber volume fraction.

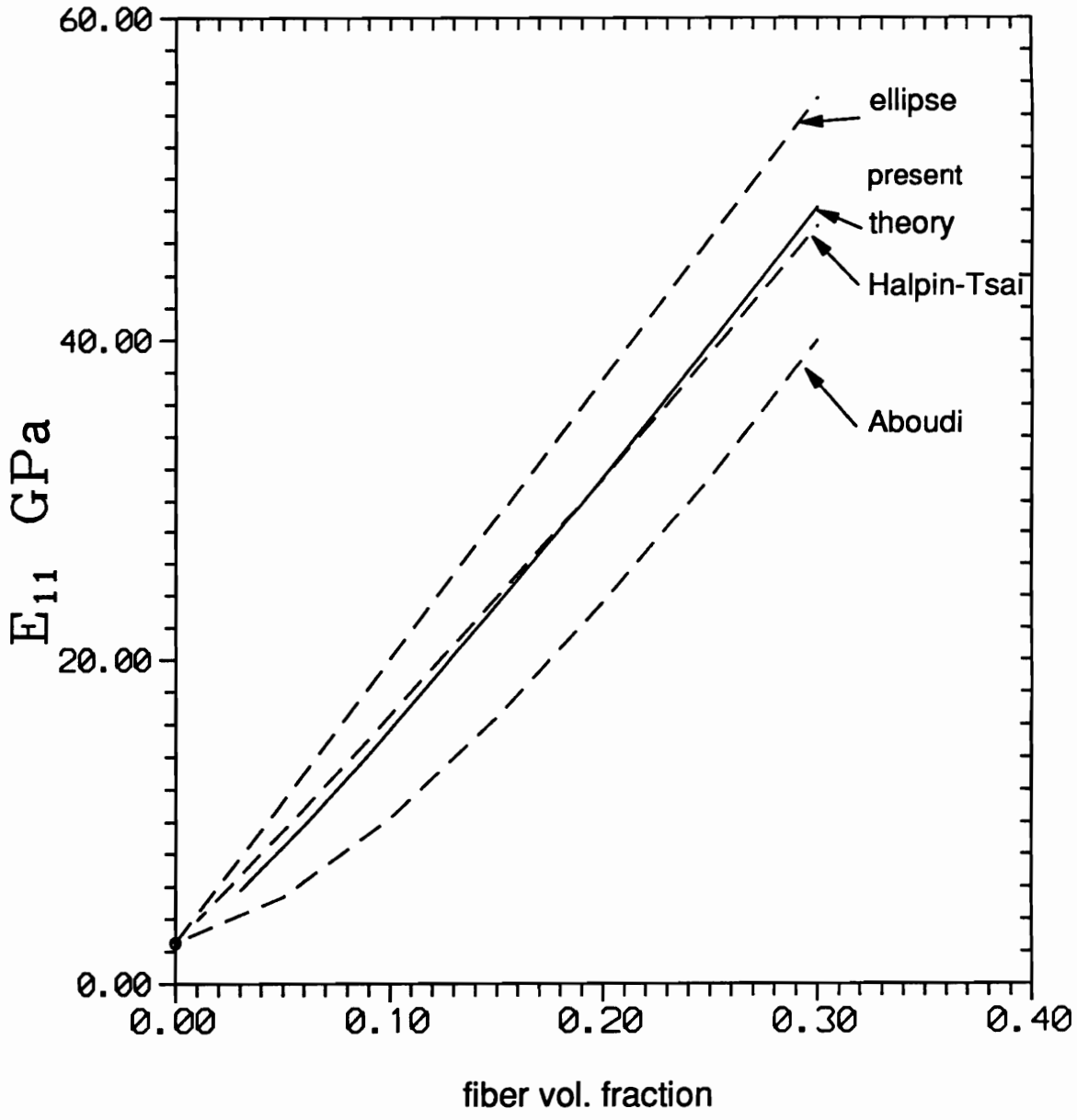

Figure 7. Axial Modulus vs Fiber Volume Fraction (theory l/d = 100): Comparison of predicted E_{11} values for various theories in an steel/epoxy material with aspect ratio of 100 as a function of fiber volume fraction.

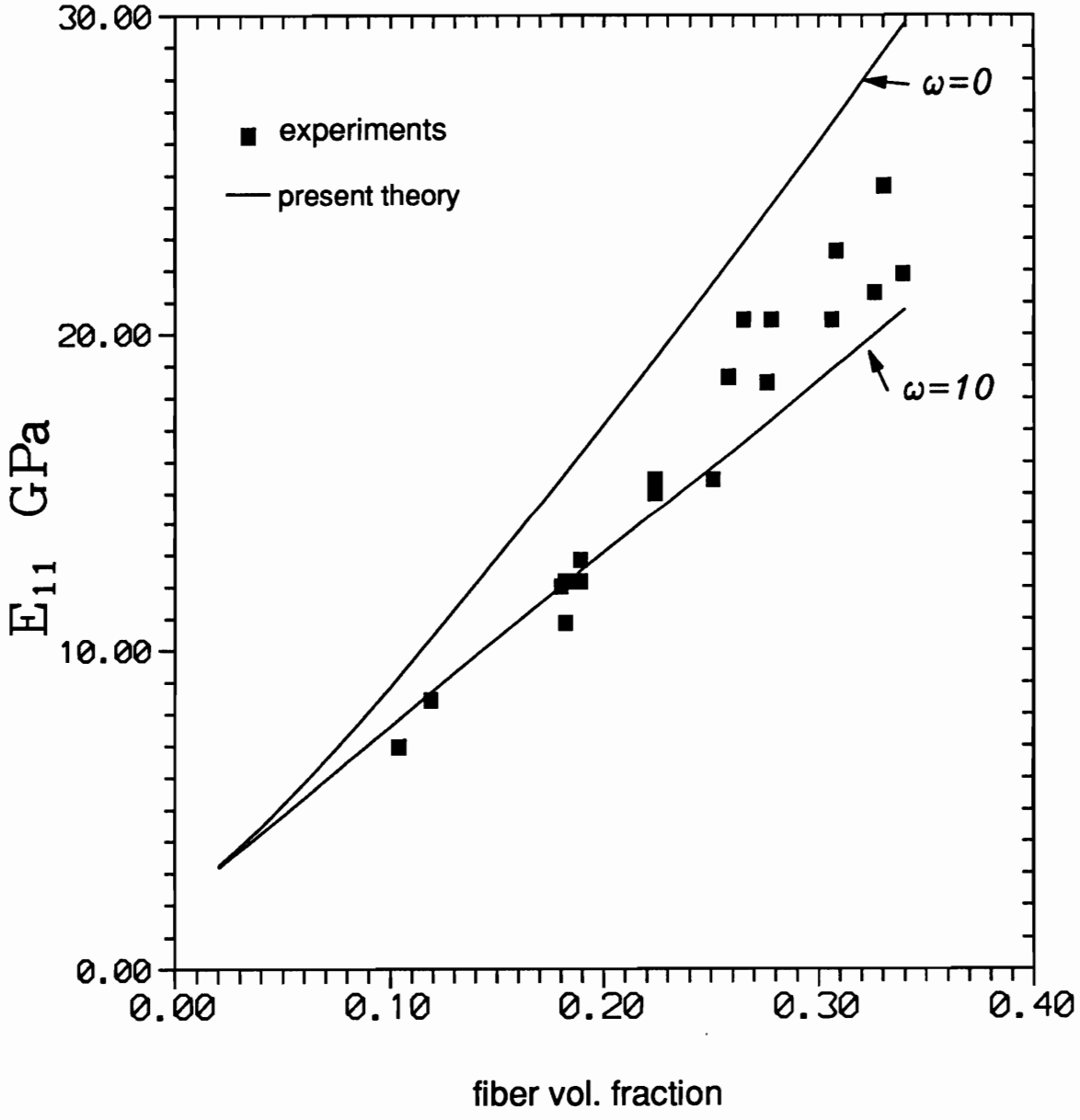

Figure 8. Axial Modulus vs Fiber Volume Fraction (copper/epoxy l/d=60): Comparison of Berthelot's [5] experimental data and the current theory for an copper/epoxy material with aspect ratio of 60 as a function of fiber volume fraction.

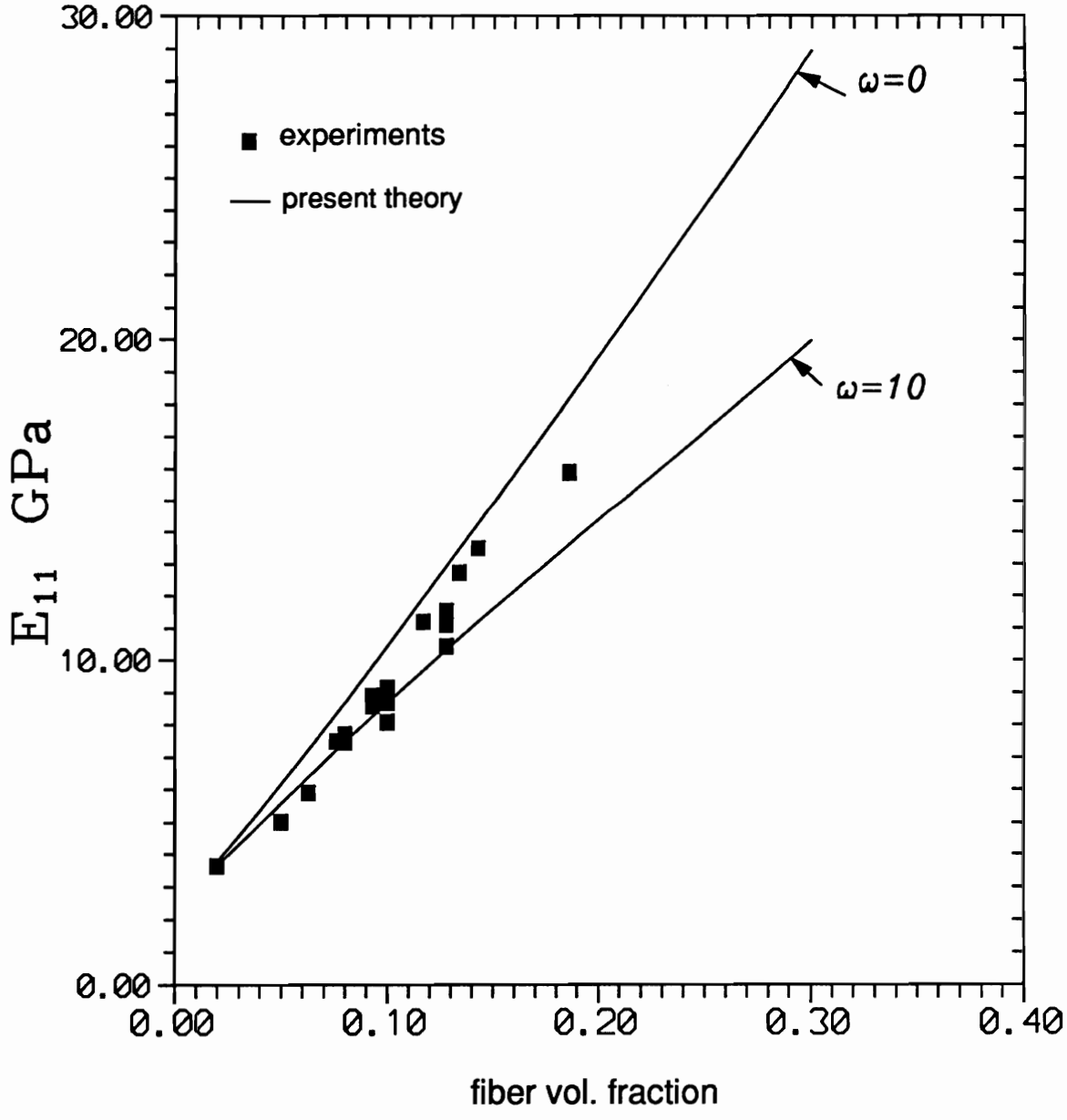

Figure 9. Axial Modulus vs Fiber Volume Fraction (copper/epoxy l/d=100): Comparison of Berthelot's [5] experimental data and the current theory for an copper/epoxy material with aspect ratio of 100 as a function of fiber volume fraction.

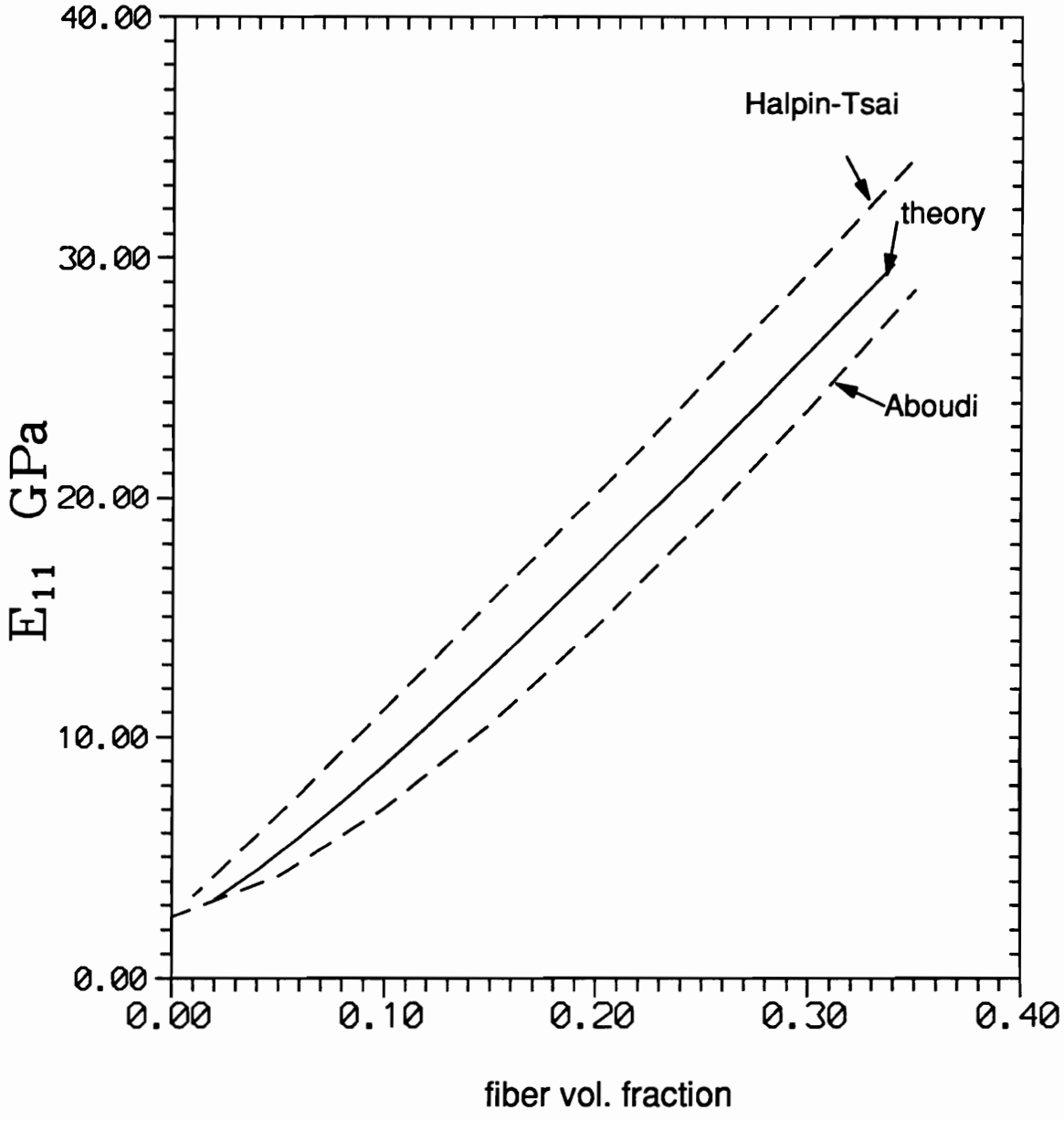

Figure 10. Axial Modulus vs Fiber Volume Fraction (theory l/d=60): Comparison of predicted E_{11} values for various theories in an copper/epoxy material with aspect ratio of 60 as a function of fiber volume fraction.

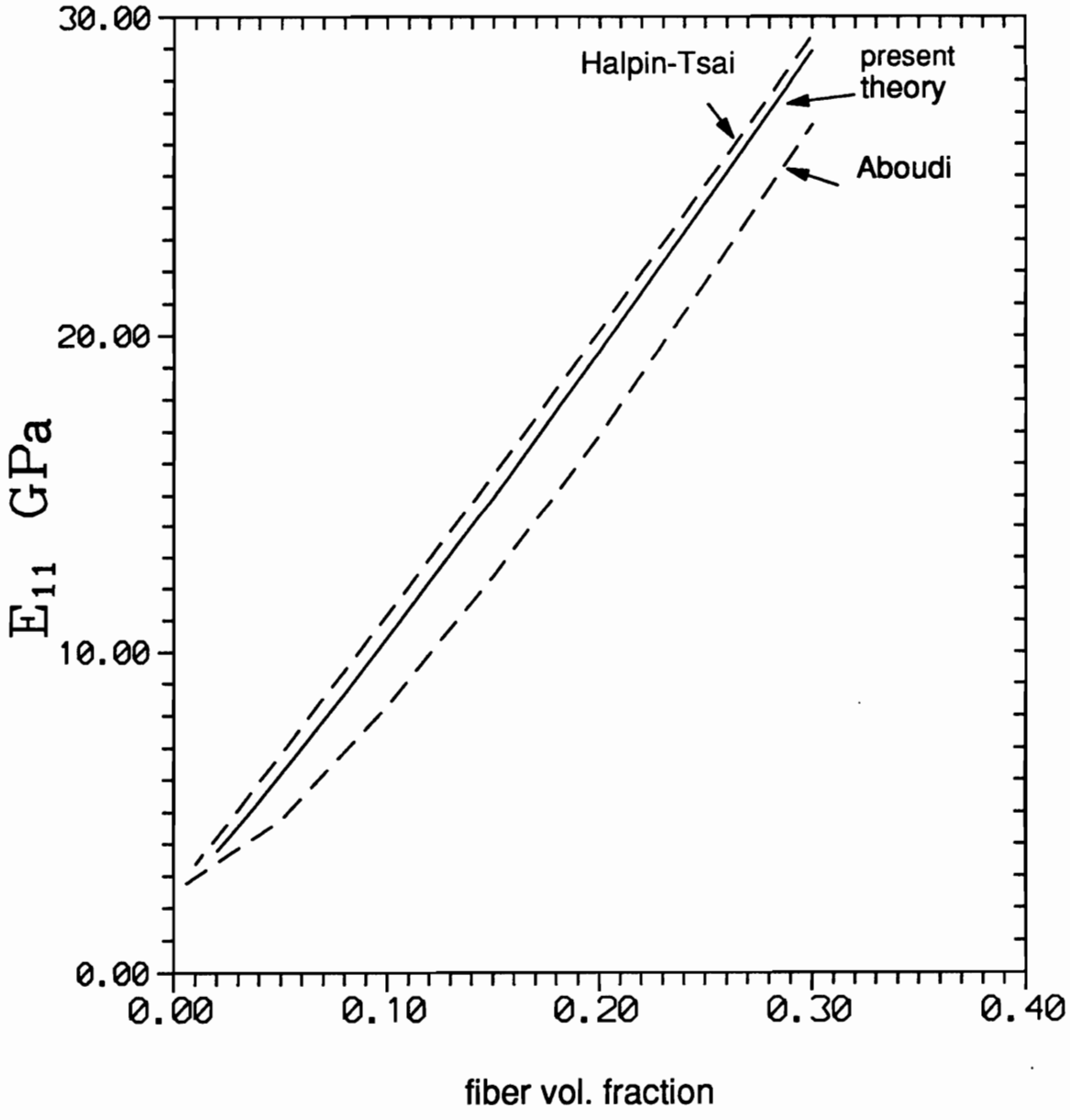

Figure 11. Axial Modulus vs Fiber Volume Fraction (theory l/d=100): Comparison of predicted E_{11} values for various theories in an copper/epoxy material with aspect ratio of 100 as a function of fiber volume fraction.

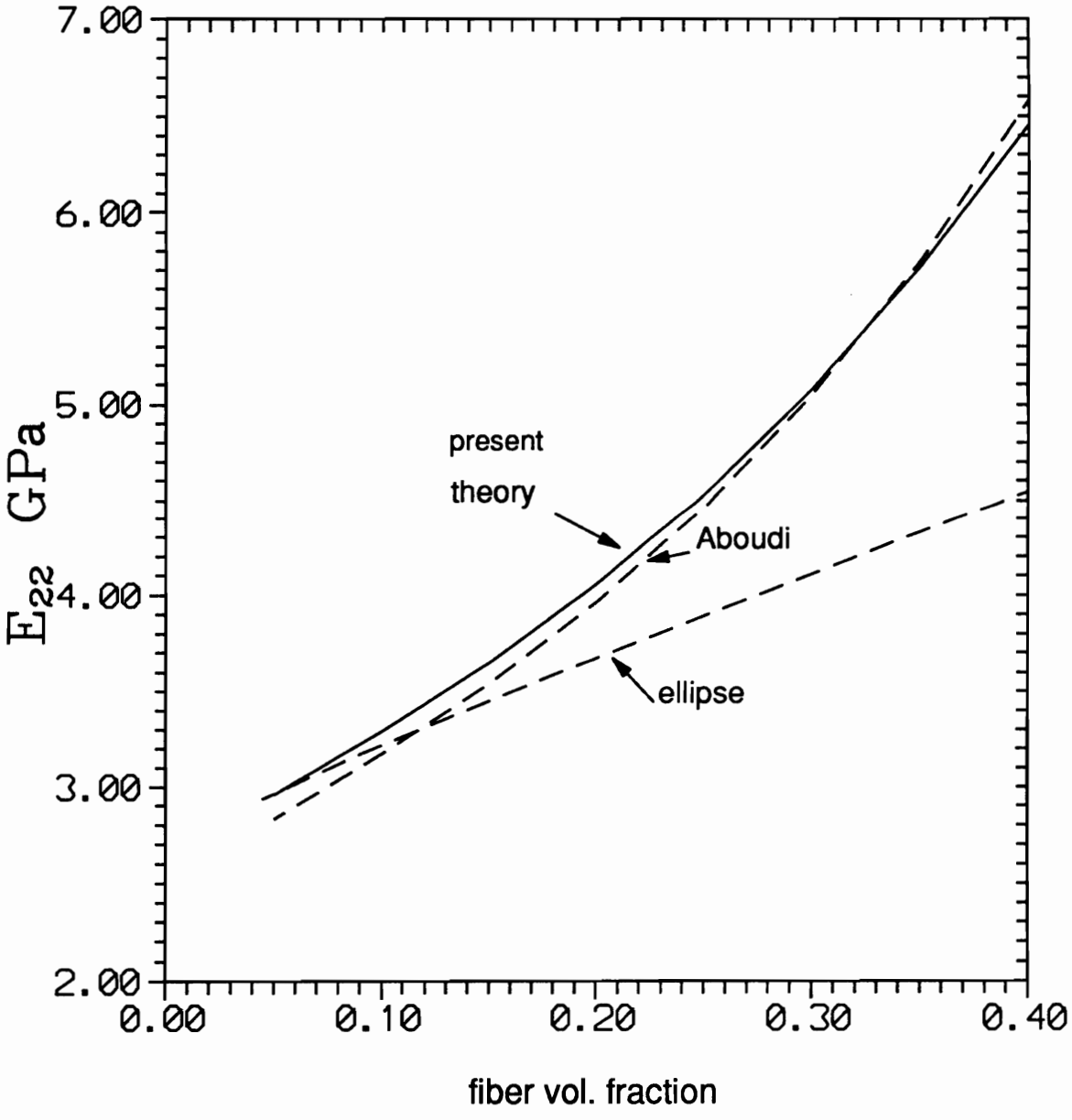

Figure 12. Transverse Modulus vs Fiber Volume Fraction: Comparison of predicted E_{22} values for various theories in an steel/epoxy material as a function of fiber volume fraction.

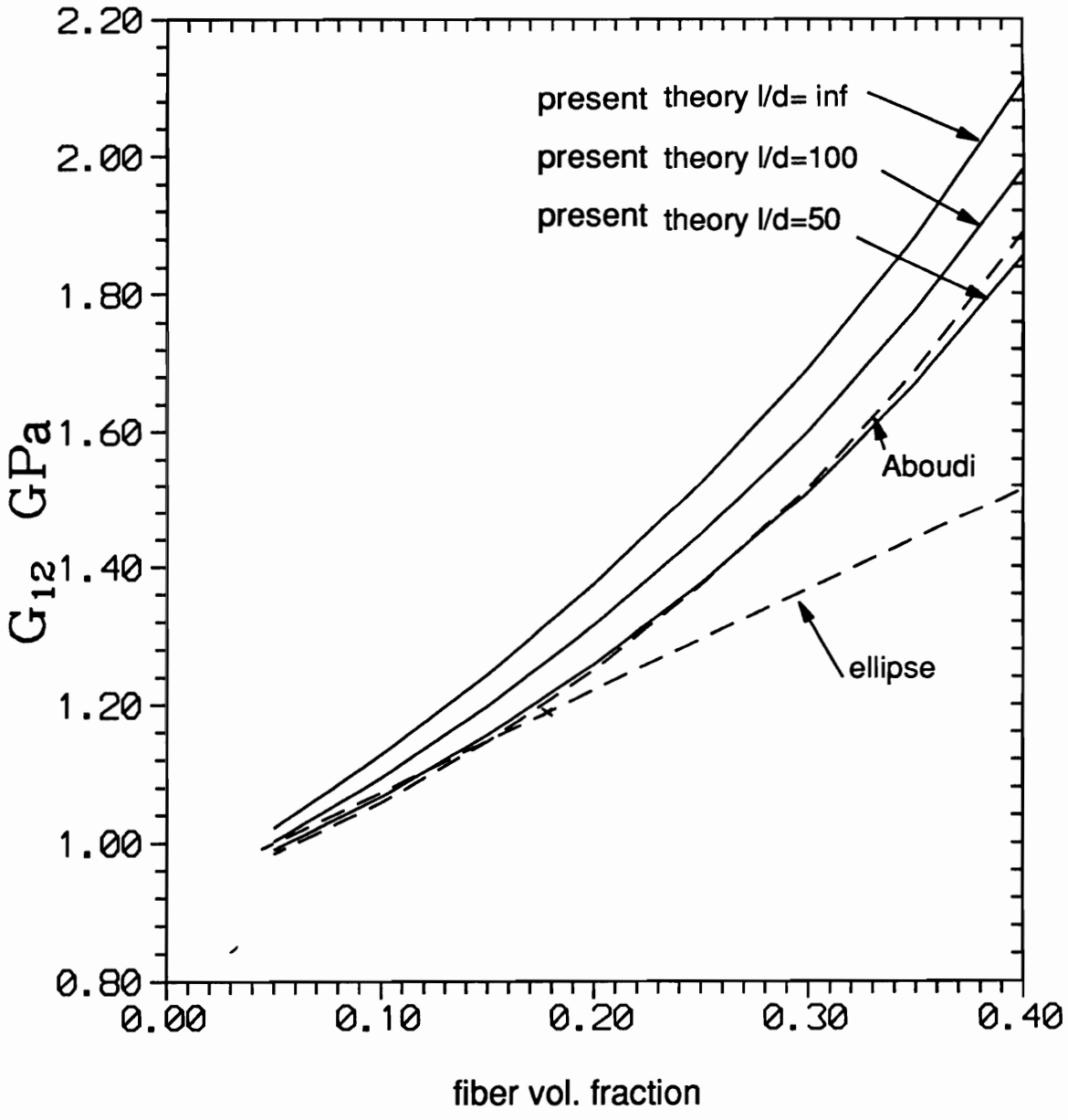

Figure 13. Shear Modulus vs Fiber Volume Fraction: Comparison of predicted G_{12} values for various theories in an steel/epoxy material as a function of fiber volume fraction.

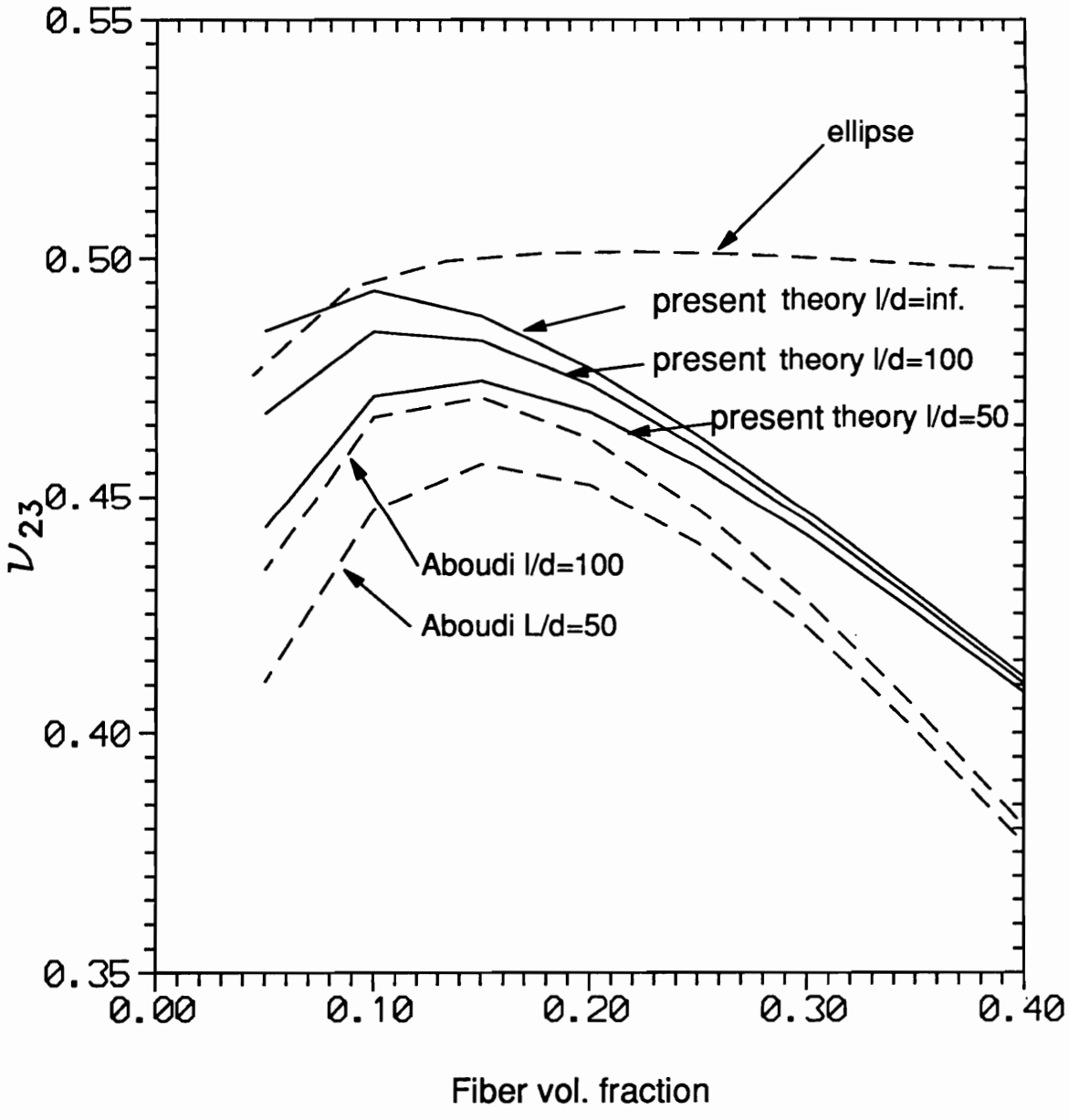

Figure 14. Transverse Poisson Ratio vs Fiber Volume Fraction: Comparison of predicted ν_{23} values for various theories in an steel/epoxy material as a function of fiber volume fraction.

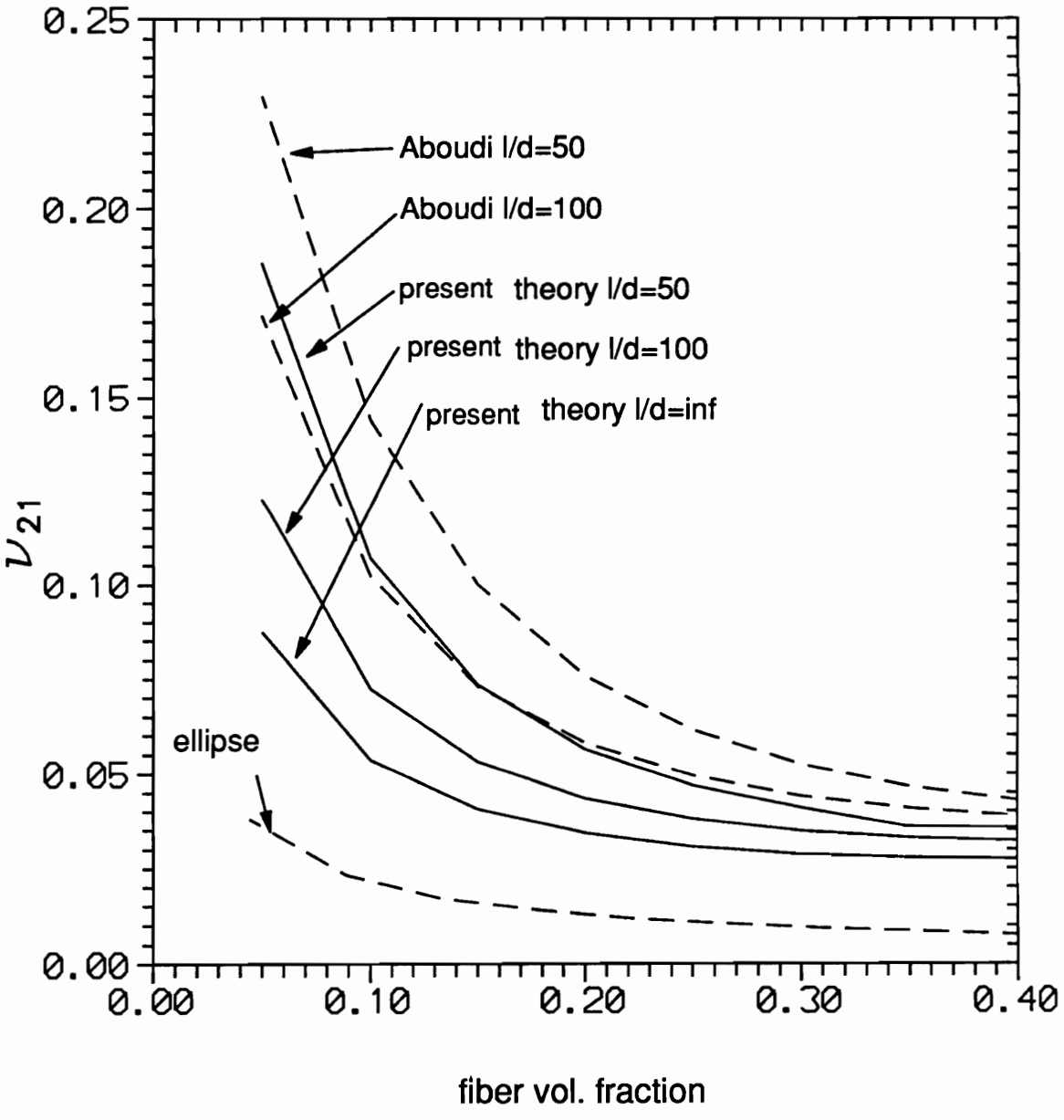

Figure 15. Axial Poisson Ratio vs Fiber Volume Fraction: Comparison of predicted ν_{21} values for various theories in an steel/epoxy material as a function of fiber volume fraction.

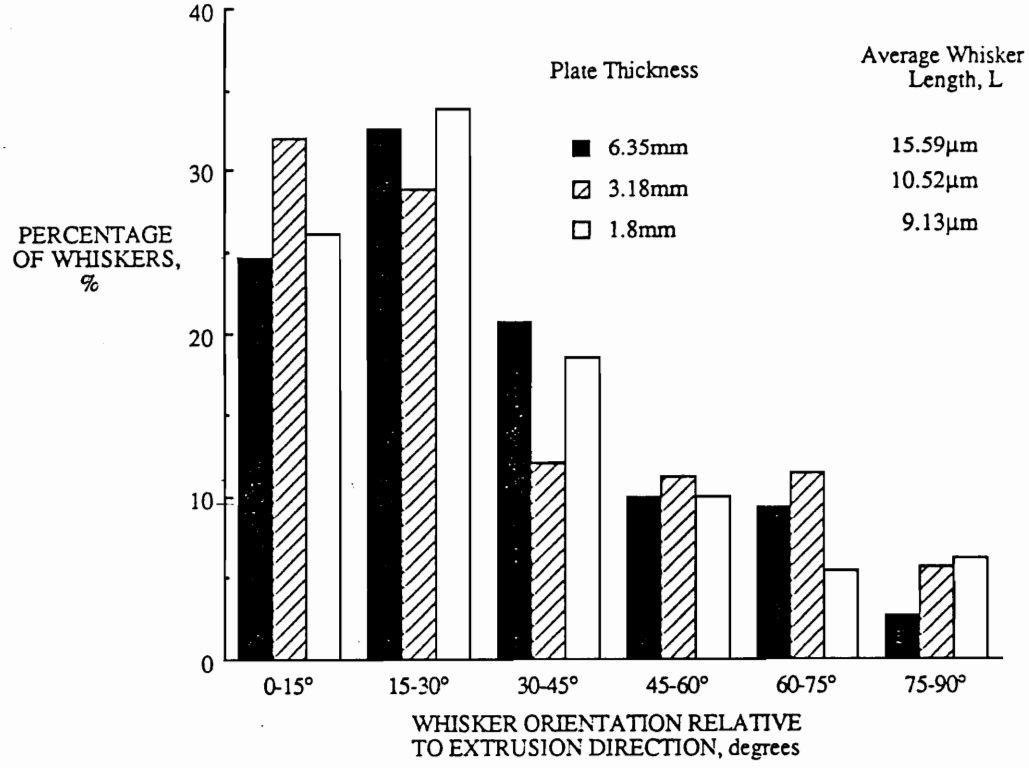

Figure 16. MMC Fiber Distribution (15%): Fiber distribution in a 15 percent MMC as published by Johnson and Birt [42].

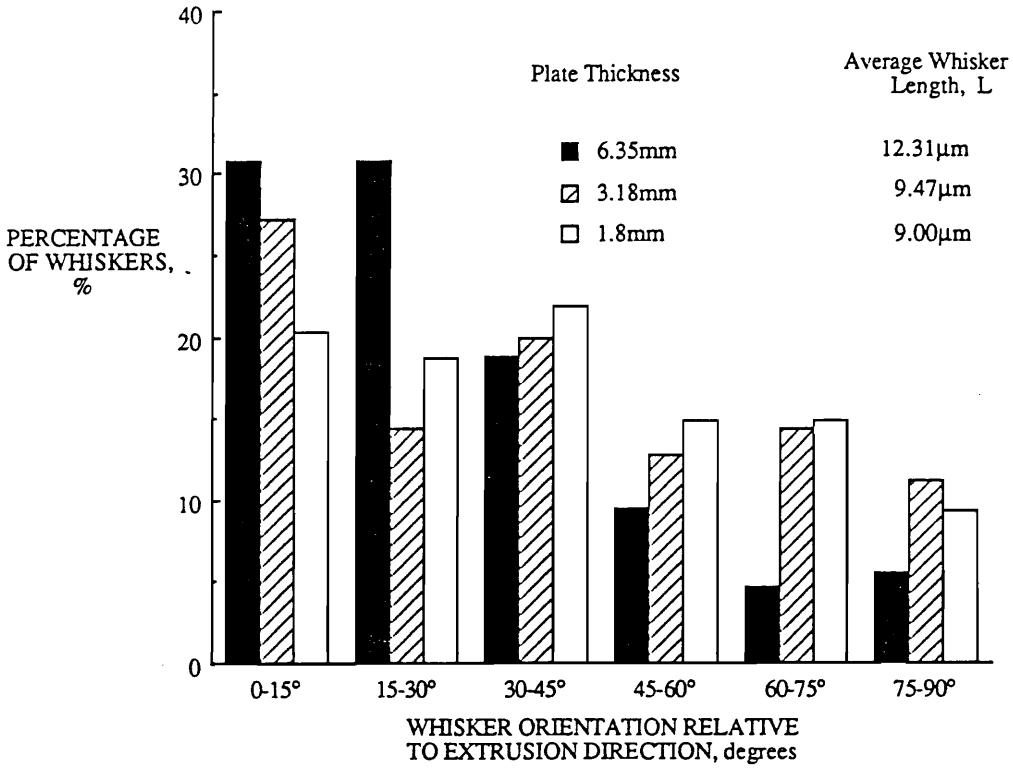

Figure 17. MMC Fiber Distribution (30%): Fiber distribution in a 30 percent MMC as published by Johnson and Birt [42].

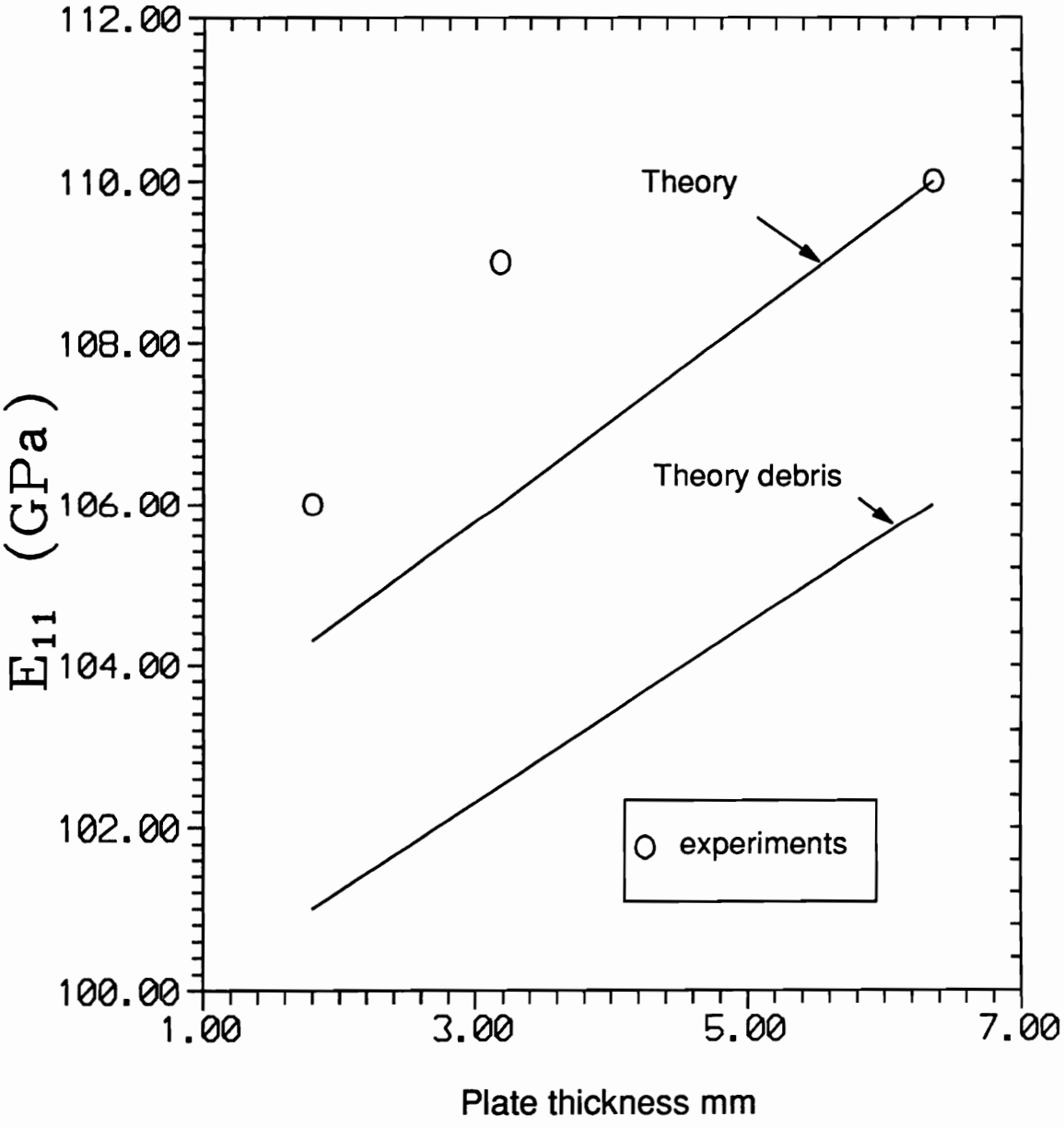

Figure 18. Axial Modulus Comparison MMC (15%): Comparison of E_{11} obtained by Johnson and Birt [42] experimentally and the current theory for a MMC $v_f = 15\%$ as a function of plate thickness.

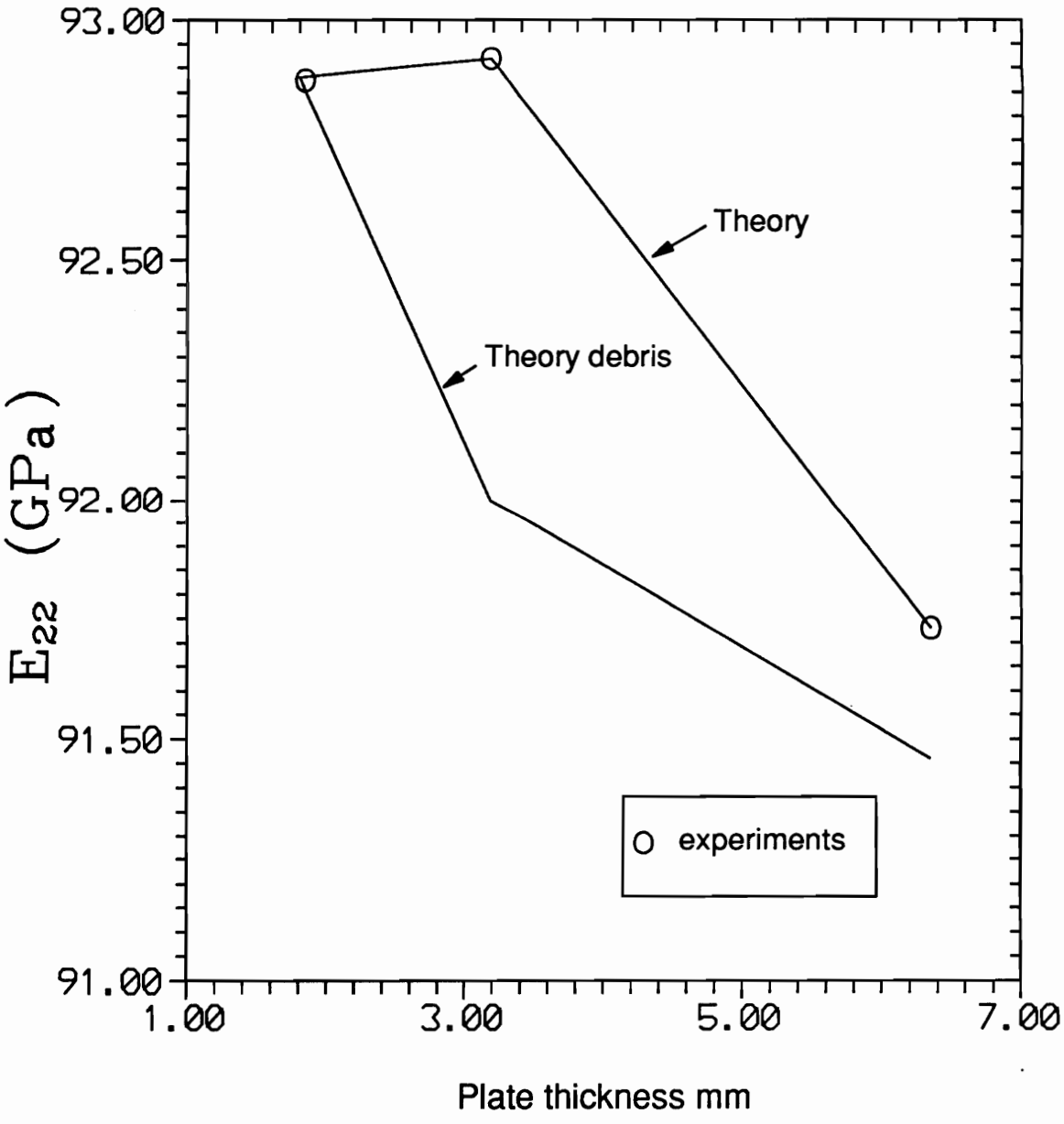

Figure 19. Transverse Modulus Comparison MMC (15%): Comparison of E_{22} obtained by Johnson and Birt [42] experimentally and the current theory for a MMC $v_f = 15\%$ as a function of plate thickness.

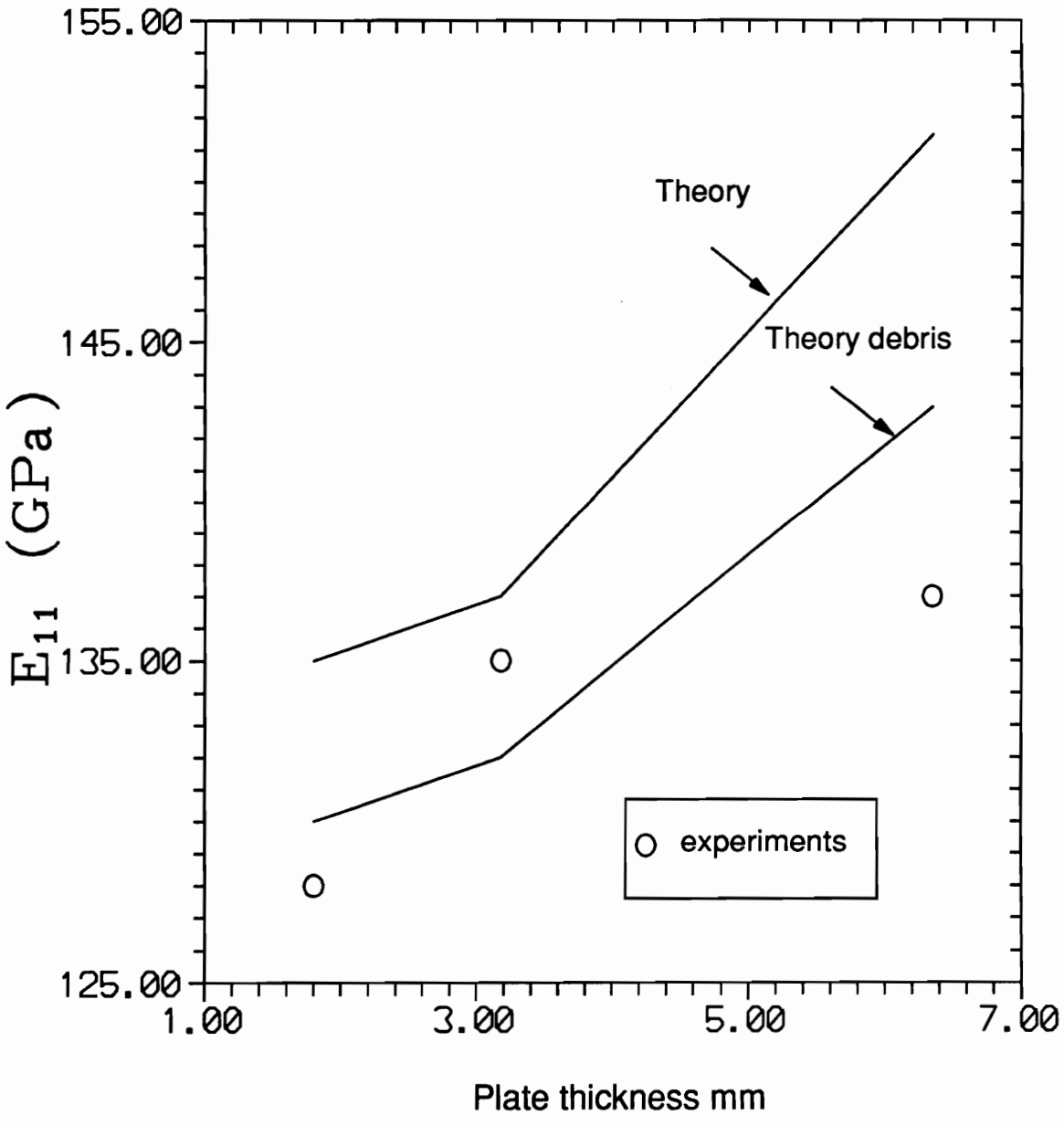

Figure 20. Axial Modulus Comparison MMC (30%): Comparison of E_{11} obtained by Johnson and Birt [42] experimentally and the current theory for a MMC $v_f = 30\%$ as a function of plate thickness.

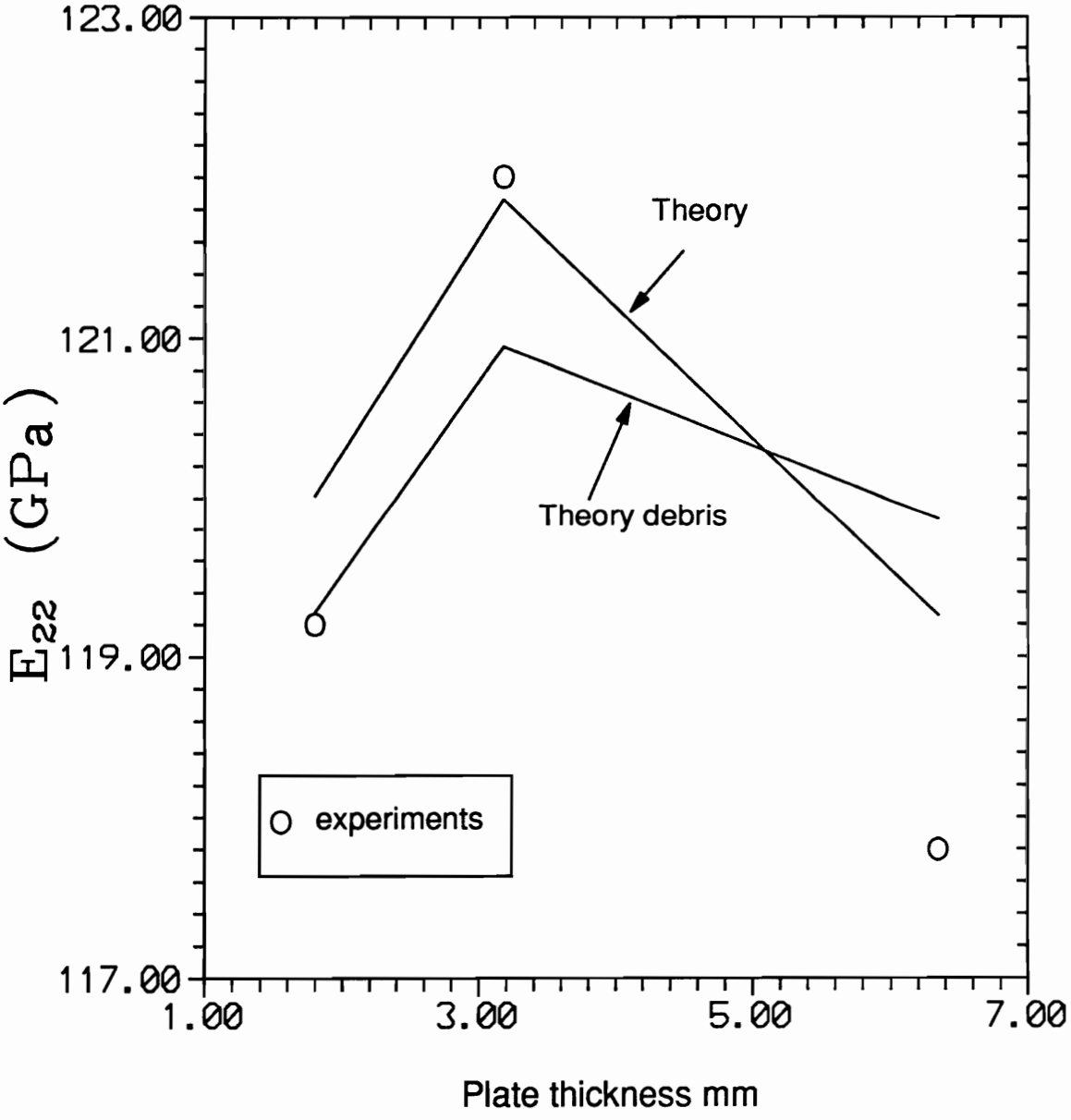

Figure 21. Transverse Modulus Comparison MMC (30%): Comparison of E_{22} obtained by Johnson and Birt [42] experimentally and the current theory for a MMC $v_f = 30\%$ as a function of plate thickness.

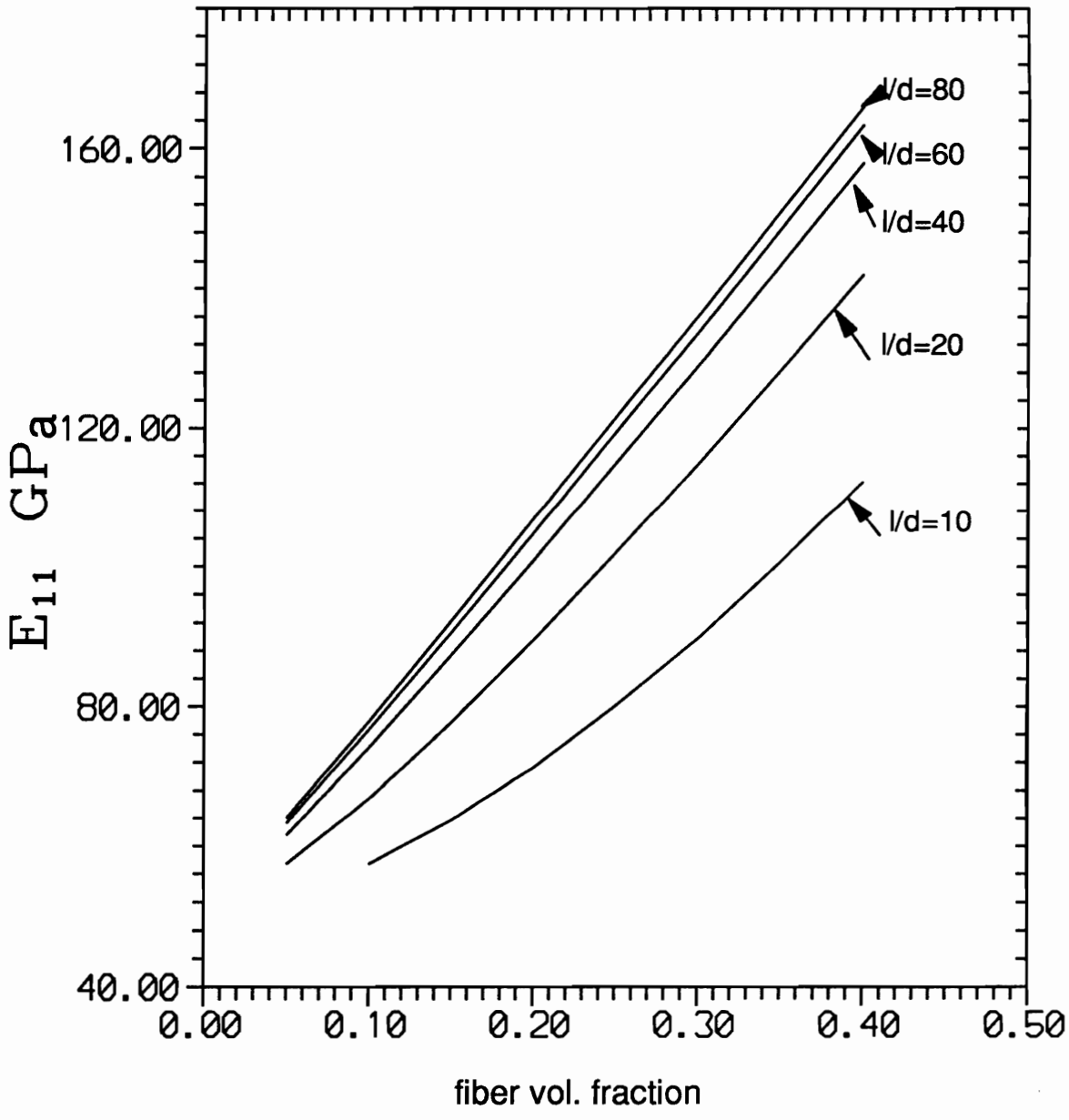

Figure 22. Axial Modulus vs Fiber Volume Fraction (BMC): Plot of E_{11} as a function of fiber volume fraction for different aspect ratios in a glass/HMU graphite composite.

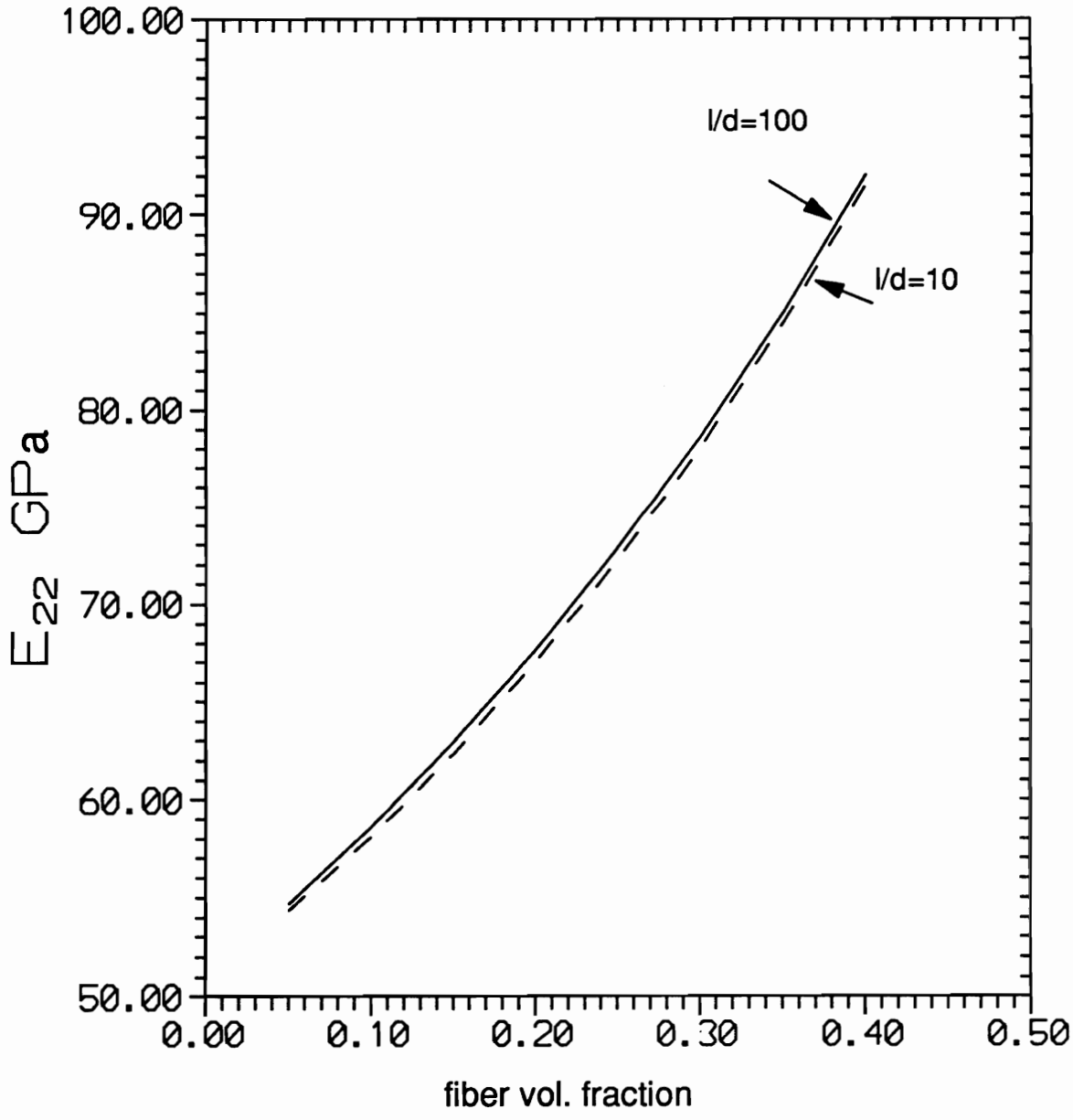

Figure 23. Transverse Modulus vs Fiber Volume Fraction (BMC): Plot of E_{22} as a function of fiber volume fraction for different aspect ratios in a glass/HMU graphite composite.

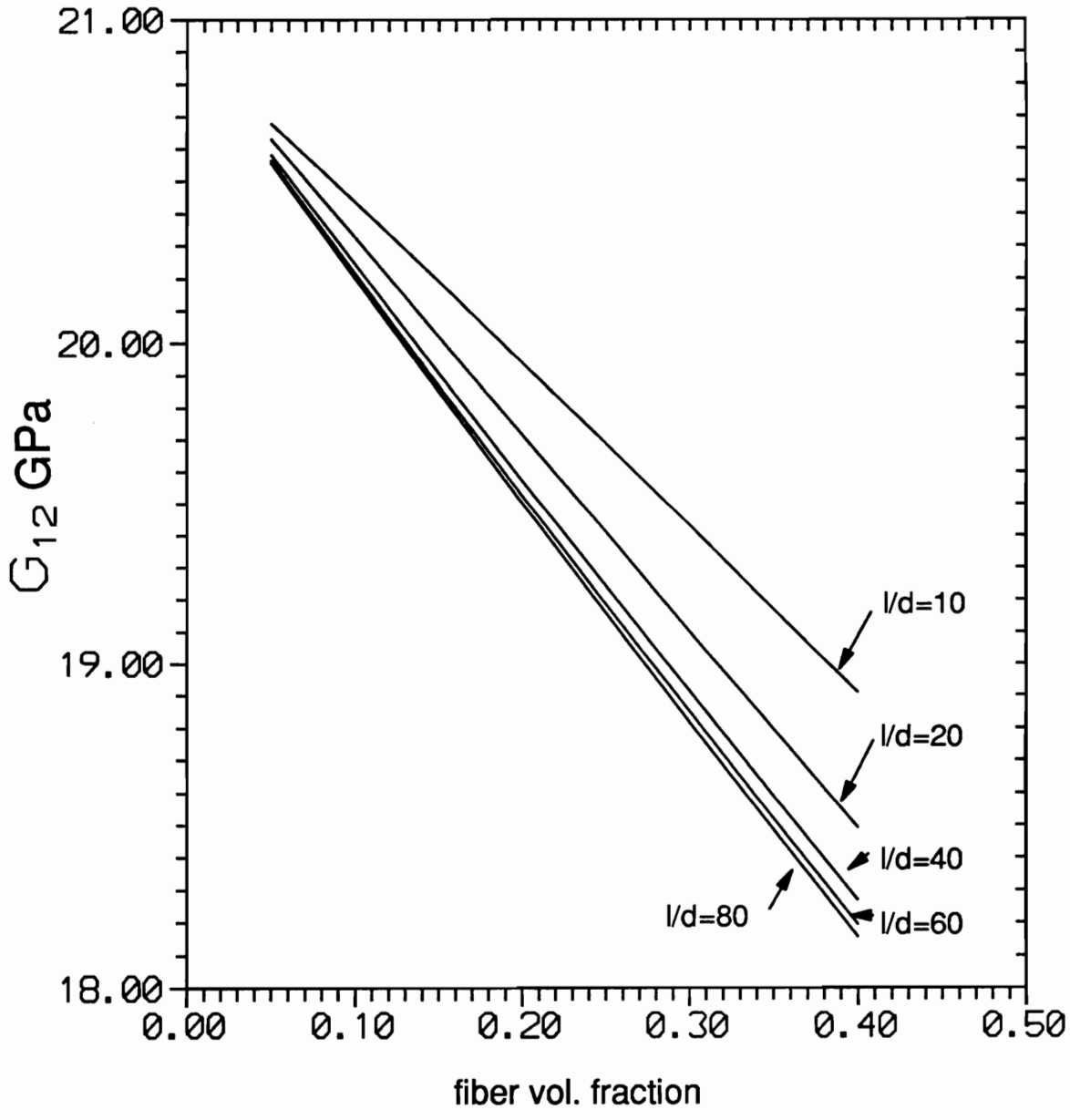

Figure 24. Shear Modulus vs Fiber Volume Fraction (BMC): Axial shear modulus as a function of fiber volume fraction for different aspect ratios in a glass/HMU graphite composite.

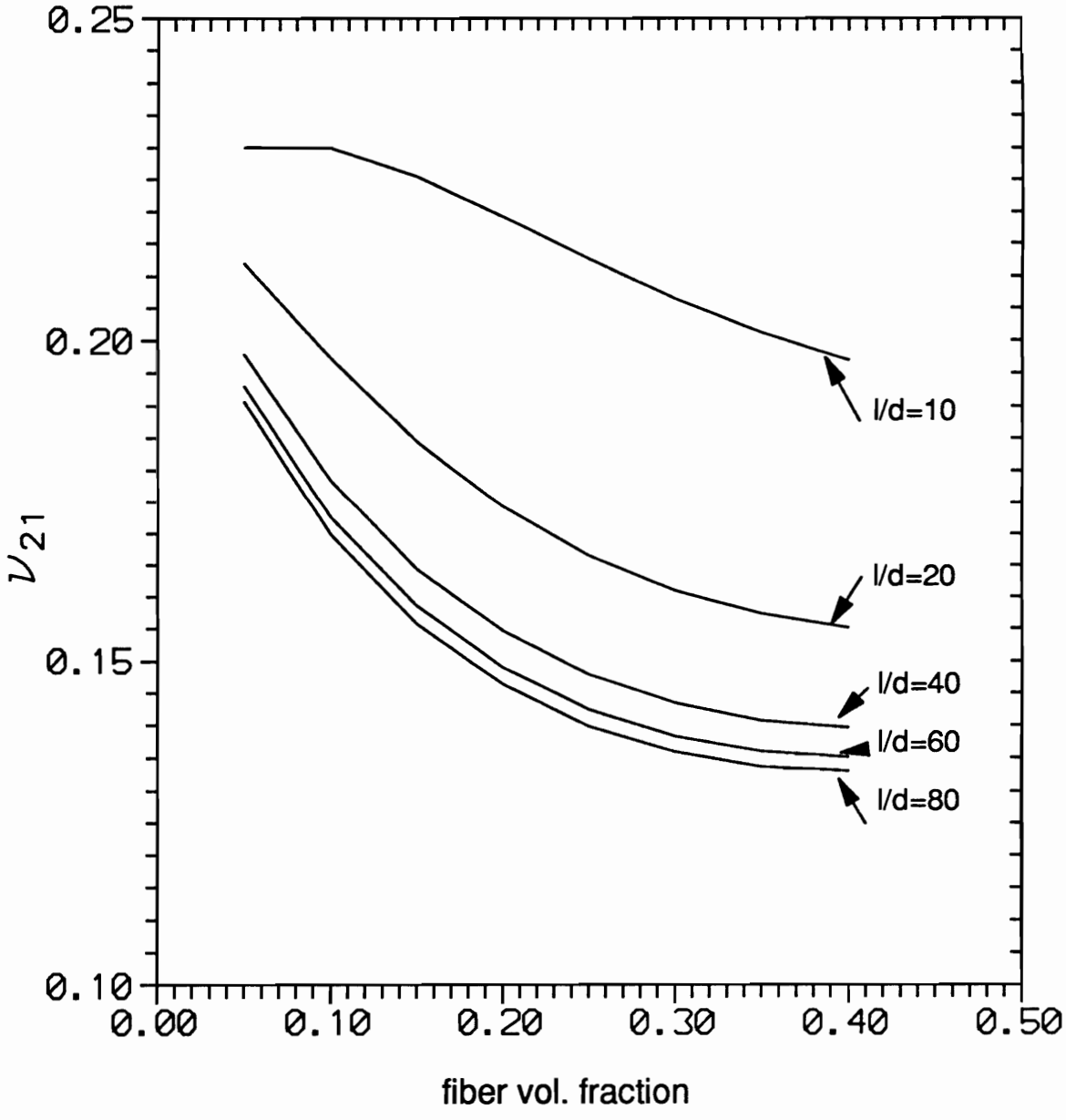

Figure 25. Axial Poisson Ratio vs Fiber Volume Fraction (BMC): Plot of ν_{21} as a function of fiber volume fraction for different aspect ratios in a glass/HMU graphite composite.

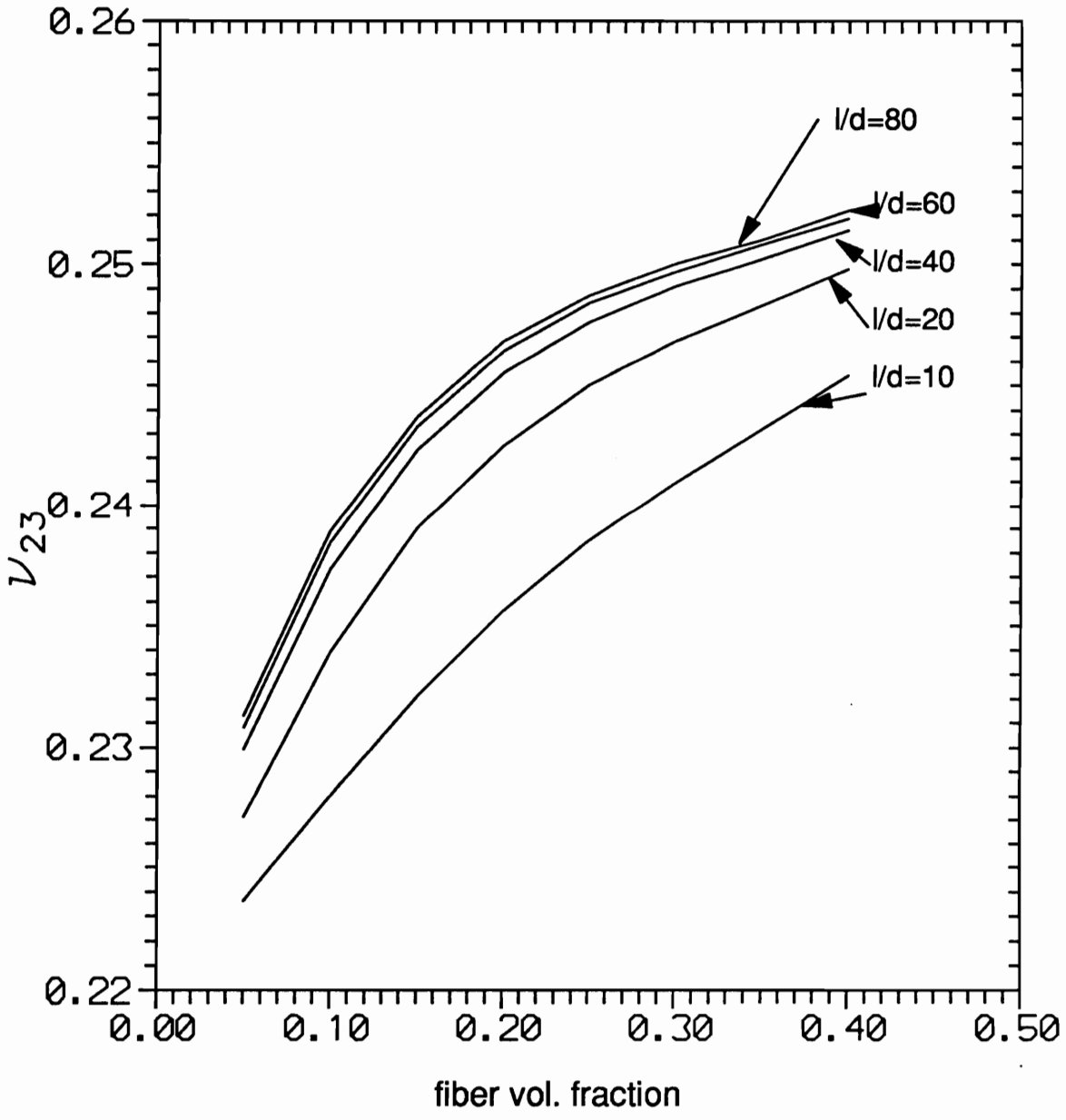

Figure 26. Transverse Poisson Ratio vs Fiber Volume Fraction (BMC): Plot of ν_{23} as a function of fiber volume fraction for different aspect ratios in a glass/HMU graphite composite.

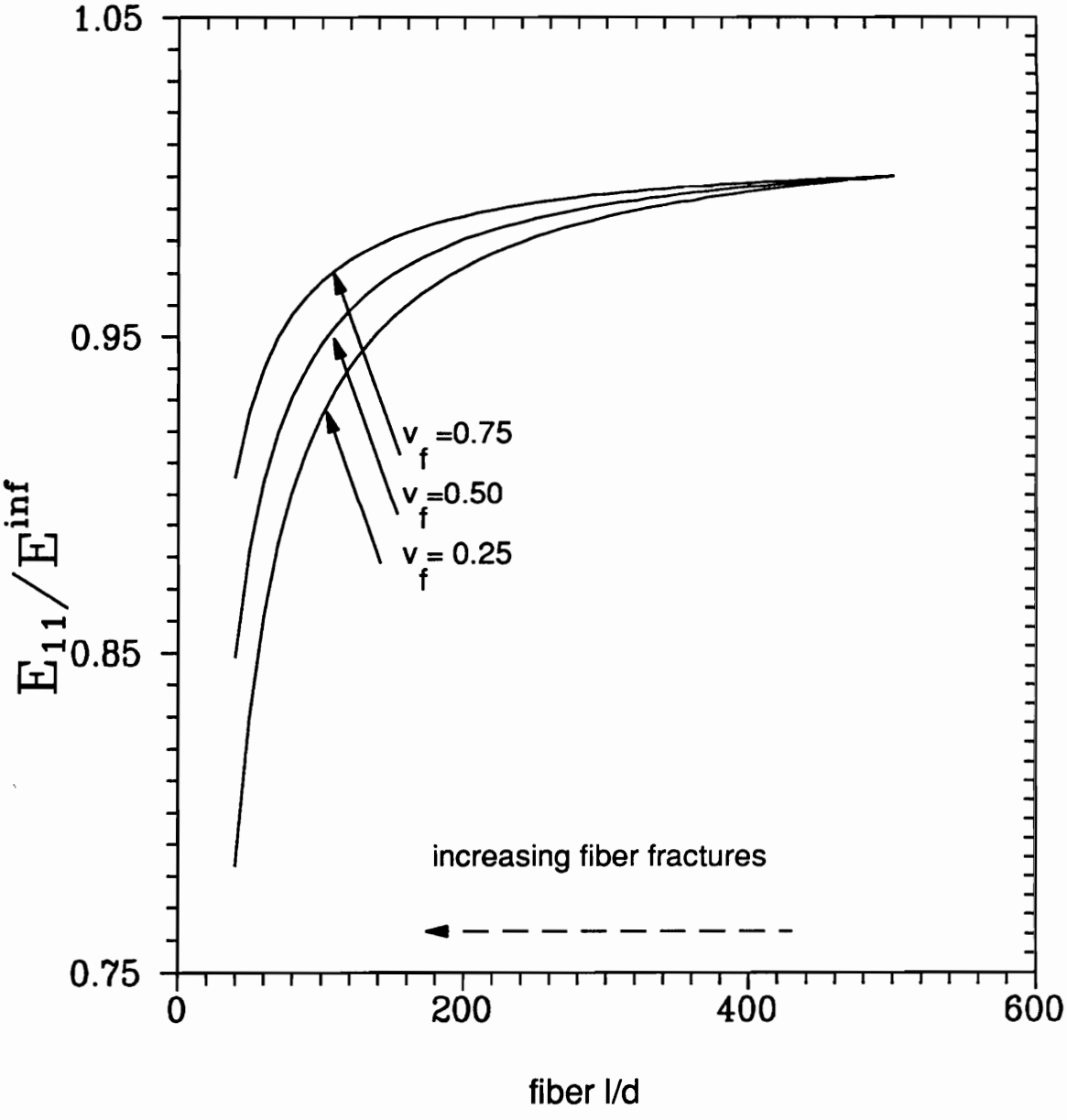

Figure 27. Axial Modulus Degradation: Figure depicting the degradation of a normalized E_{11} as a function of fiber aspect ratio in a E-glass/epoxy composite for three fiber volume fractions.

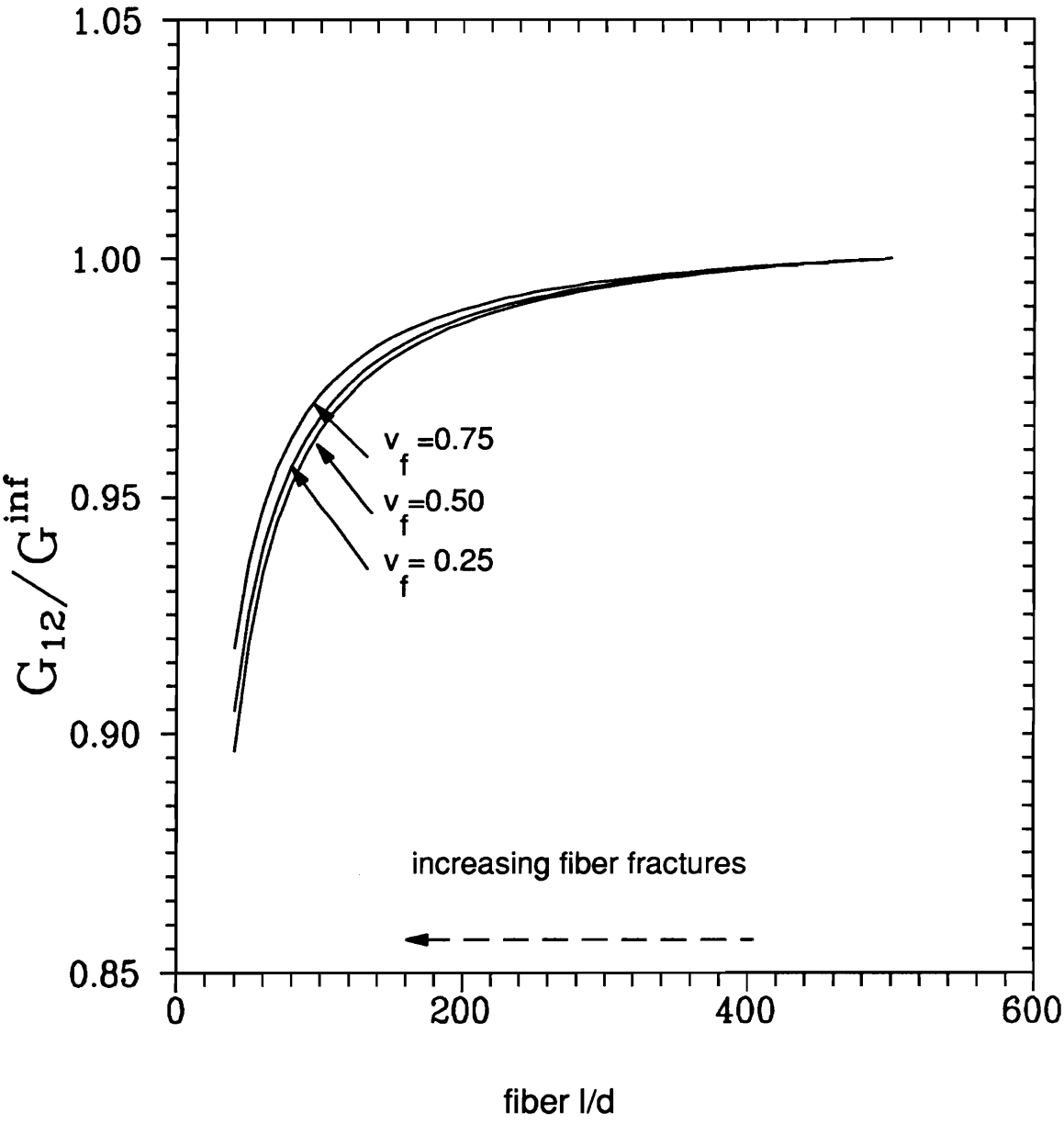

Figure 28. Shear Modulus Degradation: Figure depicting the degradation of a normalized G_{12} as a function of fiber aspect ratio in a E-glass/epoxy composite for three fiber volume fractions.

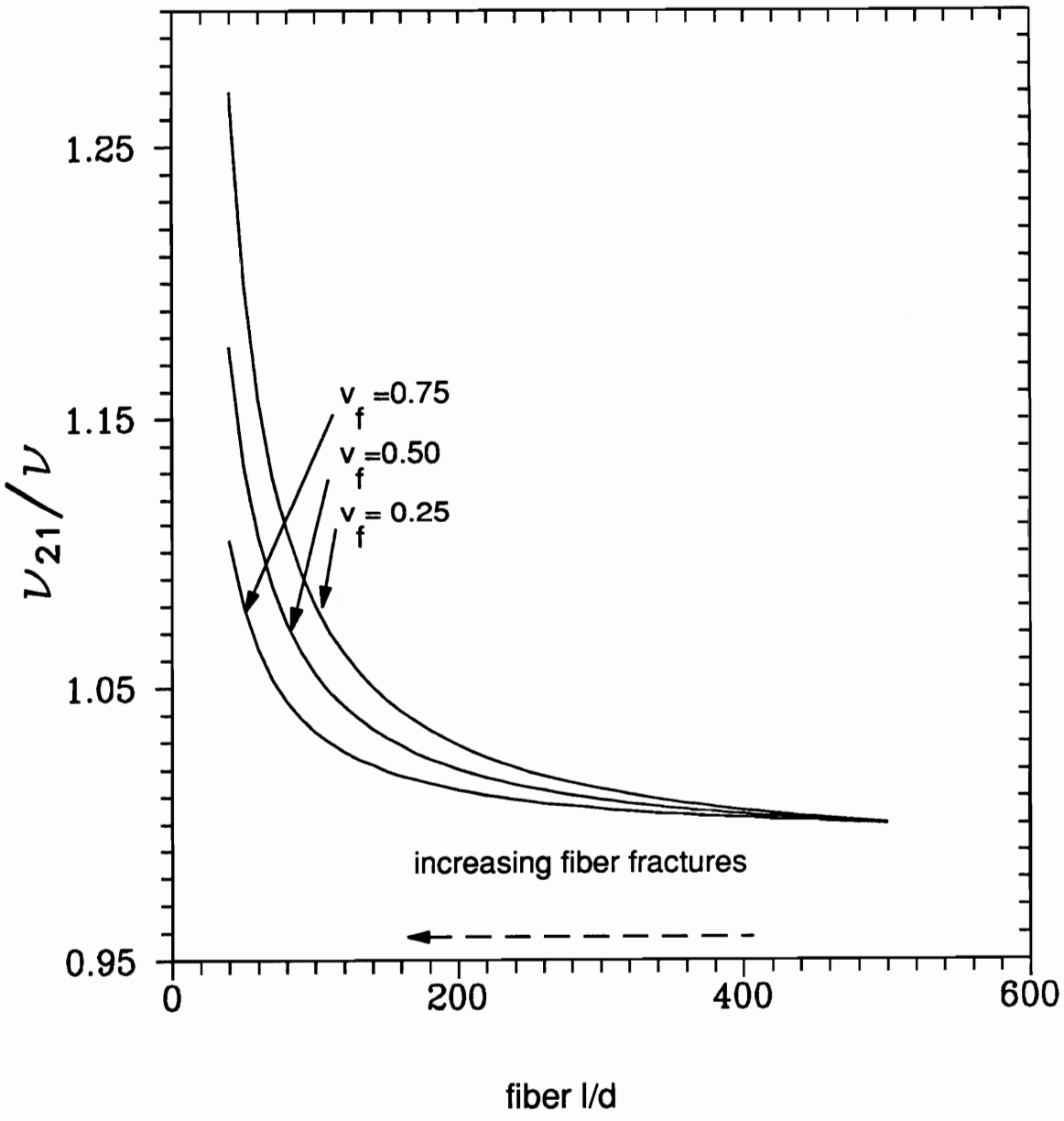

Figure 29. Axial Poisson Ratio Degradation: Figure depicting the degradation of a normalized ν_{21} as a function of fiber aspect ratio in a E-glass/epoxy composite for three fiber volume fractions.

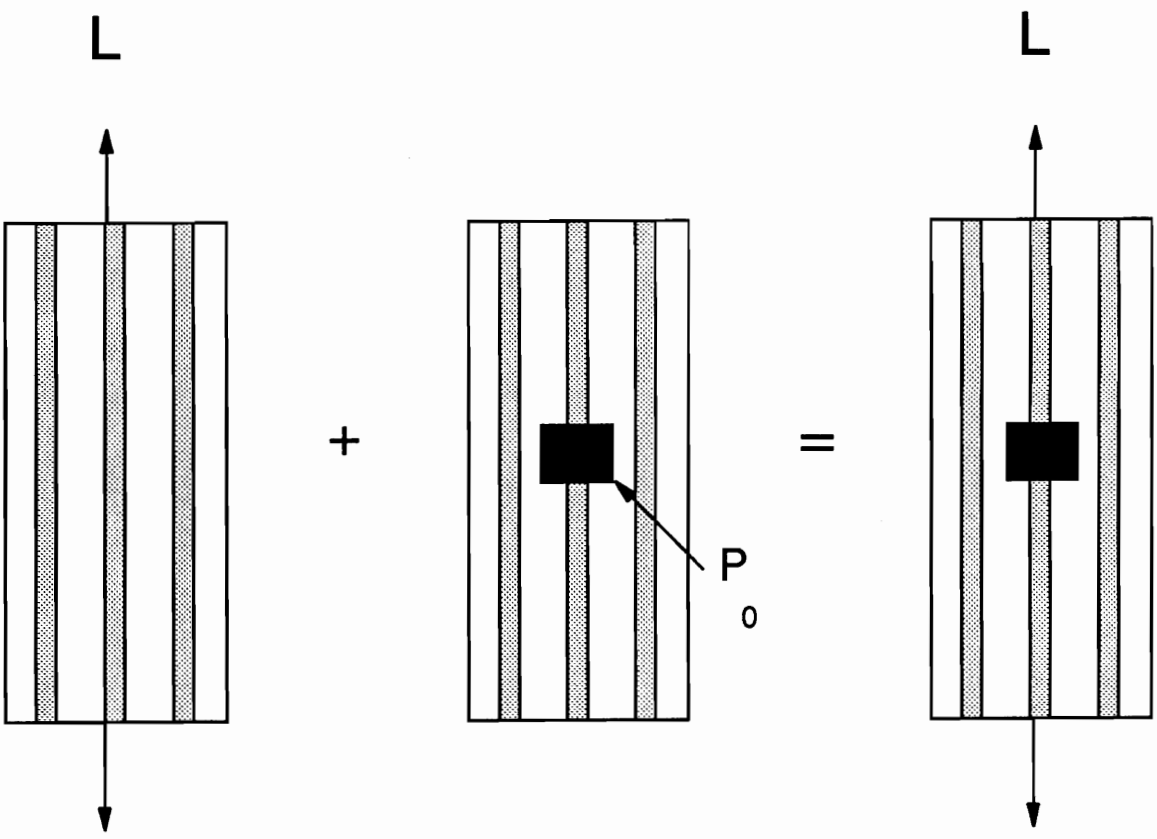

fig. 16

Figure 16, Superposition Technique: Figure depicting the superposition of the far-field solution on the fiber end solution to obtain the full field solution to the finite length fiber problem.

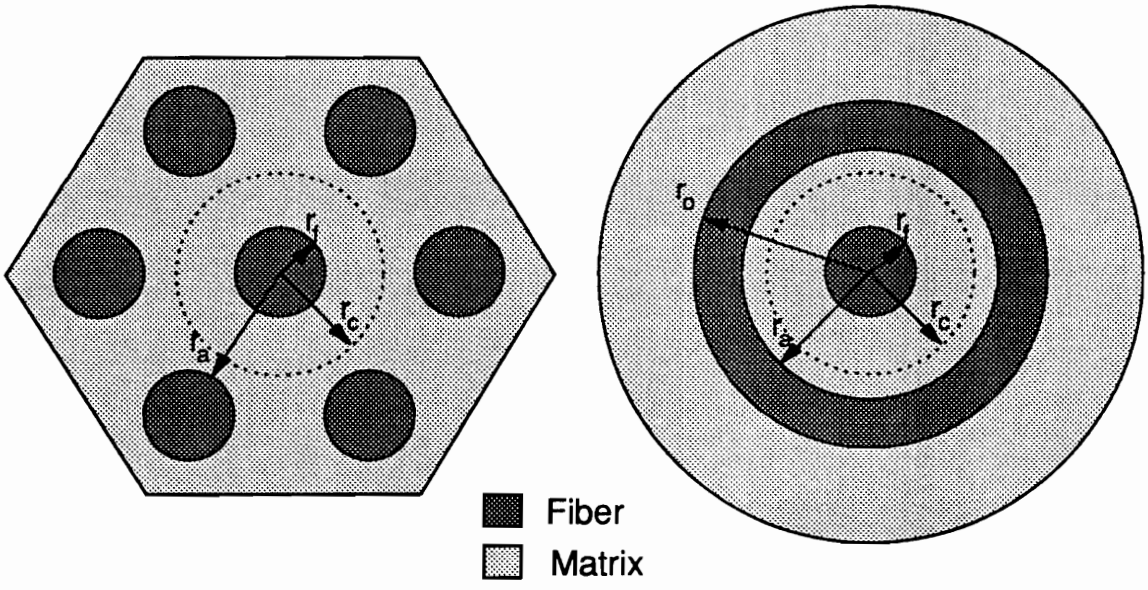

Fig. 8

Figure 31. Annular Ring Model: Illustration of a composite containing a fiber fracture that propagates a crack into the matrix which can adequately be represented by an annular ring problem.

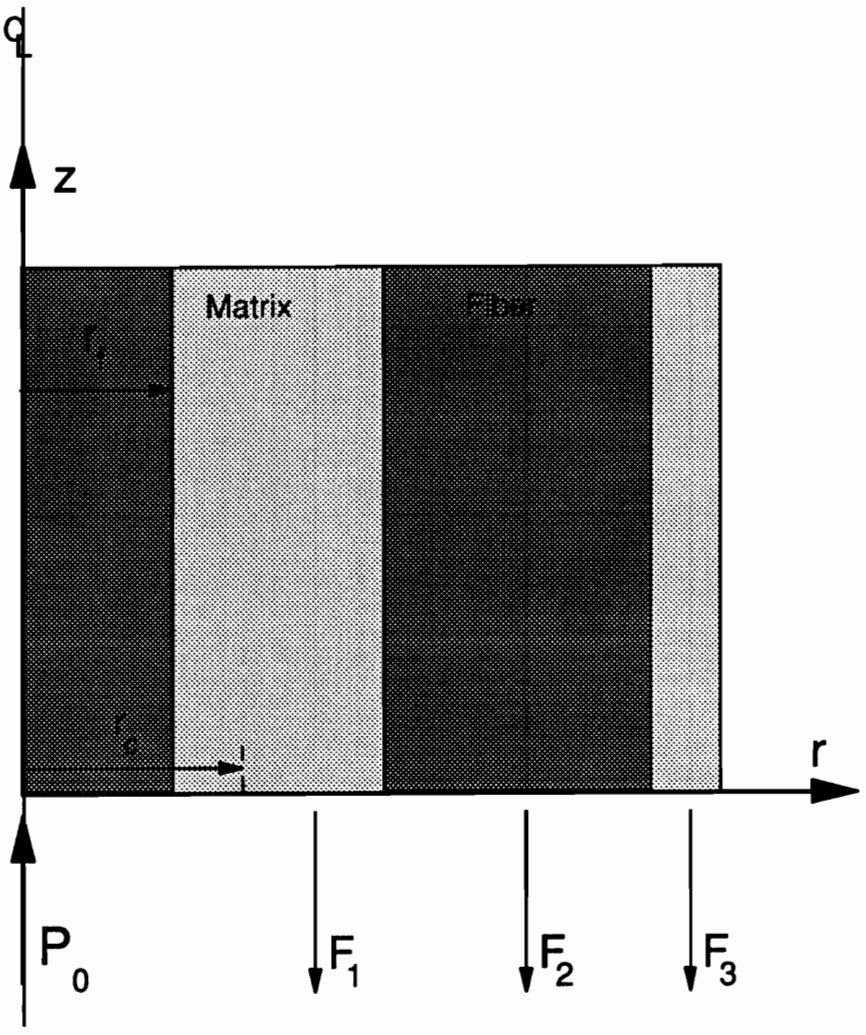

Figure 17. Elemental Force Balance: Drawing depicting the force balance in a composite element generated by the applied near field traction P_0 due to a fiber fracture.

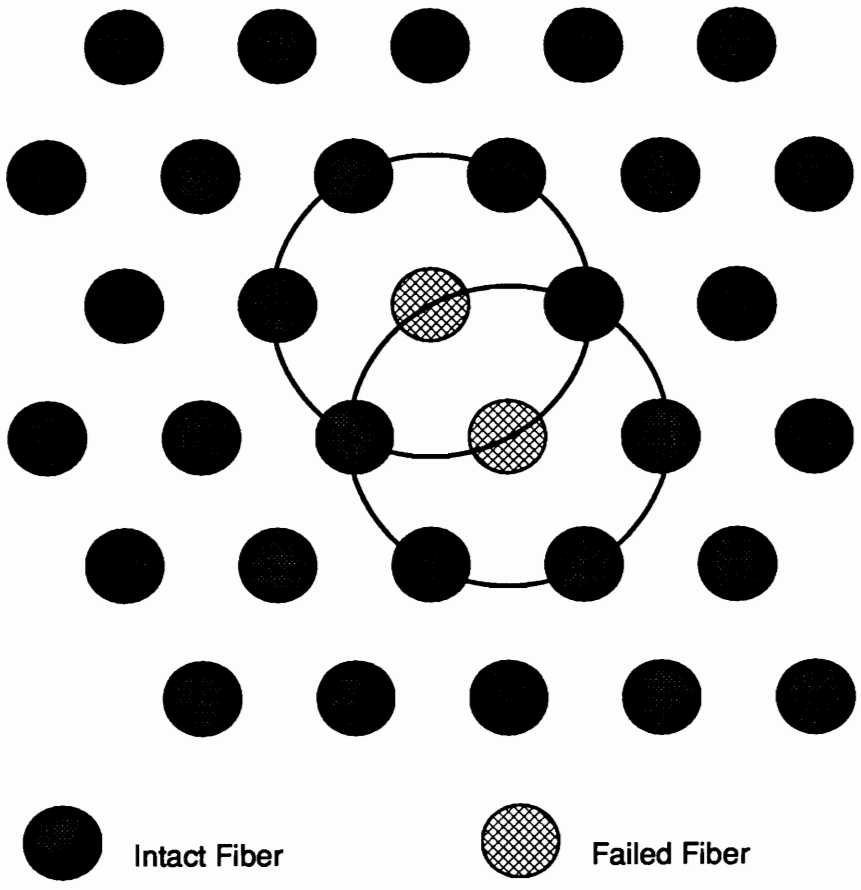

Figure 13. Multiple Fiber Fracture: Typical illustration of two adjacent fiber fractures in a composite.

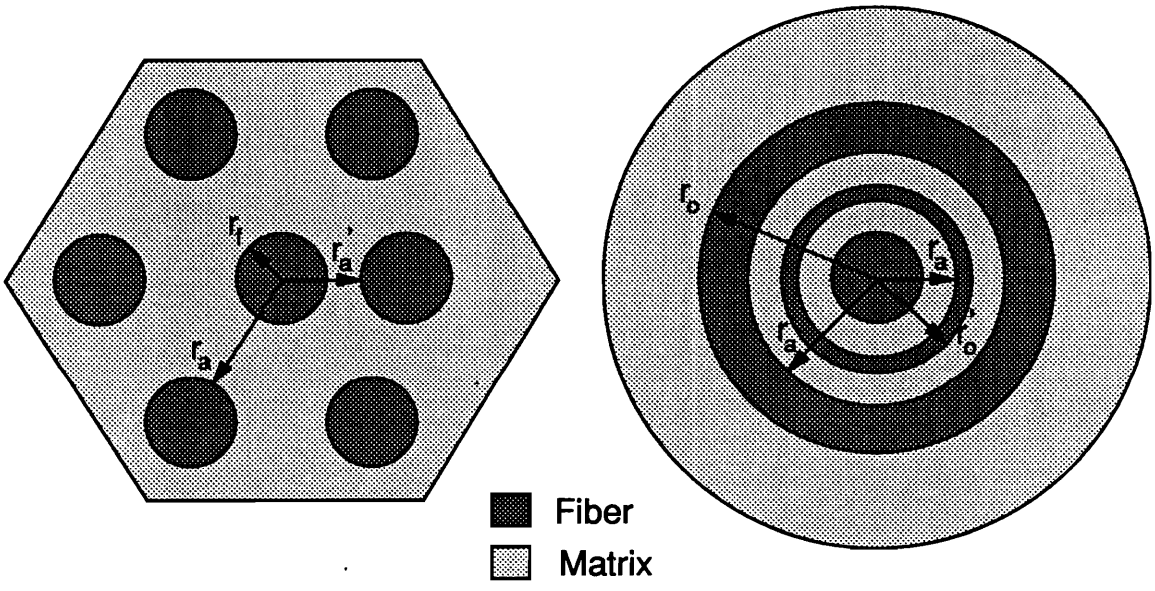

Figure 34. Annular Ring Model of Variable Fiber Spacing: Illustration of a composite containing an eccentrically located fiber and a fractured fiber which is modeled as an annular ring problem.

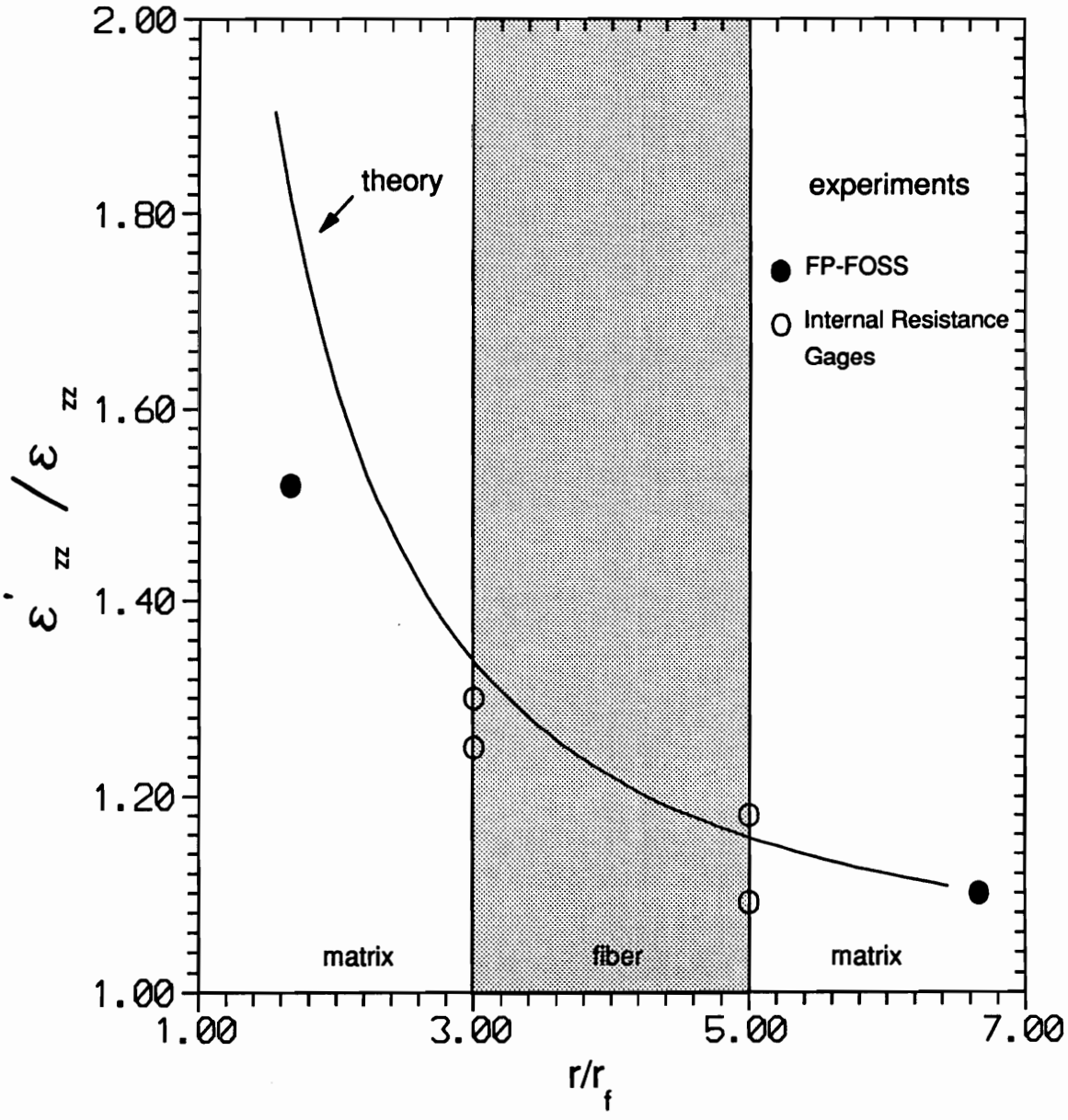

Fig 18

Figure 35. Strain Concentration vs Position (small crack; 15%): Comparison of strain concentration values determined by experimental techniques and theoretical predictions as a function of radial distance ($z=0$) from the fractured fiber. Results depict a 15% fiber volume fraction model composite where $r_c = r_f$.

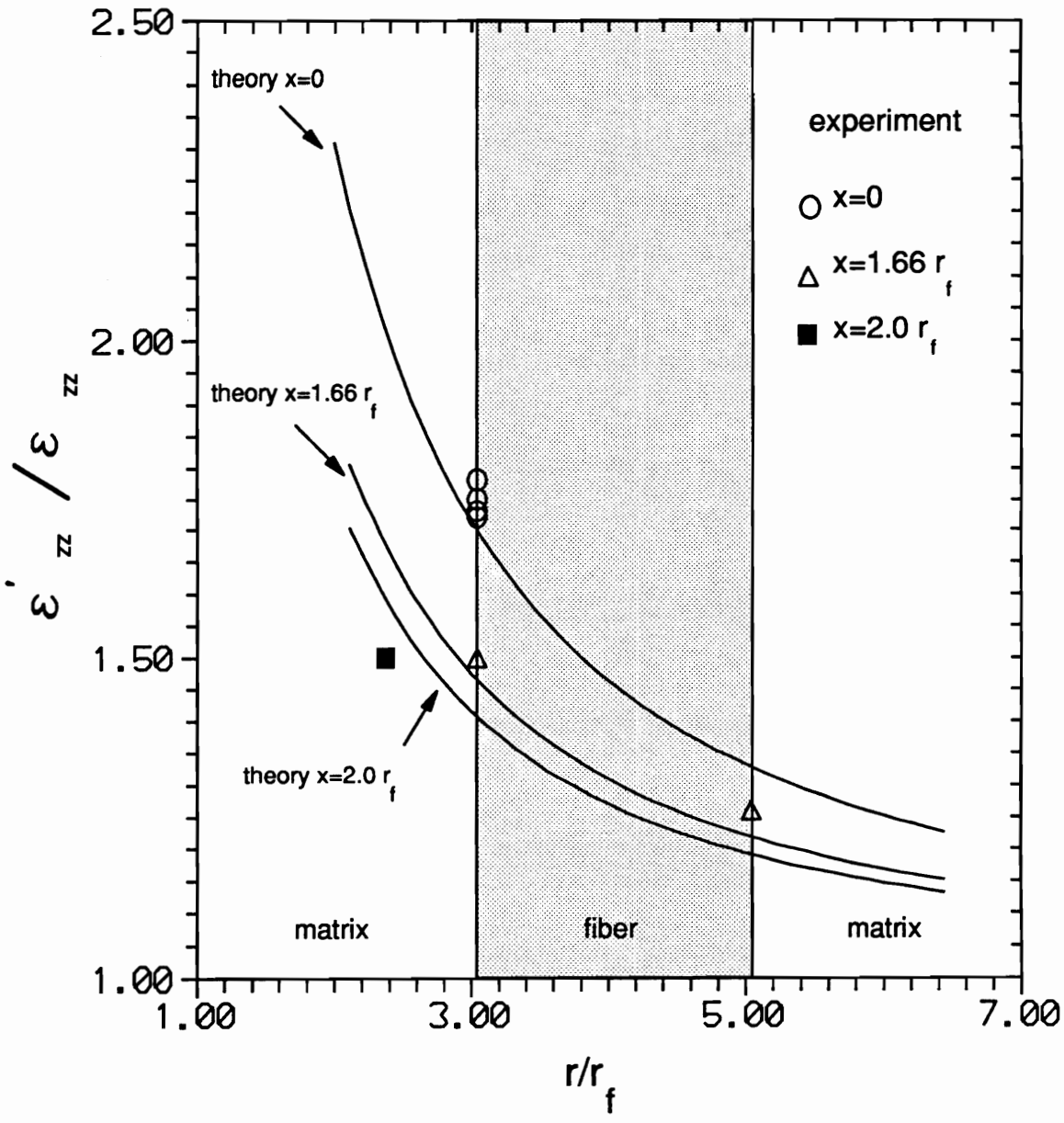

fig 19

Figure 36. Strain Concentration vs Position (large crack; 15%): Comparison of strain concentration values determined by experimental techniques and theoretical predictions as a function of radial distance from the fractured fiber. Results depict a 15% fiber volume fraction model composite where $r_c = r_a$.

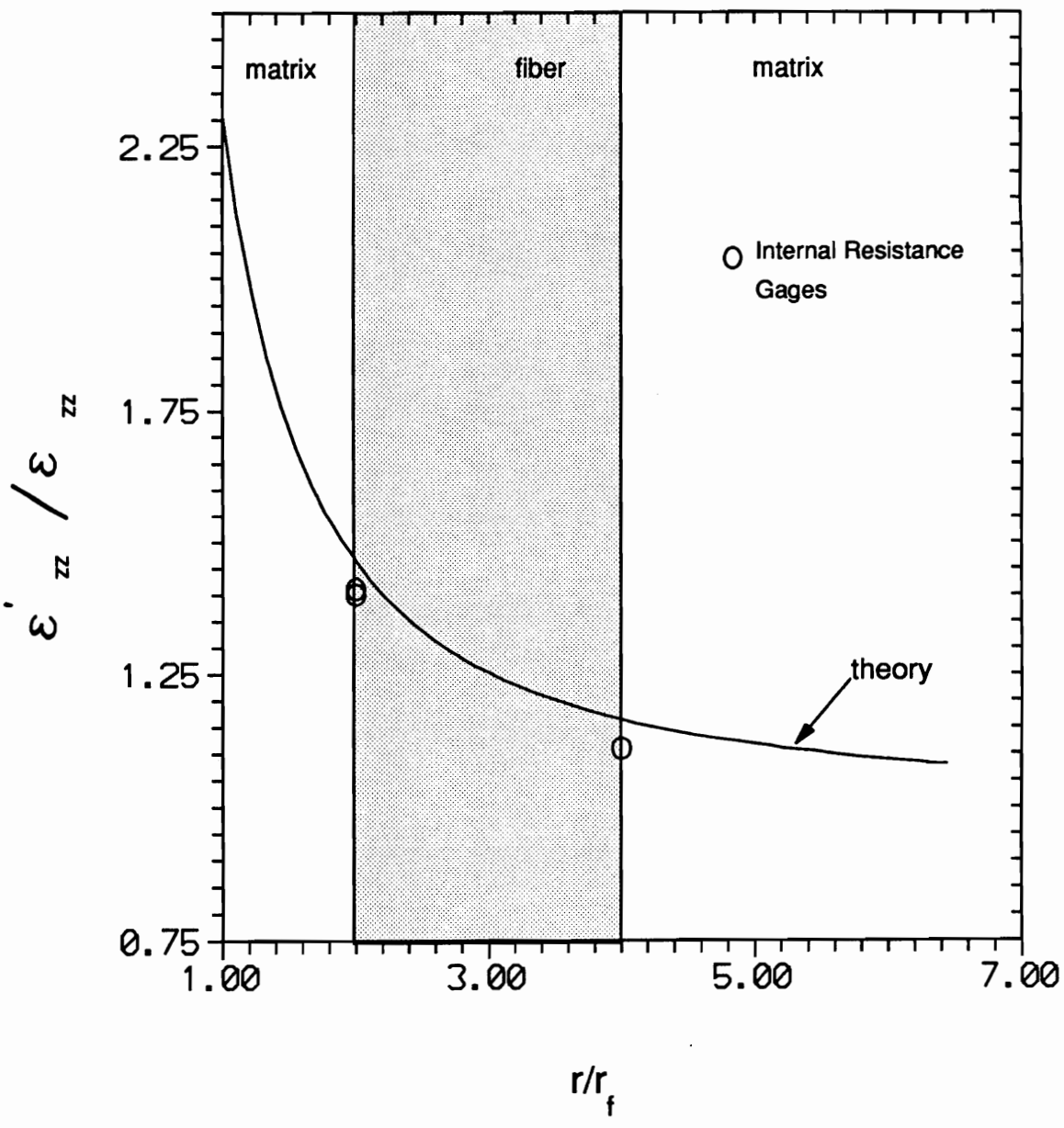

fig. 20

Figure 37. Strain Concentration vs Position (small crack; 20%): Comparison of strain concentration values determined by experimental techniques and theoretical predictions as a function of radial distance ($z=0$) from the fractured fiber. Results depict a 20% fiber volume fraction model composite where $r_c = r_f$.

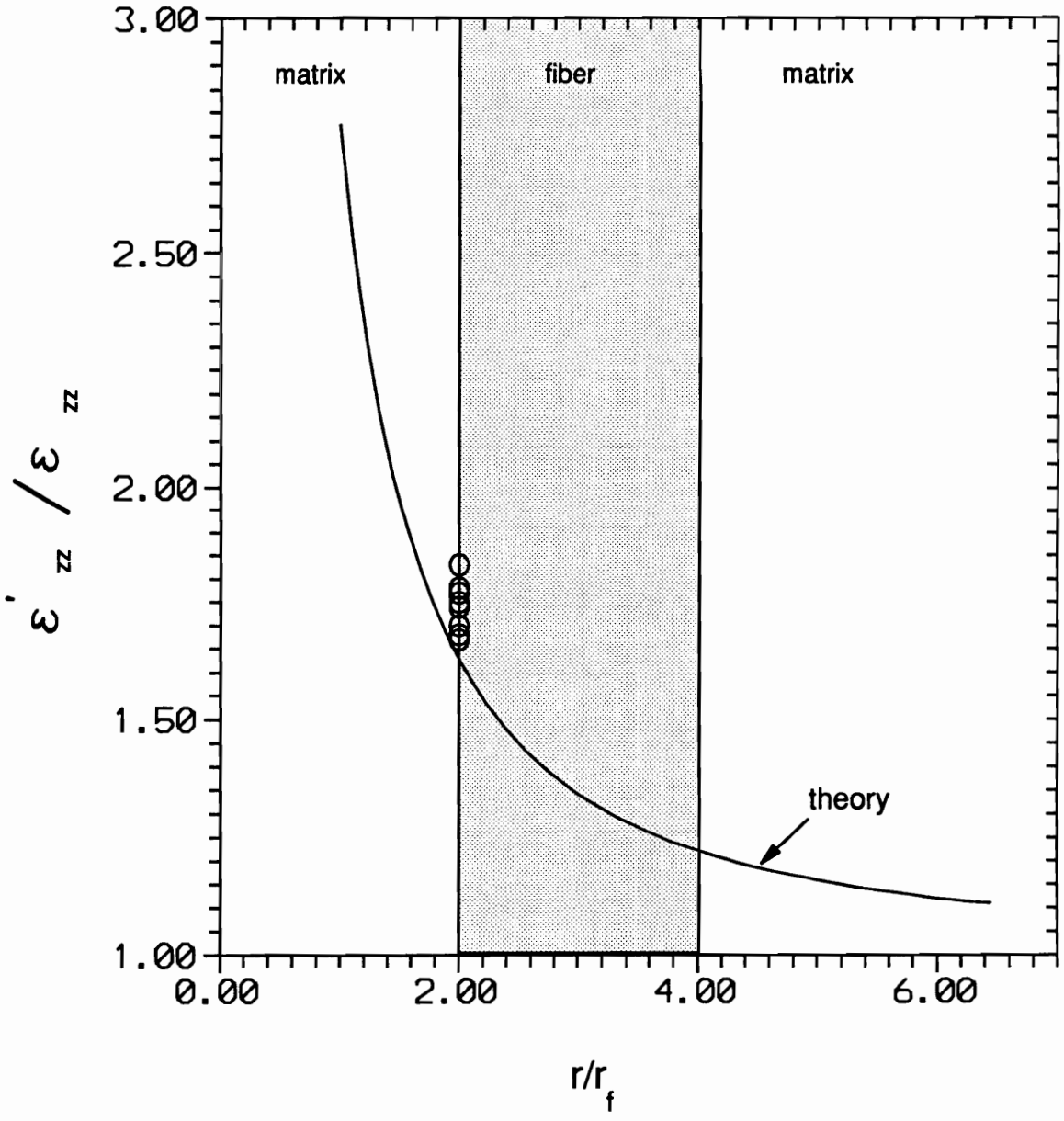

Figure 38. Strain Concentration vs Position (large crack; 20%): Comparison of strain concentration values determined by experimental techniques and theoretical predictions as a function of radial distance (z = 0) from the fractured fiber. Results depict a 20% fiber volume fraction model composite where $r_c = r_a$.

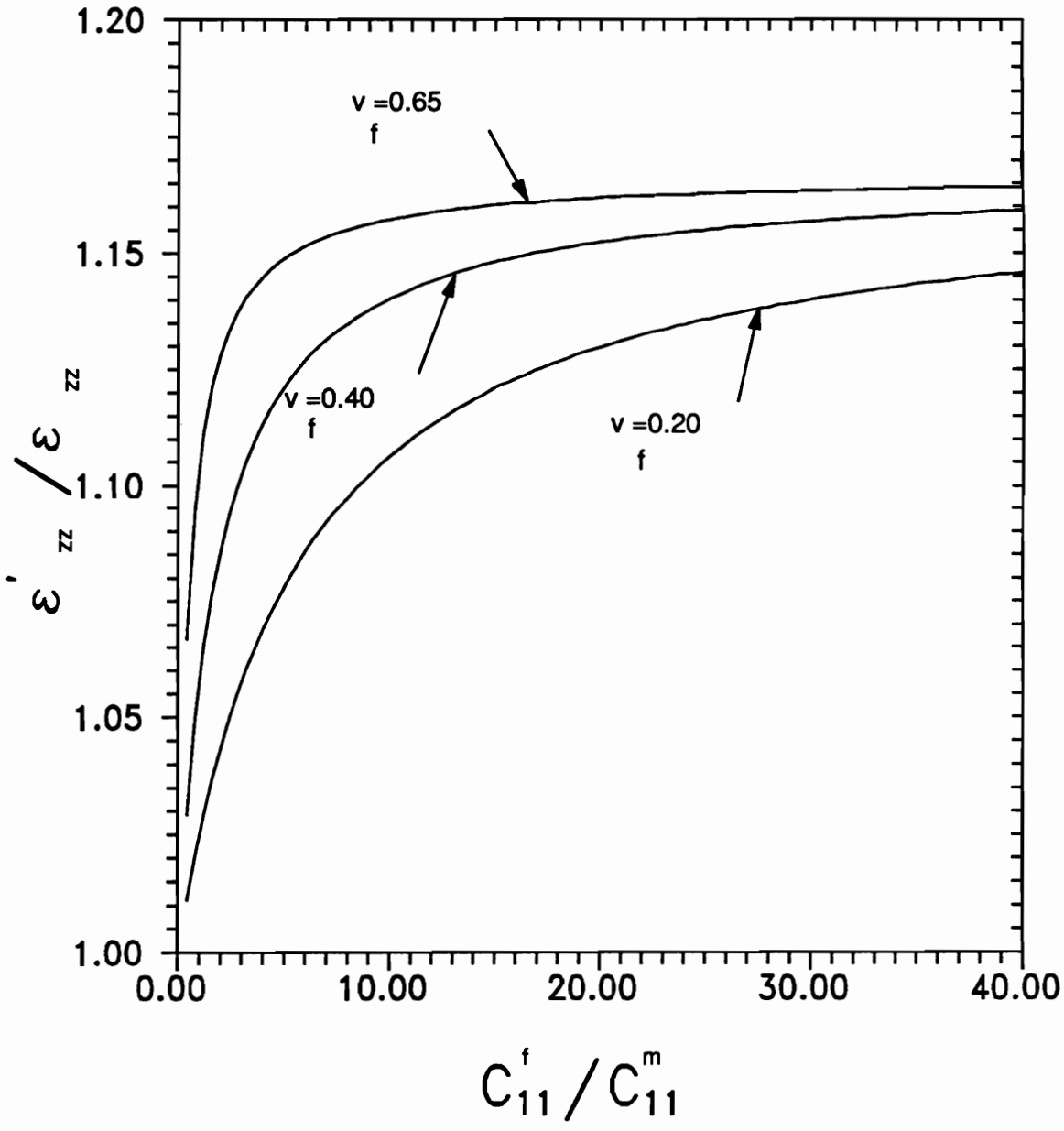

Fig. 21

Figure 39. Strain Concentration vs Stiffness ratio (small crack): Plot of average strain concentration on an adjacent fiber ($z=0$ and $r_c = r_f$) versus fiber/matrix stiffness ratio for three fiber volume fractions.

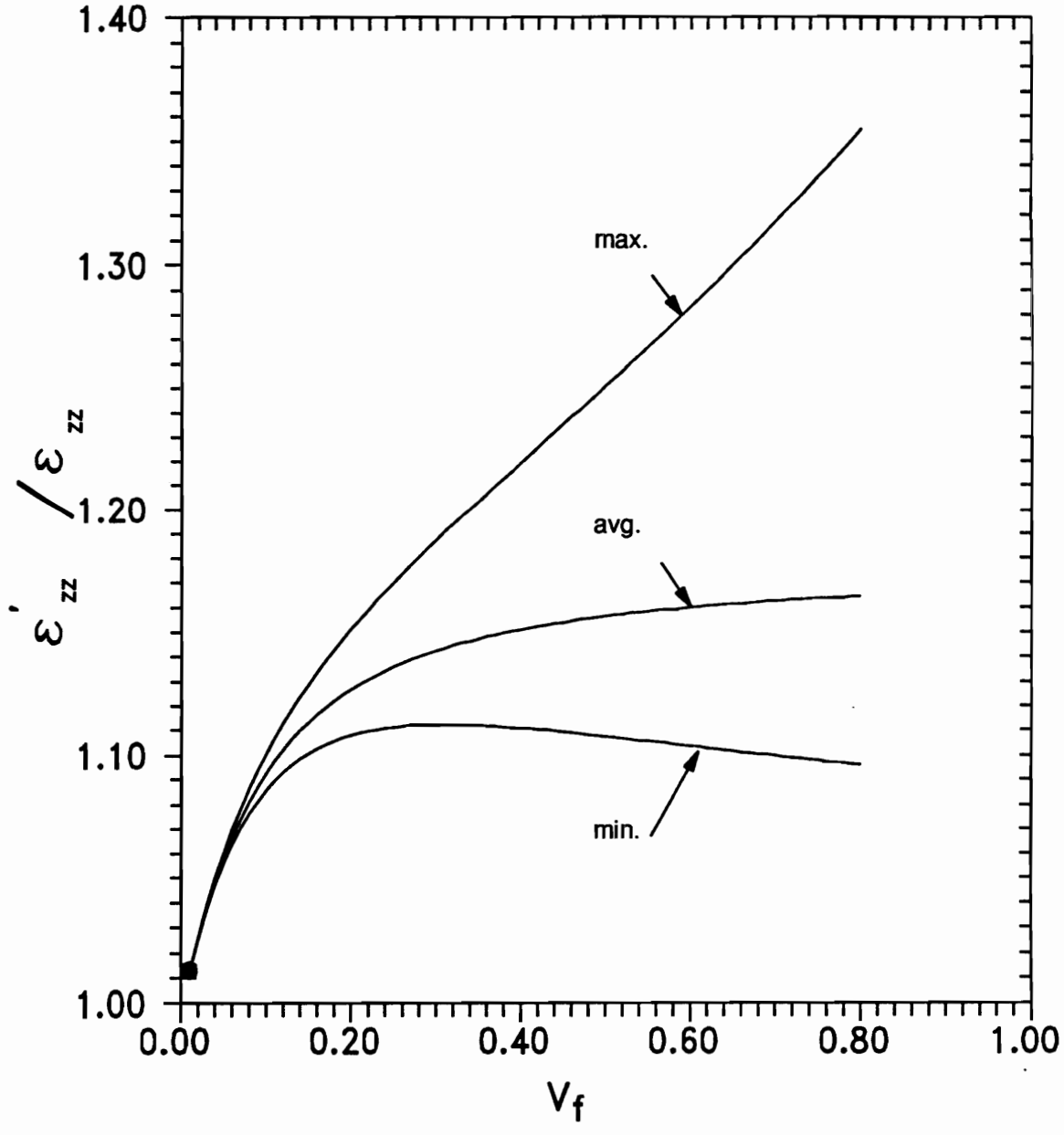

fig. 22

Figure 40. Strain Concentration vs Fiber Volume Fraction: Plot depicting the functional dependence of the maximum, minimum, and average strain concentration ($z=0$ and $r_c = r_f$) on fiber volume fraction for an glass/epoxy system.

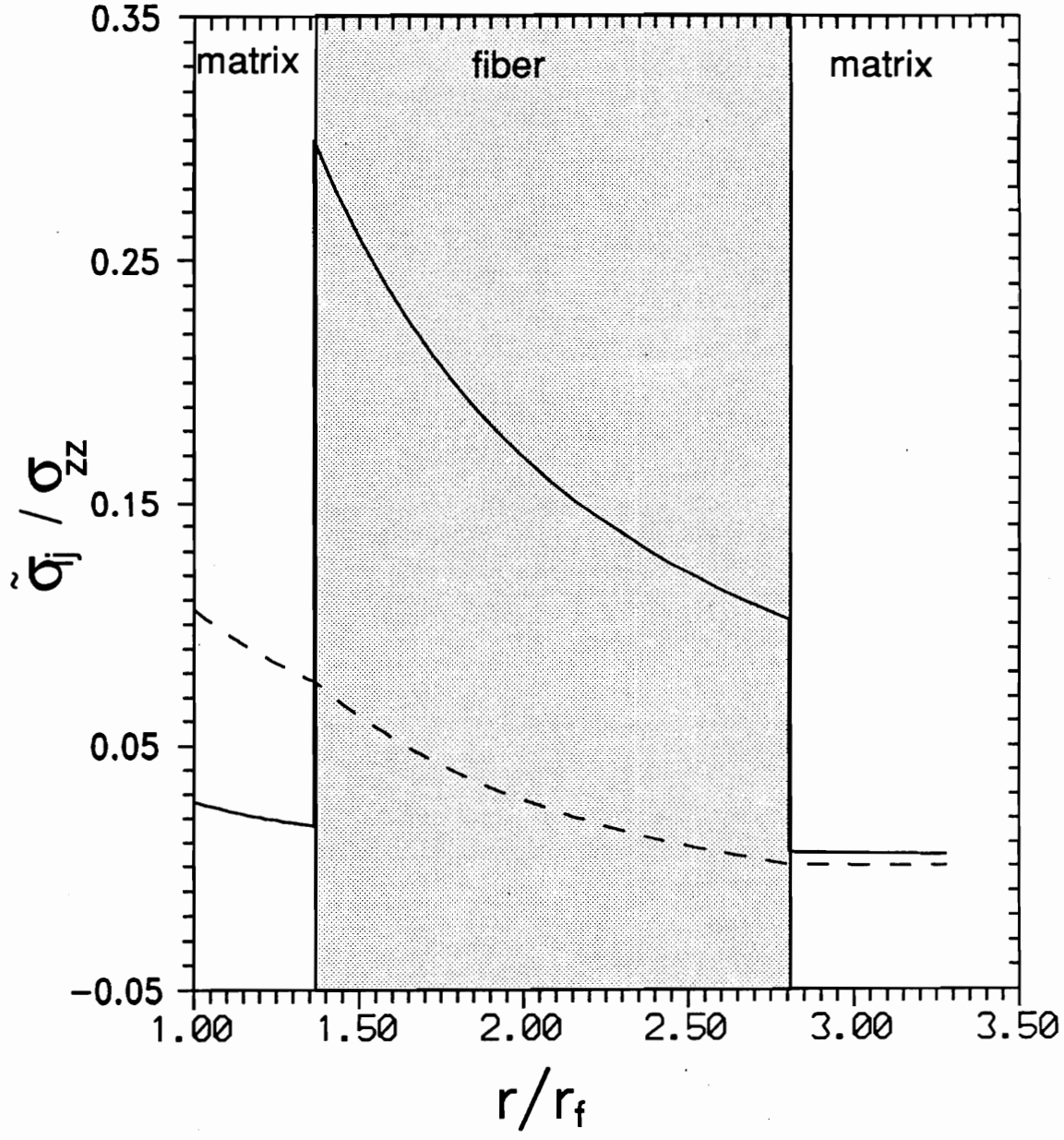

fig. 23

Figure 41. Stress vs Position (PMC): Plot of normalized stress versus normalized radial distance for axial stress ($z = 0$) and absolute value of shear stress ($z = 1/\lambda$) in a glass/epoxy composite where $v_f = 0.65$ and $r_c = r_f$.

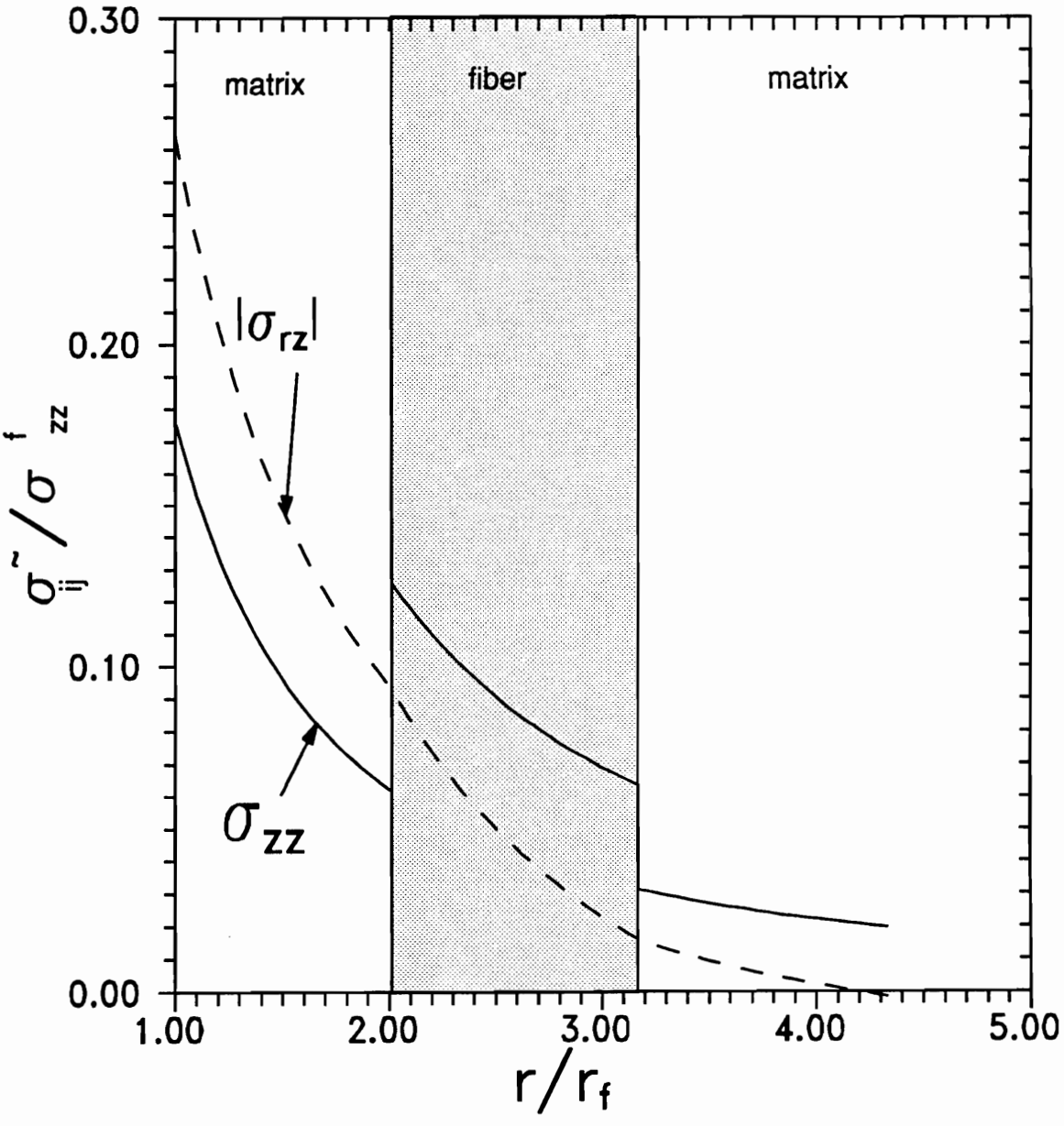

Figure 42. Stress vs Position (MMC): Plot of normalized stress versus normalized radial distance for axial stress ($z = 0$) and absolute value of shear stress ($z = 1/\lambda$) in SiC/Al MMC for $v_f = 0.40$ and $r_c = r_f$.

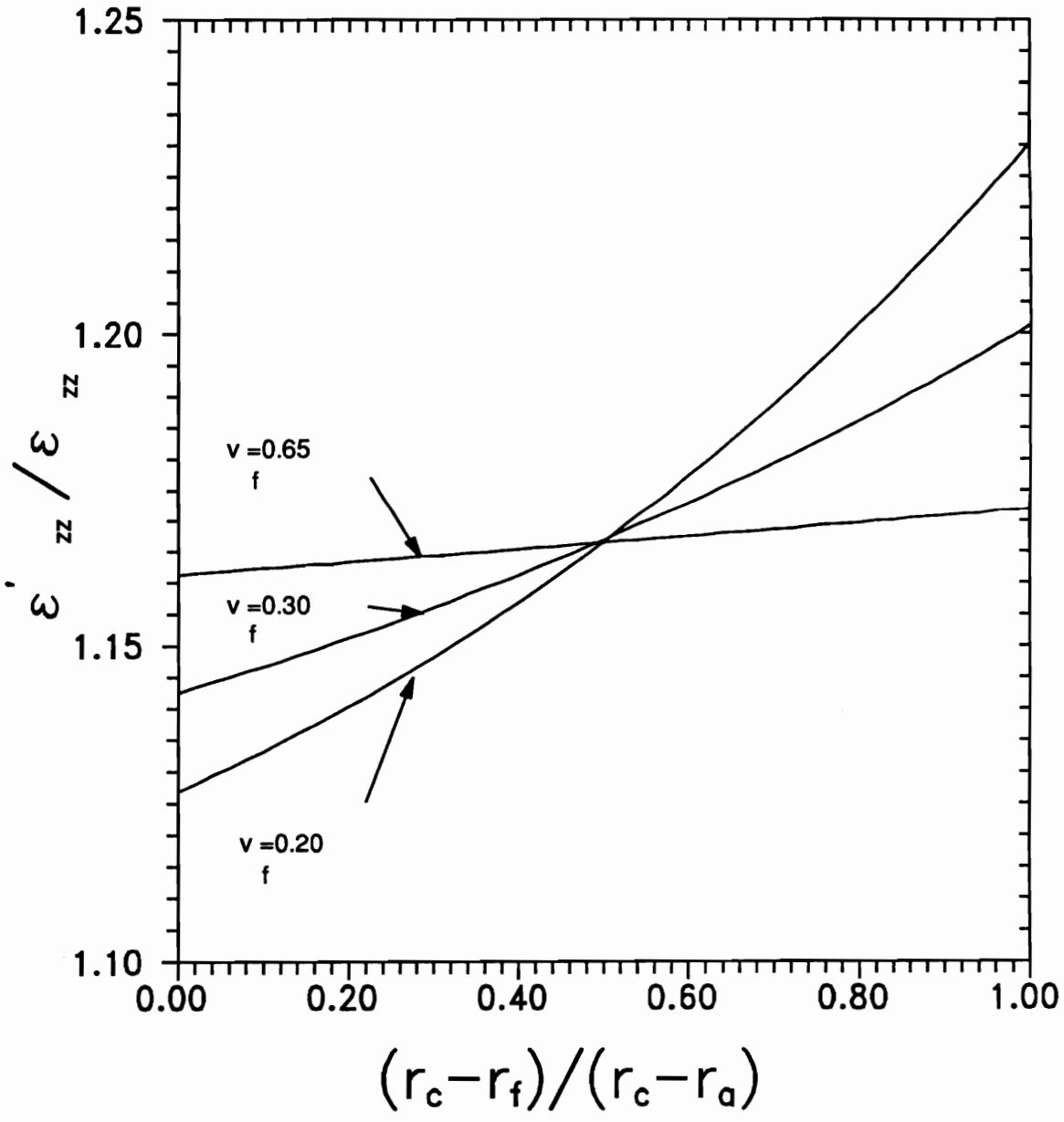

Figure 43. Strain Concentration vs Crack Size: Figure depicting the variation of average strain concentration ($z=0$ and $r_c = r_f$) on an adjacent fiber as a function of normalized crack radius for three fiber volume fractions in a glass/epoxy composite.

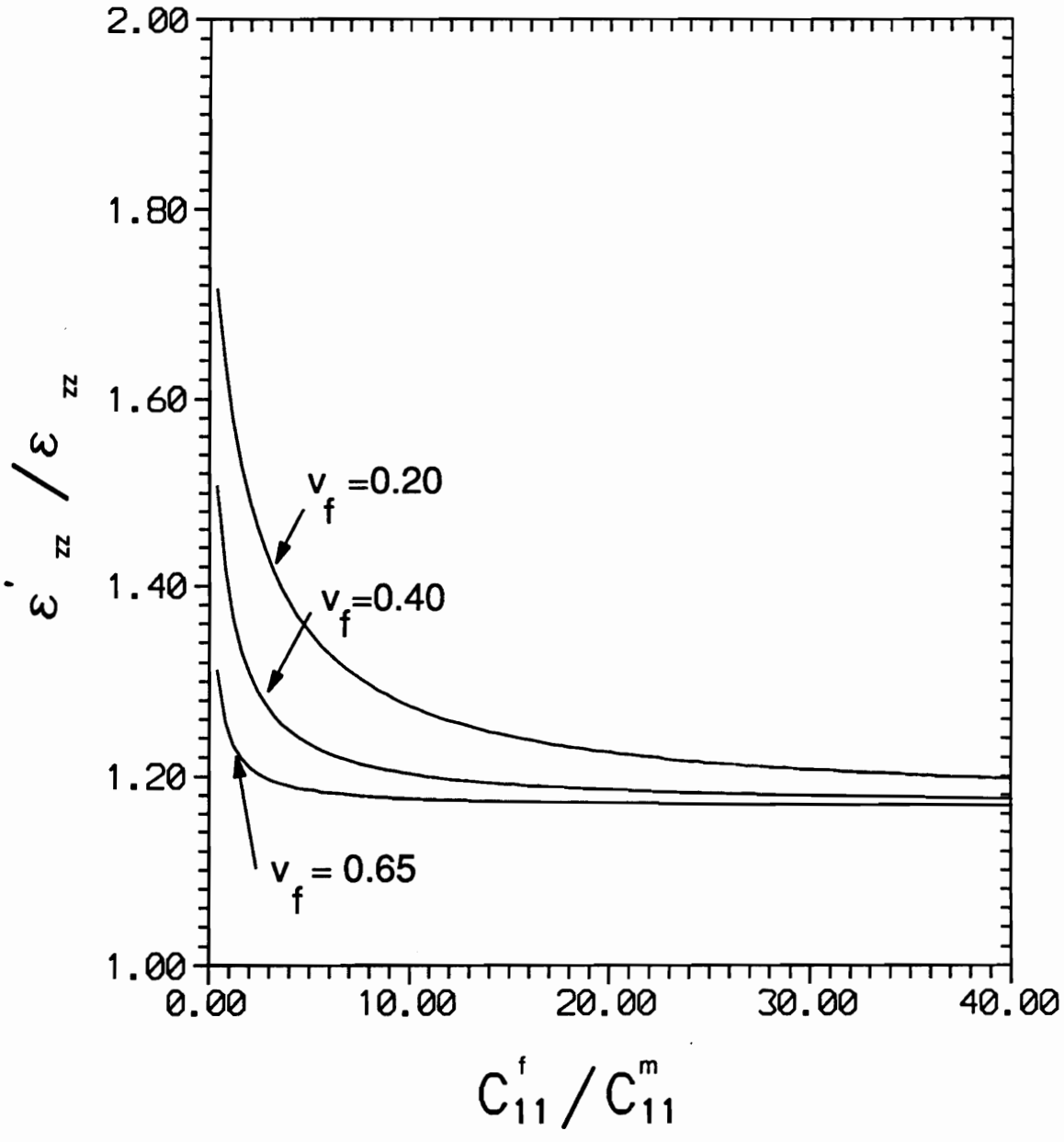

Figure 44. Strain Concentration vs Stiffness Ratio (large crack): Plot of average strain concentration on an adjacent fiber ($z=0$ and $r_c = r_a$) versus fiber/matrix stiffness ratio for three fiber volume fractions.

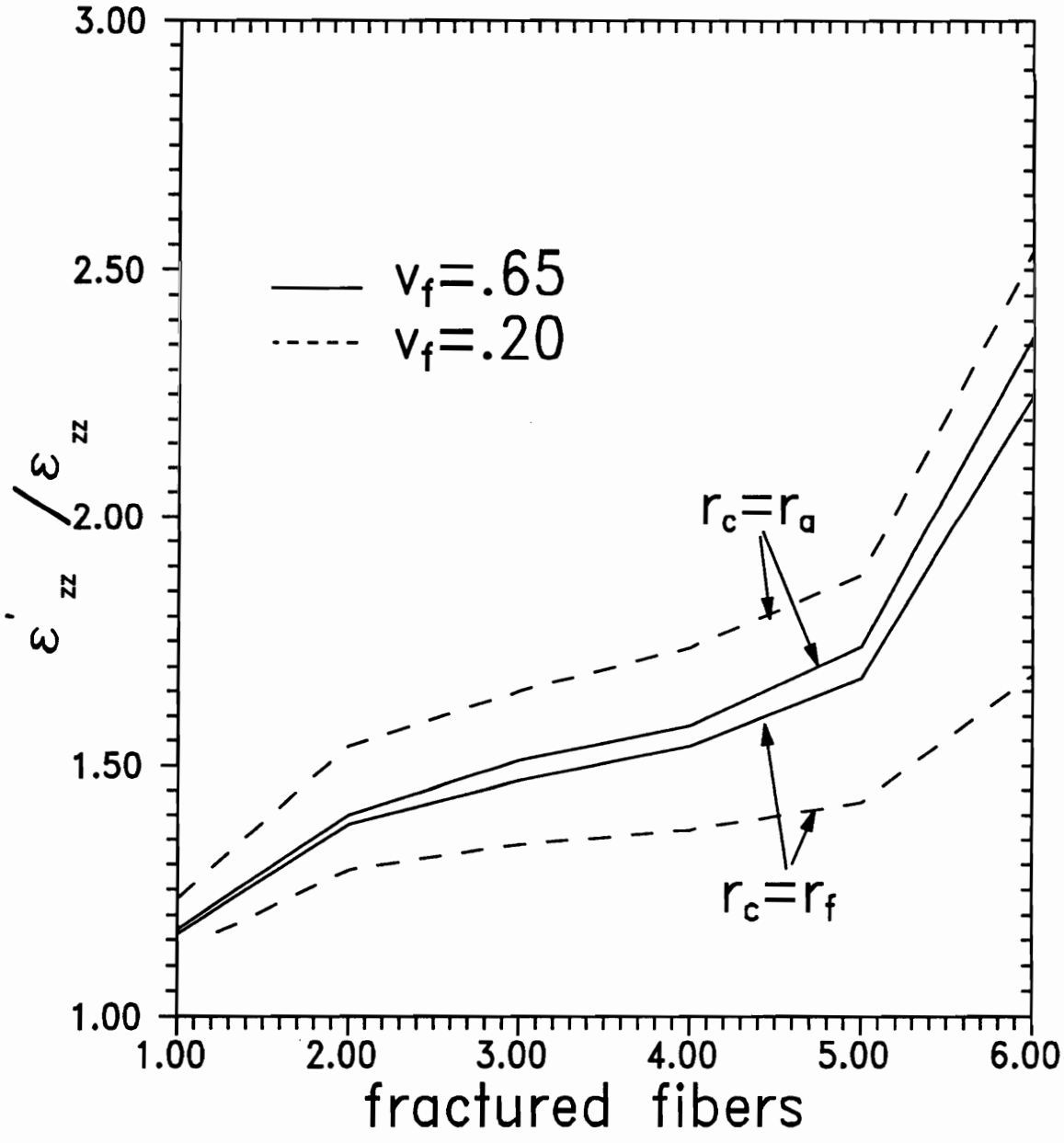

fig. 25

Figure 45. Strain Concentration vs Fractured Fibers: Figure representing the influence of the number of fractured fibers on the largest average strain in a glass/epoxy system for two different fiber volume fractions and crack radiuses.

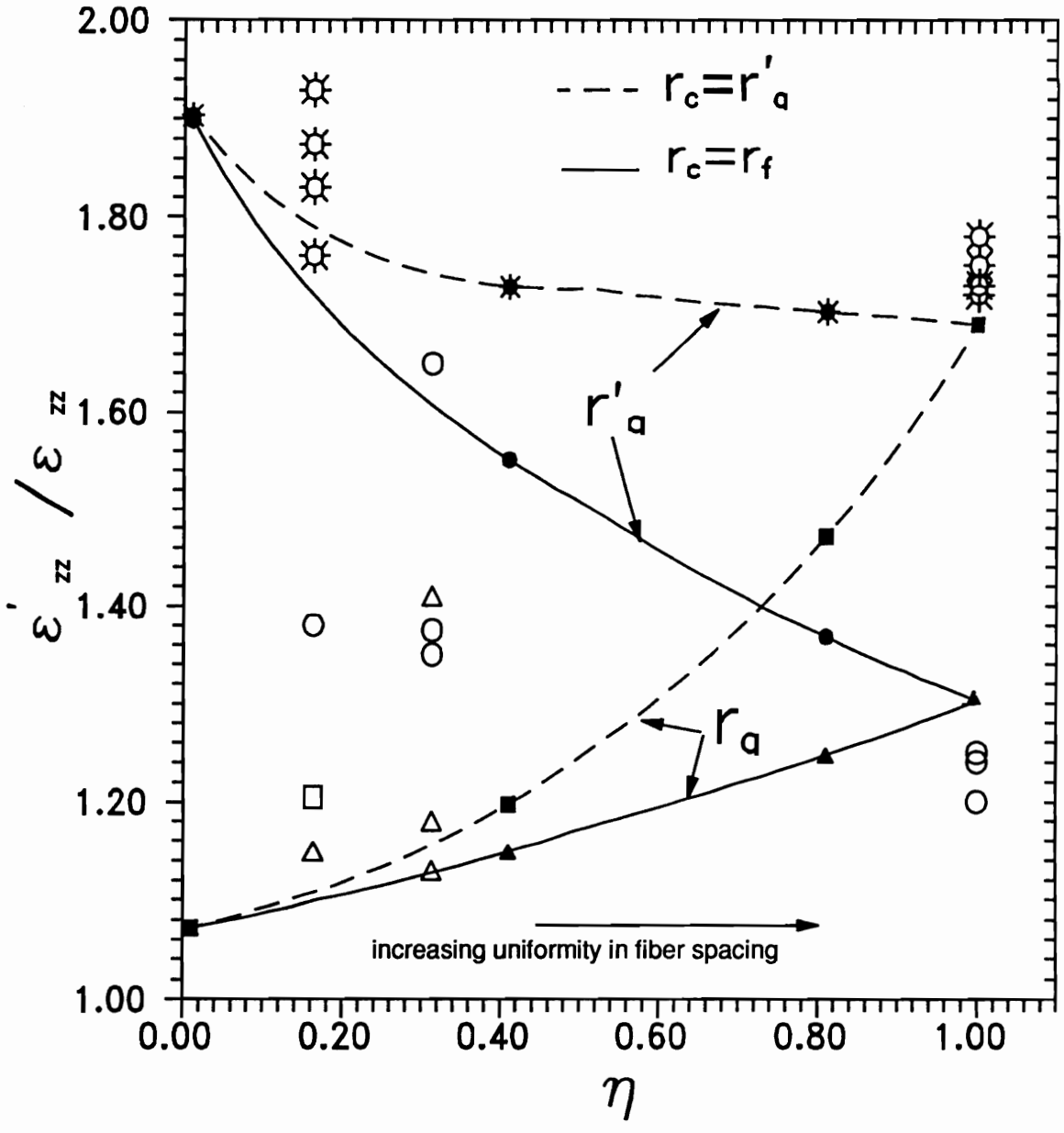

Fig. 26.

Figure 46. Strain Concentration vs Eccentricity Parameter (experimental): Comparison of strain concentration values (z=0 at distinct values of r) obtained experimentally and theoretically as a function of the eccentricity parameter for two different crack sizes. The experimental data in this figure is represented by the hollow symbols.

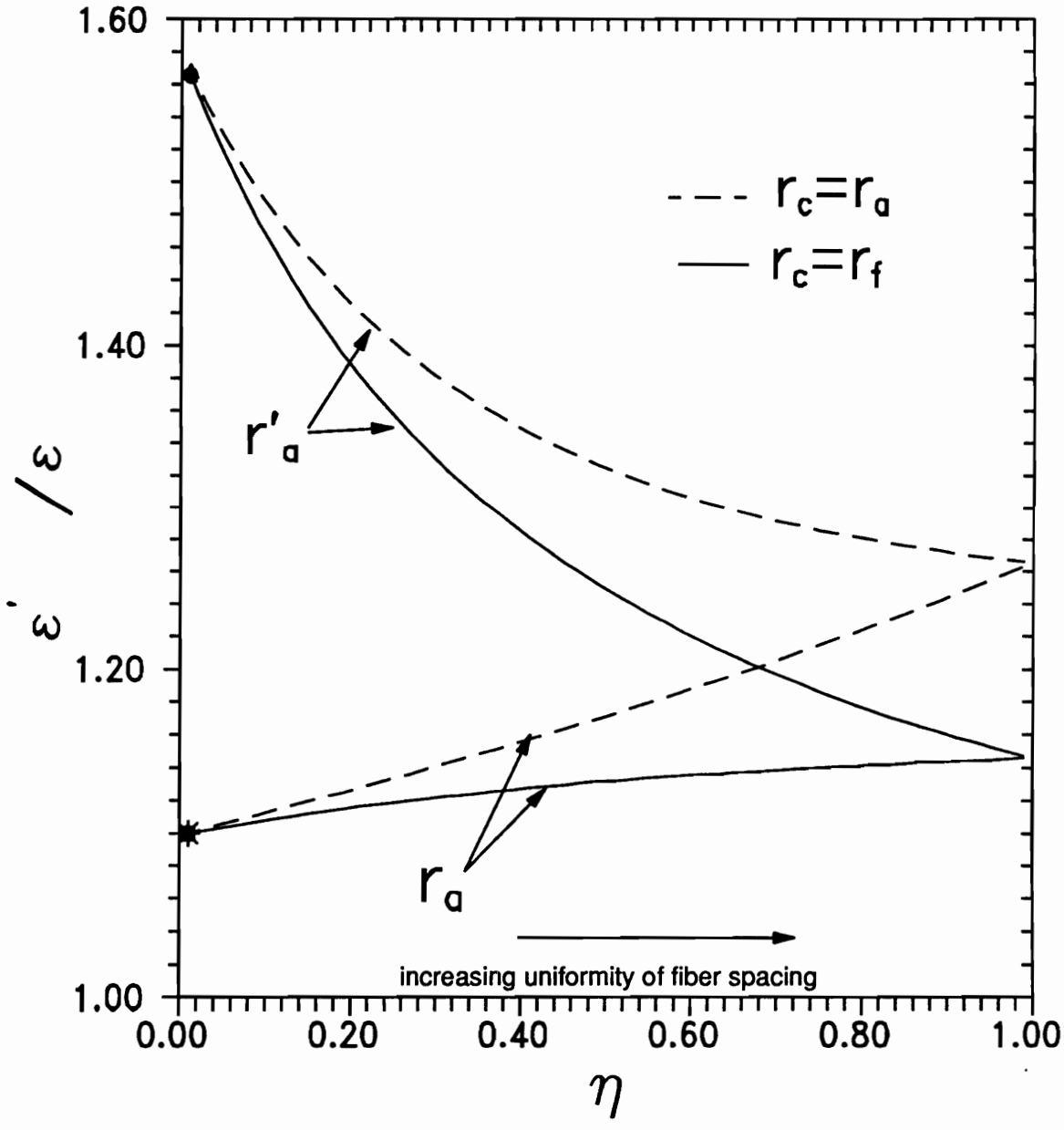

Figure 47. Strain Concentration vs Eccentricity Parameter (20%): Figure displaying the functional dependence of strain concentration (z = 0 and distinct values of r) on eccentricity parameter η for a glass/epoxy composite $v_f = 0.20$ for two different crack sizes and locations.

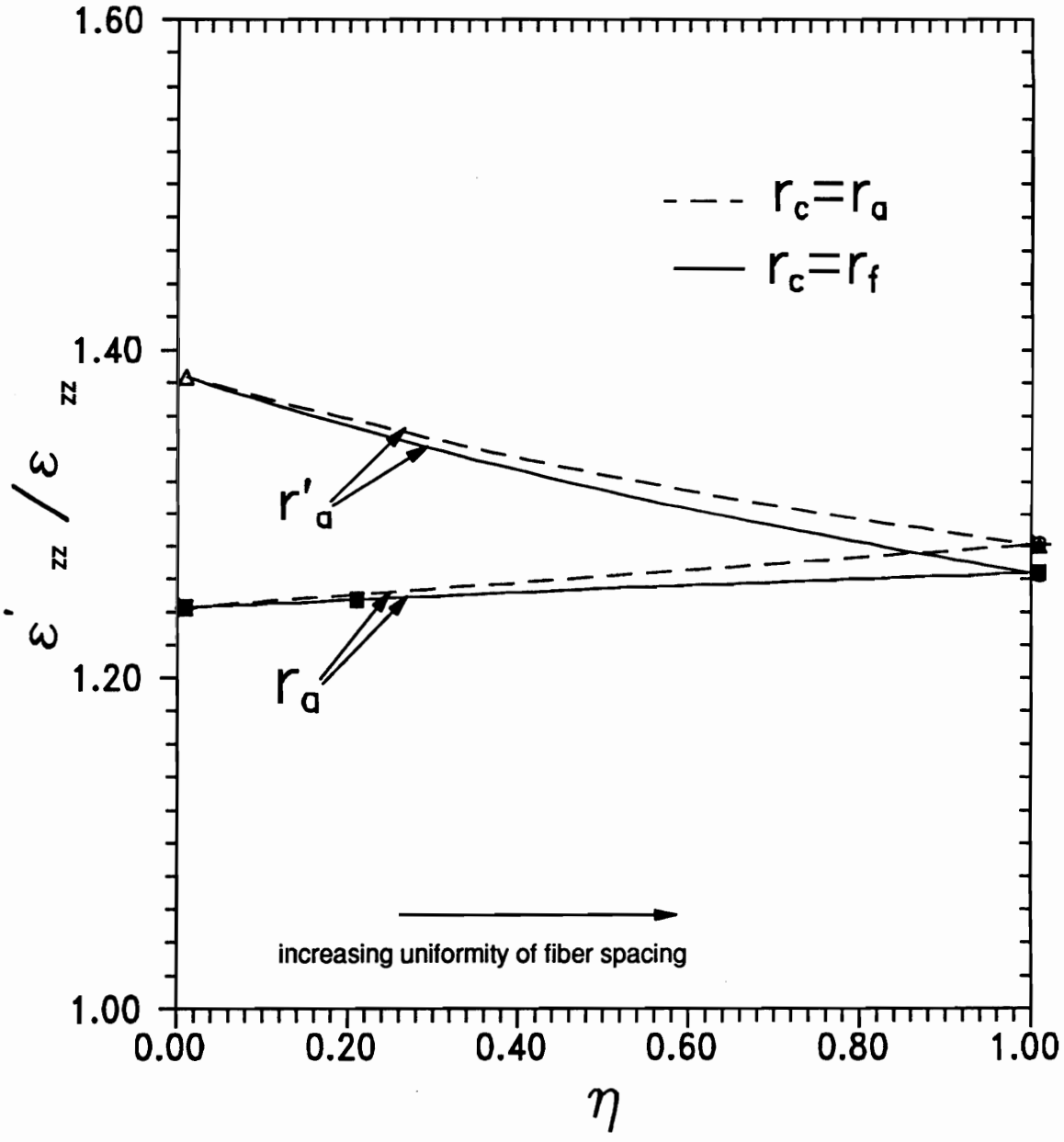

Figure 48. Strain Concentration vs Eccentricity Parameter (65%): Figure displaying the functional dependence of strain concentration ($z=0$ and distinct values of r) on eccentricity parameter η for a glass/epoxy composite $v_f = 0.65$ for two different crack sizes and locations.

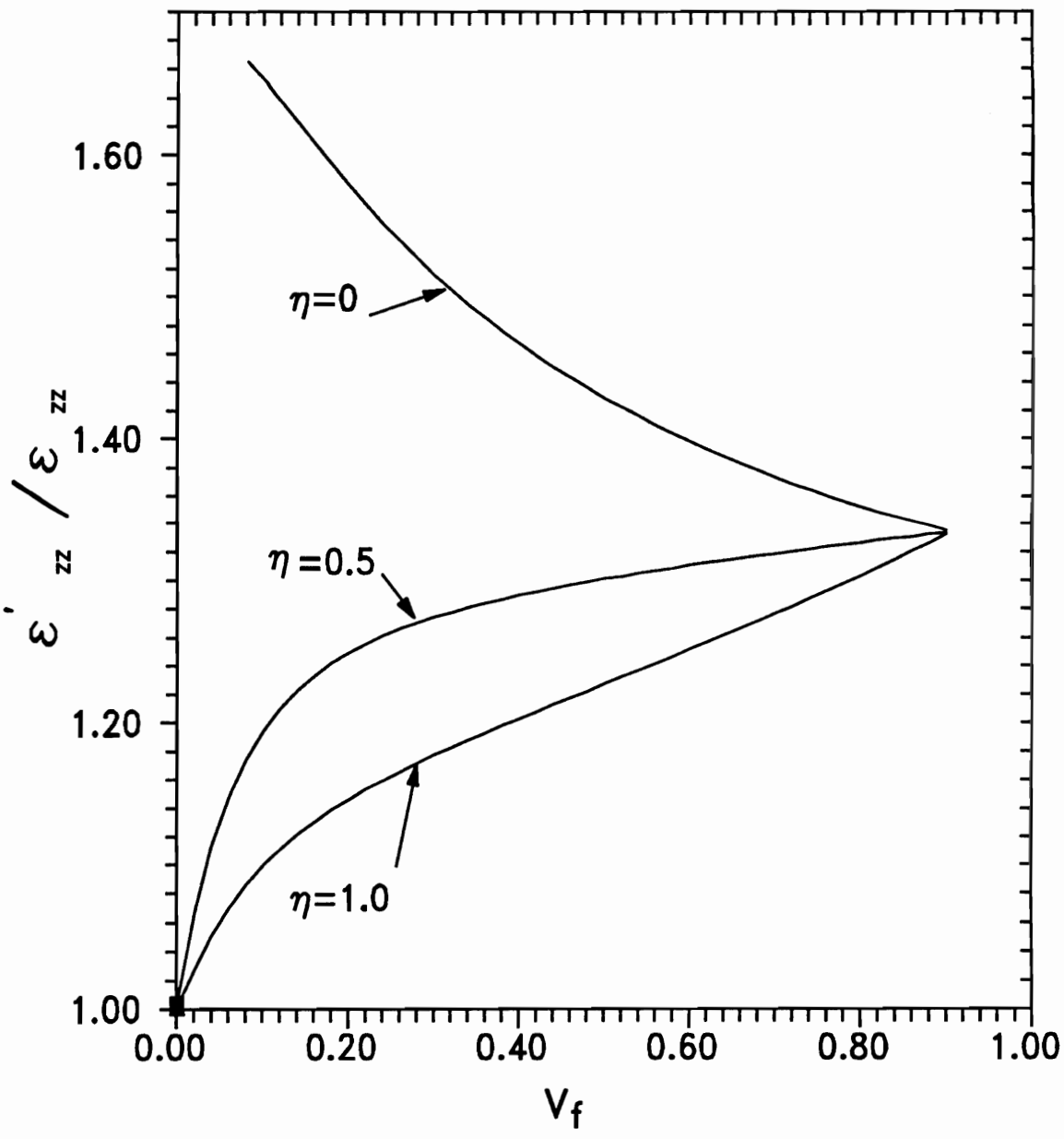

Figure 49. Strain Concentration vs Fiber Volume Fraction (eccentricity): Plot depicting the the functional dependence of strain concentration ($z=0$, $r = r_{a}$, and $r_c = r_f$) on fiber volume fraction for a glass/epoxy system for three different eccentricity parameters.

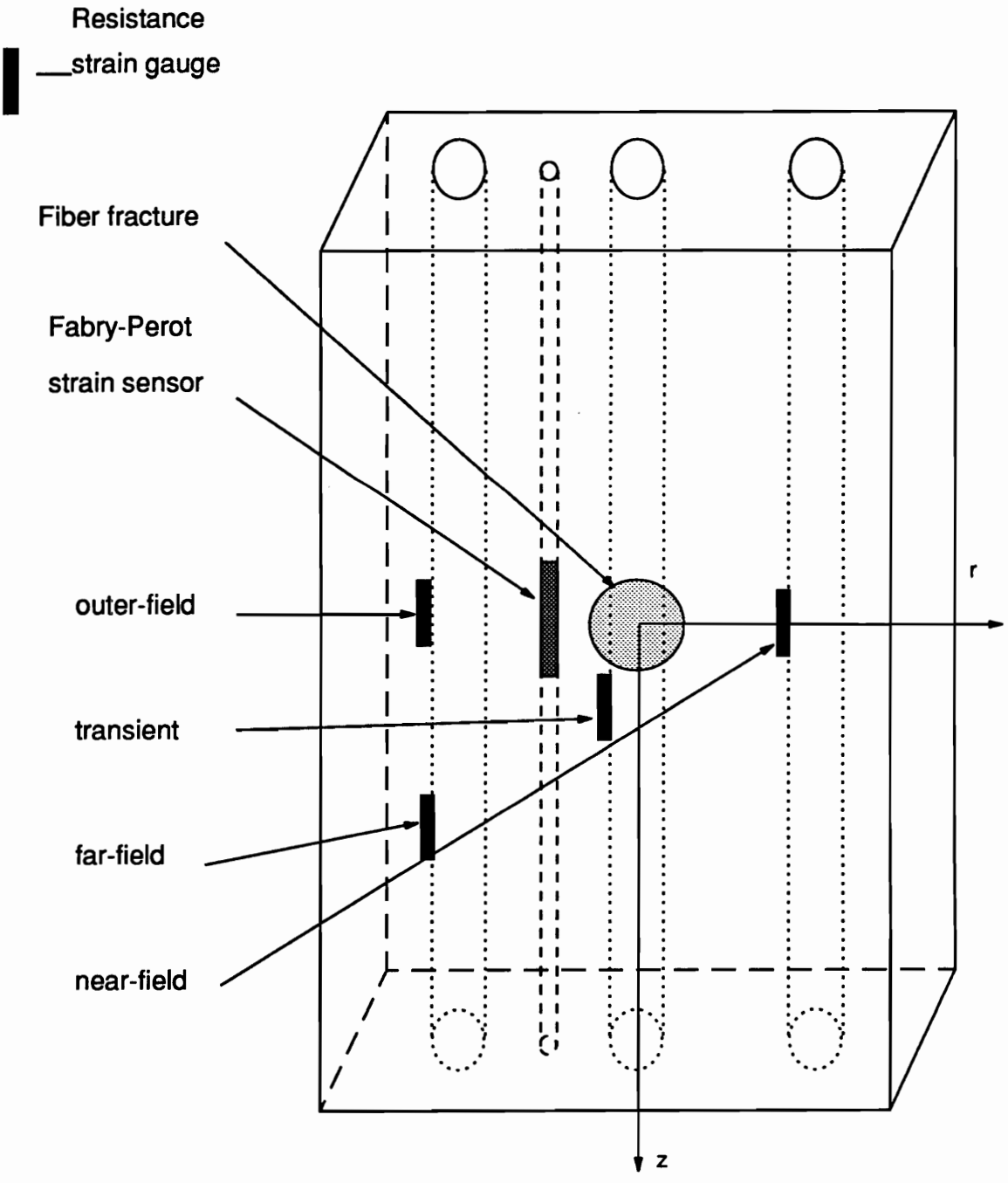

Model Composite Drawing: Illustration of the model composite with embedded strain sensors and their respective locations.

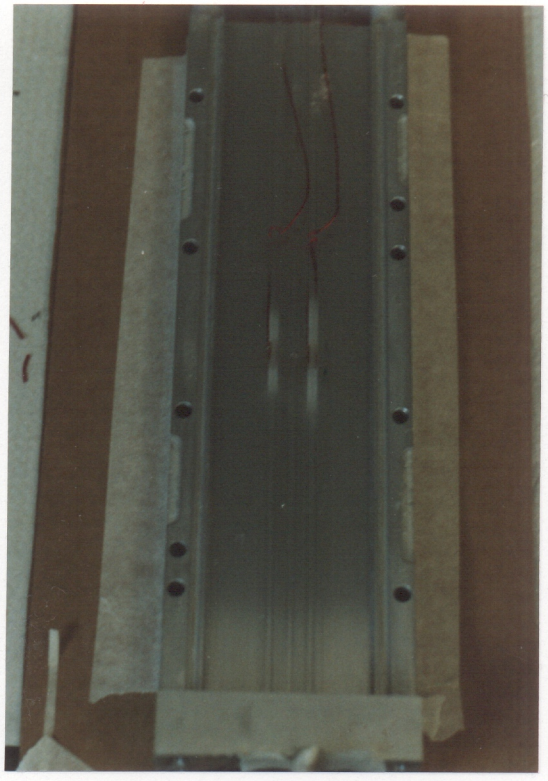

Figure 51. Embedded Sensors: Photograph of the internal strain sensors and the structural fibers placed in the mold during the manufacturing process.

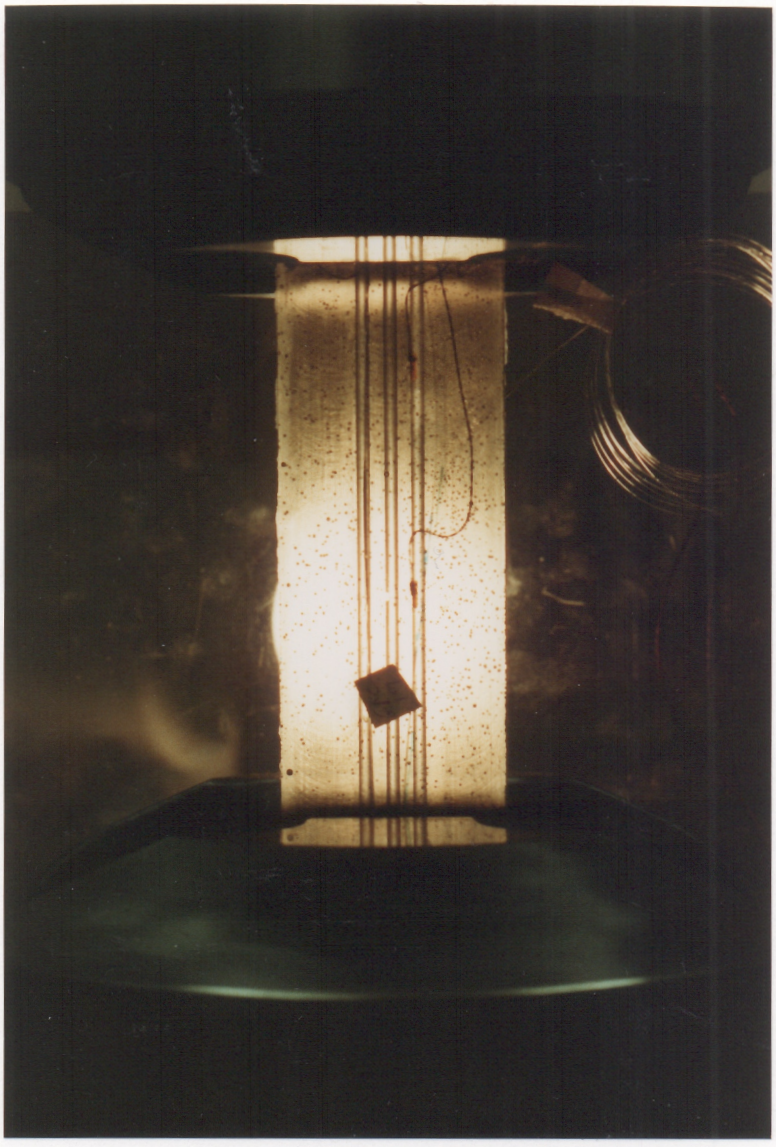

Figure 52. Model Composite Photograph: Typical photograph of a manufactured model composite containing internal strain sensors.

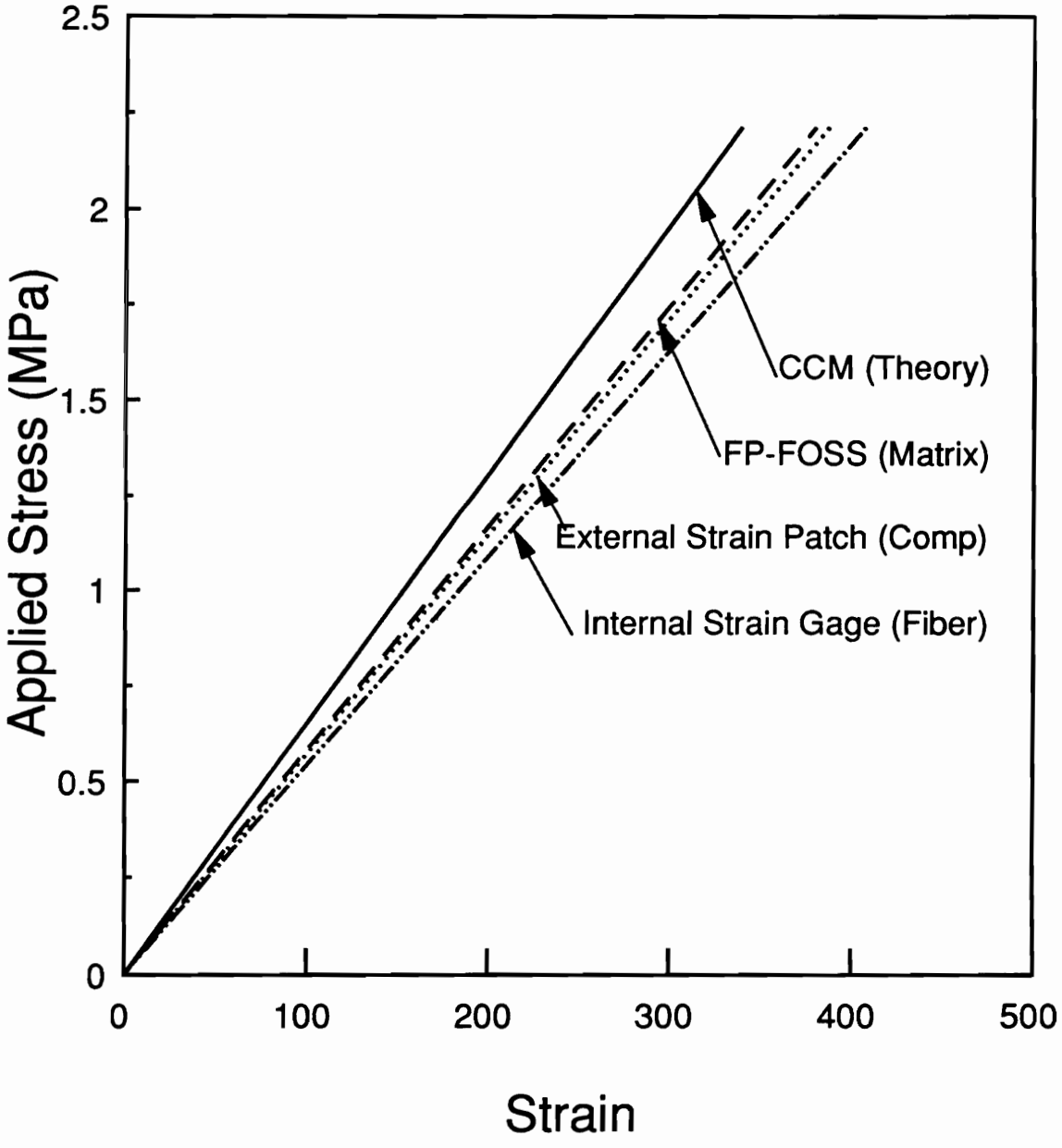

Figure 53. Internal Sensor Validation: Comparison of strain measurements obtained from an external strain patch, an internal strain gauge, and a fiber optic strain sensor to a theoretical prediction from a CCM model.

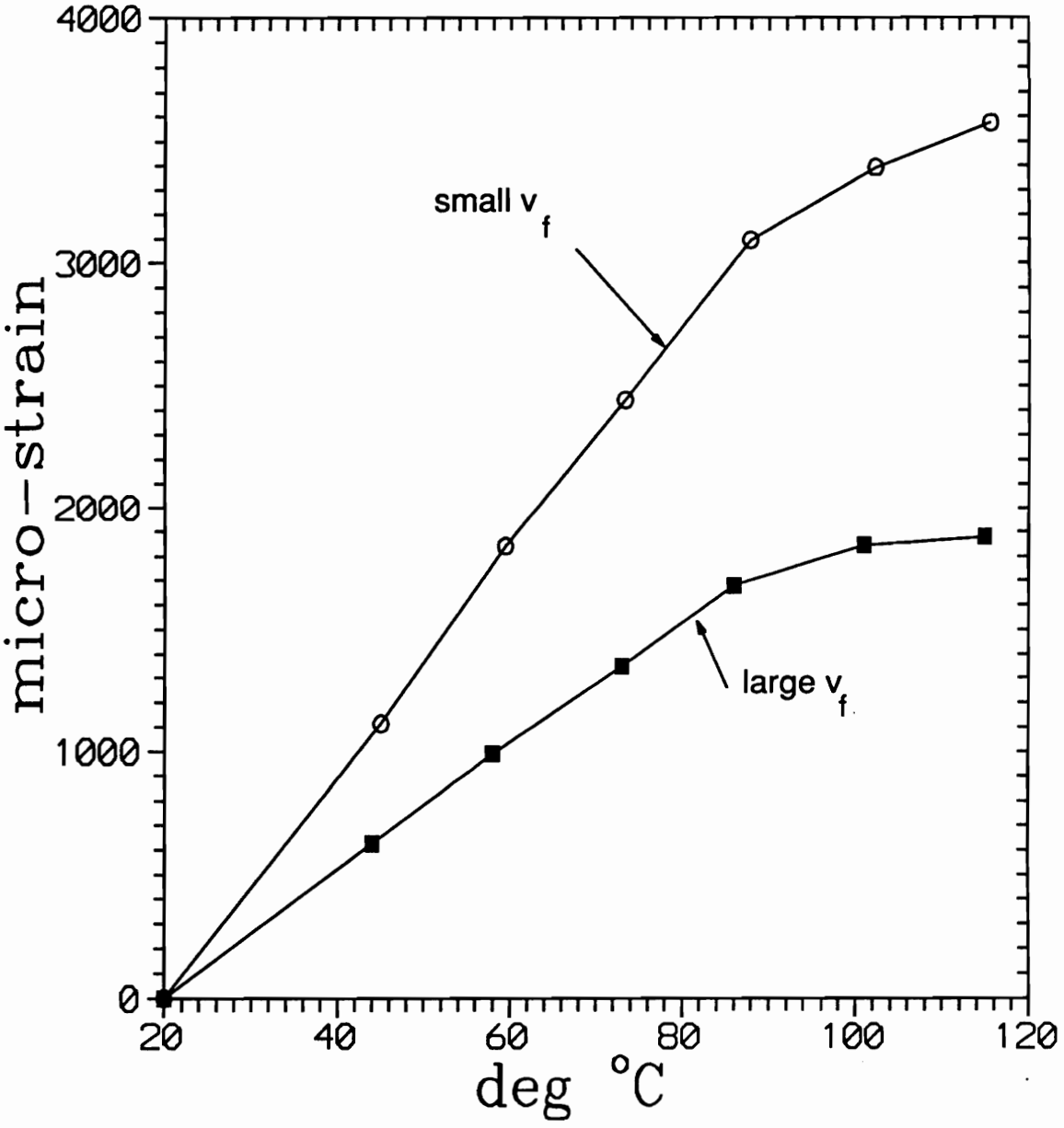

Figure 54. Strain vs Temperature: Strain temperature plot generated from data obtained with embedded resistance gauges for a single and three fiber model composite.

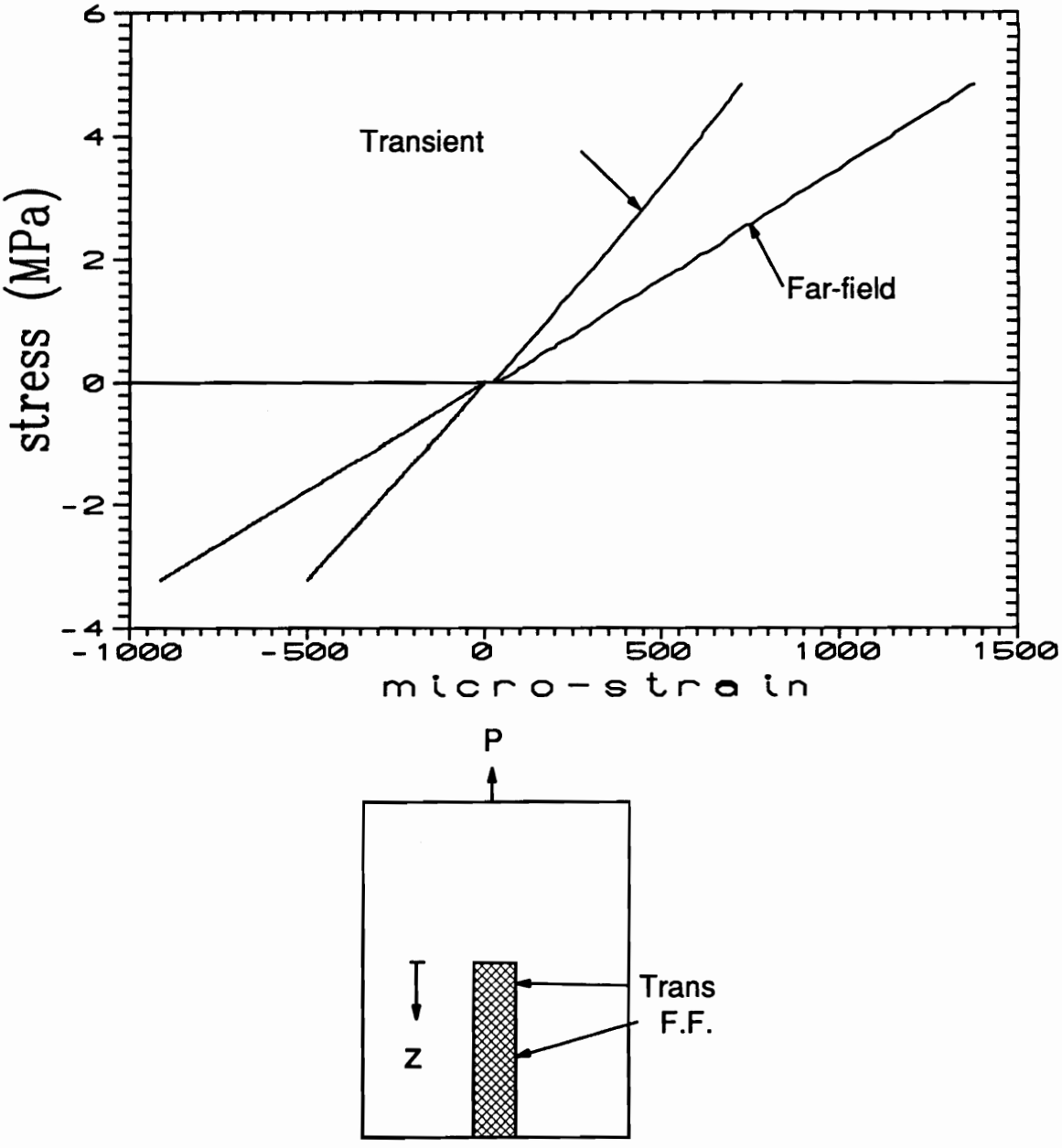

Figure 55. Stress vs Strain: Stress strain plot using the data obtained form embedded resistance gauges for a short fiber composite with the transient gauge at x=4.8 mm.

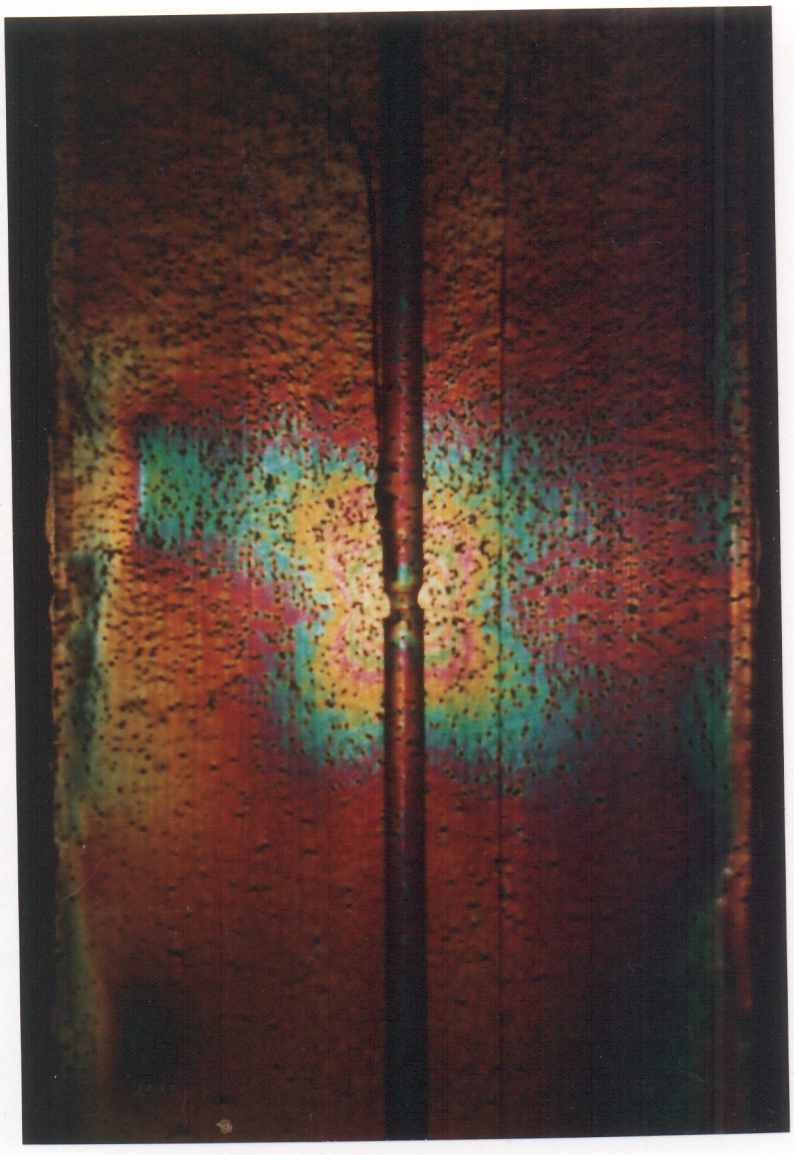

Figure 56. Stress Redistribution (single fiber system): Representative picture of the stress redistribution caused by a fiber fracture in a single fiber model composite.

Figure 57. Small Crack Size: Photograph depicting crack arrest at the fractured fiber matrix interphase ($r_c = r_f$).

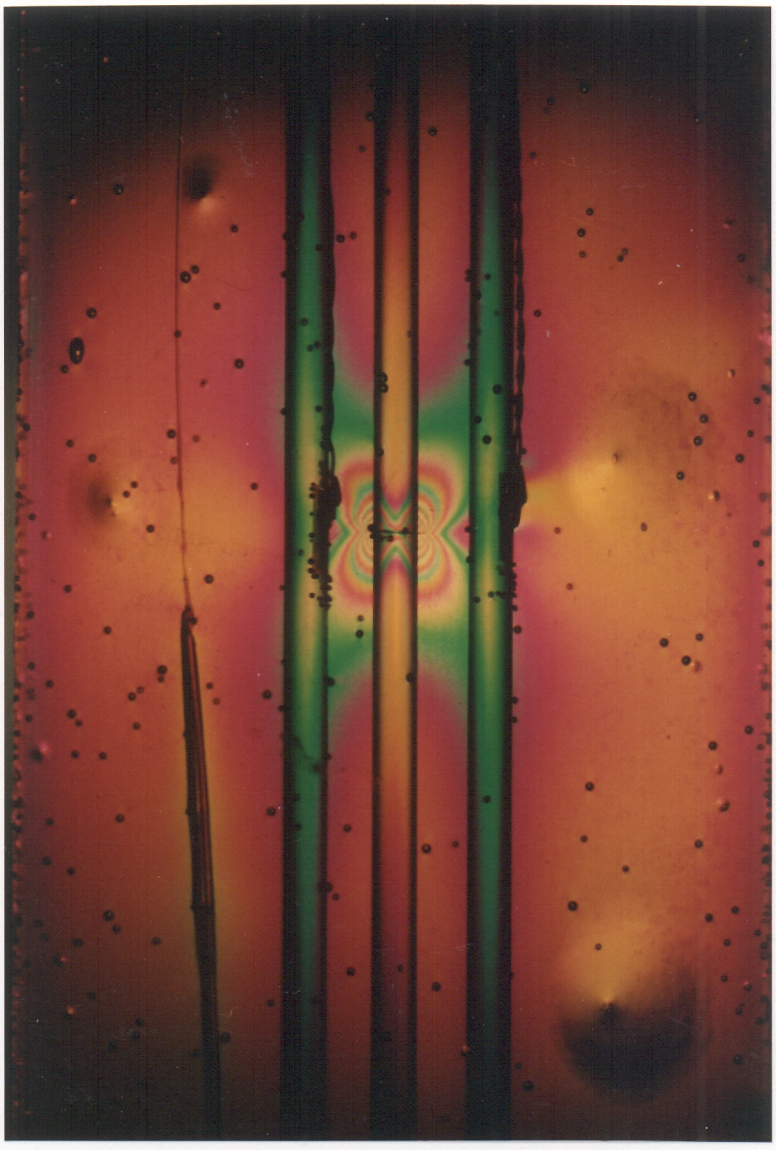

Figure 58. Stress Redistribution (small crack; 15%): Representative photograph of the stress redistribution in a model composite due to a fiber fracture ($r_c = r_f$ and $v_f = 0.15$).

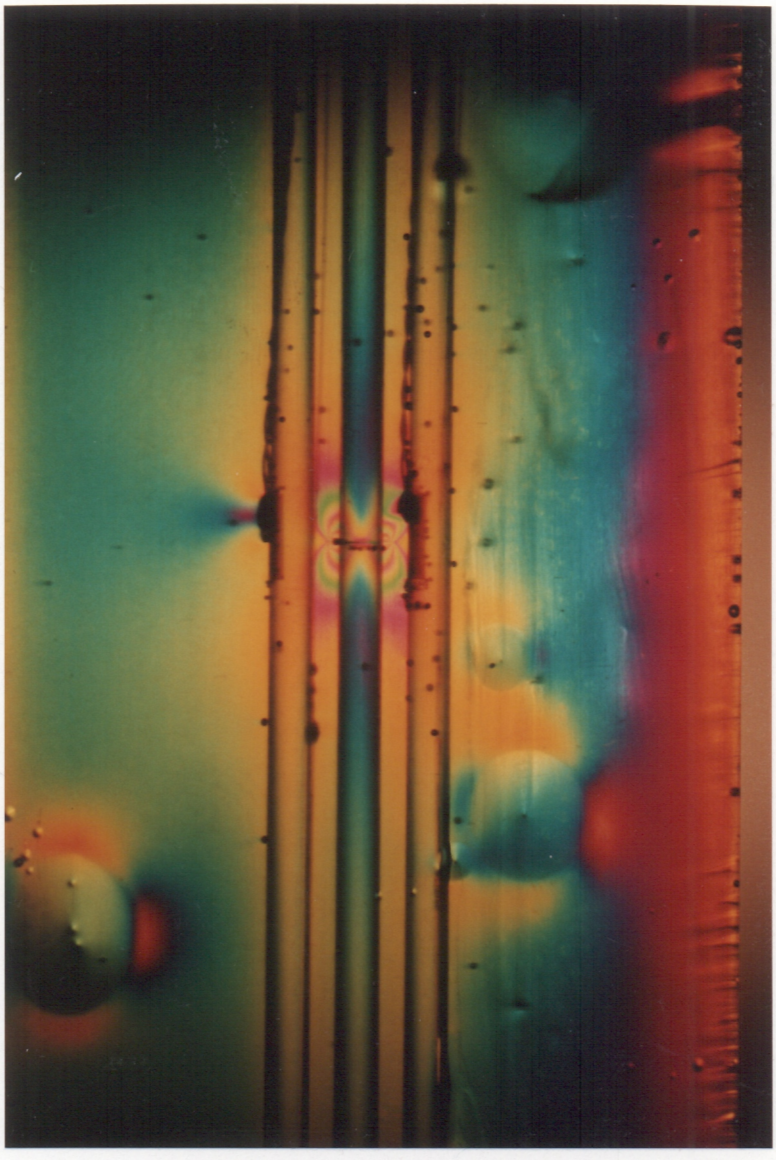

Figure 59. Stress Redistribution (small crack; 20%): Representative photograph of the stress redistribution in a model composite due to a fiber fracture ($r_c = r_f$ and $v_f = 0.20$).

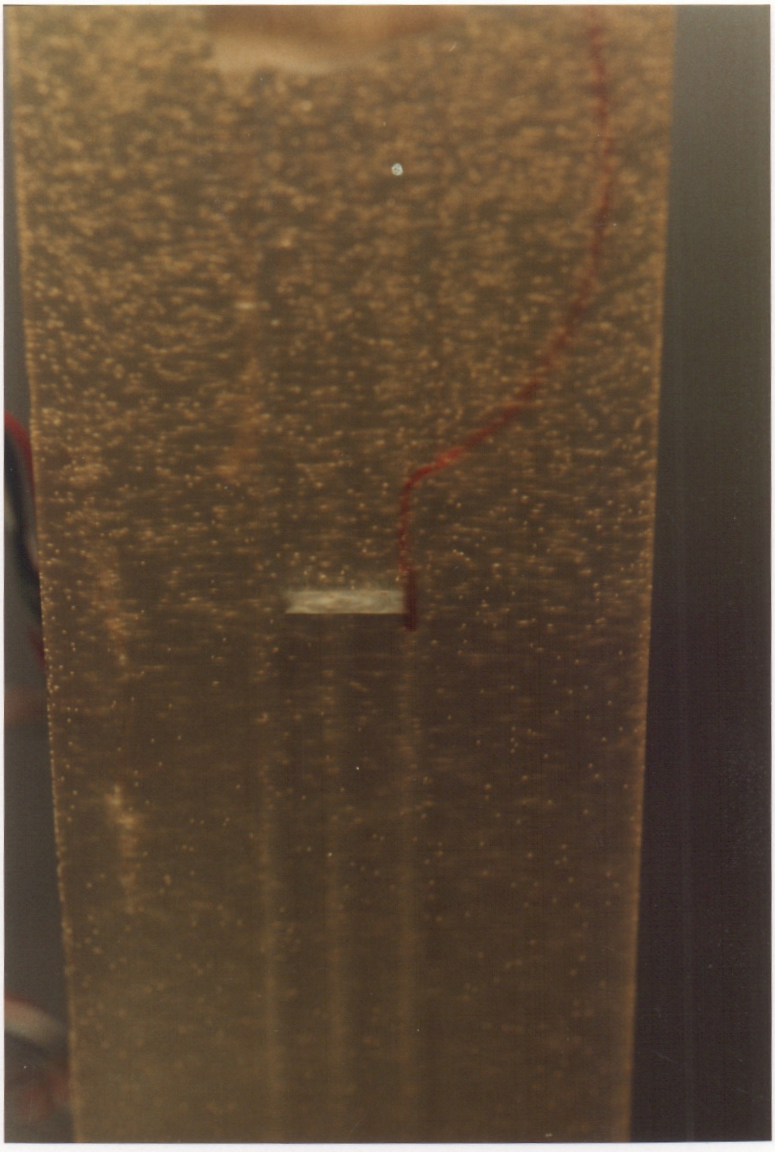

Figure 60. Large Crack Size: Photograph depicting crack arrest at the adjacent fiber matrix interphase ($r_c = r_e$).

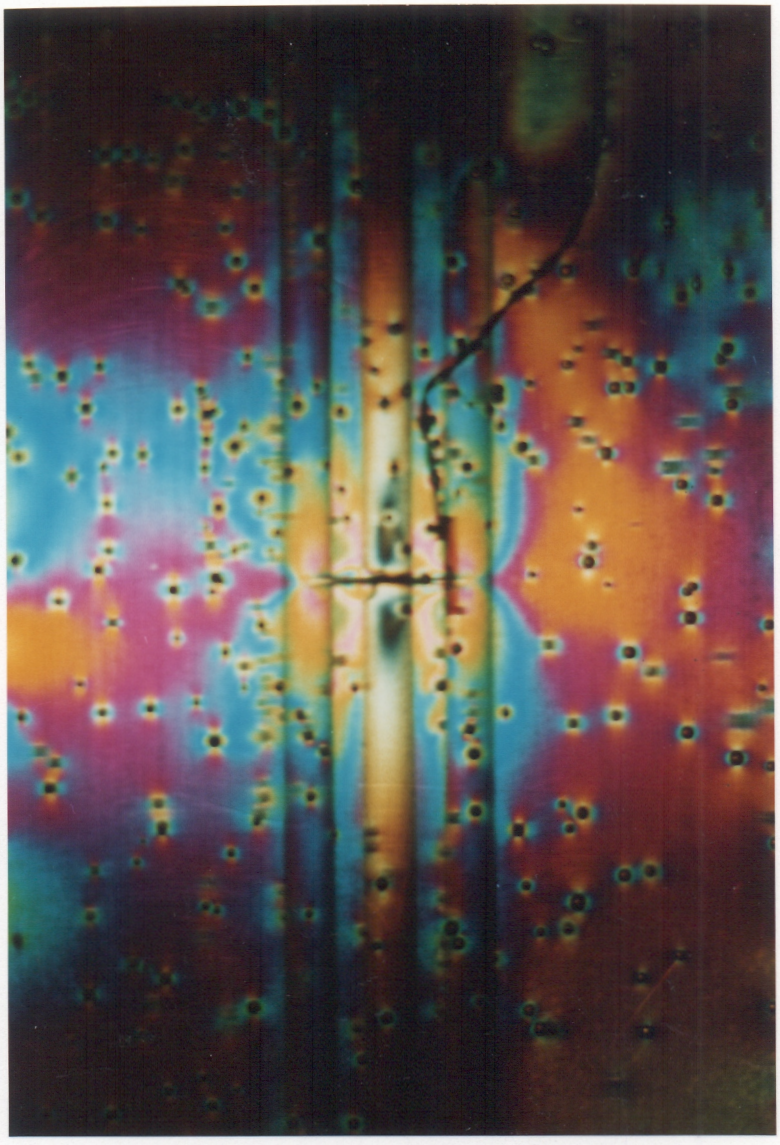

Figure 61. Stress Redistribution (large crack): Representative photograph of the stress redistribution in a model composite due a to fiber fracture ($r_c = r_a$ and $v_f = 0.15$).

Figure 62. Stress Redistribution (six fiber system): Representative figure of a six fiber model composite containing a single fiber fracture ($r_c = r_f$).

Figure 63. Stress Redistribution (two fiber fractures): Representative figure of a six fiber model composite containing two fiber fractures ($r_c = r_f$).

Figure 64. Stress Redistribution (four fiber fractures): Representative figure of a six fiber model composite containing four fiber fractures ($r_c = r_a$).

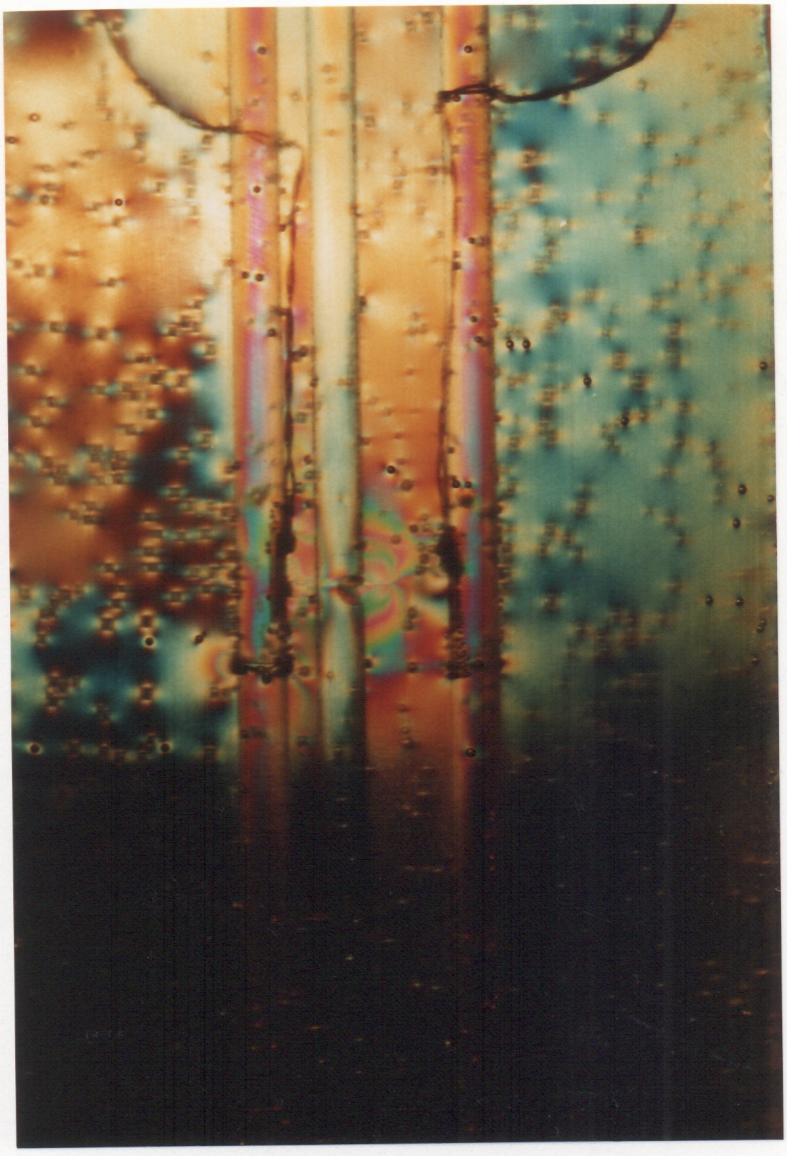

Figure 65. Stress Redistribution (variable fiber spacing): Representative figure depicting the stress redistribution around a fiber fracture in a model composite containing variable fiber spacing.

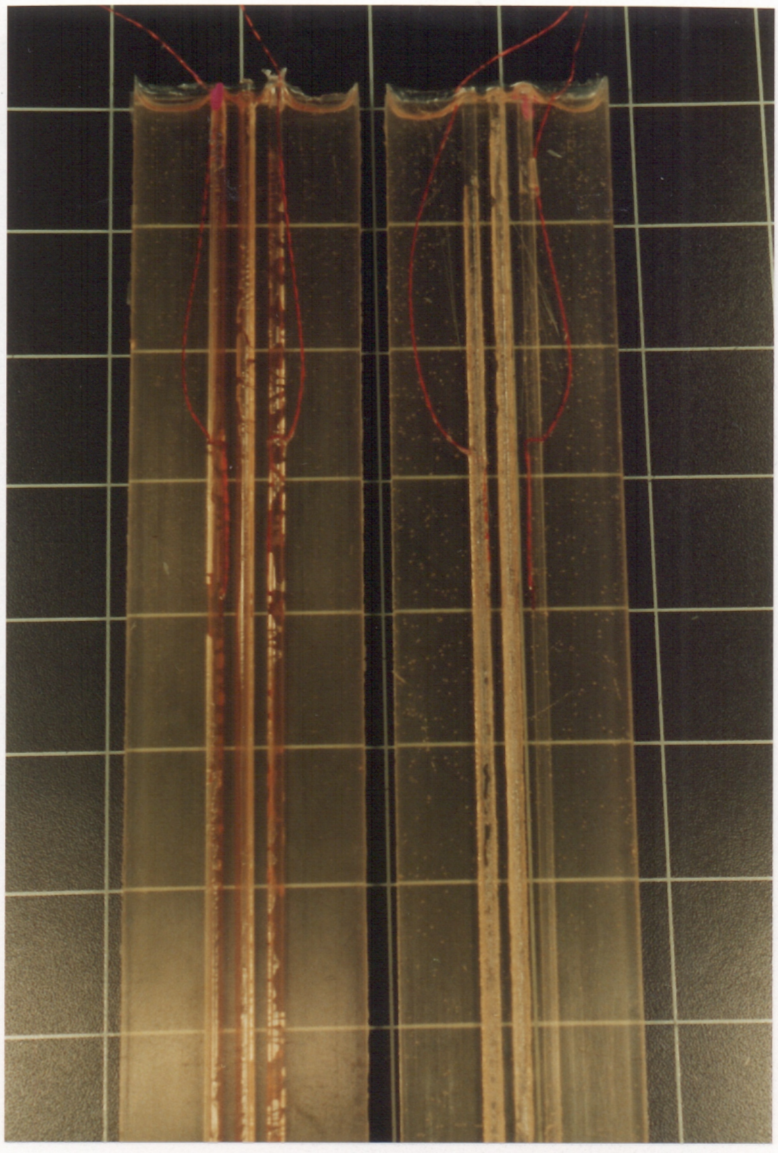

Figure 66. Interphase Coatings: Picture depicting composites manufactured with interphases. The composite on the right depicts an epoxide coated fibers system (fiber on extreme right in this composite has a different amount of hardener added to the epoxide), while the composite on the left depicts a BMI coated fiber system.

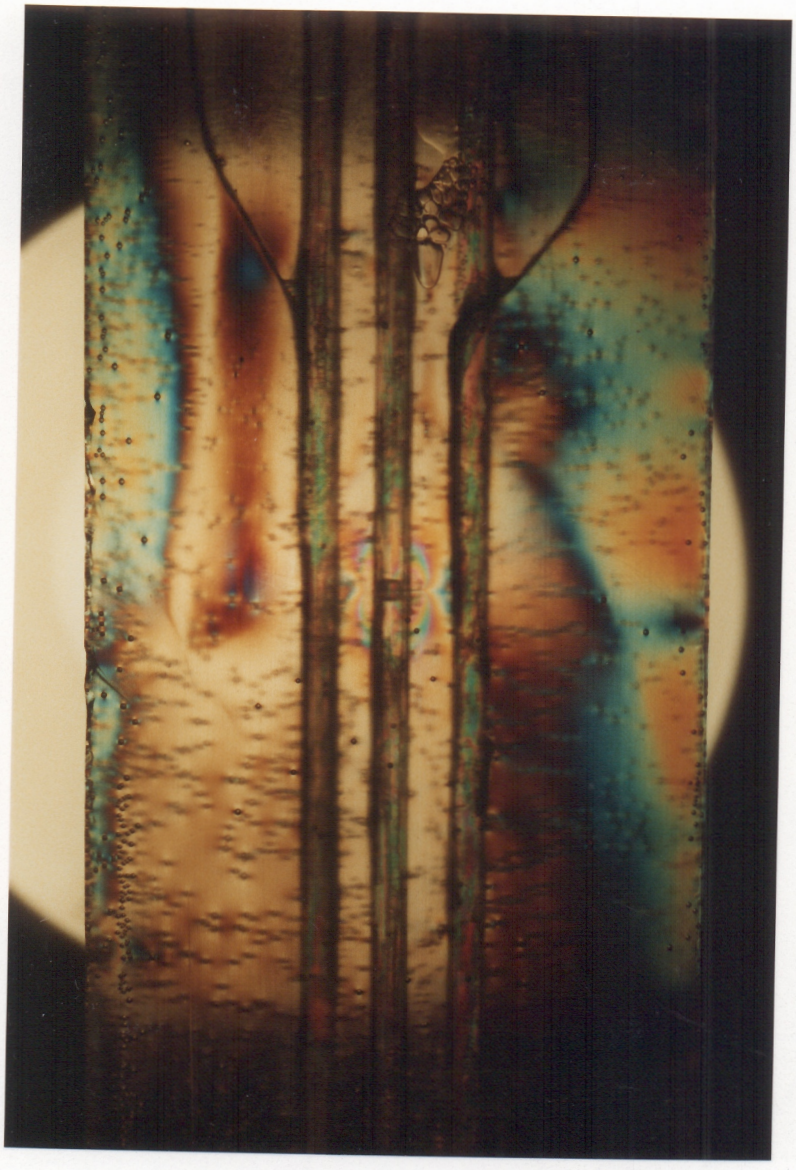

Figure 67. Stress Redistribution (PES coating): Representative illustration of the stress redistribution around a fiber fracture in a model composite containing fibers coated with PES.

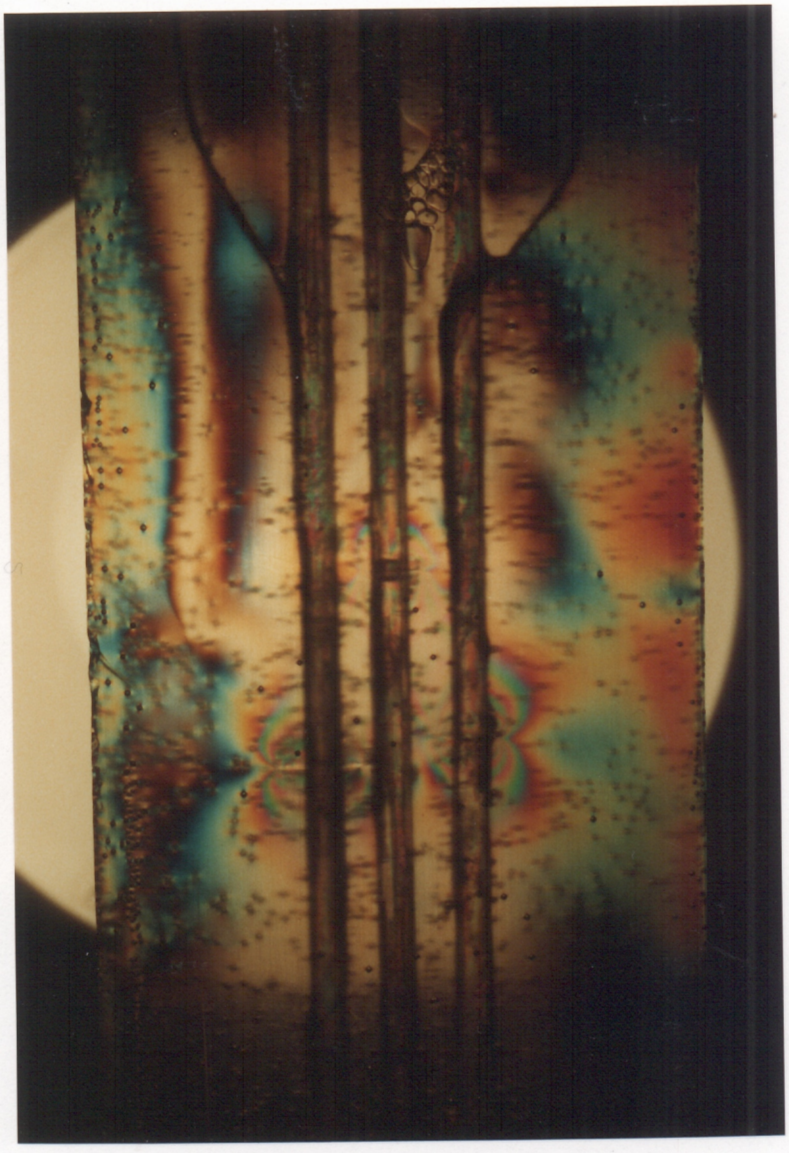

Figure 68. Stress Redistribution PES (stair-casing): Representative illustration of the stress redistribution in a model composite containing with PES coated fibers depicting the evolution of stair-casing fiber fractures.

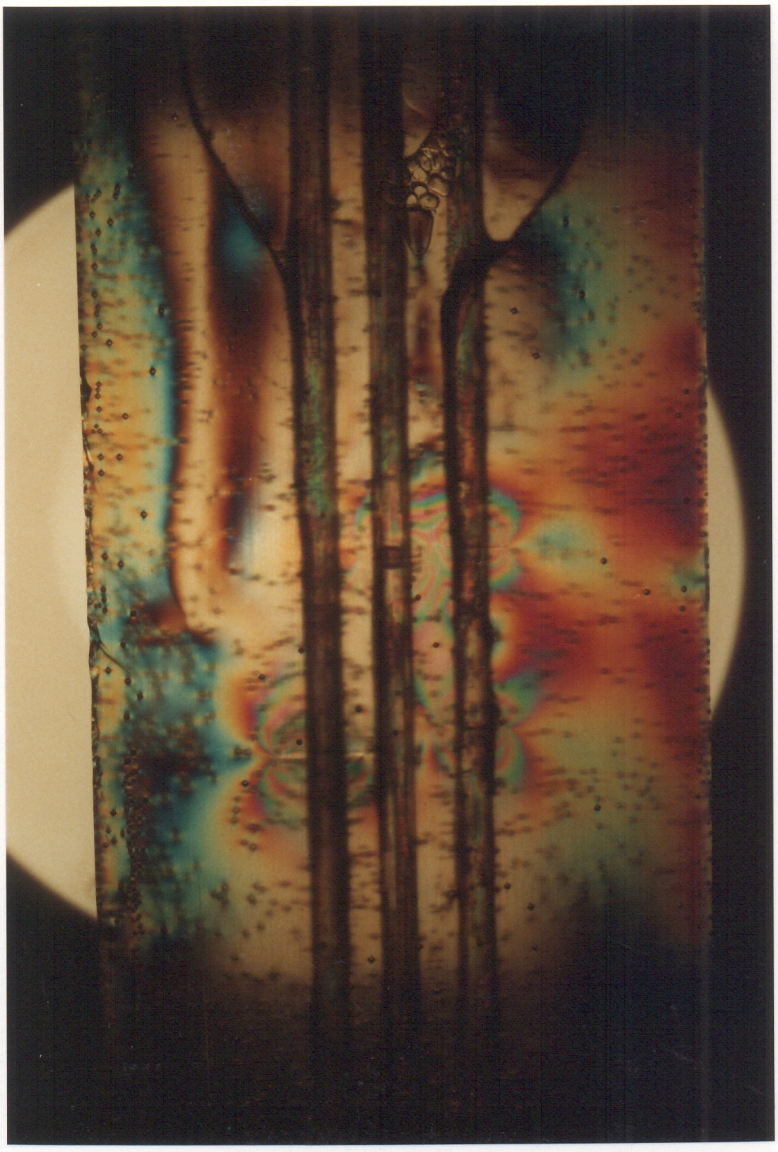

Figure 69. Stress Redistribution PES (stair-casing): Representative illustration of the stress redistribution in a model composite containing with PES coated fibers depicting the evolution of stair-casing fiber fractures.

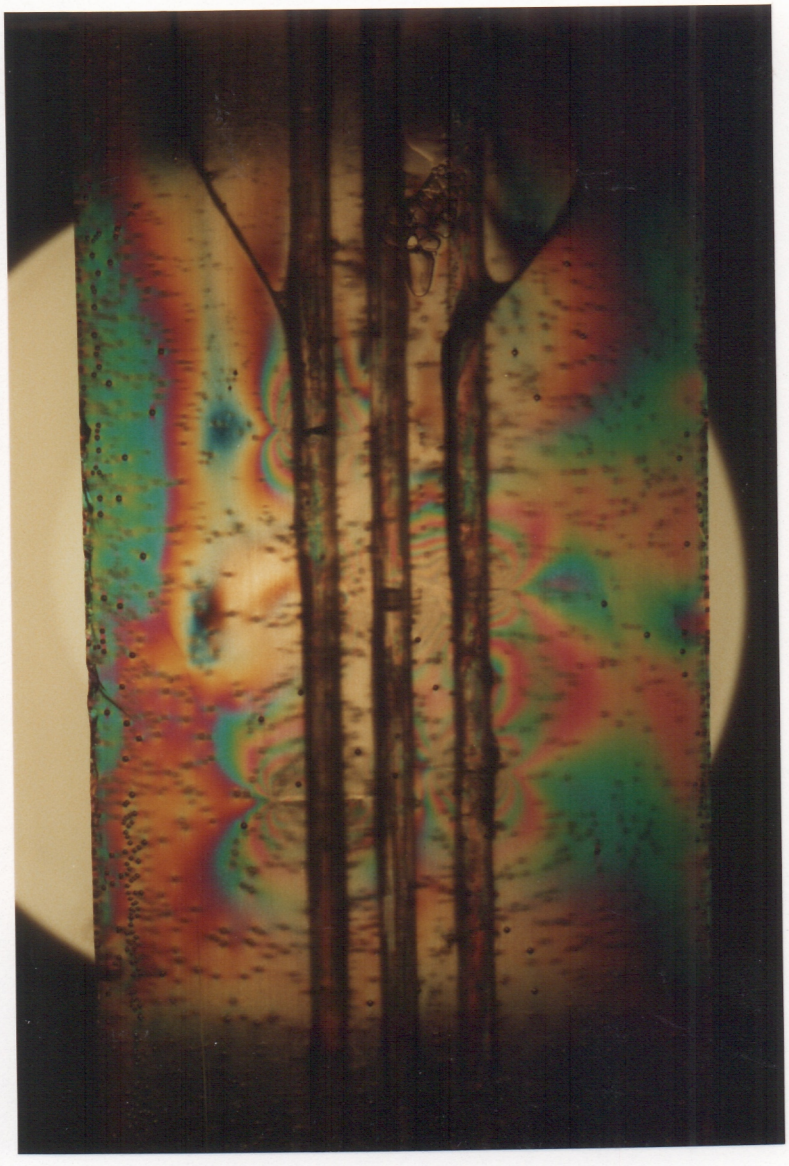

Figure 70. Stress Redistribution PES (stair-casing): Representative illustration of the stress redistribution in a model composite containing with PES coated fibers depicting the evolution of stair-casing fiber fractures.

Table 1. Mechanical properties of the polymeric matrix composite constituents used in the theoretical calculations.

Material	Tensile modulus E_{11} (GPa)	Shear modulus G_{12} (GPa)	Poisson's ratio ν_{12}
Epoxy	2.5	0.93	0.35
Epon 828	3.2	1.20	0.35
Steel	190.0	73.07	0.30
Copper	105.0	40.38	0.30
E-glass	71.2	29.20	0.22

Table 2. Measured fiber orientations from the experimental data of Kacir et al [41] for a 50% volume fraction E-glass fiber in epon-828 matrix.

fiber angle $\pm\omega$	composite a	b	c	d	e	f	g	h
	percent of fibers at $\pm\omega$ in composite							
0	3.2	18.2	25.0	15.3	25.4	37.7	27.9	37.0
5	7.1	17.0	28.7	9.1	7.7	6.7	21.3	20.0
10	8.0	23.3	24.3	13.4	16.5	20.1	26.3	24.4
15	14.3	15.7	8.1	16.2	16.5	19.0	10.7	10.0
20	6.4	5.7	4.5	7.6	7.3	4.1	5.4	3.9
25	7.2	3.8	2.5	3.8	3.3	2.6	3.3	1.6
30	5.6	6.2	1.9	3.6	5.6	1.9	2.0	1.3
35	5.6	1.3	0.6	6.6	2.0	1.1	0.7	0.3
40	5.6	3.8	0.6	3.6	2.8	1.3	0.7	0.3
50	9.5	0.6	1.9	6.6	7.3	0.2	0.8	0.3
60	6.2	1.9	0.0	3.5	2.4	0.9	0.2	0.3
70	6.2	0.6	0.6	1.9	1.2	0.9	0.4	0.3
80	10.3	1.3	0.0	1.9	1.2	1.5	0.0	0.0
90	4.8	0.6	1.3	1.9	0.8	1.1	0.3	0.3

Table 3. Comparison of the experimental data of Kacir et al [41] with the current theory for a 50 percent fiber volume fraction epon-828/E-glass composite.

Composite	Aspect ratio	E_{11} exp. (GPa)	E_{11} theory (GPa)
a	136	20.6	21.03
b	136	29.5	30.13
c	136	32.5	32.47
d	53	23.6	24.61
e	53	26.8	26.41
f	53	29.4	29.44
g	53	30.3	30.13
h	53	30.6	30.68

Table 4. Mechanical properties of the metal matrix composite constituents used in the theoretical calculations.

Material	Tensile modulus E_{11} (GPa)	Shear modulus G_{12} (GPa)	Poisson's ratio n_{12}
2009 Al.	72.0	27.0	0.320
.15 debris(.03)	77.2	27.9	0.315
.30 debris(.08)	84.2	29.1	0.308
SiC (W)	483.0	206.4	0.170
SiC (nicalon)	193.06	83.9	0.150

Table 5. Mechanical properties of the brittle matrix composite constituents used in the theoretical calculations.

Material	Tensile modulus E_{11}(GPa)	Tranverse modulus E_{22}(GPa)	Shear modulus G_{12}(Gpa)	Poisson's ratio ν_{12}	Poisson's ratio ν_{23}
Borosilcate glass	62.70	62.70	26.14	0.20	0.20
HMU graphite	358.54	10.34	14.41	0.26	0.36

Table 6. Mechanical properties determined for the PLM-9 matrix and published for the borosilicate glass rods used in the theoretical calculations.

Material	Young's Modulus E (GPa)	Poisson's Ratio ν	Thermal Coefficient α 1/ deg C	Tensile Strength σ (MPa)
7740 glass	62.7	0.20	3.25E-6	...
PLM-9 epoxy	3.3	0.36	70.0E-6	50.0

Table 7. Mechanical properties experimentally determined and theoretically predicted for model composites containing single and three continuous fiber systems.

7740-Glass PLM-9 Fiber Vol. Fract.	E_{11} (GPa) Exp.	E_{11} (GPa) CCM	α_{11} 1/ deg C Exp.	α_{11} 1/ deg C CCM
0.0187	3.5	4.4	44.5E-6	52.7E-6
0.0561	5.6	6.6	25.4E-6	35.6E-6

Vita

Gregory Paul Carman was born on March 15, 1959 to Beatrice Faye and William Charles Carman in Alexandria County, Virginia. He grew up in Woodbridge, Virginia a suburb of Washington D.C and attended Gar-field. high school. Upon graduation, he enrolled as an undergraduate student at Virginia Tech. and completed his B.S. degree in Engineering Science & Mechanics in 1985. Greg accepted an engineering position with the Department of the Army at Aberdeen Proving Ground, where he tested advanced armament systems. While employed at Aberdeen, he attended night school at Johns Hopkins University toward a M.S. degree in Materials Engineering. Greg accepted a graduate research assistant in the summer of 1987 at University of Alabama where he completed his M.S. degree in Materials Science and Engineering in December of 1988. In the summer of 1988 he began his doctoral program in the Engineering Science & Mechanics program at Virginia Tech.